Characterisation of AGATA Symmetric Prototype Detectors

Thesis submitted in accordance with the requirements of the
University of Liverpool for the degree of
Doctor in Philosophy

by

Matthew Richard Dimmock

Oliver Lodge Laboratory

April 2008

It is good to have an end to journey toward; but it is the journey that matters, in the end.

Ursula La Guin

A little rebellion now and then is a good thing.

Thomas Jefferson

Acknowledgements

Now that what seemed like a never ending struggle to deal with the bombardment of AGATA detectors at the University of Liverpool has come to an end, I would like to take this opportunity to thank everyone that helped me survive the last three years.

Firstly I would like to thank Prof Paul Nolan and Dr Andy Boston for their supervision, guidance and travel budgets that have allowed me to complete a thoroughly enjoyable, if not exhausting, PhD. I would also like to thank Dr Helen Boston for proof reading large sections of this work. It is now, looking back, that I can appreciate your frustration at having to re-read 300 pages of AGATA based facts and figures.

I would like to thank the support staff at the University for all their help. Special mentions go out to Terry Burns Dr John Cresswell, Dave Wells, Jim Thornhill and Dave Seddon. All of whom have contributed to my work over the last three years. I would also like to thank Dr Steve Barrett for his insightful discussions on electric field distributions and for the unbelievable pace at which he managed to perform data analysis with no less than four different techniques over a Christmas break.

A special thanks goes out to Dr Dave Joss and Dr Paddy *"my plane was cancelled"* Regan for the exceptional viva circumstances. After Dave rushing to get me to this point so I could graduate in the summer semester, it was a little unfortunate that Paddy decided to turn up to what was originally a 10.00am appointment at 4.00pm in the afternoon.

To the members of the nuclear physics group both past and present including Gerard, Jenny, Seb, Andy, Amy, Laura, Suzanne, Stefanos, Marina, Craig, Ste, Barry, Dave, Gez, Jimmy, Ben, Carl "you've still got some scanning to do" Unsworth and Martin. Thanks for everything and good luck to all of you who are yet to finish.

To all my good friends including Barry, Allan, Ollie, Nick, Uncle Jenky, Will, Mercer and Chris, thanks for your continued support and I can't wait for the summer so we can finally have that holiday. Also, to my family, for the last 26 years, I love you all and will be back in that there London a.s.a.p.

A final special mention goes out to those that have made the last few years so special:

- Reynald Cooper - My drinking partner and nemesis in the *bat cave* for all these years. The antics you managed to find yourself in, usually as a consequence of frequenting the RAZ, will be surpassed by no other. The competition was most definitely inspiring and .

- Alexander Grint - Again a fellow drinking partner and fellow physicist. I don't usually like to become mates with northern monkeys, but through our endless consumption of currys and missions to the gym it appears to have happened anyway. I know you'll make Wigan proud.

- David Scraggs - Well what is there to say. I thought I had seen everything and then Scraggo pops up on the radar. The most unpredictable man ever to have lived and a legend in your own right. The stories you tell never cease to amaze and also usually shock me. Good luck with becoming an author, I want first refusal on everything you publish.

- Anna McCarthy - Saving the best until last. My girlfriend for the last seven years, without whom I really wouldn't be where I am today. Words can't describe how much your unwavering support and dedication have meant. You always knew how to make me laugh which made the long hours bearable.

Thanks to you all and anyone I may have missed off the list. It's been a long time coming but worth the wait. PARTY!!!!!

Abstract

The Advanced GAmma Tracking Array (AGATA) is a European project that is aiming to construct a complete 4π High Purity Germanium (HPGe) gamma-ray spectrometer for nuclear structure studies at future Radioactive Ion Beam (RIB) Facilities. The proposed array will utilise digital electronics, Pulse Shape Analysis (PSA) and Gamma-Ray Tracking (GRT) algorithms, to overcome the limited efficiencies encountered by current Escape Suppressed Spectrometers (ESS), whilst maintaining the high Peak-to-Total ratio.

Two AGATA symmetrical segmented Canberra Eurisys (CE) prototype HPGe detectors have been tested at the University of Liverpool. A highly collimated ^{137}Cs (662keV) beam was raster scanned across each detector and data were collected in both singles and coincidence modes. The charge sensitive preamplifier output pulse shapes from all 37 channels (one for each of the 36 segments and one for the centre contact) were digitised and stored for off-line analysis. The shapes of the real charge and image charge pulses have been studied to give detailed information on the position dependent response of each detector. The singles data has enabled the investigation of the detector response through the bulk crystal. The coincidence data has been utilised to validate the electric field simulation code Multi Geometry Simulation (MGS). The precisely determined 3D interaction positions have allowed the comparison of experimental pulse shapes from single site interactions with those generated by the simulation. The data sets have also been utilised to validate the efficacy of the scanning procedure for producing comparable data sets for consecutive detectors. The absolute position sensitivity has been evaluated.

Both detectors have shown good energy resolution performance at low and high energy, 1.1keV at 60keV and 2.0keV at 1.3MeV. The levels of cross-talk have been measured and quantified. Analysis of the singles data has allowed rise time and image charge asymmetry matrices to be generated. From these, the charge transport properties through the crystal volume have been studied. MGS has been calibrated from pulse shape comparisons at over 2000 interaction sites within the detector. An average displacement of 2.5mm in x and y has been measured when comparing each of the average responses for the 2000 experimental interaction positions to a 1.0mm $\times$ 1.0mm MGS basis. Good agreement between the S002 and S003 experimental data sets has proven that the symmetric detectors respond in a similar manner and that the consecutive scans have been performed to a high precision. The absolute position sensitivity in the S002 detector has been calculated for different regions of the detector volume and levels of high sensitivity in the front ring have been observed.

Contents

List of Figures

List of Tables

Chapter 1

Introduction

The atomic nucleus is a complex quantum mechanical many-body system. The structure of such a system combines the macroscopic features of bulk nuclear matter, together with the microscopic properties of a finite number of fermions in a potential well. The stability of a given nuclear configuration is determined by the principle of minimisation of the total relativistic energy [Nil95]. If possible, a nuclear state will decay to one of lower energy, with some half-life, provided baryon number is conserved. If the nucleus is left in an excited state, following a reaction or decay from parent to daughter, it can undergo certain transitions between quantal states. The subsequent release of energy following a transition between two states can take the form of a gamma-ray photon. This is especially true if the nucleus is decaying from a state with high angular momentum. Properties of the states of a nucleus can be inferred by measuring the energies, half-lifes, angular correlations [Sta03], [Asa97] and linear polarisation [Jon02] of these photons. For the past forty years, gamma-ray spectroscopists have studied these properties with increasingly complex gamma-ray spectrometers [Bea95].

1.1 Gamma-Ray Spectrometers

Existing gamma-ray spectrometers e.g. EUROBALL [Pig01] and GAMMASPHERE [Lee90], consist of spherical arrays of escape suppressed High-Purity germanium (HPGe) detectors. They utilise Bismuth Germanate (BGO) scintillator shields that operate in anti-coincidence with the germanium detectors [Nol94]. Gamma-rays that Compton scatter into the shields

are vetoed. This increases the spectral quality, defined in terms of the Peak-to-Total (PT), the ratio of the integrated counts in the ^{60}Co photo-peaks, relative to the integrated counts in the spectrum for energies >100 keV [Sct94]. The PTs for the EUROBALL and GAMMASPHERE arrays are typically ~50-60% [Sim97]. The implementation of Compton supression does however limit the solid angle coverage of germanium. This results in photo-peak efficiencies (ϵ_{Phot}) of ~9%, where

$$\epsilon_{Phot} = \frac{Number\ of\ Full\ Energy\ Events}{Number\ of\ Incident\ Photons}. \tag{1.1}$$

For a spherical array of N detectors, the total photo-peak efficiency (ϵ_T) is given by

$$\epsilon_T = \frac{1}{4\pi} \sum_N \Omega \epsilon_{Phot}, \tag{1.2}$$

where Ω is the solid angle subtended by a single detector. Efficiencies of this magnitude were sufficient for spectroscopy in experiments with cross sections as low as 100nb [Lis00], at current stable beam facilities. High beam intensities (up to 10^{12} particles per second) allowed reaction rates sufficient to construct nuclear level schemes. However, with the development of Radioactive Ion Beam (RIB) laboratories in both Europe and the USA, a more efficient solution is required. Experiments with radioactive beams can offer intensities orders of magnitude smaller, large Doppler effects and high levels of background [Bla05]. The next major step in gamma-ray spectroscopy involves the construction of a 4π shell of germanium detectors, that utilises the technique of gamma-ray tracking [Del99] in electrically segmented germanium crystals [Rip06] to maintain good spectral quality. The development of the Advanced GAmma Tracking Array (AGATA) in Europe [Sim05], and the Gamma-Ray Energy Tracking Array (GRETA) in the USA [Bea03] are two collaborations currently working towards realising such a spectrometer. *Figure 1.1* shows the evolution of gamma-ray spectrometers since their implementation in the 1970's, in terms of the fraction of reaction channel that can be observed as a function of nuclear spin. It can be seen that both the AGATA and GRETA spectrometers will enable the study of high-spin states for nuclei produced with the smallest fraction of reaction channels.

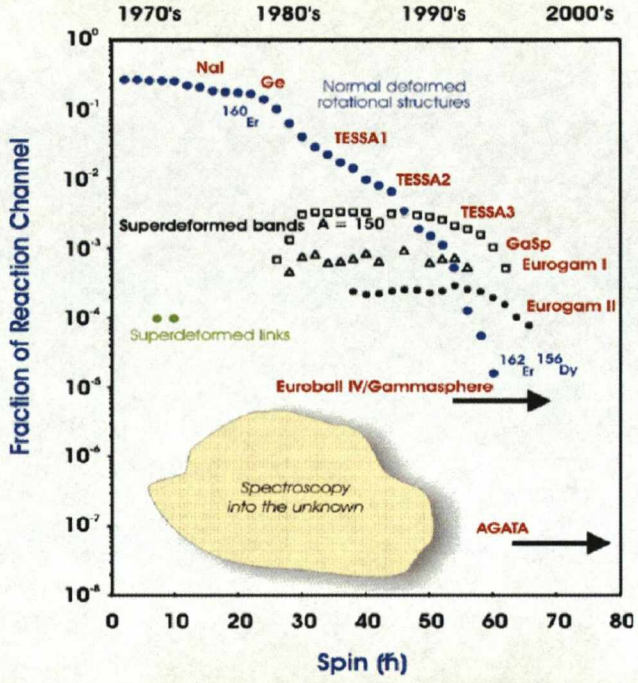

Figure 1.1: A time line showing the evolution of gamma-ray spectrometers [Sim05]. The AGATA and GRETA arrays will have the sensitivity to detect low intensity, high spin decays. This was not possible with previous, less efficient, germanium detector configurations.

1.2 Introduction to the AGATA Spectrometer

The AGATA spectrometer will be constructed from 180 large volume, encapsulated, asymmetric, electrically segmented germanium crystals (*Figure 1.2b*), mounted in 60 triple cluster cryostats. Such a configuration is necessary to give coverage over 4π while allowing a large enough inner diameter for ancillary detectors to be mounted. Each cryostat will house 3 different shapes of crystal and 111 channels of electronics. This is equivalent to 3 separate detectors per cryostat, each with 37 channels of associated electronics. A schematic representation of an asymmetric triple cluster is shown in *Figure 1.2a*. The red, green and blue crystals refer to the 3 different hexaconical shapes utilised to allow the most efficient tessellation when constructing the shell.

When a gamma-ray interaction occurs in any of the AGATA detectors, the charge pulse response of all 37 channels of that detector will be digitized. The 3D spatial coordinates and associated uncertainty of each interaction position can then be calculated from a chi-squared test of these waveforms against a look up table (basis set) of theoretically derived pulse shapes. This Pulse Shape Analysis (PSA) technique [Ola06] will be performed in real-time. Compton scattered events can then be reconstructed by algorithms that consider the kinematics of the scatter path. Such reconstruction is known as Gamma-Ray Tracking (GRT) [Lop04]. Tracking effectively utilises the maximal solid angle coverage of germanium (82%) to greatly improve the spectrometers efficiency. This technique has become possible because of the development of fast digital electronics that can deal with high count rates whilst preserving the leading edge of pulses [Laz03].

The AGATA array is being developed in several key phases:

1. The 5 triple cluster AGATA demonstrator will be assembled at INFN Legnaro in the second quarter of 2008. Testing of this *proof of principle* detector configuration will commence in the fourth quarter of 2008. It is expected that a physics campaign with existing stable beams will run throughout 2009.

2. As further triple clusters are assembled and tested, they will be added to the demonstrator. This evolving demonstrator will be moved to GANIL in France in 2010 and then to GSI in Germany in 2011. Thus allowing its performance to be tested with the widest range of beam and target combinations. At GANIL, the coupled cyclotrons and SPIRAL 1 will be used with the AGATA, EXOGAM and VAMOS spectrometers. At GSI, AGATA will be used at the target position of the Fragment Recoil Separator (FRS) to study exotic nuclei produced following high energy fragmentation

3. Development of the demonstrator in to the 1π array, consisting of 15 triple clusters, will be completed by the end of 2011. Beyond 2011, it is intended that the remaining clusters for expansion to the $4/3\pi$ and finally 4π AGATA array will be assembled and tested.

Table 1.1 summarises the expected performance of the AGATA array with respect to the GRETA array and the Compton suppressed arrays mentioned above.

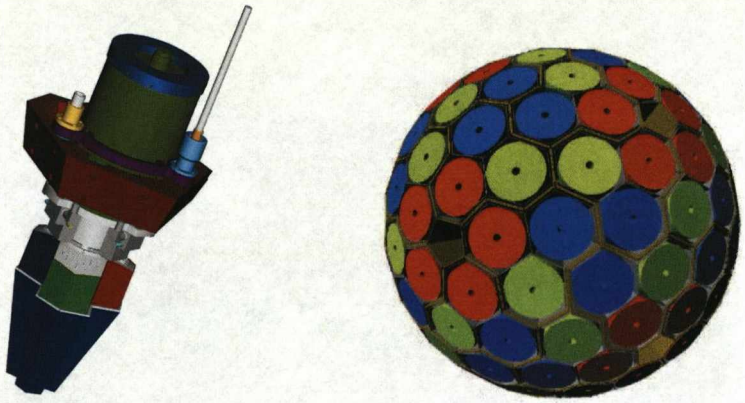

a) b)

Figure 1.2: a) A schematic diagram of an AGATA asymmetric triple cluster cryostat. The red, green and blue crystals refer to the 3 different hexaconical shapes utilised for efficient tessellation of the cryostats when assembling the 4π shell. b) A Geant model of the tessellated 180 detector, 4π AGATA shell. The two diagrams are not to scale with respect to each other.

Array	No. Crystals	Total Granularity	$\epsilon_{FEP}[P/T](\%)$ M_γ=1
EUROBALL III	239	239	9[56]
GAMMASPHERE	110	110	9[63]
AGATA Demonstrator	15	540	7[7]
AGATA 4π	180	6480	43[58]
GRETA 4π	120	4320	40[53]

Table 1.1: A summary of the performance of current detector arrays, relative to those being developed for future use (AGATA and GRETA). The values recorded [Alv04], [Lee06] and [Nol94] are for a multiplicity 1, 1 MeV gamma-ray interaction.

1.3 Thesis Overview

Precision measurements of two AGATA symmetric prototype detectors *S002* and *S003* have been performed at the University of Liverpool. Each detector was scanned with a highly collimated beam of mono-energetic photons. The resulting pulse shapes from the charge sensitive preamplifiers were digitised for off-line analysis. The analysis of this data had four

objectives:

1. The investigation into of the performance of the S002 detector in terms of energy resolutions, efficiencies, pulse shape parameterisation and levels of cross-talk.

2. Validation the the electric field simulation code Multi Geometry Simulation (MGS) with pulse shapes from single site interactions in the S002 detector in order that a accurate basis database may be constructed for on-line PSA.

3. Comparison of results from the identical scans of the S002 and S003 detectors to validate the reproducibility of the characterisation measurements.

4. Quantifiaction of the position sensitivity of each detector to set a lower limit from which two photon interaction positions can be resolved.

Chapter 2 of this thesis gives an initial introduction to the principles of radiation detection with solid state detectors. This is followed by a summary of the AGATA project in *Chapter 3*. *Chapters 4* and *5* give a detailed description of the detector simulation and experimental details. Finally, *Chapters 6* and *5* present the detailed analysis and interpretation of the results.

Chapter 2

Solid State Gamma-ray Spectroscopy

The principle of operation of any gamma-ray spectrometer is based on the generation of an electrical signal that is proportional to the energy deposited in the detector. The following chapter summarises the mechanisms through which gamma rays interact with matter, the processes that result in the detector response for both semiconductor and scintillation detectors, and the metrics used to quantify detector performance.

2.1 Interactions of Gamma-Rays With Matter

In the energy range from ~10keV to ~6MeV, photons interact with a material by transferring part or all of their energy to atomic electrons. There are three dominant interaction mechanisms through which this can occur. These are, Photoelectric Absorption (PA), Compton Scattering (CS) and Pair Production (PP).

2.1.1 Photoelectric Absorption

At photon energies of <150keV the dominant interaction mechanism is photoelectric absorption, shown schematically in *Figure 2.1a.* In this process the incident gamma ray will impart its full energy, E_γ, to a bound electron in an atom of the absorber. The resulting photoelectron is ejected from its shell (e.g. K shell) with kinetic energy,

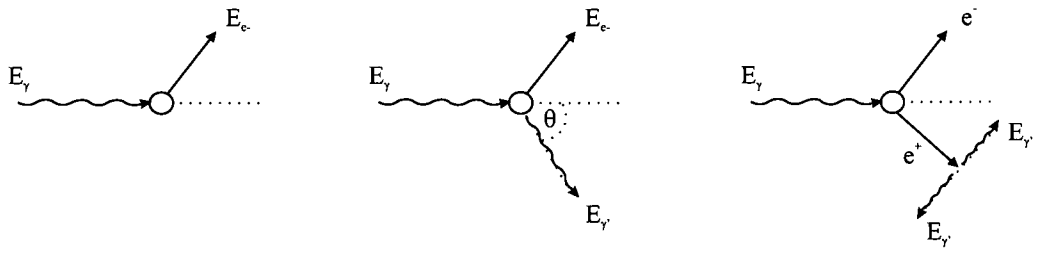

a) Photoelectric Absorption b) Compton Scattering c) Pair Production

Figure 2.1: A schematic illustration of gamma-ray interaction mechanisms in the energy range up to 6MeV

$$E_{e^-} = E_\gamma - E_b, \tag{2.1}$$

where E_b is the binding energy of that electron (12keV for germanium). This equation assumes that the recoil of the atom is negligible. The cross section for a gamma ray undergoing photoelectric absorption, σ_{PA}, varies with the Z of the absorber and the energy of the photon, and is given by:

$$\sigma_{PA} = k\left(\frac{Z^m}{E_\gamma^n}\right), \tag{2.2}$$

where m and n are numbers between 3.5 and 5 [Dav52].

2.1.2 Compton Scattering

For photons with energies in the range of ~150keV to ~6MeV, Compton scattering is the most probable form of interaction, shown schematically in *Figure 2.1b*. If Compton scattering occurs, the incident photon will impart a fraction of its incident energy to the recoil electron that is related to the angle θ through which it scatters. The energy of the scattered photon is given by,

$$E_{\gamma'} = \frac{E_\gamma}{1 + \frac{E_\gamma}{m_0 c^2}(1 - cos\theta)}, \tag{2.3}$$

where m_0c^2 is the rest mass energy of the electron, 511keV. The angular distribution of such incoherently scattered gamma rays can be described by the Klein Nishina formula [Kno00]. It gives the probability of a gamma-ray, with energy E_γ, scattering through an angle θ into a unit solid angle $d\sigma \ / \ d\Omega$ as,

$$\frac{d\sigma}{d\Omega} = Zr_0^2 \left(\frac{1}{1+\alpha\,(1-cos\theta)} \right)^2 \left(\frac{1+cos^2\theta}{2} \right) \left(1 + \frac{\alpha^2\,(1-cos\theta)^2}{(1+cos^2\theta)\,[1+\alpha\,(1-cos\theta)]} \right), \quad (2.4)$$

where $\alpha = E_\gamma \ / \ m_0c^2$, and r_0 is the classical electron radius (2.817fm). *Figure 2.2* shows a schematic representation of the differential scattering cross section distribution, as a function of incident photon energy. One can see the increased tendency for forward scattering as the photon energy increases.

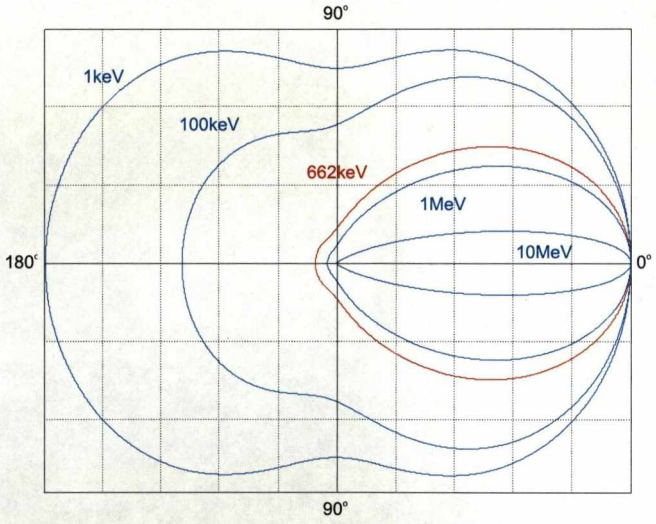

Figure 2.2: A plot showing the angular distribution of gamma-rays that scatter in germanium, as a function of incident photon energy, E_γ. As E_γ increases, the probability of forward scattering is shown to increase.

2.1.3 Pair Production

Photons with energies >1022keV can undergo pair production, shown schematically in *Figure 2.1c.* Pair production occurs when a photon interacts with the Coulomb field of a nucleus. The incident photon can be thought of as disappearing with the spontaneous creation of an electron and positron. The positron then thermalises through ionisation interactions before annihilating with a free electron. This annihilation results in the emission of (usually) two approximately co-linear gamma rays. The cross section for PP only becomes significant for photon energies >2.0MeV. Any excess energy (E_γ - 1022keV) is shared as the kinetic energy of the electron-positron pair.

2.1.4 Other Interaction Mechanisms

Photons can also interact with matter through other less probable mechanisms including coherent (Rayleigh) scattering and photo-nuclear reactions. Neither process is considered in this work as coherent scattering plays no role in signal generation and photo-nuclear reactions only become probable for E_γ >5MeV.

2.1.5 Photon Attenuation

The total cross section for an interaction occurring inside a material is the sum of the individual cross sections and is given by,

$$\sigma_{TOT} = \sigma_{PA} + \sigma_{CS} + \sigma_{PP}. \tag{2.5}$$

Thus, the probability per unit path length of a photon being absorbed by a material (linear attenuation coefficient) is the product of the total cross section and the density of atoms in the material given by,

$$\mu = N\sigma_{TOT} = \left(\frac{N_A\rho}{A}\right)\sigma_{TOT}, \tag{2.6}$$

where N_A is Avogadro's number (6.022mol^{-1}), ρ is the density and A is the atomic mass. For a beam of photons incident on a material, one can now use this coefficient to calculate

the relative number of photons that will traverse a given thickness, t, of that material, using the relation,

$$I(t) = I_0 e^{-\mu t}, \tag{2.7}$$

where I_0 is the intensity with no absorber present.

2.2 Solid State Detectors

Solid state crystalline detectors are widely used for gamma-ray spectroscopy and can be categorized as either inorganic scintillation or semiconductor detectors. Their high density offers much greater stopping power than for other detectors, for example gas based equivalents.

2.2.1 Band Theory of Solids

In solids, the discrete atomic electron energy levels form broad bands. The electrical properties of a material are determined by the occupation of these bands. Most crystalline materials can be grouped into one of three categories; conductor, semiconductor or insulator. Conductors can be considered as having either a partially filled valence band, or overlapping valence and conduction bands. Such overlap gives rise to the high electron mobility inherent to all conductors. This is not the case for intrinsic (pure) semiconductors or insulators. In both instances, the valence band is fully occupied, the conduction band is empty (at 0k), and the bands are separated by a set of *forbidden* energies. This energy distribution between the top of the valence band and bottom of the conduction band is termed the energy gap, E_g. For semiconductors, E_g is sufficiently small ($\sim$1.12eV for Si and $\sim$0.67eV for Ge) that electrons can be promoted across by thermal excitations. This gives rise to leakage currents experienced by all semiconductor detectors operated at non-zero temperatures. When an electron traverses the energy gap into the conduction band, the empty lattice site from which the electron moved is termed a *hole*.

Inorganic scintillators are essentially wide band gap insulators. For a scintillator such as thallium activated sodium iodide (NaI(Tl)), E_g is $\sim$7eV. Thermal excitations are not

sufficient to promote electrons across the energy gap, allowing them to be operated at room temperature with no leakage current.

The probability that an electron will occupy an electronic state at energy E can be calculated from the Fermi-Dirac distribution function, *f(E)*. It therefore follows that the concentration of electrons and holes that occupy each band is given as product of this distribution and the density of states, *g(E)* [Sze01]. For intrinsic semiconductors in thermal equilibrium (T >0k), the density of conduction electrons, n, is equal to that of the of valence holes, h. The Fermi energy, E_F, is the highest lying state that can be occupied at absolute zero temperature. For both insulators and intrinsic semiconductors, E_F lies midway between the valence and conduction bands.

2.3 Production of Charge Carriers

The unbound electrons resulting from the photon interactions described above can lose energy through collisions and radiative emission (Bremsstrahlung). These processes result in the creation of secondary charged particles that generate the detector response. For dense materials such as germanium, electrons resulting from photon energies <1MeV will have a range of ~1mm and lose energy predominantly through ionisations [Muk76]. The rate of collisional energy loss as a function of migratory distance can be calculated from the Bethe-Bloch formula [Knp65]. At higher energies, >20MeV, the losses due to Bremsstrahlung become comparable to those resulting from ionisation [Leo94].

Since the number of secondary charged particles generated has a direct effect on the signal to noise ratio of a spectrometer, an important parameter for both semiconductor and scintillation detectors is ionisation energy, ϵ_{pair}. ϵ_{pair} is the average energy required to make one electron-hole pair. For germanium and NaI(Tl), ϵ_{pair}≈3eV and ≈100eV respectively. The number of electron-hole pairs, N_{pair}, created per absorbed photon, with energy E_γ, is given by,

$$N_{pair} = \frac{E_\gamma}{\epsilon_{pair}}. \tag{2.8}$$

Experimentally, the statistical spread in the number of electron-hole pairs produced differs from that of simple Poisson statistics. The Fano factor (F) [Fan47] was introduced to account for this deviation and is given by,

$$\Delta N_{pair} = \sqrt{F N_{pair}} = \sqrt{F \cdot \frac{E_\gamma}{\epsilon_{pair}}}. \tag{2.9}$$

The Fano factor is ~0.08 for germanium and ~1.0 for NaI(Tl).

2.3.1 Semiconductor Diode Detectors

A semiconductor diode detector typically consists of an intrinsic (pure) semiconductor material with contacts bonded to each surface. The contacts are usually coupled to Field Effect Transistors (FETs) that offer the primary stage of amplification for the induced current signal. The current pulse is then integrated by a charge sensitive preamplifier that interfaces the detector to the electronics signal processing chain.

Although many of the principles outlined in the remainder of this section relate to semiconductor detectors in general, the detail of the information is specifically concerned with the properties of coaxial HPGe detectors. For further information on general semiconductor detector principles please refer to [Kno00].

Semiconductor Doping

The electrical properties of intrinsic semiconductors can be modified by the addition of small amounts of impurities (doping). If a pentavalent (Group V) dopant is added to an elemental tetravalent (Group IV) semiconductor, the resulting material is said to be n-type due to the presence of extra loosely bound electrons. Similarly, if a trivalent impurity is added, the structure is said to be p-type due to the presence of extra *holes*. The donor (n-type) and acceptor (p-type) sites are within 0.025eV of the valence and conduction bands respectively, shown in *Figure 2.3a.* Thus ensuring that the impurity energy levels are ionised at finite temperature.

Doping alters the charge carrier concentrations to the extent that they become completely dominated by the contributions from the donor (N_D) and acceptor (N_A) impurities, such

that,

$$n \cong N_D \tag{2.10}$$

and

$$p \cong N_A. \tag{2.11}$$

The p-n Junction

A p-n junction is formed when a p-type and n-type semiconductor meet in good thermodynamic contact. At the junction between the two materials, there is a net diffusion of electrons from the n-type region of high concentration to the p-type region of low concentration. The electrons and *holes* recombine leaving a net positive space charge on the n side and a net negative space charge on the p side. The electric field formed between the regions of opposite potential (*Figure 2.3b*) limits further diffusion and a steady state charge distribution is established (*Figure 2.3c*). This volume of space charge with depleted *free* charge carriers is termed the depletion region and extends into both sides of the junction. The interaction of gamma rays in the small depletion region of the junction results in the generation of electron-hole pairs. However, the electric field is not sufficient to prevent trapping and recombination. A detector of this nature would have poor operational characteristics as the signal to noise ratio would be small.

For HPGe detectors, the crystal is cut from a zone-refined high purity crystal that has a given impurity gradient. Whether the crystal is mildly p-type or n-type depends on the section from which the detector crystal is cut. The p-n junction is formed at the boundary between the crystal and its opposingly doped contact (p-i-n diode).

The Diode

The depleted region described above exhibits the properties of a diode, in that it will readily conduct current when a forward bias is applied, but will conduct minimal current if the bias is reversed. The voltage-current curve for such a junction is shown schematically in *Figure 2.4*. For the junction to perform successfully as a detector, it must be operated in the

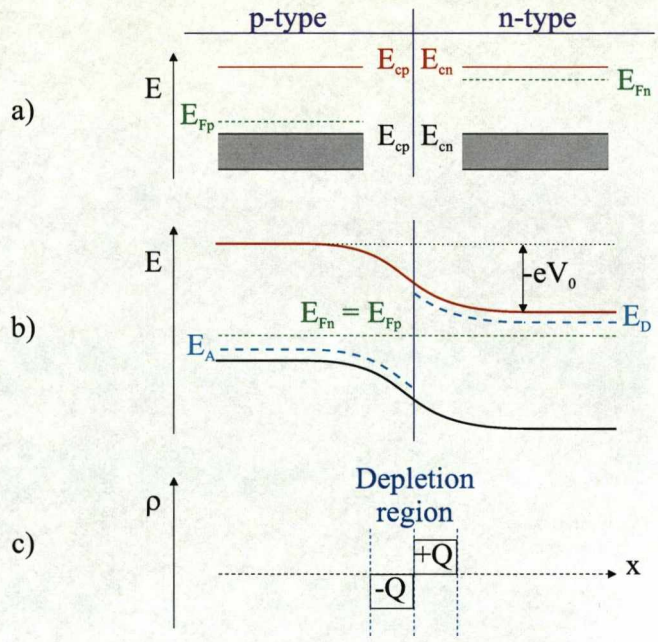

Figure 2.3: A schematic representation of an ideal (abrupt) p-n junction in equilibrium. a) The band structure of separated p-type and n-type materials. b) A junction in equilibrium: a potential gradient is induced in the depletion region following *free* charge annihilation. V_0 is the built-in potential. c) The space charge density in the depletion region.

reverse bias region, indicated in green. This ensures the current that flows is a result of minority carriers and is small compared to that generated from photon interaction. If too great a reverse bias is applied the diode will fail (breakdown).

A reverse bias applied across the volume will serve to increase the width of the depletion region, significantly enhance the strength of the electric field, and diminish the junctions capacitance. The width of the depletion region as a function of the applied bias, V, is given by [SB00],

$$W = \left[\frac{2\epsilon\,(V_0 - V)}{q}\left(\frac{N_A + N_D}{N_A N_D}\right)\right], \tag{2.12}$$

where ϵ the dielectric constant; the product of permitivity of free space, ϵ_0, and the permitivity of the medium, ϵ_r, and V_0 is the built-in potential. For mildly n-type crystals, such as

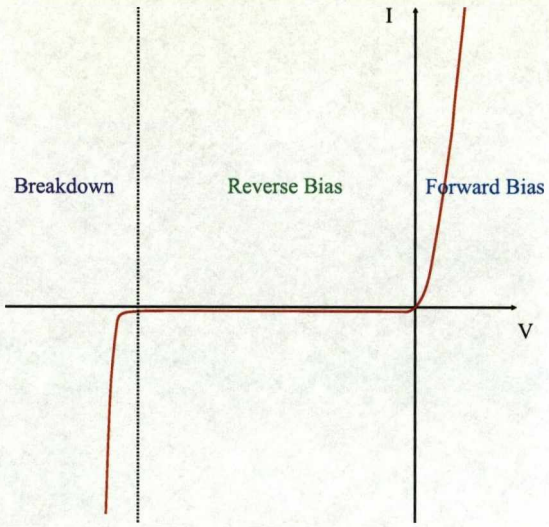

Figure 2.4: Voltage - current characteristics of a p-i-n diode. When operated with a forward bias, the current increases with applied voltage. However, when operated with a reverse bias, the induced current is suppressed. If too high of a reverse bias is applied, the diode will fail (breakdown).

those utilised in the AGATA array, N_D dominates and the width is inversely proportional to this number of impurities, for a fixed bias voltage. Thus, the highest purity material is utilised to maximise the operational volume of the detector. A bias of 1000-5000V is required to deplete a large volume HPGe detector.

The magnitude of the electric potential, φ, inside the depletion region can be calculated at any point inside the volume by solving Poisson's equation,

$$\nabla^2 \varphi = -\frac{\rho(\vec{r})}{\epsilon}, \tag{2.13}$$

where ρ is the net charge density given by,

$$\rho(\vec{r}) = e(N_D - N_A). \tag{2.14}$$

The electric field that extends over the width of the depleted volume can be calculated from,

$$E(\vec{r}) = -\frac{d\varphi}{d\vec{r}}. \tag{2.15}$$

For a HPGe detector of simple coaxial geometry, the electric field is calculated as [Kno00],

$$E(\vec{r}) = \frac{-\rho}{2\epsilon} + \frac{V + \left[\frac{\rho}{4\epsilon}\left(r_2^2 - r_1^2\right)\right]}{r \cdot ln\left(\frac{r_2}{r_1}\right)}, \tag{2.16}$$

where r_1 and r_2 are the inner and outer radii of the crystal.

Detector Contacts

In order to collect the charge generated from a photon interaction, the surfaces of the detector must be furnished with contacts. For a p-i-n diode, such as an AGATA detector, a p^+ contact is applied to one surface and an n^+ contact to the other. The n^+ contact is formed by lithium evaporation and diffusion. The p^+ contact is formed by ion implantation of boron acceptor ions. In order to reverse bias the detector, a positive voltage is applied to the n^+ contact with respect to the p^+ surface.

For an n-type crystal under reverse bias, the p^+ surface is the injecting (also termed *rectifying*) contact and the n^+ surface is non-injecting (also termed *blocking*). This situation is the reverse for a p-type crystal. When the voltage is applied across the contacts, the depletion region extends from the *rectifying* contact toward the *blocking* contact. Once a sufficient potential is reached to fully deplete the detector, any excess potential increases the electric field strength uniformly through the volume.

Properties of Germanium

Germanium is a group IV semiconductor with a face-centered cubic (FCC) diamond lattice structure as shown in *Figure 2.5a.* The properties of the crystal depend on the atomic arrangement of the different lattice planes. The lattice planes are defined in terms of their Miller indices [Sze01], shown in *Figure 2.5b.* The important physical properties of germanium are presented in *Table 2.1.*

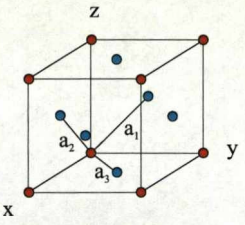

a) Germanium crystal structure

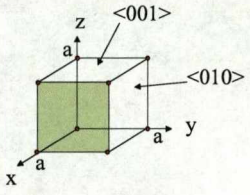

b) <100> plane

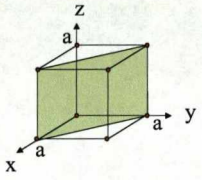

c) <110> plane

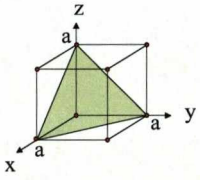

d) <111> plane

Figure 2.5: A schematic representation of the crystal structure of germanium. a) Ge crystal showing tetrahedral bonding and the primitive lattice, $a_{1,2,3}$. b), c) and d) show the major lattice planes labelled by their corresponding Miller indices.

Atomic number (Z)	32
Atomic weight (A)	72.6
Atoms	10^{22}cm^{-3}
Density	5.32gcm^{-3}
Crystal structure	FCC (diamond)
Lattice parameter	5.658A
n_i (T = 300k)	2.4x10^{13}
Dielectric constant, ϵ_r	15.8
Intrinsic resistivity (T = 300k)	16Ωcm
Energy gap (T = 300k)	0.67eV indirect
Energy gap (T = 0k)	0.75eV indirect
Electron mobility, μ_e (T = 300k)	3900cm^{2}Vs^{-1}
Hole mobility, μ_h (T = 300k)	1900cm^{2}Vs^{-1}

Table 2.1: A table showing the physical properties of germanium. Values taken from [Che07]

Anisotropic Drift Velocity in Ge

Both electrons in the conduction band and *holes* in the valence band undergo a net migration in the presence of an applied electric field. The drift of the charge carriers is the result of the combination of thermal diffusion and net drift velocity. The velocity vector with which each charge carrier migrates is in a direction parallel to the $\vec{E}$-field lines and is proportional to the magnitude of the field. The charge carrier drift velocities $\vec{v}_e$ and $\vec{v}_h$ are related to $\vec{E}$ by,

$$\vec{v}_e(\vec{r}) = -\mu_e \vec{E}(\vec{r}), \ \vec{v}_h(\vec{r}) = \mu_h \vec{E}(\vec{r}), \tag{2.17}$$

where μ_e and μ_h are the electron and *hole* mobilities respectively. At high electric fields, the charge carrier mobilities and hence the drift velocities are anisotropic. They depend on the direction of the electric field vector with respect to the crystallographic lattice orientation. This is a direct result of the band structure in semiconductor materials such as germanium. The detailed energy band diagrams for semiconductors are very complex and require the solution of the Schrodinger equation for a periodic potential. They show the relation between the electron energy and the electron wave vector, k. *Figure 2.6* presents the calculated band structure for germanium. The minimum energy of the conduction band is shown in red, whilst the maximum energy of the valence band is shown in blue.

From this diagram, it can be seen that the absolute minimum of the conduction band lies along the <111> axis, while the maximum of the valence band lies along the <110> axis. As the bottom of the conduction band occurs where the effective momentum is non-zero, germanium is classified as an indirect semiconductor. For all indirect semiconductors, both a change in energy and also momentum ($\rho = \hbar k$) is required to promote an electron from the top of the valence band to the bottom of the conduction band.

In 3D lattice space, the band structure of the material will determine the number of wave vector states available for each energy level. Interpolation between the states for each specific energy forms iso-energetic surfaces. Integration of the wave vectors in each 3D surface yields the density of vector states for a given energy. At any position in the crystal lattice, the charge carrier drift velocity can be calculated from the charge carrier

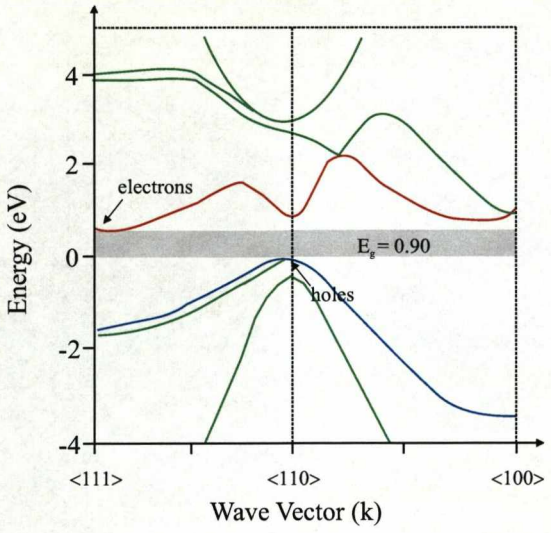

Figure 2.6: A schematic representation of the calculated band structure in germanium. The maximum in the valence band is taken as the zero reference. The minimum energy of the conduction band is shown in red, whilst the maximum energy of the valence band is shown in blue.

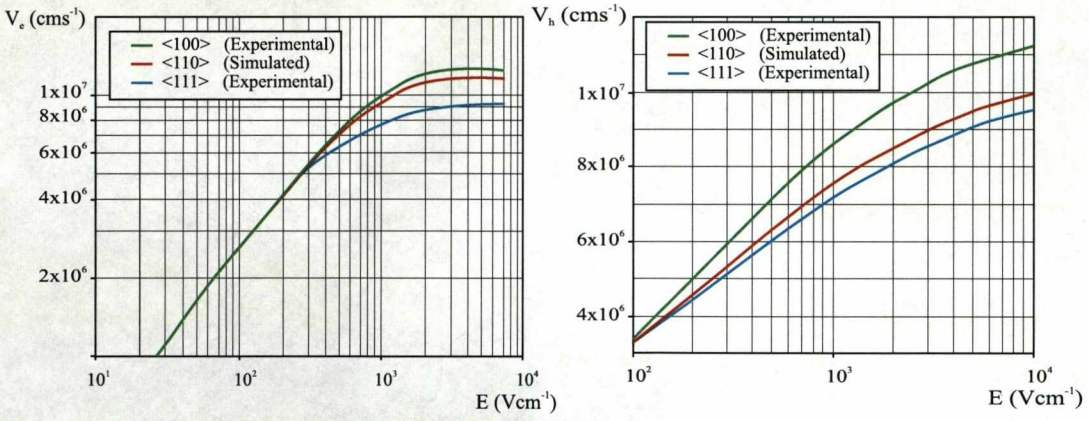

Figure 2.7: a) Electron [Mih00] and b) *hole* [Bru06a] drift velocities as a function of electric field strength for germanium (at 80k) along the three major crystallographic axes, <111>, <110>, and <100>.

concentrations and the $\vec{k}$ dependence of the energy states. The electron and *hole* drift velocities in HPGe detectors have been investigated in [Mih00], [Bru06a] and [Bru06b]. The trends for the three major crystallographic orientations, plotted as a function of electric field strength, are presented in *Figure 2.7*. Note the different scales on each plot. In all cases, the drift velociy is shown to increase linearly with the applied electric field and plateau at high field strengths. Also, the *hole* drift velocity is shown to be systematically slower than the electron drift velocity in each direction. The parameters used to fit the data in [Mih00] and [Bru06b] were extracted using an empirical formula that describes the projection of the drift velocity in the field direction [Oma87], given as,

$$v_l = \frac{\mu_0 E}{\left(1 + (E/E_0)^{\beta}\right)^{1/\beta}} - \mu_n E, \tag{2.18}$$

where μ_0 is the ohmic (low field) mobility, β is a fitted parameter and μ_nE accounts for the negative differential velocity of electrons at high fields (>3kVcm^{-1}). The values for the parameters expressed in *Equation 2.18* are presented in *Table 2.2* and *Table 2.3*.

Ref.	<100>			
	μ_0 cm^2/V·s	β	E$_0$ V/cm	μ_n cm^2/V·s
[Mih00] (elec)	40180	0.72	493	589
[Bru06b] (elec)	38609	0.805	511	-171
[Reg77] (*hole*)	66333	0.744	181	-
[Bru06b] (*hole*)	61824	0.942	185	-

Table 2.2: Parameters for the calculation of electron and *hole* drift velocities for an electric field applied along the <100> direction.

Signal Generation in Germanium

The localised distributions of electrons and *holes* resulting from a photon interaction can be considered as charge clouds. The Coulomb fields that emanate from these charge clouds extend throughout the entire crystal volume. As the charge clouds drift toward their collecting electrodes, according to the strength of the electric field, this Coulomb field changes. For a multi-electrode detector, a current is induced on all conducting electrodes in contact

Ref.	<111>			
	μ_0 cm^2/V·s	β	E_0 V/cm	μ_n cm^2/V·s
[Mih00] (elec)	42420	0.87	251	62
[Bru06b] (elec)	38536	0.641	538	510
[Reg77] (*hole*)	107270	0.580	100	-
[Bru06b] (*hole*)	61215	0.662	182	-

Table 2.3: Parameters for the calculation of electron and *hole* drift velocities for an electric field applied along the <111> direction.

with the crystal volume. The charge, and hence the current induced on an electrode can be calculated from Gauss' law,

$$Q = \oint_S \epsilon E \cdot ds, \tag{2.19}$$

where ϵ is the dielectric constant of the medium and E is the electric field through the closed surface, S. However, this would be an arduous process that would require solving for the instantaneous electric field E calculated at each position along the charge carriers trajectory. A simpler method for calculating the instantaneous charge and current induced on an electrode of infinite planar configuration was first proposed by Ramo [Ram39], using the equations,

$$Q = -q\varphi_0(x) \tag{2.20}$$

and

$$i = qv \cdot E_0(x), \tag{2.21}$$

where v is the instantaneous velocity of the charge carrier q. The parameters $\varphi_0(x)$ and $E_0(x)$ are the electric potential and electric field that would exist at the instantaneous position of the charge if the selected electrode is at unit potential, all other electrodes are at zero potential, and all charges are removed from the system. The parameters φ_0 and E_0 are known as the weighting potential and weighting field and form a mathematical construct that is a measure of electrostatic coupling between the moving charge and the sensing electrode.

The application of Ramo's theorem to the case of a multi-electrode semiconductor diode detector is non-trivial, due to the non-uniform electric field. This concept has been reviewed by [Rak88] and [He00]. For a charge moving an infinitesimal step, dl, between positions in an inter electrode space, it has been shown that the instantaneous induced current on an electrode, $i_{electrode}$, can be calculated as a function of the normalised potential ($V/V_{electrode}$) at that position,

$$i_{electrode} = \frac{d\left(\frac{qV}{V_{electrode}}\right)}{dt} = q \cdot \frac{d\left(\frac{V}{V_{electrode}}\right)}{dl} \cdot \frac{dl}{dt}, \tag{2.22}$$

where $V_{electrode}$ is the external bias (1V) on the given electrode and V is the potential at the position of charge q. This step allows the time dependence of the calculation to be translated into a position dependence. As stated previously, this calculation is valid provided all other electrodes are grounded. The normalised potential is the weighting potential. The gradient of the potential is the weighting field E_w, given by,

$$\nabla\left(\frac{V}{V_{electrode}}\right) = -E_W. \tag{2.23}$$

Figure 2.8 shows a schematic representation of the calculated weighting potential for a multi-electrode planar detector. Electrode one is at unity potential and all other electrodes are grounded. Plots of the induced current on electrode one are shown for two separate interaction positions, *q1* (purple) and *q2* (blue). The gaps between the lines represent the gradient of the potential. The field is strongest close to the contact and falls off as a function of distance. Note the change in scale from 0.05 per step to 0.01 per step at large distances from electrode one. The form of the weighting field depends on the specific geometry of the detector. From the formalism described above, the induced current onto electrode one is calculated as,

$$i(t) = -q \cdot v(\vec{r}(t)) \cdot E_w(\vec{r}(t)). \tag{2.24}$$

Thus the collected charge, Q, is given as,

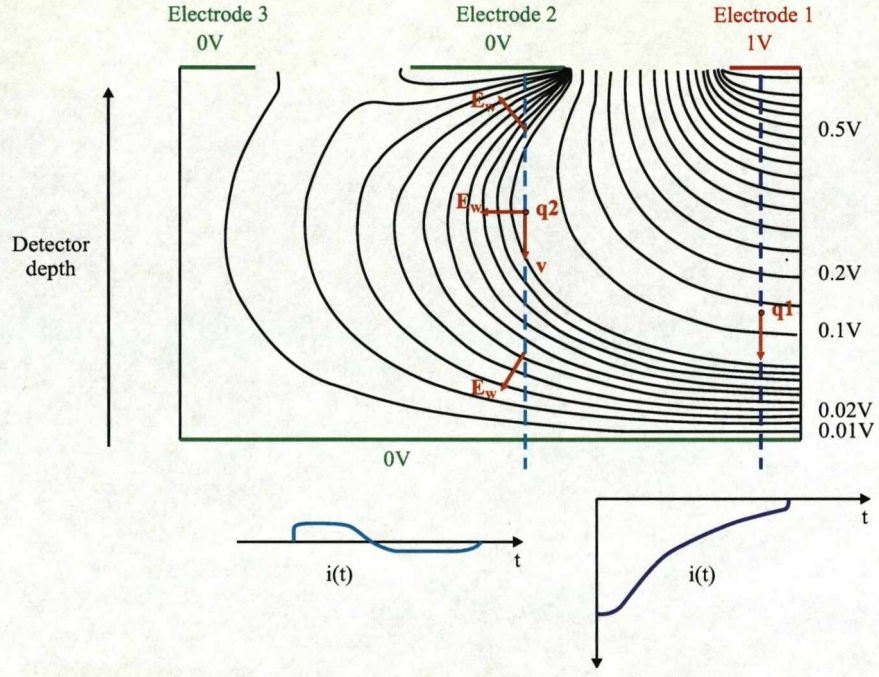

Figure 2.8: The calculated weighting potential distribution for a multi electrode planar HPGe detector [Rak88]. The black lines are the potential surfaces. The gaps between the lines represent the gradient of the potential. Note the change of scale from 0.05 per division to 0.01 per division at large distances from electrode 1. Electrode 1 is at unity potential and all other electrodes are grounded. Plots of the induced current on electrode one are shown for two separate interaction positions, q1 and q2.

$$Q = \int i(t)\,dt = -q\int_{x2}^{x1} E_W dl = q\left[V_W(x1) - V_W(x2)\right], \tag{2.25}$$

where $x1$ and $x2$ are the positions before and after the displacement of charge q.

The application of the weighting field to coaxial detectors is discussed in more detail in *Section 4.4.7.*

2.3.2 Scintillation Detectors

An array of BGO and NaI scintillators was utilised in the scanning of the AGATA prototype detectors. As such, an overview of the properties of scintillation detectors is given in this

section for completeness. For a comprehensive discussion of the operational characteristics of scintillators please refer to [Kno00].

A scintillation detector consists of a scintillator material coupled to a photosensitive device and preamplifier. An effective scintillation detector requires:

1. High efficiency for converting incident energy into light.
2. Light yield that is proportional to the incident energy (linearity).
3. Good light collection. The material must be transparent to the wavelength of its own light emission.
4. A refractive index that is close to that of glass in order that the scintillation light may be efficiently coupled to a photomultiplier tube (PMT) or photo diode.
5. A short decay time to ensure the detector can process high count rates.

NaI(Tl) detectors have better energy resolution than BGO detectors, see *Section 2.3.4* but are less efficient due to their lower density.

2.3.3 Detector Preamplifiers

The role of the preamplifier is to interface the detector to the electronics signal processing chain. It shapes and amplifies the input signal. For germanium detectors, the input stage is the amplified current signal from a FET. The FETs are mounted close to the feed throughs from the detector contacts to minimise capacitive loading.

Charge sensitive preamplifiers are used for most gamma-ray spectroscopy applications. A simplified representation of a charge sensitive preamplifier is shown in *Figure 2.9*. The preamplifier integrates the current on the input capacitor, C_i, before discharging through the the resistive feedback network. The decay time constant of the feedback circuit ($\tau = R_F C_F \approx 50\mu s$) is chosen to be large relative to the charge collection times in the given detector material. The magnitude of this pulse is proportional to the energy deposited in the detector.

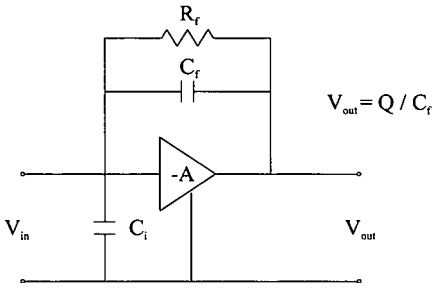

Figure 2.9: Simplified circuit diagram of a charge sensitive preamplifier.

Figure 2.10 shows the charge sensitive preamplifier response from all thirty six outer contact channels of the S002 AGATA symmetric segmented HPGe detector. The detector segment labelling convention is also shown. The response shown is for a photon that interacts once in the detector, a multiplicity one event. As the charge is collected in only one segment, the event is also classified as fold one. The charge pulse induced on the cathode that collects the charge, segment A2, is highlighted in red. The movement of the charge carriers in segment A2 also induces signals on all other electrodes. These signals are refered to as transient or image charge pulses. The magnitude of these image charges depends on the amount of energy deposited and the proximity of the interaction to the neighbouring segments. Thus, in general, image charges are only observed in the segments directly surrounding the interaction segment (highlighted in green).

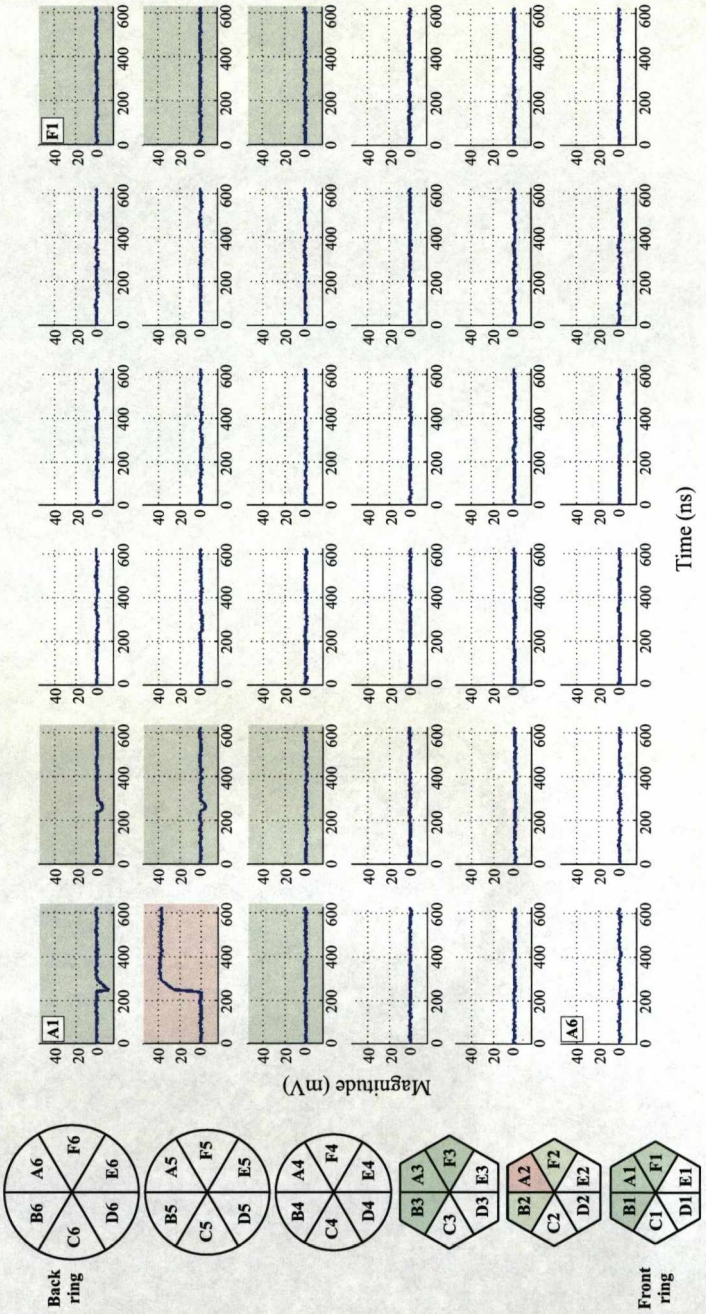

Figure 2.10: A diagram showing the charge sensitive preamplifier output for a multiplicity one event and the detector segment labelling convention. The outer contact responses for all thirty six segments of the S002 AGATA symmetric prototype detector are shown. The segment in which the real charge is deposited is highlighted in red. The segments directly surrounding the interaction segment are highlighted in green.

2.3.4 Detector Performance Metrics

As introduced in *Section 1.1*, the photo-peak efficiency (ϵ_{Phot}) and peak-to-total ratio (PT) are two simple parameters that give a quantitative measure of the sensitivity of a given detector configuration. The application of such detectors in nuclear spectroscopy requires the ability to resolve closely spaced photopeaks in complex spectra. As such, the energy resolution of the spectrometer is also a metric of fundamental importance.

Energy Resolution

The intrinsic energy resolution of a detector, ΔE_i, is given by the quadrature sum of the statistical, detector and electronic noise contributions [Kno00]:

$$(\Delta E_i)^2 = (\Delta E_D)^2 + (\Delta E_X)^2 + (\Delta E_E)^2 \tag{2.26}$$

- ΔE_D accounts for the inherent statistical fluctuation in the number of charge carriers created by an interaction and is given by:

$$\Delta E_D = 2.35\sqrt{\frac{F}{N_{pair}}} \tag{2.27}$$

- ΔE_X represents the variations due to signal losses. For semiconductor detectors this would relate to problems with incomplete charge collection. This effect is most prominent in large volume detectors with regions of low E-field strength. For scintillators, this term would account for losses in light yield through the signal chain.

- ΔE_E accounts for the electronic noise that results from the electronic components following the detector e.g. preamplifiers.

The standard measure of the energy resolution is the Full Width at Half the Maximum height ($FWHM$) of the photopeak. For HPGe semiconductor detectors, the FWHM is typically 1.9keV at 1.3MeV (0.14%). Typical energy resolutions for scintillation detectors are of the order of $\sim$ 7% for NaI(Tl) and $\sim$ 10% for BGO.

For experiments with accelerated beams ($\beta = v/c$), the residual nucleus may emit gamma rays whilst moving with a velocity that is an appreciable fraction of the speed of light. Thus the detected energy, E_γ, will be Doppler shifted according to,

$$E_\gamma = E_{\gamma 0}\sqrt{1-\beta^2}\frac{1}{1-\beta cos\theta_\gamma}, \tag{2.28}$$

where $E_{\gamma 0}$ is the true energy and θ_γ is the reference photon emission angle relative to the trajectory of the recoiling nucleus. Thus, for a finite detector opening angle ($\Delta\theta_\gamma$), the observed photon energy is broadened by,

$$\frac{\Delta E_\gamma}{E_\gamma} = \frac{\beta sin\theta_\gamma}{1-\beta cos\theta_\gamma}\Delta\theta_\gamma, \tag{2.29}$$

For a detector configuration used with accelerated beams, the relation for calculating the total photopeak FWHM (ΔE_γ) must incorporate both intrinsic (ΔE_i) and Doppler effects. This equation is given as,

$$\Delta E_\gamma = \sqrt{\Delta E_i^2 + \Delta E_\theta^2 + \Delta E_\phi^2 + \Delta E_v^2}, \tag{2.30}$$

where ΔE_θ, ΔE_ϕ and ΔE_v are the contributions to Doppler broadening resulting from the opening angle of the detector, the angular spread of the recoils, and the velocity spread of the recoils respectively.

The development of segmented large volume HPGe detectors has allowed the localisation of the first interaction position to the volume of a given segment. Thus constraining $\Delta\theta_\gamma$ and reducing the effects of Doppler broadening [Wie02].

Resolving Power

In order to quantify a spectrometers ability to resolve two closely spaced peaks, a figure of merit termed the resolving power, R, was introduced [Nol90]. The resolving power incorporates both PT and ΔE_γ and is given by,

$$R = \frac{SE_\gamma}{\Delta E_\gamma}PT, \tag{2.31}$$

where SE_γ is the average peak separation.

Efficiency

The counting efficiency of germanium detectors can be defined by three primary measures.

1. *Absolute efficiency* (ϵ_{abs}) - The ratio of the number of detected events to the number of photons emitted by the source. This ratio is affected by the source/detector geometry.

2. *Intrinsic efficiency* (ϵ_{int}) - The ratio of the number of detected events to the number of photons incident on the detector.

3. *Relative efficiency* (ϵ_{abs}) - The efficiency of a germanium detector relative to a NaI(Tl) crystal, 76mm in diameter and 76mm in length, measured with ^{60}Co source placed 250mm from the crystal. This can be calculated by dividing the absolute efficiency, for detecting 1.3MeV full energy peak events, by $1.244\text{x}10^{-3}$ [Gil95] and gives a means of comparing the efficiency of any geometry of germanium detector with any other.

The efficiency parameters listed above are usually defined in terms of counts in the photo-peak.

Chapter 3

Development of the AGATA Spectrometer

The AGATA demonstrator is the *proof of principle* precursor to the 4π AGATA array. Initial operation of the demonstrator will allow the performance of the hardware and software to be fully tested. As further detector and processing elements are constructed, they will be added to the array increasing the spectrometers efficiency. This chapter discusses the components of the demonstrator and summarises their implementation.

3.1 AGATA Triple Cluster Detector Construction

Both the demonstrator and final array will be constructed from a tessellated shell of asymmetric triple cluster cryostats. Each cryostat contains:

1. Three hexaconical segmented, encapsulated, asymmetric n-type HPGe crystals of closed ended coaxial geometry.
2. Cold FETs to offer the primary stage of signal amplification.
3. Feed-through electronics.
4. Charge sensitive preamplifiers to interface to the signal processing chain.

The encapsulated crystals supplied by Canberra Eurisys are transported to the Institut fur Kernphysik in Cologne, Germany, where they are mounted in cryostats manufactured by Cryostat and Detector Technique Thomas (CTT). The FETs, feed-through electronics and preamplifiers are also installed by CTT. All components except for the preamplifier boards are cooled with liquid nitrogen (LN2). The cold sections of the cryostats are operated at ~86k. A copper cold finger that branches out to the back of the encapsulated crystals ensures that heat is conducted away from the cold components. The volume of the dewar enables the triple cluster to remain operational for a 24 hour period. Both the dewar and crystal temperatures can be monitored over separate platinum thermistors (PT100s). The cryostat is held under vacuum at a pressure of less than 10^{-6} mbar. This ensures thermal isolation of the cold components from the outer wall of the cryostat. The inner encapsulated crystals are separated from their outer walls by ceramic spacers of minimal surface area.

3.1.1 AGATA Detector Specifications

The three asymmetric crystals are labelled red, green and blue, corresponding to their different geometries. *Figure 3.1* shows a schematic representation of the asymmetric crystals and the cryostat that holds them.

Each crystal has a lithium drifted (p^+) centre contact and 36-way electrically segmented boron implanted outer contact (n^+). The crystal volume is fashioned from a 90mm long, 80mm diameter cylinder of refined HPGe. The final hexiconical shape is formed by grinding away 6 tapered surfaces, that extend 76.8mm from the front face of the cylinder. A 5mm radius hole is bored from the centre of the back plane, 77mm through the depth of the crystal. The lateral segmentation splits the crystal into six rings of depth 8:13:15:18:18:18mm, measured from the front. In turn, each ring is electrically segmented into six equal portions whose volumes depend on the ring in which they are located.

3.1.2 AGATA Symmetric Prototype Detector Construction

The first three AGATA encapsulated crystals delivered from Canberra were of symmetric hexaconical shape. Each of these prototypes were mounted separately in their single symmetric tapered test cryostats, also manufactured by *CTT*. The symmetric shape of the

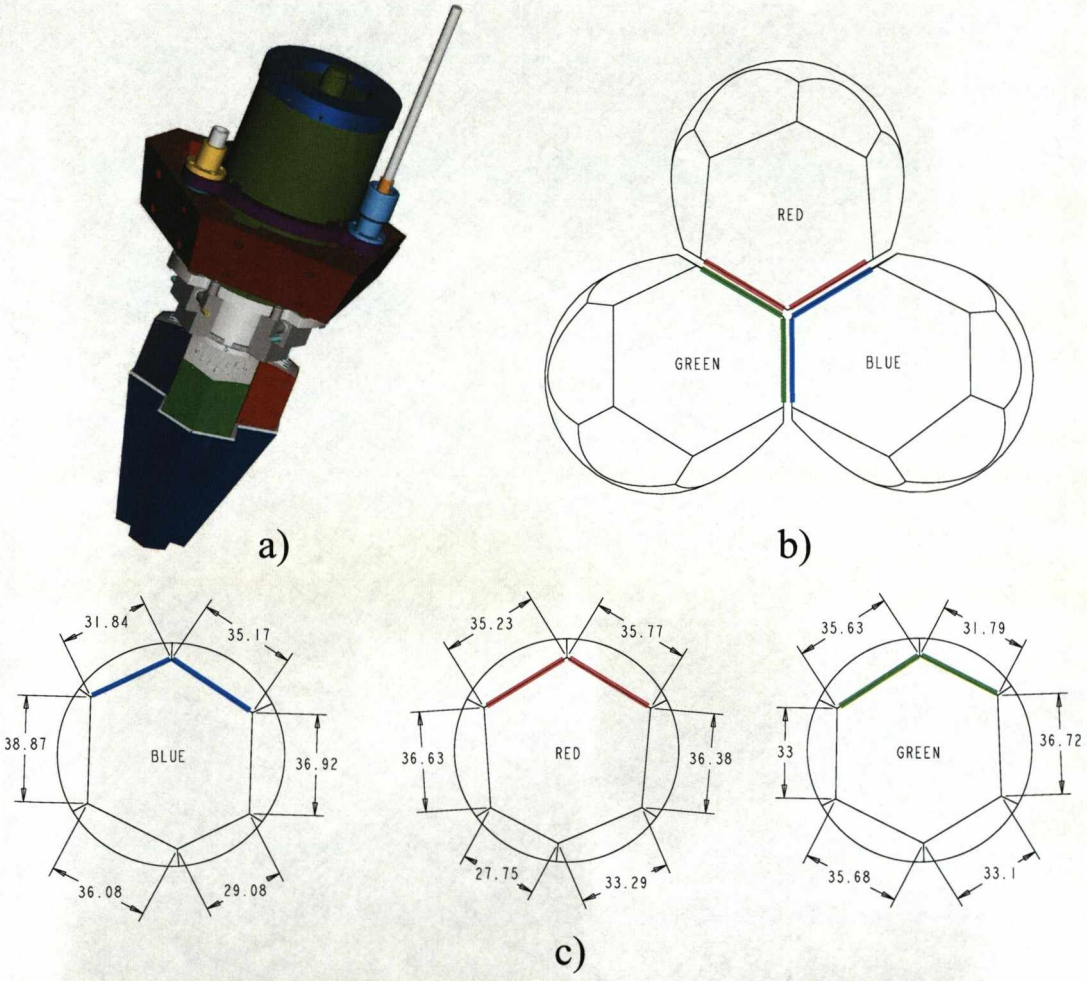

Figure 3.1: The AGATA asymmetric cryostat *ProEngineer* model and projections. a) Representation of the asymmetric AGATA triple cluster cryostat. b) Schematic diagram of the asymmetric crystal configuration. c) Blue, red and green asymmetric crystal geometry specifications.

S001, S002 and S003 detectors minimised the cost and simplified the characterisation techniques in the initial analysis of experimental data. The principle of construction of each of the three AGATA symmetric prototype cryostats with associated electronics were essentially the same. However, differences in preamplifiers and internal grounding components occurred as the project evolved. Each encapsulated crystal consists of the germanium separated from its aluminium can by 0.4mm at the front and sides, and by 21.8mm at the back. The aluminium can is 0.8mm thick and is suspended in its cryostat from a copper cold finger, fixed to the back plane of the aluminium encapsulation. *Figure 3.2a* shows a photograph of the S002 AGATA symmetric prototype detector mounted on its side. *Figure 3.2b* and *Figure 3.2c* show a zoomed view with and without its lower casing, respectively. In *Figure 3.2c*, the feed-through electronics are masked by insulating foil.

A schematic representation of the symmetric prototype crystal geometry is shown in *Figure 3.3*. One can see a 3D reconstruction of the crystal, *Figure 3.3a*, and its projections, *Figure 3.3b* to *Figure 3.3d*. *Table 3.1* lists the operational characteristics of the three AGATA symmetric prototype detectors. For a detailed view of the detector specifications, please refer to *Appendix A*.

Parameter	AGATA S001	AGATA S002	AGATA S003
Inner contact voltage	+4000V	+5000V	+4000V
Outer contact voltage	0V	0V	0V
Impurity concentration (front)	$1.5\text{x}10^{10}\text{cm}^{-3}$	$1.8\text{x}10^{10}\text{cm}^{-3}$	$1.55\text{x}10^{10}\text{cm}^{-3}$
Impurity concentration (back)	$4.3\text{x}10^{9}\text{cm}^{-3}$	$5.1\text{x}10^{9}\text{cm}^{-3}$	$5.5\text{x}10^{9}\text{cm}^{-3}$

Table 3.1: A table that summarises the operational characteristics of the three symmetric AGATA prototype detectors.

3.2 Detector Preamplifiers

Figure 3.4 shows a schematic representation of the components of the AGATA charge-sensitive preamplifiers. The architecture of the AGATA preamplifier circuit consists of a charge-sensing loop (which also comprises the cold devices), a passive Pole Zero (PZ) stage, and a differential output buffer. The differential output helps prevent RF pickup and

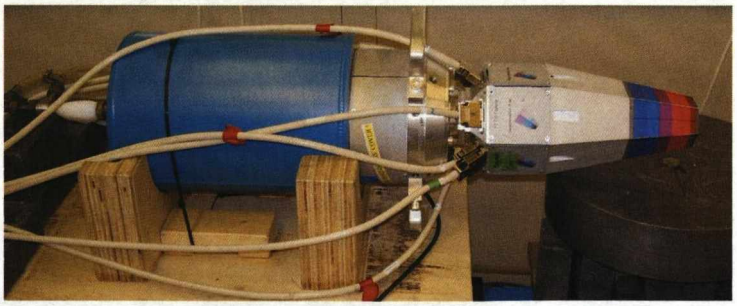

a) AGATA symmetric prototype detector and dewar

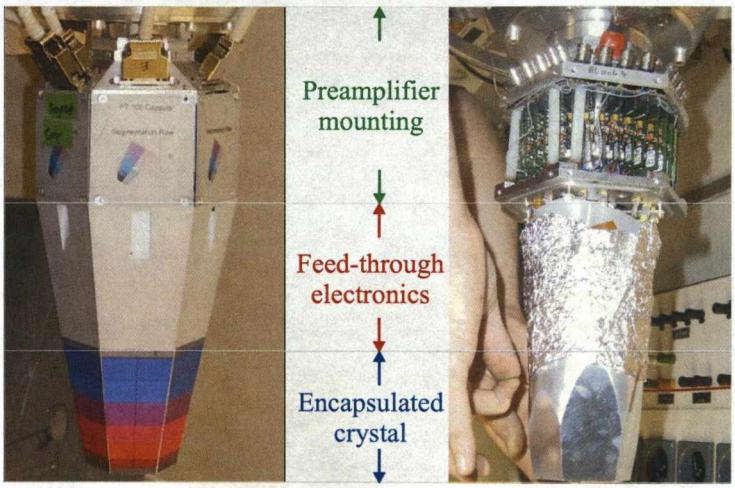

b) Detector in cryostat

c) Detector without cryostat

Figure 3.2: Photographs of the S002 AGATA symmetric prototype detector. a) Detector cryostat, mounted on its side. The dewar (blue) holds enough LN2 for the detector to remain operational for 24 hours. b) Zoomed view of detector and lower cryostat. c) Zoomed view of internal components. The feed-through electronics are surrounded with insulating foil.

ground bounce, as the subtracter that converts the differential signal back to a single ended signal effectively ignores the wires' voltages with respect to ground. If the preamplifier is saturated by an energetic event or burst of pile-up events, an additional de-saturation circuitry is engaged that quickly resets the preamplifier, highlighted in green.

Each detector has 36 segment preamplifiers and 1 centre contact preamplifier, with associated feed-through electronics. Three different preamplifier configurations were developed

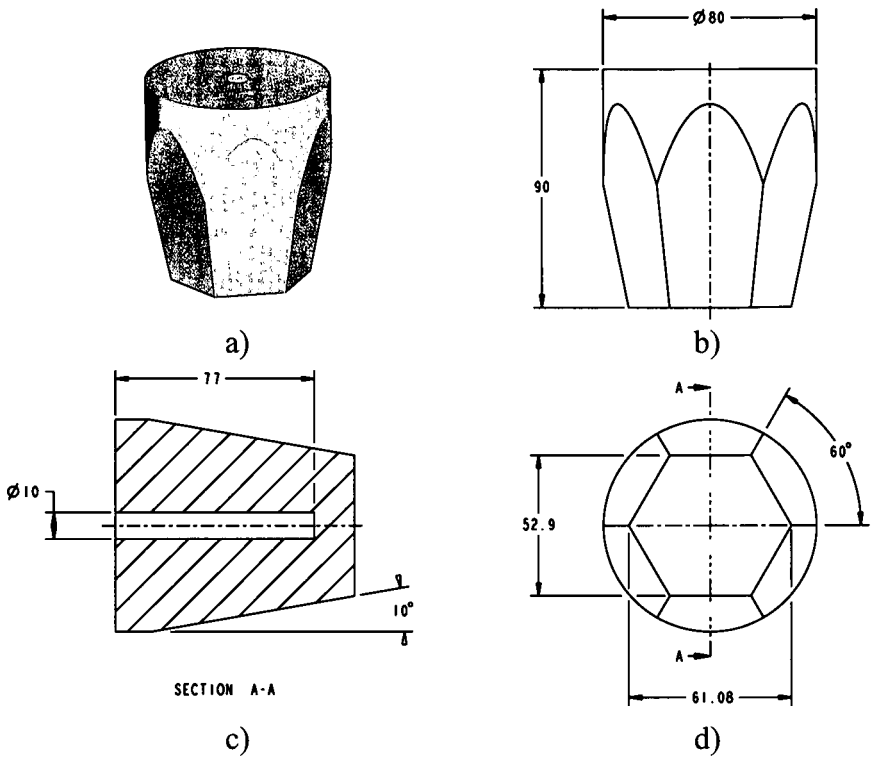

Figure 3.3: AGATA symmetric detector *ProEngineer* model and projections. a) 3D reconstruction of the crystal volume. b) to d) Front, side and plan projections of crystal geometry, respectively.

during the test-phase of the project (2003 to 2008). The initial design specifications are shown in *Table 3.2.*

The three preamplifier configurations were developed by the Milan, GANIL and Cologne groups. Milan and GANIL built the segment preamplifiers, whilst Cologne built those used for the centre contact (core) of each detector. The segment preamplifiers, in both instances, are mounted three to a board. There are two key differences in the competing segment designs. Firstly, the substrate from which the PCBs are constructed is FR4 for the GANIL variant and alumina for that of Milan. Secondly, the compensating capacitor that determines the bandwidth of the preamplifier is fixed at 8MHz for GANIL but variable between 8MHz and 12MHz for Milan. The centre contact design also incorporates the FR4 substrate, however, each core channel is mounted on a separate board. This is to allow

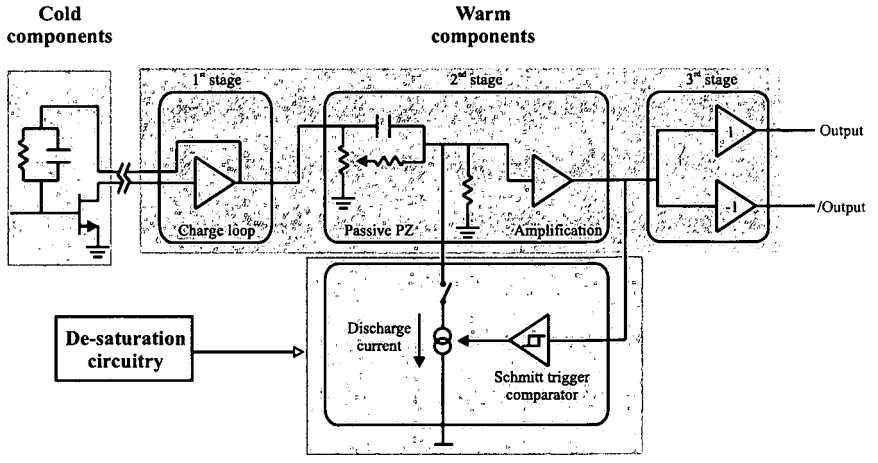

Figure 3.4: The architecture of the AGATA symmetric prototype detector preamplifiers.

Property	Value	Tolerance
Conversion gain	100 mV / MeV (terminated)	±10%
Noise FWHM (0pF)	0.6keV	
Noise slope	12ev/pF	±2eV/pF
Rise time (0pF)	10ns	±2ns
Rise-time slope	~0.3ns/pF	
Decay time	50μs	±5%
Integral non linearity	<0.025%	
Output polarity	Differential, Z=100Ω	
Power supply	±6V, ±12V	
Power consumption of input FET	<25 mW	
Power consumption (except diff. buffer)	<250 mW	
Mechanical dimension	<22mm x 48 mm x 7 mm	

Table 3.2: AGATA segment preamplifier design specifications

space for the pulser circuitry that is not present on the segment boards. As the centre contact triggers at several times that of any individual segment, the fall time was reduced to 300μs (τ = 15μs), as opposed to 1ms (τ = 50μs) for the segments, to enable count rates of up to 50kHz with minimal pile-up.

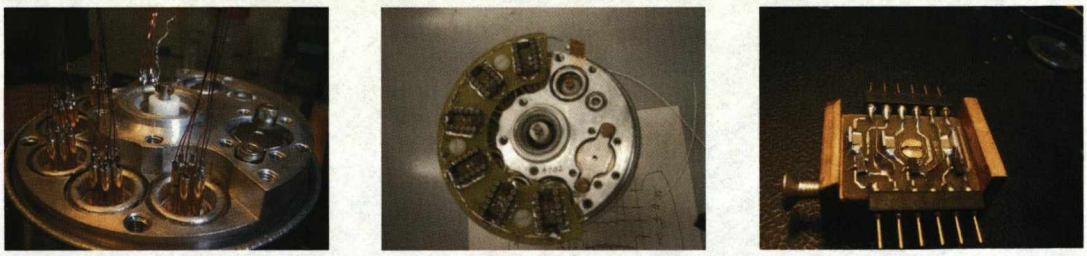

a) b) c)

Figure 3.5: Photographs of the AGATA detector FET mountings. a) Back plate of encapsulated crystal with cables from the detector contacts. b) The FET motherboard with 6 FET mountings (one for each of the segment banks). c) FET bank with 6 FETs for a single sector of the detector.

The preamplifier input FET used in all cases is the Philips BF862. It was tested with a drain voltage of 2 to 2.6V and a drain current of ~8mA. Operating under these conditions, a noise of 0.9keV FWHM for a pulser input of 120keV was observed (0.75%) [Pul05]. In order to maintain the signal integrity and minimise noise effects it was important that the FETs were mounted as close to the crystal as possible. *Figure 3.5* shows how the signal is conveyed from the crystal to the FETs. *Figure 3.5a* to *Figure 3.5c* show photographs of the cables from the detector contacts on the back of an encapsulated crystal, the FET motherboard with six FET mountings (one for each of the segment banks) and an FET bank respectively. Each segment FET bank consists of the circuitry for the 6 FETs for that sector. The FET for the centre contact is mounted separately.

The S001 and S002 cryostats contained GANIL preamplifiers, whilst the S003 cryostat was the first to incorporate the Milan design. All three cryostats were furnished with Cologne preamplifiers for the centre contact.

3.3 AGATA Signal Processing

The AGATA tracking methodology requires each crystal to be treated as a separate entity that triggers on the centre contact of that detector. Thus, for real-time tracking to work, the AGATA electronics are required to deal with high count rates whilst preserving the fast leading edge of the charge sensitive preamplifier signals through the digitisation process. In

order to achieve this, the signal processing will be split into several phases:

1. Front-end Processing - This will require two separate units per detector; the digitiser box [Bau07] and preprocessing card [Laz05]. After digitisation, the charge pulses will be tagged with channel IDs, trigger points, timestamps and energy information.

2. Pulse Shape Analysis - Following pre-processing, the tagged pulse shape data will be passed to a computer farm where it will be filtered and processed to derive the 3D spatial coordinates with associated uncertainties for all photon interaction positions inside the AGATA array. For segments with more than one interaction, the PSA algorithms will deconvolve the pulse shapes to determine the number of interactions that have occured, their locations, and the energies deposited at each location.

3. Event Building - The subsequent event data provided by the PSA algorithms will be merged with data from any ancillary detectors. Data read out in list mode will be pooled to give an overall event number for a given trigger configuration.

4. Gamma-ray Tracking - Tracking algorithms will process each data pool to reconstruct the time correlated events by analysing the kinematics of the scatter paths.

5. Analysis and Archiving - The characteristics of each event will be analysed, resulting in spectroscopic information such as the linear polarisation of the photons [Gor01].

Figure 3.6 shows a schematic representation of the data flow for the AGATA demonstrator.

3.3.1 The AGATA Digitiser

The principle aim of the digitiser is to provide an interface between the detector preamplifiers and preprocessing unit. The digitiser units will be located within 10m of their respective detector cryostat in order to minimize the risk of induced noise. Each digitiser receives the differential output from its corresponding detector preamplifier. The signal then passes through a driver and Flash ADC (FADC). The driver adds the appropriate signal offset. Included in the driver is the anti-aliasing filter. This ensures that the detector signal is band-limited, according to the Nyquist-Shannon sampling theorem [Jer77], before the

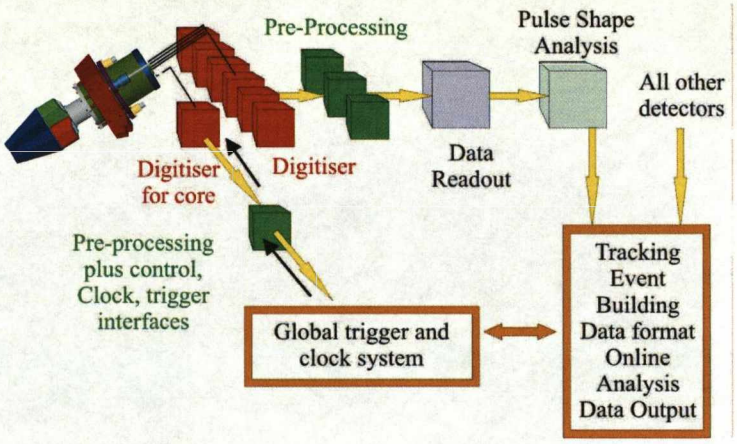

Figure 3.6: A figure showing a schematic representation of the AGATA data processing chain.

digitization process. A 14-Bit FADC samples the signals at 100MHz. 16 data bits are sent to the Virtex2 Pro Field Programmable Gate Array (FPGA); bits 0 to 13 are the data, bit 14 is the FADC overload and bit 15 can be used as a synchronisation pulse. It is intended that the normal operational gain range of 0 to 5MeV will be utilised for most experiments, however, an extended range of 0 to 20MeV is also available. The FPGAs perform the local synchronisation functions by adjusting the clocks for all channels to be in phase. The digitised pulses are then transmitted to the pre-processing card as a 2Gbit/sec serial bitstream, via optical links. A digital Constant Fraction Discriminator (CFD) signal is also transmitted to provide a latency-free trigger for the ancillary detectors.

3.3.2 AGATA Pre-processing

The functionality of each pre-processing card requires it to accept data from the digitiser system and calculate pre-determined parameters, and pass these, along with the leading edge of the digitised trace (128 samples), to the PSA computer farms. These parameters include the timestamp, channel ID, energy derived from the Moving Window Deconvolution (MWD) calculation [Geo93], the trigger point for the MWD and the point at which there is no data so the baseline can be sampled. All functions must be performed in real-time and on a per channel basis. The pre-processing also interfaces with the global trigger and clock system from which a clock for the digitiser and timestamp information is derived. At

high count rates, this trigger system can be used to control the input data rate to ensure that the processing capacity in the PSA farm is not exceeded. This is performed on a pre-selection basis, determined by criteria such as crystal multiplicity or a coincidence with ancillary detectors or the beam pulse.

3.3.3 On-line Pulse Shape Analysis

The 36 fold outer contact segmentation was chosen to minimise the number of interactions in a given segment and maximise the magnitude of the image charges for PSA [Gor03]. This segmentation effectively divides each crystal volume into 36 approximately $10^3 mm^3$ voxels (segments). If a photon interacts in the detector, one can determine the segment in which the energy was deposited by observing a charge pulse at the preamplifier output. Although a localisation of the interaction position to the centre of each segment would allow an enhanced Doppler correction, an uncertainty of this magnitude would not allow the resolution of multiple scatters within a single segment. Thus limiting the ability to perform gamma-ray tracking (GRT).

It it intended that the real-time localisation of each photon interaction to a voxel of $<5mm^3$ will be achieved by comparing experimentally digitised pulse shapes with a theoretically derived basis set on a well-defined grid. A simulated basis is required as it would be too time consuming to develop the basis with experimental data, the reasons for which will be explained in *Section 5.7*. Such a basis will be constructed by dividing each crystal volume into a finite number of lattice points. Each point will have a set of 37 unique pulse shapes generated by an electric field simulation code. Thus, the most likely set of interaction positions can be determined by a chi-squared test of the digitised pulses against linear combinations of pulse shapes from basis points within that segment. This is possible as the shapes of the charge and induced pulses depend on the drift times of the charge carriers and the proximity of the interaction to segment boundaries. Several forms of algorithm have been developed to perform such calculations including, Adaptive Grid Search (AGS) [Des05a], Genetic Algorithms (GAs) [Kro06] and Matrix Inversion [Ola06]. The output of such PSA algorithms will be a set of timestamped 3D spatial coordinates with associated uncertainties and energy fractions, for all interaction positions in the AGATA array.

3.3.4 Event Building

Following a local trigger, each event per detector is issued a local timestamp that is automatically validated by the centre contact mezzanine. This timestamp is then distributed to the segment mezzanines by the Global Trigger System (GTS). Thus providing the user with a continuous stream of timestamped events that can be grouped as required by the event builder software. Although running in list mode is the intended goal for the AGATA array, the electronics have been designed so that a true global trigger can be invoked for simultaneous data readout during the test phase of the project. The role of the event builder is to merge the position and energy information concerning the photon tracks through the AGATA array with time correlated data from the ancillary detectors. Thus providing a data group for the tracking algorithms to process.

3.3.5 Gamma-Ray Tracking (GRT)

Tracking algorithms will enable the reconstruction of time-correlated photon interactions. The Compton scatter formula relates the angle of scatter of a photon to the energy deposited [Ham04]. The Klein-Nishina formula gives information on the probability of a photon of given energy scattering through a certain solid angle. Data describing the energy, timestamp and 3D spatial coordinate with associated uncertainty of every photon interaction inside the AGATA array is read in. The GRT algorithms then processes the event kinematics and determine the most likely scatter path. Three forms of algorithm exist at present; clusterisation [Sch99], backtracking [Mil03] and fuzzy tracking [Alv03]. The accuracy of these codes depends on the uncertainty in the spatial resolution of the array. During the development of the algorithms, the accuracy to which the interaction positions could be determined was not known. As such, interaction positions determined from simulation were smeared and clustered according to a 5mm resolving distance [Mil04]. Experimentally, the uncertainty of interaction positions will depend on the reliability of the simulated pulse shape basis.

3.3.6 Analysis and Archiving

The processed data will be stored to raid disk and analysed to extract information regarding the subject nuclei. Following the initial test phase of the demonstrator, it is intended that

the data volume from each experimental run will be sufficiently small that it may be stored on a central server and accessed remotely.

Chapter 4

Characterisation Methods

Analogue pulse shape analysis has been used for many years to extract energy and timing information from HPGe detector signals. With the advent of fast digitisers, it is now possible to store and analyse these waveforms in software, in order that the detector response can be characterised as a function of the photon interaction position. The digitised pulses can be utilised to validate the pulse shapes derived from electric field simulation codes. The codes can then be used to explore the effect on the detector response of varying characteristics such as the operating voltage, impurity gradient and detector geometry. The validated software can also be used to generate a data set for basis matching, as described in *Section 4.3.10*. This chapter gives an overview of the factors that influence the pulse shapes observed in different regions of the AGATA prototype detectors, the metrics used to quantify this variation and the implementation of the electric field simulation code Multi Geometry Simulation (MGS).

4.1 Detector Response

Figure 4.1 shows a schematic representation of the signal processing elements required to digitise and store the preamplifier output in order that useable information may be extracted through pulse shape analysis.

In order to explain the factors that influence both the current and charge pulse response observed for the AGATA geometry, three example interaction positions will be referred to

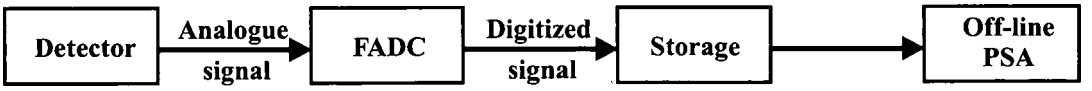

Figure 4.1: Schematic representation of the signal processing chain for digitising, storing and analysing the detector preamplifier response.

in several of the following sections. Both the detector labelling convention and location of the interaction sites are presented explicitly in *Figure 4.2*. *Figure 4.2a* shows a plan view of the six rings of the prototype detector, with the manufacturer defined segment labelling convention. The radii of the three example interaction sites, in segment F6 of the detector, are also defined. The interaction sites are at small (7mm), mid (24mm) and large radii (32mm). They are represented by the green, blue and red dots respectively. All three interactions are at a depth of 47.7mm, measured from the front face of the detector, see *Figure 4.2b*. The angle of each interaction position, measured from the A6 / F6 segment boundary is shown in *Figure 4.2c*. The 7, 24 and 32mm interactions are at angles 7.5^o, 30^o and 52.5^o respectively. The nearest neighbour segments are labelled, A4 (anticlockwise), E4 (clockwise), F5 (upper) and F3 (lower).

4.2 Current Pulse Response

The shape of the current pulse induced on the collecting electrodes of a detector depends on the drift of both the electron and *hole* charge clouds, such that,

$$i_{tot} = i_{elec} + i_{hole}. \tag{4.1}$$

Figure 4.3 shows simulated examples of current pulses induced on both the centre (anode) and outer (cathode) contacts of the AGATA S002 geometry, for the 7mm, 24mm and 32mm radial interactions defined above. The electron current is shown with the brown dashed line, the *hole* current is shown with the magenta dash-dotted line, and the total current is shown with the plain black line. The area of the total current is proportional to the energy deposited in the detector. The simulation assumes a 1MeV single-site interaction for ease of calculation. However, this is highly improbable due to the Compton scatter cross section.

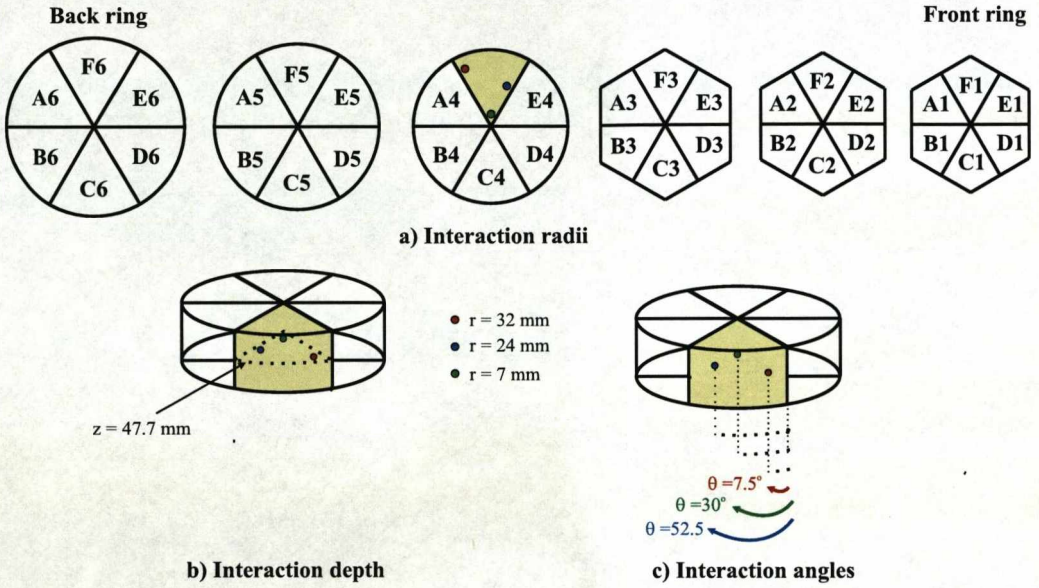

Figure 4.2: The coordinates of example interaction positions in the AGATA prototype detector. a) Plan view of the six rings of the prototype detector, with the manufacturer defined segment labelling convention. The radii of the three example interaction sites, in segment F6 of the detector, are also defined. The interaction sites are at small (7mm), medium (24mm) and large radii (32mm). b) The depth of all three interaction positions is shown to be 47.7mm, measured from the front face of the detector. c) The angle of each interaction position, measured from the A6 / F6 segment boundary. The nearest neighbour segments are labelled, A4 (anticlockwise), E4 (clockwise), F5 (upper) and F3 (lower).

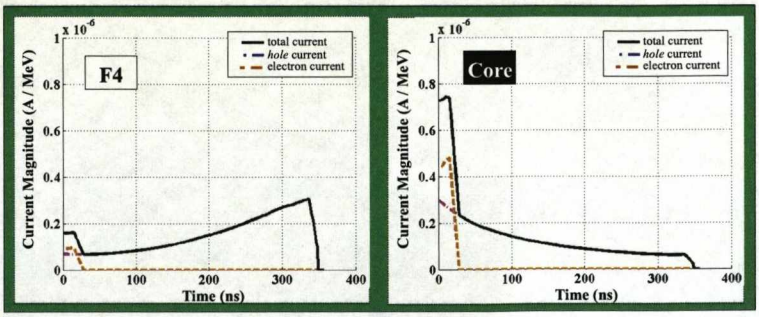

a) r = 7mm, θ = 30°, *z = 47.7 mm)*

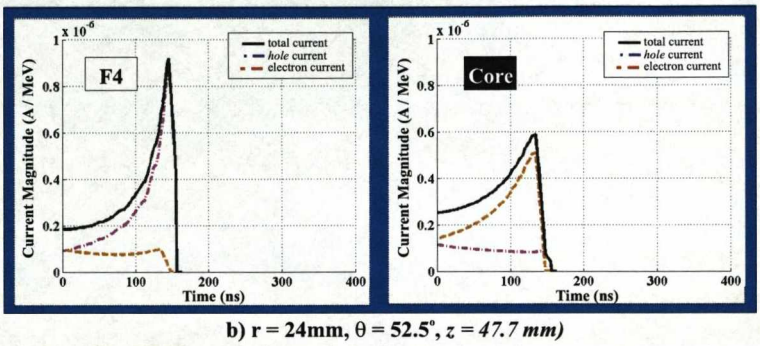

b) r = 24mm, θ = 52.5°, *z = 47.7 mm)*

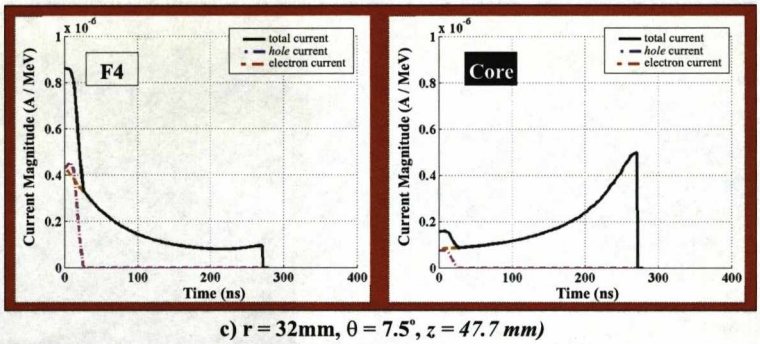

c) r = 32mm, θ = 7.5°, *z = 47.7 mm)*

Figure 4.3: Evolution of induced current shown as a function of photon interaction position, in the back (coaxial) region of the S002 AGATA prototype detector. The 7mm, 24mm and 32mm radial interaction sites are highlighted in green (top), blue (middle) and red (bottom) respectively. In each case, the total current pulse (plain black line) induced on each contact is the sum of the currents induced by the electrons (brown dashed line) and holes (magenta dash-dotted line). The simulation assumes a 1MeV single-site interaction for ease of calculation. The duration of the total current pulse is dependent on the drift time of both charges.

4.2.1 Centre Contact (Core) Response

As the interaction radius increases, the duration of the electron induced current also increases. The final magnitude stays approximately constant as the coupling between the electron and the anode always reaches its maximum. However, the magnitude of the current induced by the *hole* decreases as the coupling with the anode is smallest at large radii.

4.2.2 Outer Contact Response

As the distance to the cathode decreases, the duration of the *hole* induced current decreases. The final magnitude varies as the coupling to the outer cathode, described by the weighting field, changes as a function of azimuthal angle across the segment. A more detailed discussion of the weighting field in the AGATA prototype detector geometry can be found in *Section 4.4.7.*

At a depth of 47.7mm, the outer radius of the AGATA prototype detector is 40mm. By accounting for the 5mm drilled hole and considering the charge carrier with greatest drift distance, the net charge carrier displacements for the 7mm, 24mm and 32mm interactions are 33mm, 19mm and 27mm respectively. Assuming that the saturated charge carrier drift velocity is $10^7 \mathrm{cms}^{-1}$, the durations of the total current pulses should be approximately 330ns, 190ns and 270ns. The actual corresponding values are 355ns, 165ns and 270ns. This crude calculation, which neglects the effects of the anisotropic drift velocity and slower *holes* [Kno00], agrees well with the simulated results.

The drift of the charge carriers towards their respective collecting electrodes will also induce a current signal on all other electrodes of the detector. While the area of the total current pulse for the collecting electrodes always has some net magnitude, for all other electrodes the current pulse must be bipolar with equal positive and negative areas, if there is no net energy deposition.

4.2.3 Current Pulse Parameterisation

For an overview of the methods involved in parameterisation of the current pulse response of segmented HPGe detectors, please refer to [Pal96] and [Cre07]. The work contained in

this thesis focuses on the investigation of the charge pulse response. Thus, the remainder of this section will describe the techniques required to perform such analysis.

4.3 Charge Pulse Response

The output from the charge sensitive preamplifier of each channel of the detector is the integral of the respective current pulse, given by,

$$Q_{tot}(t) = \int i_{tot}(t)\,dt = \int i_e(t)\,dt + \int i_h(t)\,dt. \tag{4.2}$$

For a single site interaction, as described above, integration of the current pulse will yield the growth of a net charge pulse on the collecting electrodes, however the pulse shapes on all other electrodes must return to the baseline. This is true if:

1. Cross-talk effects are neglected. Cross-talk effects will be discussed in *Sections 5.6.1* and *6.1.2*.

2. Charge sharing does not occur. For interactions close to segment boundaries in regions of weak field, the charge cloud may split between neighbouring segments as it drifts towards the outer contact. The effects of charge sharing in planar HPGe detectors are described in [Coo07].

The magnitude and shape of both the real and image charge pulses varies as a function of interaction position and depends on:

1. The proximity of the charge carriers to the electrodes and segment boundaries.

2. The magnitude of the weighting field. The weighting field is a mathematical model that describes the electrostatic coupling between a charge carrier and an electrode and can be used to derive the pulse shape response at that electrode.

3. The number of charge carriers generated following an interaction.

4. Any variation in charge carrier drift velocity due to regions of weak field.

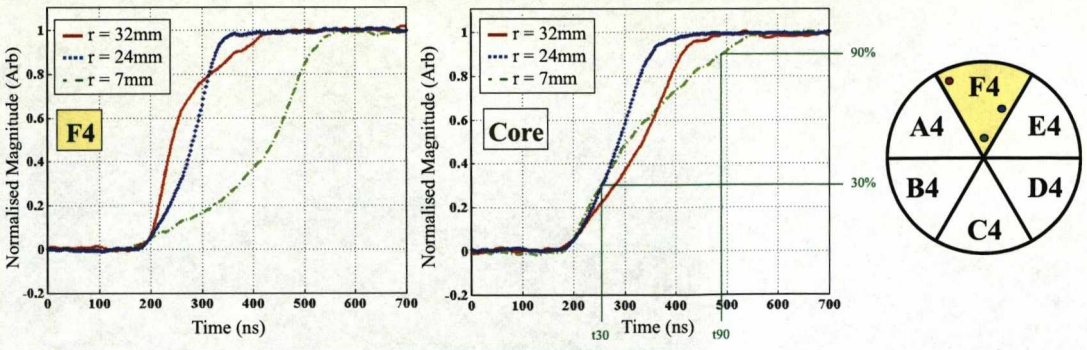

Figure 4.4: Charge pulse response as a function of increasing photon interaction radius. The pulse shapes are shown for the interaction segment (F4) and the centre contact, for the same interactions as those in *Figure 4.3*. In each case the green dashed lines, blue dotted lines and plain red lines show data for the 7mm, 24mm and 32mm radial interaction positions respectively. The time to 30% (t30) and 90% (t90) of the centre contact pulse for the interaction at r = 7mm are also indicated to show how the parameterisation of these shapes can be used to give information on the radius of interaction.

To illustrate the variation in pulse shape response, average real charge and image charge pulses are shown in *Figure 4.4* and *Figure 4.5* respectively. The data presented was collected from the S002 detector for the same interaction positions as those displayed in *Figure 4.3*. For a description of how the average pulse shapes are generated, please refer to *Section 5.8* The green dashed lines, blue dotted lines and plain red lines show data for the 7mm, 24mm and 32mm radial interaction positions respectively.

4.3.1 Real Charge Pulse Response

At radii close to either contact, 7mm and 32mm, one charge cloud is collected very quickly whilst the other has much further to drift. This results in a relatively long net rise to the maximum amplitude. For interactions at central radii, 24mm, the net charge collection time is much shorter.

4.3.2 Image Charge Pulse Response

For interaction positions where the charge carrier drift is dominated by the electron cloud (32mm), the resulting image charges are negative. The opposite is true for interactions

dominated by the drift of the *hole* cloud (7mm). Bipolar image charges are generated at some intermediate radii between these two extremes. From *Figure 4.5*, a large negative image charge can be observed in Segment A4 due to the proximity of the 32mm interaction to the segment boundary. As the distance between the 32mm interaction position and segment E4 is maximal, for a nearest neighbour electrode, the image charge induced on E4 is small and unobservable above the baseline noise. Similar arguments can be constructed for the image charges observed as a result of the 24mm and 7mm interactions. These relationships between the image charges in directly adjacent electrodes, can be exploited to give information on the azimuthal angle and depth of an interaction. For example, the upper (F5) image charges for all three interactions, shown in *Figure 4.5*, have similar shapes and magnitudes to their respective lower (F3) image charges. As the interactions are all at the same depth, positioned midway between the upper and lower segment boundaries, this distribution is expected.

4.3.3 Charge Pulse Parameterisation

By analysing the characteristics of both the real and image charge response of the detector it is possible to extract several metrics for quantifying the change in pulse shapes as a function of interaction position. These metrics can then be used to determine the event-by-event position for single site interactions, allowing an improved Doppler correction [Nel08].

4.3.4 Rise Time Parameterisation

Parameterisation of the real charge pulse response observed on both the central and outer contacts can be achieved by evaluating the time the pulse takes to rise to a given percentage of its maximum amplitude. This value is typically taken relative to some threshold value. An example of this could be T30, given by

$$T30 = t30 - t10, \tag{4.3}$$

where t30 is the time to 30% of the maximum amplitude and t10 is the time to 10% of the maximum amplitude, defined as the threshold value. Similarly, T90 = t90 - t10. The time to varying fractions of the maximum amplitude gives information on different aspects of the

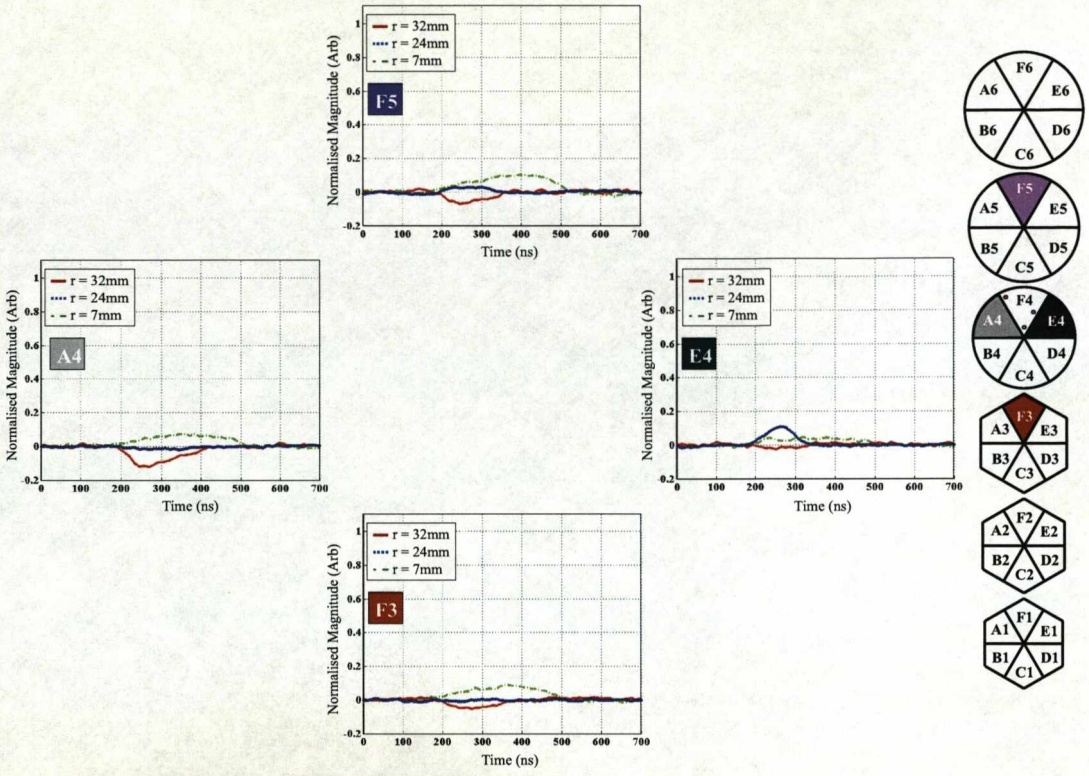

Figure 4.5: Evolution of induced image charge as a function of photon interaction angle. The pulse shapes are shown for nearest neighbour segments, A4, E4, F5 and F3, for the same interactions as those in *Figure 4.3*. In each case the green dashed lines, blue dotted lines and plain red lines show data for the 7mm, 24mm and 32mm radial interaction positions respectively. The polarities and magnitudes of the image charges are shown to vary depending on the charge carrier drift times and the proximity of the interaction to segment boundaries.

charge collection. The *t30* and *t90* values for the 7mm centre contact pulse are indicated on *Figure 4.4* to illustrate how this technique can be implemented. Changes to the threshold value will alter the sensitivity of the parameter accordingly. This will be discussed further in *Section 5.5*.

4.3.5 Properties of T30

The T30 parameter is a measure of the initial charge carrier drift. For interactions close to the central anode, where the electric field is strongest, the initial rise of the pulse will be

fastest as the charge carrier drift velocity is saturated. Opposingly, for interactions close to the outer anode, there are regions of weak field resulting in much slower drift velocities. Thus the T30 for interactions at these locations will be much slower. The regions of weak field are a direct consequence of the complex tapered hexaconical geometry of the AGATA detectors, see *Section 4.4.5.*

4.3.6 Properties of T90

The T90 parameter gives information on the combination of the overall charge carrier drift. In the examples given above, it has been shown that in the coaxial regions at intermediate and large depths in the detector, T90 is slow for interactions close to either contact. T90 is fastest for interactions where the charge carriers have equal drift times. This argument still holds for the planar (front) regions however the field has a different shape.

4.3.7 T30 Versus T90

In regions of the detector where T90 can have similar values (at small and large radii close to either contact) these ambiguities can be resolved by plotting the profile of T30 versus T90. The T30-T90 technique was first used by [Kro01], who studied the general application of such distributions to data collected from closed-ended coaxial geometries. Extensive analysis of these correlations for EXOGAM detectors is presented in [Gro05]. The correlations are shown to distinguish between single and double interactions that occur within a single segment. Thus allowing the rejection of Compton scattered events.

4.3.8 Image Charge Asymmetry (ICA)

Rise time analysis gives accurate information on the radius of a gamma-ray's interaction. However in order to localise the event in all three spatial dimensions, information regarding both the depth and azimuthal angle of interaction must also be extracted. This can be achieved by measuring the asymmetry in either the absolute magnitude or area of the signals induced on directly adjacent electrodes. The *asymmetry* can be quantified by use of *Equations 4.4* and *4.5.*

$$ICA_{Mag} = \frac{Magnitude_m - Magnitude_n}{Magnitude_m + Magnitude_n}, \tag{4.4}$$

$$ICA_{Area} = \frac{Area_m - Area_n}{Area_m + Area_n} \tag{4.5}$$

where m and n are the segments immediately clockwise and anticlockwise of, or immediately above and below the interaction segment.

Although parametric PSA is sufficient for simple Compton rejection and Doppler corrections, it is not suitable for gamma-ray tracking with the AGATA spectrometer. The use of large volume coaxial detectors in the AGATA array will result in a significant fraction of events that interact more than once in a single segment. As such, the deconvolution of these interaction positions is required and this can only be realised with the use of a pulse shape database.

4.3.9 Detector Sensitivity

The arguments used above to discuss the detector response have concentrated on the properties of the coaxial regions of the detector volume. The reality of the AGATA geometry and its construction from a hexaconical crystal requires that the volume is split into 3 distinct regions, presented in *Figure 4.6a*. The electric field distributions can be considered as, planar (zone 1), semi-planar (zone 2) and bulk (zone 3). The influence of these regions on the charge carrier trajectories are shown in *Figure 4.6b*, *Figure 4.6c* and *Figure 4.6d* respectively. The electron trajectory is shown by the red path, while that of the *holes* is shown in black.

The planar region, directly beneath the central anode, can be considered as influencing the charge carrier trajectories as if it were the bulk region rotated by 90°. Thus the qualitative change in T90 as a function of interaction depth resembles that of the radial variation in the bulk region. The most difficult section of the volume to interpret is that of zone 2. The complex shape of the outer cathode causes large variations in the radius as a function of depth and azimuthal angle. The surface on which the hole trajectories terminate also

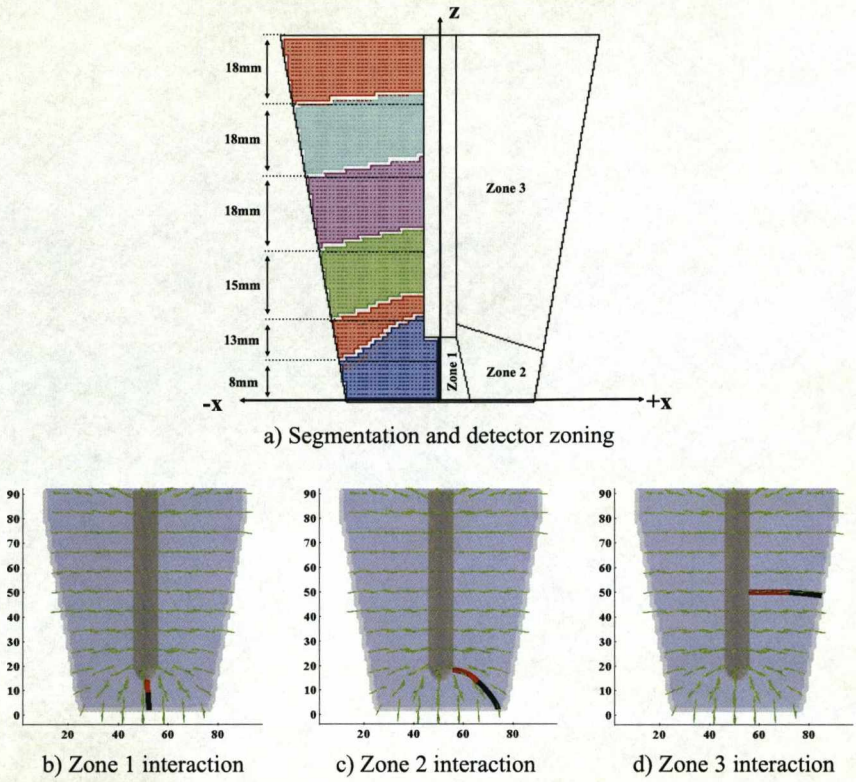

Figure 4.6: Simulated representation of the AGATA prototype detector geometry showing the effect of the complex electric field on the charge carrier trajectories. a) A schematic diagram showing the effective segmentation for an AGATA prototype detector [Gor03]. The crystal volume can be split into three distinct zones where the drift of the charge carriers is influenced by the planar, semi-planar and bulk electric field. The bulk electric field vectors are equivalent to those that would be expected in an entirely coaxial detector. b) to d) show the simulated charge carrier trajectories for each of these zones respectively. The electron trajectory is shown by the red path, while that of the *holes* is shown in black.

varies with interaction position and there are regions of weak electric field in the corners of the detector. The combination of these effects give rise to a large change in pulse shape response as a function of interaction position. This is also referred to as a high position sensitivity. The position sensitivity S^2 can be quantified as [Vet00],

$$S_{ij}^2 = \frac{\Delta r_{ij}^2}{\Delta s_{ij}^2}, \tag{4.6}$$

where Δr_{ij}^2 is the distance between two interaction positions i and j, and Δs_{ij}^2 quantifies the difference of the signals in terms of noise. The parameter Δs_{ij}^2 is defined as,

$$\Delta s_{ij}^2 = \sum_{k=1}^{37} \sum_{t=t10}^{t90} \left[\frac{q_i^k(t) - q_j^k(t)}{\sqrt{2}\sigma^k} \right]^2, \tag{4.7}$$

where k is the channel number, and σ is a measure of the signal noise. Therefore a high sensitivity refers to a small value of S_{ij}^2. For effective on-line PSA, regions of high sensitivity make the deconvolution of scattered events less complex due to the large differences in pulse shapes. However for validation purposes, small uncertainties in the experimentally determined interaction location can give rise to pulse shapes that do not match those derived from the idealistic case of the electric field simulation code. This factor has proved to be a significant challenge for detector characterisation.

4.3.10 Pulse Shape Matching

For on-line PSA to be implemented successfully, it has been estimated that in excess of 30,000 basis sites per crystal, for a 2.0mm cartesian grid [Ven07], are required. Theoretically, the basis can be obtained from either experimental or simulated data. However, on average, ~2hours of data collection are necessary for the generation of thirty seven average pulses at each basis site, see *Section 5.7*. Average pulses are required to reduce the contribution from random noise. Thus, the duration for acquiring pulses for 180 crystals would not be practical in the scope of the AGATA project. As such, electric field simulation codes such as Multi Geometry Simulation (MGS) are essential if on-line PSA is to be realised. Over the last two years, MGS has been used to generate variants of a single crystal basis. This has allowed the performance of the PSA algorithms to be tested for several different basis configurations. Two of these configurations are presented simultaneously in *Figure 4.7*. An overview of the performance of the 2mm and 5mm symmetrically spaced grids are presented in *Table 4.1*. The results presented are from the analysis of data collected during the in-beam symmetric triple cluster test performed in Cologne in 2005 [Rec07]. The FWHM of the Doppler corrected 1382keV photo peak gives a direct measure of the position resolution achieved with a given basis.

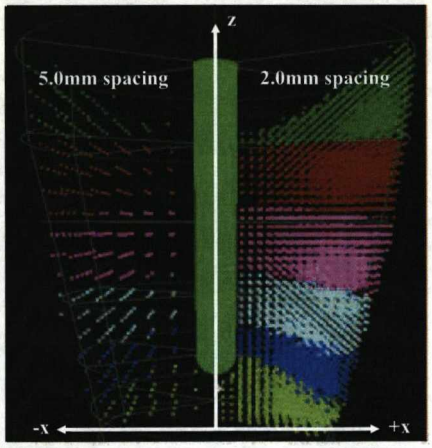

Figure 4.7: A schematic representation of the basis points for two contrasting equi-spaced grids that could be used for the AGATA prototype detectors. The number of bytes held in memory is related to the number of grid points. As such, the grid spacing must be a compromise between deconvolution accuracy and processing time. The figure is taken from [Ven07].

Grid Spacing (mm)	Event Multiplicity	FWHM (keV)	Processing Time (ms / event)
5	All	6.0	0.50
5	1	5.8	0.22
2	All	5.3	3.70
2	1	5.1	1.80

Table 4.1: Summary of the performance of matrix inversion PSA algorithm for 2mm and 5mm symmetric basis grids, simulated with MGS. The algorithms were tested with the in-beam triple cluster data collected in Cologne in 2005 [Rec07]. The FWHM of the Doppler corrected photo peak gives a measure of the performance of the simulated basis. As expected, the 2mm grid spacing gives an enhanced Doppler broadening correction, at the expense of increased processing time.

It can be seen that the performance of the 2mm grid gives rise to an improved Doppler broadening correction with respect to the 5mm grid. However, the processing time is significantly increased due to the greater number of basis sites for pulse shape comparison. For successful on-line PSA to be implemented, there must be a balance between the accuracy of the tracking and the processing time per event. It is expected that the use of an asymmetric basis grid will achieve this as the density of sites can be maximised in regions of

high sensitivity and offset against the density of sites in regions of low sensitivity. However interpolation between asymmetrically distributed points becomes more complex.

The application of MGS in producing these bases has, until now, not been fully validated by comparison to experimental data. In order to verify the accuracy with which MGS reproduces the experimentally collected pulses, full pulse shape matching has been utilised. The simulated pulses have been quantitatively compared to those collected at well-defined 3D interaction positions inside the S002 AGATA symmetric prototype detector. The results of this analysis are presented in the following chapters.

4.4 Detector Simulation

MGS [Med04] was developed at the Institut de Recherche Subatomique (IReS) in Strasbourg France. It utilises MatLab's matrix environment [Mat07] to derive the expected pulse shape response at the contacts of any geometry of HPGe detector. The stand alone package has been compiled for use with both Linux and Microsoft Windows operating systems.

Environments such as FEMLAB [Fem07] and DIFFPACK [Dif07] can also be adapted for providing an analytical solution to the complex electric field distribution inside the AGATA detectors. They utilise Finite Element Methods (FEM) for solving partial differential equations, such as the solution to Poissons' equation. MGS was developed as an alternative specialised solution to these commercial packages.

4.4.1 Description of the MGS Package

MGS utilises the multi-step algorithm, shown in block format in *Figure 4.8*. The calculations are performed on a user specified 3D grid that maps a given detector volume. Results from each stage of the calculations are stored in matrices. The values at each point in the matrices are then recalled to generate the pulse shape response, as determined by the trajectories of the charge carriers through the weighting field.

In order to compute the pulse shape response for a given interaction position in the detector volume, the following routines must be performed:

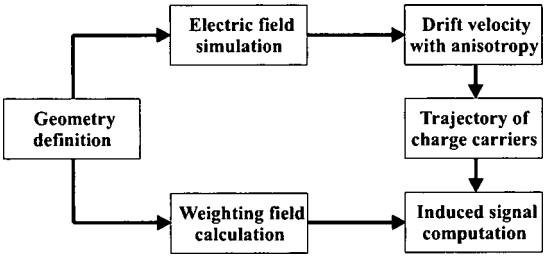

Figure 4.8: MGS data flow diagram for the simulation of the expected pulse shapes at the contacts of any arbitrary HPGe detector geometry. For a given detector, the crystal volume is divided into a cubic matrix of lattice sites. Values for the electric potential, electric field and weighting field are calculated at each position. The drift velocity matrices are calculated from the electric field matrix. The detector response for a given interaction site is calculated by tracking the trajectory of the charge carriers through the weighting field.

1. Specification of the detector geometry. This requires an input text file that contains the coordinates of the apices of the crystal. The user is then prompted to enter parameters relating to the operating bias voltage, impurity concentration, operating temperature, spacing between the crystal and the encapsulating medium, the properties of the bore hole (if the detector is coaxial), the segmentation and passivation.

2. Calculation of the electric potential surfaces and electric field lines, starting from the solution of the Poisson equation.

3. Implementation of charge carrier transport in a semiconducting medium. Data derived from work described by [Mih00] and [Bru06a] has been incorporated to describe the anisotropic mobility of electrons and *holes* respectively.

4. Calculation of the trajectories of charge carriers for arbitrary interaction positions.

5. The application of Ramo's theorem [He00], providing the resulting charge recovery at the contacts.

6. Weighting potential and weighting field resolution.

4.4.2 Features of the Simulation

MGS is operated via an interactive Graphical User Interface (GUI). It allows the user to generate both the current and charge pulses at any interaction position in the detector matrix. Data can be processed in both Cartesian and polar coordinates. The user can incorporate the anisotropy of charge carrier drift velocities, the influence of temperature on the charge carriers mobility and the influence of neutron damage.

In order to simplify the computational steps performed by the software, several assumptions have been incorporated in to the simulation:

1. The impurity gradient is assumed to be linear through the depth of the crystal. This assumption has been made as Canberra Eurisys only supply values for the impurity concentration at the front and back surfaces of each crystal. A non-linear function could be implemented in MGS if experimental data were provided by the manufacturer. One should also note that no consideration is given to the distribution of impurities across the radius of the detector.

2. Values for the electron and *hole* mobilities have been calculated from empirical formulae. The parameters have been defined from fits to experimental data derived from materials with a different impurity concentrations.

3. MGS only processes the trajectory of a single electron and single *hole* for each interaction position. This is a limiting factor of the weighting field approximation. Experimentally, the mean free path of a photoelectron resulting from a 1MeV photon interaction can be up to 1mm, resulting in a charge *cloud*. Thus the assumption of point-like energy deposition introduces an uncertainty that will affect the resulting pulse shapes.

4. Because the detector consists of a hexaconical volume with cylindrical bore hole simulated on a cubic grid, for most interaction positions, the path of the charge carriers to their collecting electrodes does not terminate at an integer grid point. Thus the final movement of each charge carrier must involve interpolation which can also introduce an uncertainty in the pulse shape response.

5. A correction for the limited bandwidth of the preamplifier and limited sampling of the digitiser must be folded into the signals generated by MGS to allow an accurate comparison between experimental and simulated data.

4.4.3 Simulation of a Symmetric AGATA Detector

MGS has been used to simulate the S002 AGATA symmetric prototype detector. Several iterations of this procedure were required over a twelve month period in order to debug the software. The iterations, problems encountered and solutions rendered are discussed in *Appendix C.*

4.4.4 Geometry Definition

The user-supplied MGS input parameters for the S002 detector are shown in *Table 4.2.* The isolant refers to the passivation at the back of the detector. The effect of adding a passivated layer to the back of the crystal was investigated and found to distort the electric field lines, see *Appendix C.* As a result, the passivated layer was not included in the simulation described below.

Parameter	S002 Value
Grid size	1mm
Inner contact voltage	5000V
Outer contact voltage	0V
Impurity concentration (front)	$1.8 \times 10^{7} cm^{-3}$
Impurity concentration (back)	$5.1 \times 10^{6} cm^{-3}$
Temperature	86Kelvin
Forward spacing	1mm
Back spacing	50mm
Lateral spacing	1mm
Distance to cathode	13mm
Anode radius	5mm
Length of layers	8:13:15:18:18:18
Consider isolant	no

Table 4.2: MGS input parameters for simulation of the S002 AGATA prototype detector.

Figure 4.9 shows the symmetric prototype detector geometry generated by MGS. The central anode and outer cathode are coloured red and blue respectively. The MGS coordinate systems and labelling convention differs from that of the experimental configuration. To orient the reader, a comparison of these systems is presented in *Figure 4.10.* The simulated results presented in the remainder of this section are displayed in terms of the MGS coordinates.

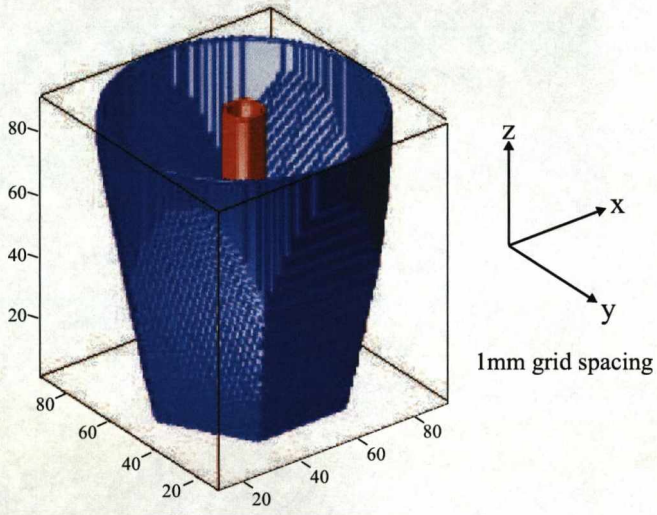

Figure 4.9: An MGS simulation of the AGATA symmetric prototype detector geometry.

4.4.5 Electric Potential and Electric Field Calculation

The electric potential $\varphi(x,y,z)$ at each point in the geometric matrix is given by the solution to Poissons equation,

$$\frac{d^2\varphi}{dx^2} + \frac{d^2\varphi}{dy^2} + \frac{d^2\varphi}{dz^2} = -\frac{\rho(x,y,z)}{\epsilon}, \tag{4.8}$$

where $\rho(x,y,z)$ is the volumetric space charge density governed by the impurity concentration and ϵ is the dielectric permitivity of germanium. Due to the complex shape of the AGATA detector, *Equation 4.8* has to be solved numerically. MGS solves this using two relaxation formalisms, *Successive Over Relaxation (SOR)* and *relaxation.* Relaxation methods [Pre99] replace the partial differential equations (PDEs) with approximate Finite Difference (FD)

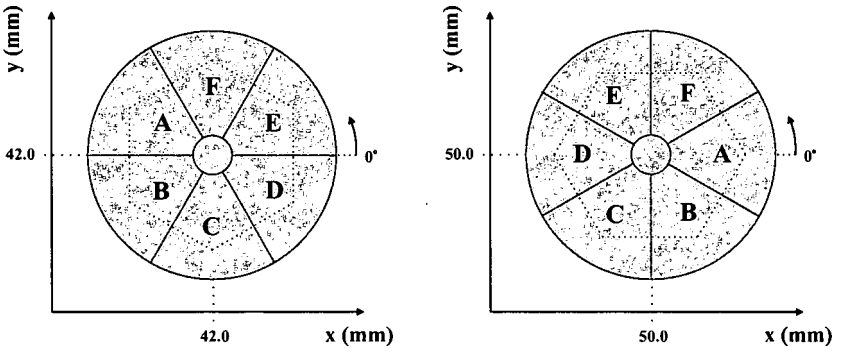

a) S002 experimental geometry b) MGS geometry

Figure 4.10: A schematic representation of the experimental and MGS labelling conventions and coordinate systems. The geometry is shown looking down the length of the crystal from back (coaxial) to front (hexagonal).

equations. The boundary conditions for these equations are given by the contact potentials, $\rho(x,y,z)_{anode} = +5000\text{V}$ and $\rho(x,y,z)_{cathode} = 0\text{V}$.

Relaxation routines start with a *guess* at the solution. This solution is then iterated. At each stage of the iteration, the difference between the initial guess and the improved solution is evaluated by a correction factor (or error). The optimum solution is achieved when the value of the correction becomes constant as a function of iteration. MGS allows the user to specify either the minimum error or number of iterations that the solution can converge on for each given relaxation method. The iterative process stops when either criteria is met. *Figure 4.11* shows a representation of the evolution of the error as a function of iteration. This trend is generated for the AGATA symmetric geometry when the required precision of *best* is selected by the user. The SOR method converges after ~700 iterations. The relaxation method requires a further 150 iterations before convergence to an error value of $\sim 5\text{x}10^{-7}$.

Figure 4.12a shows the electric potential profile calculated by MGS for the z-x plane along y = 51mm. The potential is strongest close to the AC coupled anode and decreases as a function of radius to 0V at the cathode. The electric field distribution through the detector volume is then calculated using,

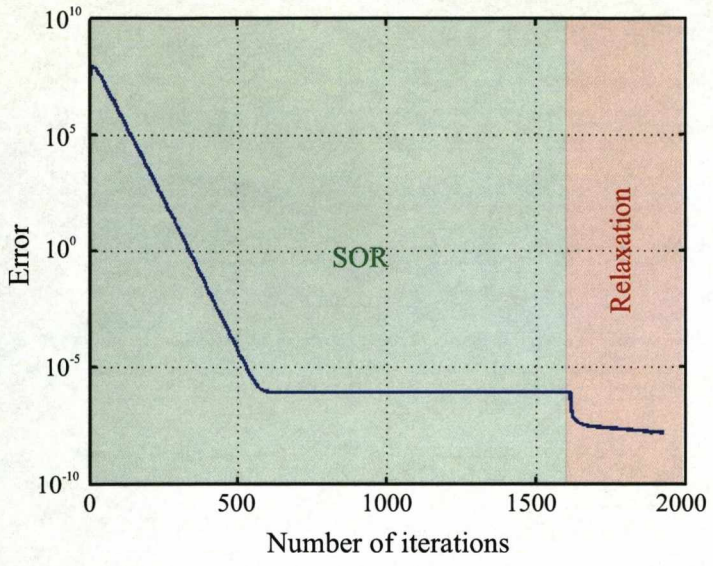

Figure 4.11: Evolution of error during the calculation of the electric potential. The *SOR* method converges after ~700 iterations at an error of ~8x10^{-6}. The *relaxation* method requires a further 150 iterations before convergence to an error value of ~5x10^{-7}.

$$\vec{E} = -\vec{\nabla}\varphi(x, y, z), \tag{4.9}$$

with the boundary conditions defined above. *Figure 4.12b* shows the calculated electric field distribution, the field is strongest beneath the central anode where the distance between the two electrodes is small. In this region (zone 1), the field has a planar configuration. The electric field strength in zones 2 and 3 falls away quickly as a function of increasing radius. To gain a more detailed understanding of the electric potential and field distributions through the detector, the profiles have been plotted at various depths in the detector. *Figures 4.13a-c* and *Figures 4.13d-f* show the electric potential and electric field distributions for depths 5mm, 40mm and 85mm respectively.

- At z = 5mm, the hexagonal corners resulting from the tapered cuts to the crystal show regions of weak potential and field strength. The field strength decreases quickly from ~1500Vcm^{-1} beneath the central anode, to as low as ~200Vcm^{-1} at the corners.

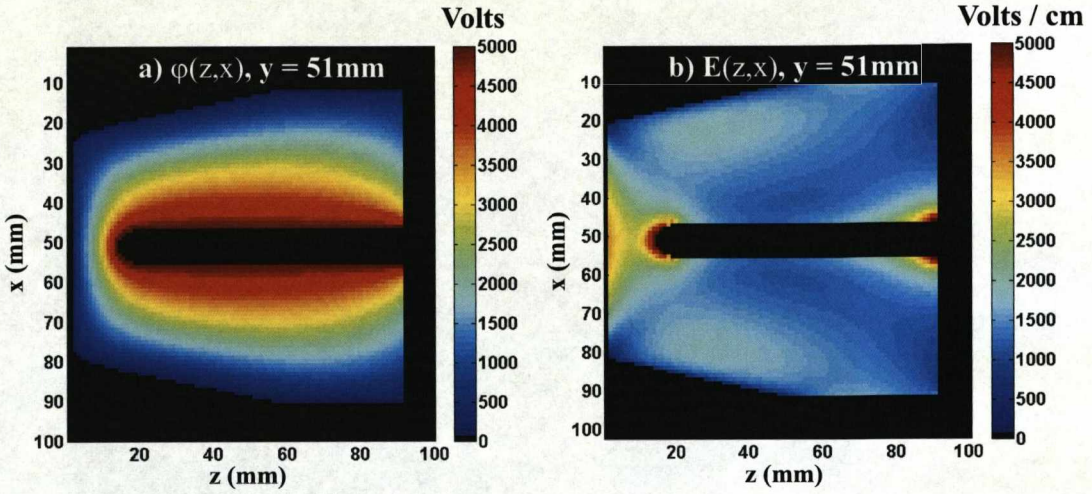

Figure 4.12: a) Electric potential and b) Electric field values in the z-x plane at y = 51mm (centre of the crystal). The results show the decrease in potential and field strength as a function of increasing radius from the central anode.

- At z = 40mm, the profile is representative of that of the majority of the bulk coaxial region (zone 3). Again both distributions vary from strong to weak as a function of increasing radius from the central anode. However the gradient is more uniform at mid and large radii. The field strength is seen to be zero in the very centre of the detector as the field cannot extend into the region of the drilled hole.

- For regions close to the back of the detector (z = 85mm), the field is still coaxial, however beyond this depth the field strength starts to decrease at large radii due to the distorted termination of the potential surfaces. This distortion occurs as the potential surfaces have to form a closed loop due to the imposed 0V boundary condition at the back of the crystal. Regions of weak field will result in unsaturated charge carrier drift velocities, thus changing the pulse shapes observed at the preamplifier output.

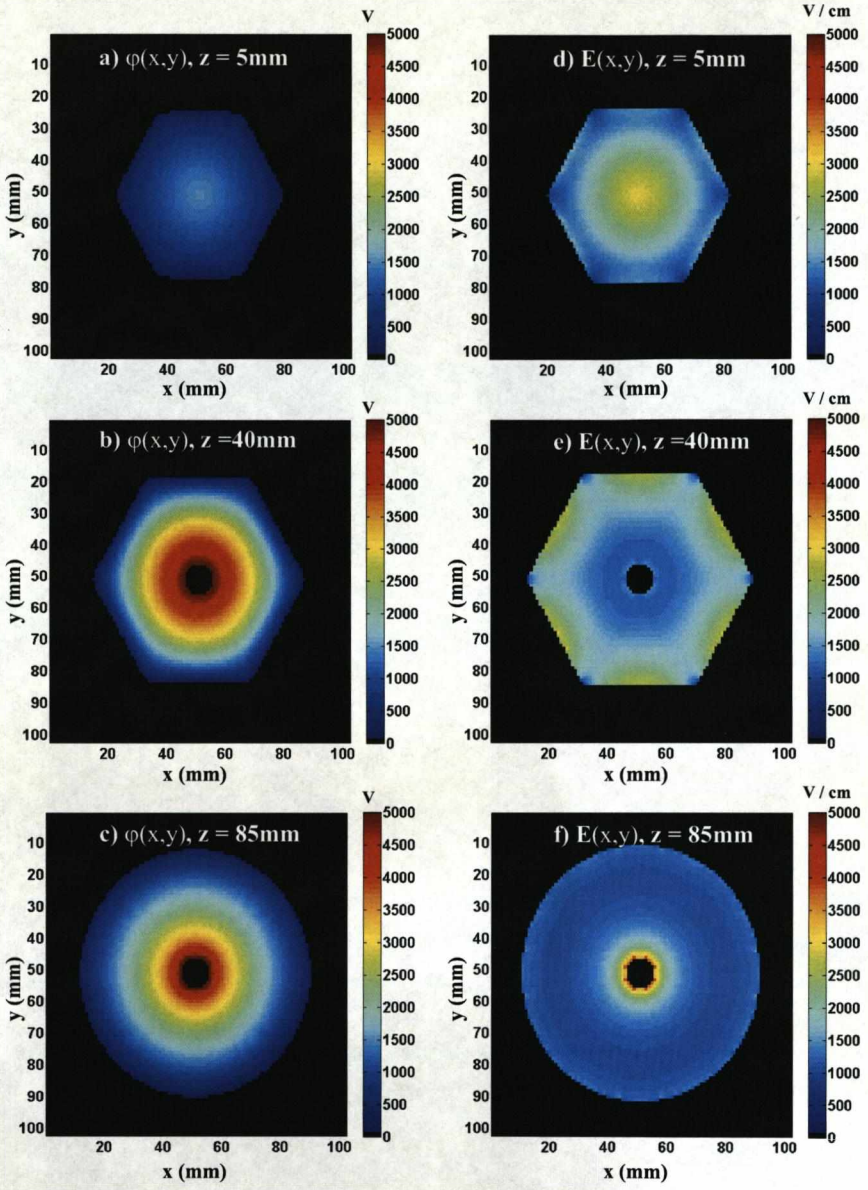

Figure 4.13: Electric potential (a to c) and electric field (d to f) values in the x-y plane at z = 5mm, 40mm and 85mm. At a depth of 5mm the electric field and electric potential are strongest at central radii. Regions of weak potential and field strength exist in the hexagonal corners of the detector. In the coaxial regions of the detector (z >= 30mm to z <= 80mm) the trend is similar, however, the field is more uniform as the geometry becomes more coaxial. At depths >85mm the field strength falls away very quickly as a function of radius due to the termination of the potential surfaces at the back of the detector.

4.4.6 Charge Carrier Drift Velocity Calculation

At high electric fields and low temperatures the charge carrier drift velocities in germanium become anisotropic [Nat63]. They depend on the electric field vector with respect to the crystallographic lattice orientation. The electron drift velocities, V_e, are saturated at field strengths >3000Vcm^{-1} for the <100> and <110> directions, and at $\sim$ 4000Vcm^{-1} for the <111> direction. The *hole* drift velocities V_h are saturated for fields $\sim$ 4000Vcm^{-1} along all three major crystallographic axes. At electric field strength of $\sim$4000Vcm^{-1}.

The models for anisotropic drift of the electrons and *holes* in n-type HPGe detectors implemented in MGS have been derived from work presented in [Mih00] and [Bru06a] respectively. A discussion of the underlying theory of these models is presented in *Section 2.3.1.* *Figure 4.14a* and *Figure 4.14b* show the electron and *hole* drift velocity profiles calculated by MGS, for the z-x plane along y = 51mm. The drift velocities are saturated beneath and alongside the central anode in the regions of the crystal where the electric field

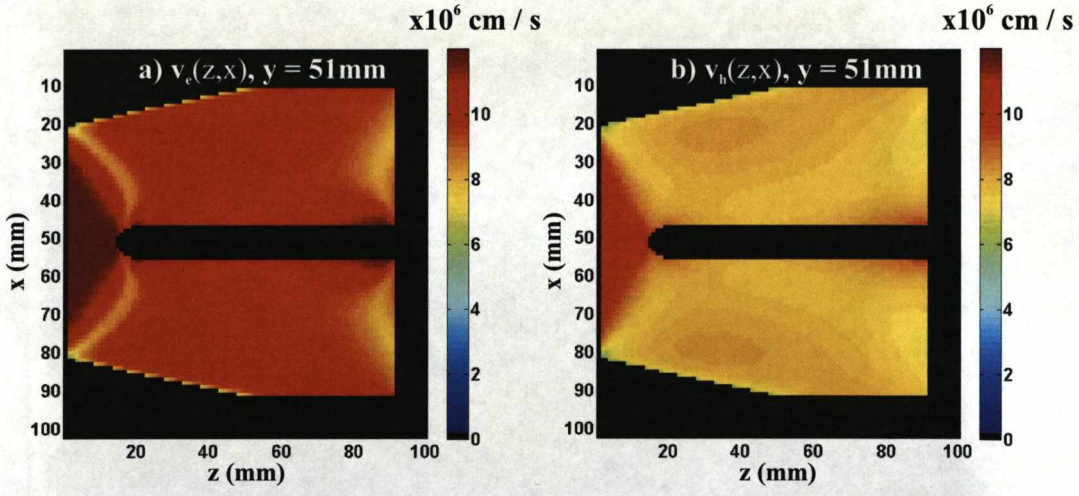

Figure 4.14: a) Electron and b) *hole* drift velocity values in the z-x plane at y = 51mm (centre of the crystal). The drift velocities are saturated in the regions of strongest electric field, beneath and alongside the central anode. Non-saturated regions (values <1.0·10^{7}cms^{-1}) are apparent in the corners and along the tapered surfaces of the crystal. The results also show that the *hole* drift velocity is systematically slower than that for the electrons.

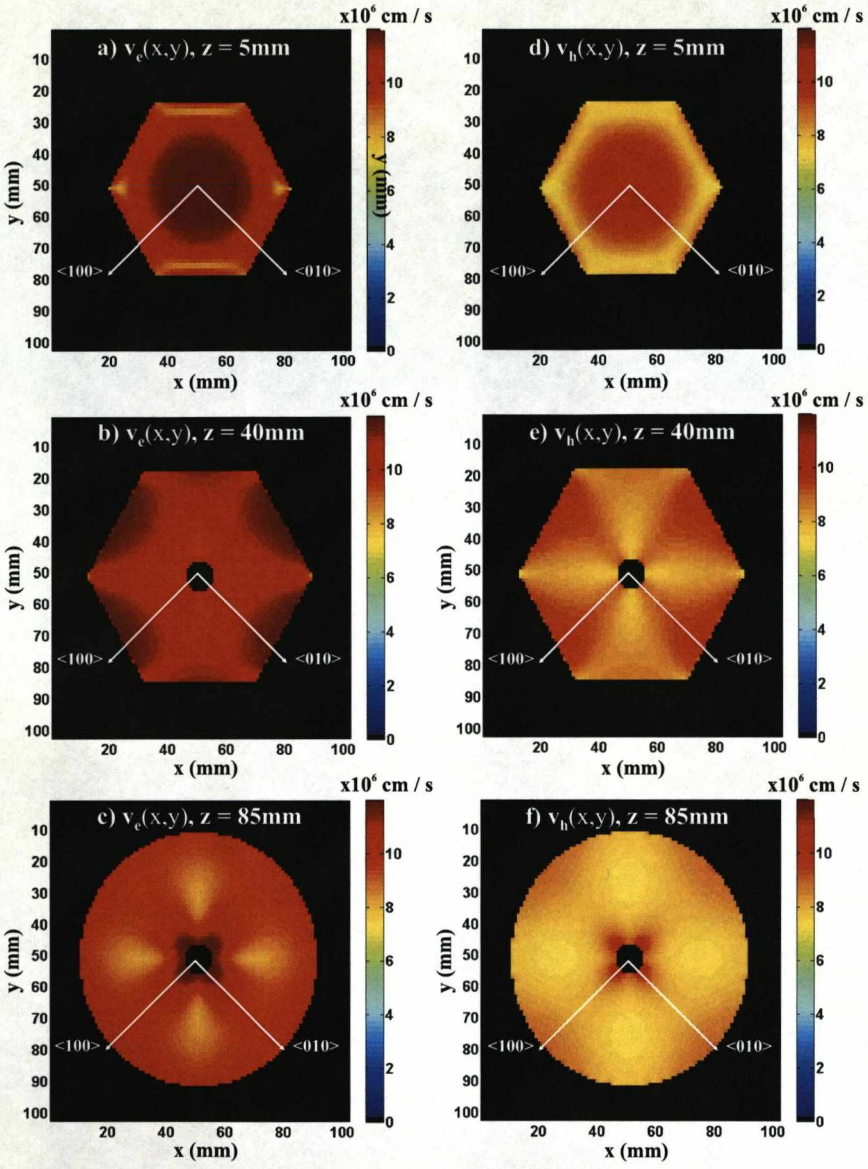

Figure 4.15: Electron (*a* to *c*) and *hole* (*d* to *f*) drift velocity profiles in the x-y plane at z = 5mm, 40mm and 85mm. The charge carrier drift velocities are saturated at central radii. Regions of unsaturated charge carrier drift velocity can be seen in the hexagonal corners at the front of the crystal and at large to mid radii near the back of the crystal where the electric field strength is weak. The crystallographic axes are shown in white.

is strongest. Non saturated regions (values $<1.0{\cdot}10^{7}\mathrm{cms}^{-1}$) are apparent in the corners and along the tapered surfaces of the crystal. The results also show that the *hole* drift velocity is systematically slower than that of the electrons throughout the crystal.

Figures 4.15a-c and *Figures 4.15d-f* show the electron and *hole* drift velocity distributions for depths 5mm, 40mm and 85mm.

- At z = 5mm, the hexagonal corners show regions of low charge carrier drift velocity resulting from the weak electric field. Both the electron and *hole* drift velocities decreases quickly from saturation beneath the central anode, to as low as $\sim 4{\cdot}10^{6}\mathrm{cms}^{-1}$ at the corners.

- At z = 40mm, the profile is representative of that of the majority of the bulk coaxial region (zone 3). Again both distributions vary from strong to weak as a function of increasing radius from the central anode. However, the regions of saturation extend to larger radii.

- At the back of the detector, z >85mm, there are large regions where the drift velocities for both the electrons and *holes* are not saturated.

These distributions will directly influence the pulse shapes generated for the basis data set. The effects of neutron damage, which results in lattice defects that cause *hole* trapping [Des05b], can also be folded into the simulation. Such defects in the crystal would result in longer charge carrier drift times.

4.4.7 Weighting Field and Pulse Shape Calculation

Before the induced current at each electrode can be calculated, the weighting potentials and weighting fields must be generated. As with the electric potential, the weighting potential is solved using the combination of SOR and relaxation methods. The calculation is performed with a null space charge density and the boundary conditions specified in *Section 2.3.1* (+1V on the sensing electrode with all other electrodes grounded). For a given interaction position, the charge pulse response observed at any electrode depends on the trajectory of the charge carriers through the weighting potential of that electrode, such that,

$$Q = -q \int_{x2}^{x1} E_W dl = q \left[V_W (x1) - V_W (x2) \right], \tag{4.10}$$

where *x1* and *x2* are the positions before and after the displacement of charge q, V_W is the weighting potential and E_W is the weighting field. In order to explain the shape of the real and image charge signals calculated for the AGATA geometry, a test example for two interactions in segment *A4* of the detector is presented in *Figure 4.16*. In this example position A is close to the centre contact and position B is close to the outer contact. The green dashed lines show the path of the charge carriers to the electrodes. *Figure 4.16a*, *Figure 4.16d* and *Figure 4.16g* show the weighting potentials for the core, segment *A4* and a neighbouring segment, *A3*. The weighting potential for the core shows a qualitatively similar distribution to that of the electric potential. It has a maximum value in the centre of the detector and decreases as a function of radius. Conversely, the weighting potential for segments A3 and A4 are strongest at large radii, and fall away quickly as the radius approaches the core. The weighting potential for each electrode extends throughout the volume of the detector and is related to the geometry of that electrode. As the outer electrode size is small, compared to the volume of the detector, the weighting potential surfaces fall to close to zero beyond the nearest neighbour electrodes.

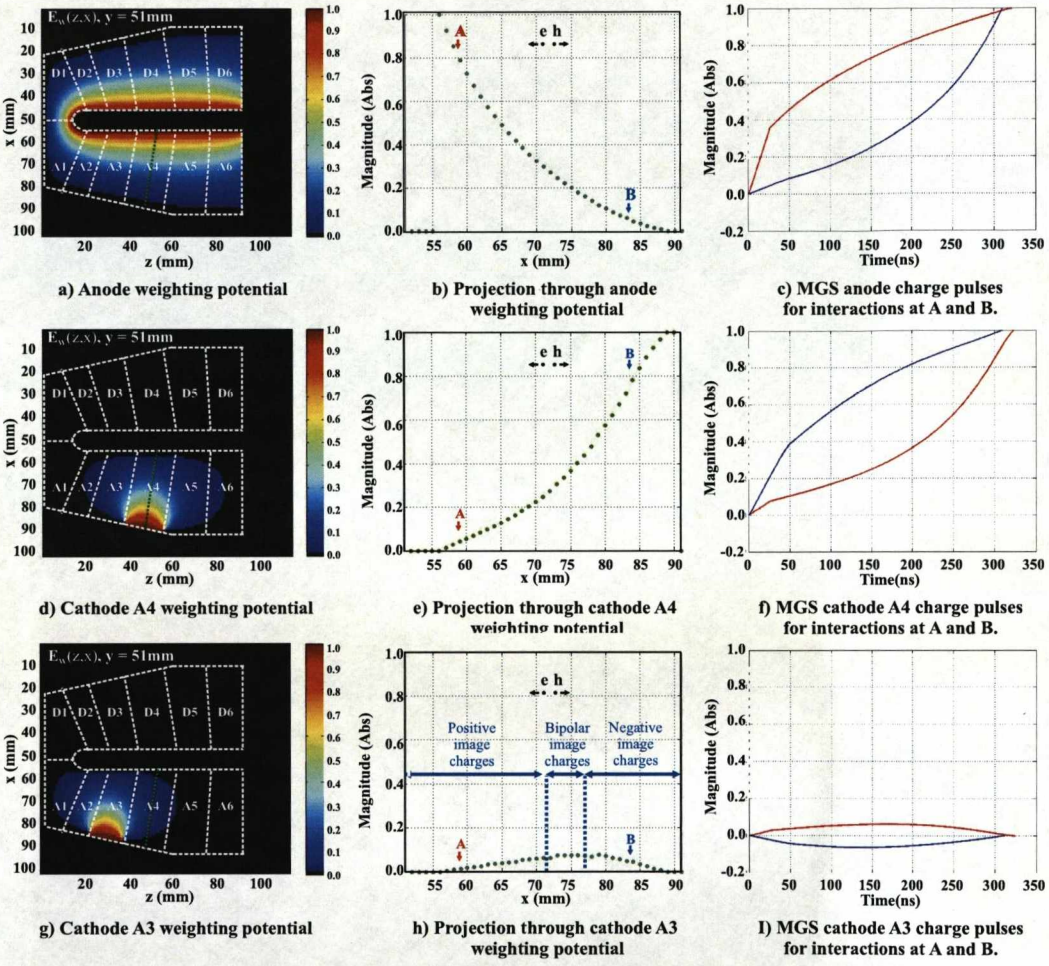

Figure 4.16: A figure showing how MGS calculates the charge pulse response from the trajectory of the charge carriers through the weighting potentials of the electrodes. Two interaction positions in segment A4 are considered. Position A is close to the centre contact and position B is close to the outer contact. a), d) and g) show the simulated core, *A4* and *A3* weighting potential distributions for the z-x plane at y = 51mm. The trajectory of the charge carriers is shown by the green dashed lines. b), e) and h) show the projections through the weighting potentials along these trajectories. c), f) and i) present the charge pulse response for interactions at A (red) and B (blue) for the core, segment *A4* and segment *A3* respectively.

Figure 4.16b, *Figure 4.16e* and *Figure 4.16h* show projections through the weighting potentials along the trajectory of the charge carriers for the central anode, segments *A3* and segment *A4* respectively. For an interaction close to the centre contact (position A), the charge induced on the anode will initially be large due to the steep weighting potential. The electron will be collected quickly due to its proximity to the anode. Thus the remainder of the induced signal will be governed by the contribution from the drift of the *hole*. As the majority of this drift will be in the region of shallow gradient, the induced charge will be smaller. Thus the charge pulse will have a fast initial T30, followed by a slow rise to T90. The opposite is true for the anode charge pulse response for an interaction at position B. Similar arguments can be used to describe the shape of the charge pulse observed from electrode A4 for positions A and B, when considering the projection indicated in *Figure 4.16e*.

The projection through the weighting potential for any segment that is not the interaction segment will resemble a skewed parabola. An example of this is shown in *Figure 4.16h*, for electrode *A3*. The shape of the distribution increases steadily up to a radius of 72mm, then turns over between 72mm and 78mm and returns back to zero. This parabolic shape is the result of the fact that the lines of equipotential for a segment must form a closed surface. The resulting charge pulse response for interactions at A and B are shown in *Figure 4.16i*. For the interaction at position B, initial drift of the electron and *hole* in the region where the weighting potential has a steep negative gradient will induce a negative signal. After the *hole* has been collected, the remaining drift of the electron in the region of shallow positive gradient will return the signal to the baseline. The opposite is true for the interaction at position A. For interactions that occur at some intermediate radii, both charge carriers first induce a positive signal, then when the electron crosses the stationary point of the projection, the drift of the hole induces a large negative signal.

4.4.8 Correction For Experimental Factors

For each simulated interaction, MGS outputs the induced current as a function of time. As shown in *Equation 4.2*, the contributions from the electron and *hole* must be summed and integrated in order to obtain the charge pulse response. However, this simple integration does not account for the limited bandwidth of the charge sensitive preamplifier, the low-pass Nyquist filter at the input stage of the GRT cards, or the sampling of the 14bit 80MHz FADC. In order to compensate for these experimental factors, several corrections have been applied to the data. The simulated data is adjusted to fit the experimental data as the correction factors can be applied independently of the noise.

4.4.9 Preamplifier Correction

The limited bandwidth of the preamplifier effectively slows the response of the output charge pulse. This factor, along with the continuous decay resulting from the resistive feedback circuitry, alters the shape of the leading edge of the charge pulse. The transfer function, for the AGATA preamplifier, used to correct the pulse shape response is taken from [Scb05]. The original Java routine has been translated into Matlab. The output signal *V(t)* from the preamplifier is a convolution of the input current *I(t)* with the response function *R(t)*, such that,

$$V(t) = \int_0^t I(t - t') \cdot R(t')\, dt'. \tag{4.11}$$

R(t) was derived from the adjusted (R(t=0) = 0) Sigmoid function [Scb05] as,

$$R(t) = \frac{1}{1-c} \cdot \left(\frac{1}{1 + \frac{1-c}{c} \cdot exp(-b \cdot t)} - c \right), \tag{4.12}$$

where b controls the slope, in this instance the rise of the pulse, and $\frac{1-c}{c}$ shifts the point where the curvature changes. By rearranging *Equation 4.12*, the rise of the pulse is given as,

$$t_{10}^{90} = \frac{ln\left(\frac{c}{1/9+c}\right) - ln\left(\frac{c}{9+c}\right)}{b}. \tag{4.13}$$

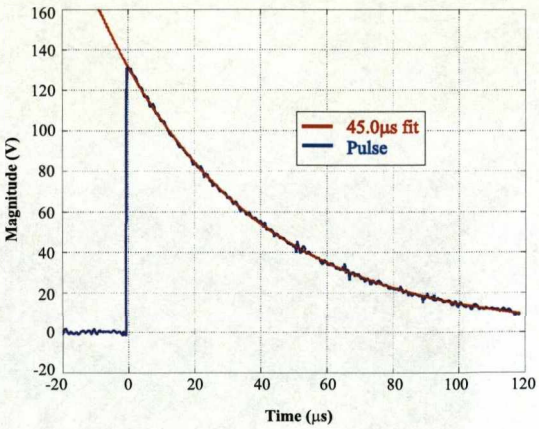

Figure 4.17: Plot showing an example of the digitised preamplifier output for the centre contact of the S002 AGATA prototype detector. From the optimum fit (red), a decay time constant of 45.0μs was obtained.

The parameters used to fit this function were calculated from pulser measurements performed at IKP Cologne. The input to the preamplifier was a +1.0V step function with 5ns rise time. Values for b and c of 0.1675 and 0.3021 were determined. Thus a value for t_{10}^{90} of 18.59ns was obtained. Finally, in order to account for the gain, g, and the decay of the preamplifier, *Equation 4.12* is adjusted to,

$$R(t) = g \cdot \frac{1}{1-c} \cdot \left(\frac{1}{1 + \frac{1-c}{c} \cdot exp\left(-b \cdot t\right)} - c \right) \cdot exp\left(-\frac{t}{t_d}\right). \tag{4.14}$$

A decay time of $t_d = 45.0\mu$s was obtained from least squares fits to the S002 core and segment pulse shapes. An example fit is presented in *Figure 4.17*. A core pulse shape is shown in blue and its optimum fit in red.

4.4.10 GRT Card Correction

The GRT cards [Laz03] were developed at STFC Daresbury Laboratory in collaboration with the University of Liverpool. At the input stage is a 40MHz Nyquist high frequency filter, followed by an 80MHz FADC. A correction for both the filter and sampling of the ADC (1 sample every 12.5ns) have been applied. These corrections have also been folded

into the MatLab routine outlined above.

To correct for the high frequency filter, a Fast Fourier Transform (FFT) was performed on every signal to transform the data into the frequency domain. A 40MHz threshold was applied with a first order tail. An Inverse Fast Fourier Transform (IFFT) was then used to recover the filtered pulse shapes. To correct for the limited sampling of the ADC, the transformed signals were sampled every 12.5ns. They were then interpolated to 2.5ns per sample for alignment to the experimental data.

Figure 4.18 shows the *raw* (red) and fully corrected (blue) MGS charge pulse shape response for a single interaction position in segment *A2*. The pulses for the interaction segment (*A2*), centre contact and nearest neighbour (*B2*, *F2*, *A3* and *A1*) electrodes are shown. It can be seen that the combination of correction factors both slows and smoothes the observed response.

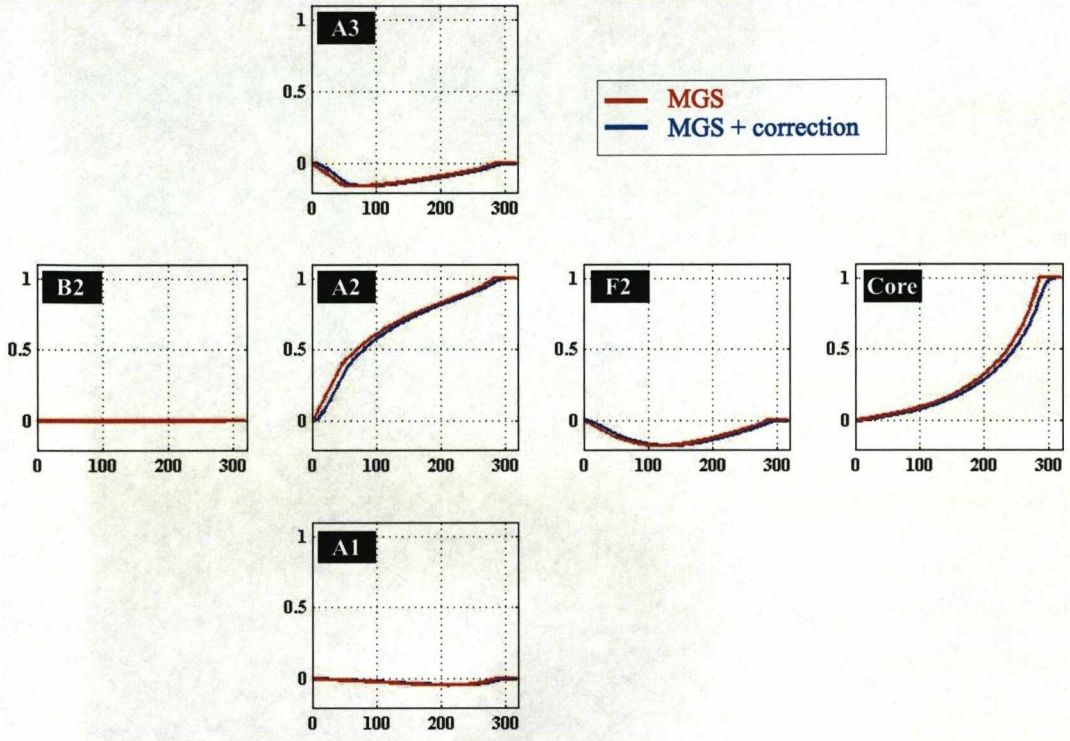

Figure 4.18: A figure showing how the corrections applied for experimental factors alter the simulated MGS pulse shapes. The pulses are corrected for the limited bandwith and exponential decay of the preamplifiers, and the 40MHz Nyquist filter and 80MHz sampling of the FADCs in the GRT cards. The raw MGS pulses are shown in red, while the corrected pulse shapes are shown in blue.

Chapter 5

Characterisation Measurements

The performances of two symmetric AGATA prototype detectors, S002 and S003, have been measured in detail at the University of Liverpool. On arrival, each detector was set up and tested to ensure that the manufacturers specifications were met. Following these tests, the detector was moved to the scanning table where the crystal volume was interrogated with a 1mm collimated beam of ^{137}Cs (662keV) photons. The beam was moved to various locations (x-y) beneath the detector and the resulting pulses digitised so that the position dependent response could be characterised. Data were collected in both singles and coincidence modes. The singles fine-scan gave a fast way of probing the bulk crystal, as no constraint on the depth (z) of the photon interactions was required. Contrastingly, the coincidence scan was a drawn out process. The requirement of 90^o scatters through a collimator network, to ensure full 3D spatial localisation, diminished the count rate. This chapter presents a summary of the procedure for accepting, testing and scanning each detector. The results from the S002 detector are discussed in detail.

5.1 Initial Setup

On arrival in the laboratory, the detector cryostat was pumped to ensure operation at vacuum pressure. The combination of a rotary pump and turbo pump were utilised to reduce the cryostat pressure to $\sim 1.7\text{x}10^{-6}$mbar. The Platinum Thermistor (PT100) values were then measured to test the temperature readout. Resistances of 108.2Ω (21^oC) and 108.9Ω (23^oC) were recorded from the back of the capsule and dewar PT100s respectively.

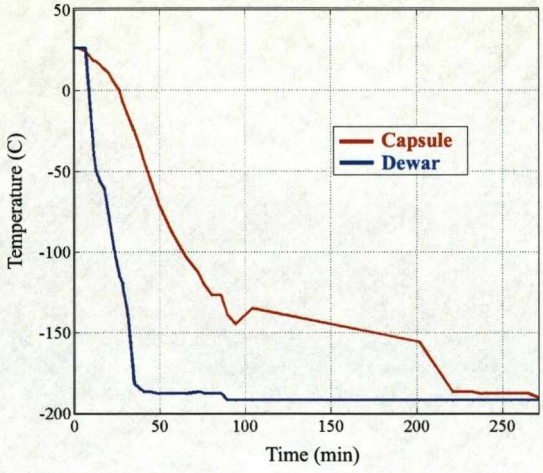

Figure 5.1: PT100 measurements for the S002 AGATA symmetric prototype detector capsule (red) and dewar (blue). More than four hours of cooling were required to achieve an operating temperature of -185^{o}C, or 88k

Once evacuated, the cryostat was cooled by filling the dewar with liquid nitrogen (LN_2). *Figure 5.1* shows the cooling cycles for both the capsule (red) and dewar (blue). From this plot it can be seen that the capsule required more than four hours to cool to an operating temperature of -185^{o}C, or 88k. The detector was then left connected to the LN_2 auto-fill system overnight for the temperature to stabilise before measurements were taken.

5.2 Analogue Measurements

Once a signal response from all 37 channels had been observed, the level of the baseline noise was measured with a digital oscilloscope. The average peak-to-peak noise for the S002 detector was 2.8mV, the RMS noise was 0.99mV. With a preamplifier gain of 100mV/MeV, these results equate to 28keV and 9.9keV respectively. Analogue energy resolution and absolute efficiency measurements were then collected as an initial validation of the detectors operational performance. The energy resolutions of the 37 channels of the detector were measured one at a time in order to obtain the optimum results. The experimental detector labelling convention is presented in *Figure 5.2*. To measure the resolutions, each channel

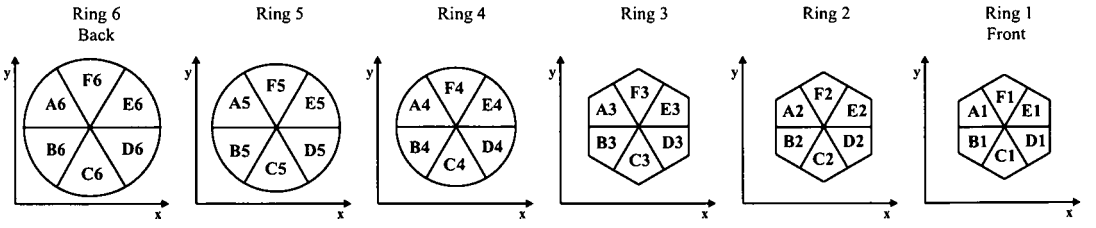

Figure 5.2: Detector labelling convention as supplied by Canberra Eurisys. The x and y refer to the orientation of the scanning table.

of the detector was individually connected to an Ortec 671 spectroscopy amplifier (6μs shaping time) through the same converter box. Spectra were collected with an 8k ADC and Ortec Maestro Multi Channel Analyser (MCA) software and fitted in GF3 [Rad00]. Data were collected with ^{241}Am (60keV) and ^{60}Co (1.33MeV) sources, with the count rate maintained at <1kHz. A detailed description of the step-by-step procedure for recording these analogue measurements, along with the full set of results for both the S002 and S003 detectors, is presented in *Appendix B.* The results from the S002 prototype detector, are displayed in *Figure 5.3a.* The energy resolution (FWHM) is shown to vary as a function of ring number at both 60keV (blue) and 1.33MeV (red). This is the result of different segment capacitances due to the different segment sizes in each ring. The segment capacitances as a function of ring, measured at the University of Cologne, are presented in *Table 5.1.*

For the absolute efficiency measurement, a ^{152}Eu source was placed 250mm from the detector face and data were collected for three hours. The results from the centre contact of the S002 detector are presented in *Figure 5.3b.* The efficiency decreases as a function of photon energy as gamma rays entering the detector are more likely to Compton scatter out of the detector without depositing their full energy. The peak in efficiency at low energy is not displayed as the necessary data were not collected. An absolute efficiency of 1.1×10^{-4} at 964keV is equivalent to an intrinsic efficiency of 19.8% for the AGATA prototype detector geometry at that energy. A relative efficiency of 73.5±2.5% was calculated at 1332keV, with a ^{60}Co source also positioned 250mm from the crystal face. The relative efficiency as specified by the manufacturer was 71.3%.

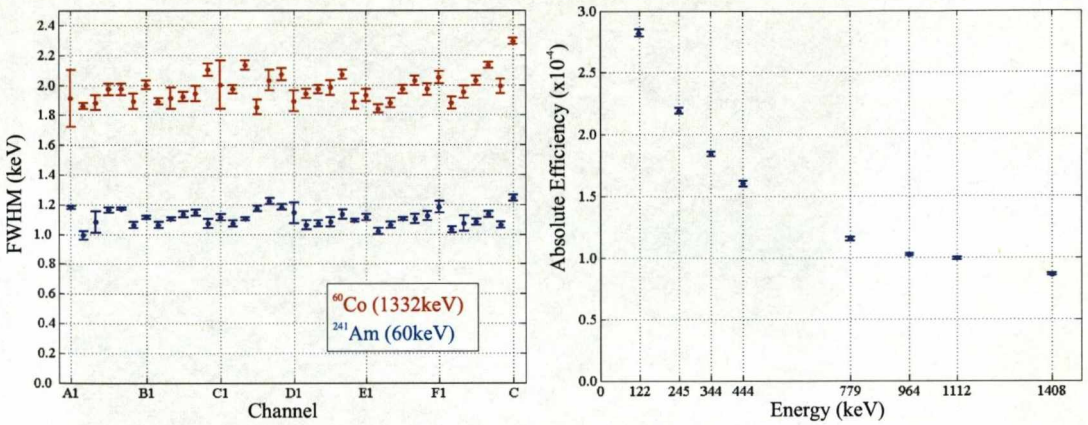

a) Energy resolution

b) Absolute efficiency

Figure 5.3: Analogue energy resolution and absolute efficiency measurements for the S002 AGATA prototype detector. a) Energy resolution for the 36 outer contacts and centre contact at 1.33MeV (red) and 60keV (blue). The FWHM varies as a function of segment capacitance. b) Absolute efficiency measured with a ^{152}Eu source placed 250mm from the detector face.

Ring	Capacitance (pF)
1 (Front)	0.943
2	0.666
3	0.980
4	1.190
5	1.160
6 (Back)	0.980

Table 5.1: AGATA symmetric prototype detector capacitances. The values listed are from measurements taken at the University of Cologne.

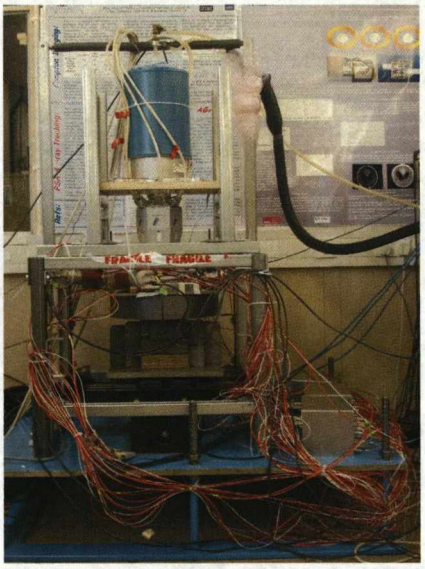

a) Photograph of the S002 detector on the scanning table.

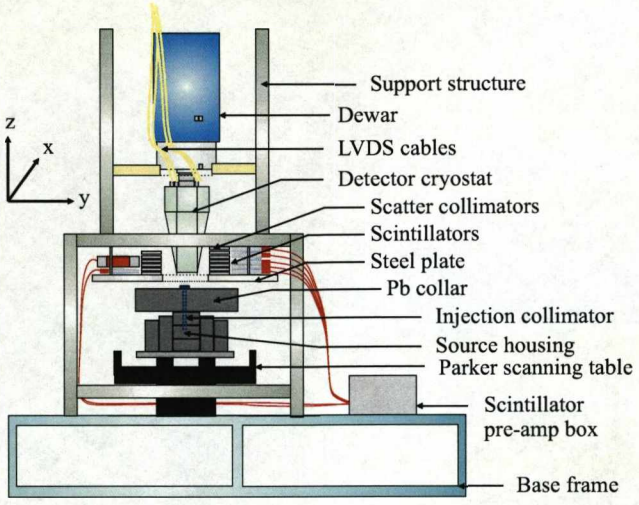

b) Schematic representation of the S002 detector on the scanning table.

Figure 5.4: a) Photograph of the S002 AGATA prototype detector mounted on the scanning table. b) Schematic representation of a). The AGATA cryostat was suspended in a vertical position above the collimated ^{137}Cs source. When operated in singles and coincidence modes, the source was positioned at various locations beneath the detector. The pulse shape response was measured at each location. The 90^o scatter collimators and scatter detectors were only required for the coincidence measurements, however they were positioned prior to the singles scan to ensure that the data sets were comparable.

5.3 Liverpool Scan Setup

The setup and scanning procedures for each detector were performed in an identical fashion, in order that the data sets could be compared. *Figure 5.4* and *Figure 5.5* show a schematic representation and detailed view of the scanning table infrastructure.

A 920MBq ^{137}Cs source was positioned by a precision Parker scanning table. When setting up the table, the source was inserted inside a lead block mounted on a base plate and fixed to the motorised runners. A cubic lead shield ~16cm in diameter was then built around the source. The lead block, located immediately above the source had a 1cm diameter hole bored through its centre. A lead collar, also with a 1cm hole bored from its

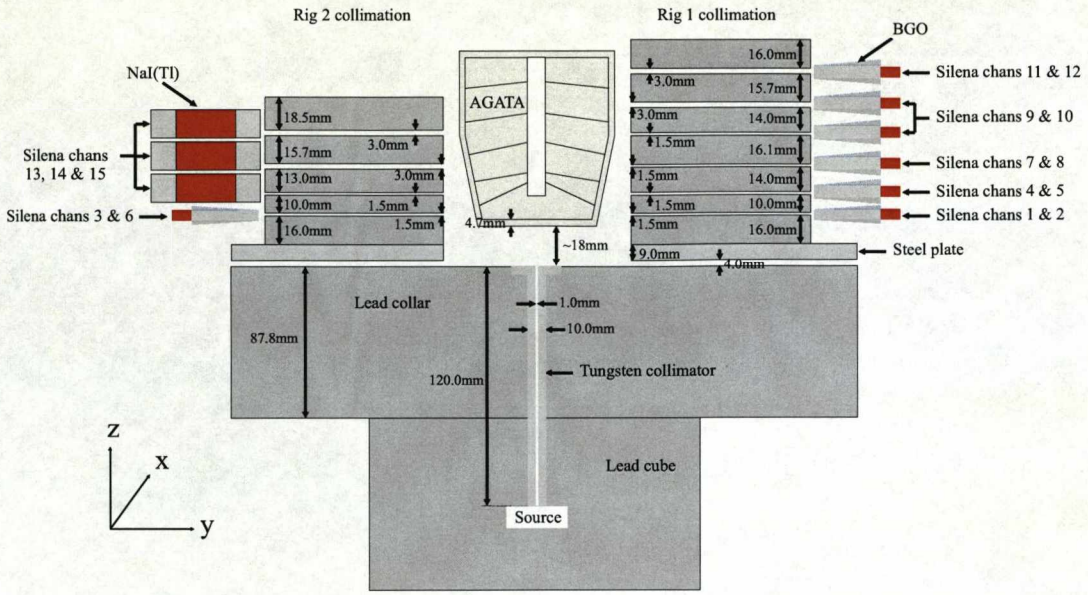

Figure 5.5: A detailed schematic representation of the AGATA S002 prototype detector mounted on the Liverpool scanning table. The coincidence scatter detectors and scatter collimator dimensions are labelled. There were six collimation depths on rig one and four collimation depths on rig two. The distance from the top of the Tungsten collimator to the front face of the crystal was ~23mm.

centre, was positioned on top of the block. This arrangement allowed a coaxial tungsten collimator, 120mm in length and 1cm in diameter, to be inserted to a position just above the source. The tungsten cylinder had a 1mm diameter hole bored from its centre, ensuring that the isotropic source emission was collimated to a 1mm *pencil* beam.

A steel frame was constructed around the scanning table. From this, a steel plate was suspended by threaded rods, on which the scatter collimators and scatter detectors could be supported. The rods enabled the plate, and hence the collimators, to be moved up and down in the z-direction. The steel plate had a square cut from its centre and was positioned to a height just above the lead collar. The AGATA detector was then inserted into the frame and positioned in the centre of the plate. This configuration ensured that the cryostat was suspended in a vertical position above the collimated source.

	Rig 1		Rig 2	
Gap	Depth in Crystal (mm)	Depth in Segment (mm)	Depth in Crystal (mm)	Depth in Segment (mm)
1	7.3	7.3	7.3	7.3
2	18.8	10.8	18.8	10.8
3	34.3	13.3	34.0	13.0
4	51.9	15.9	52.7	16.7
5	68.1	14.1	-	-
6	86.8	14.8	-	-

Table 5.2: A table showing the measured depths at which gamma rays must scatter out of the S002 crystal to pass through the centre of each collimation gap. The absolute depths with respect to the front face of the crystal are shown in columns two and four. The translations of these depths with respect to the ring in which the collimators were located is shown in columns three and five. A constant factor of ~3mm must be subtracted from each depth when considering the measurements performed with the S003 detector.

The scatter collimator configuration was constructed from semicircular sheets of lead of various thicknesses, stacked on top of each other. The gaps through which the photons could pass were formed by the insertion of polythene spacers between the required sheets. The aim of this setup was to enable the simultaneous scanning of a single depth in each of the six rings of the detector, for every x-y position of the scanning table. The spacers for the depths towards the back of the detector were larger than those at the front in order to provide enough statistics. This extra spacing increased the count rate of deep interactions to compensate for attenuation of the γ-ray photons inside the detector. The scatter collimation was assembled in two halves, rings one and two. Where rig one refers to the section surrounding sectors A, F and E of the AGATA detector, and rig two refers to that surrounding sectors B, C and D. *Table 5.2* lists the measured depths at which gamma rays must scatter out of the S002 crystal to pass through the centre of each collimation gap. The absolute depths with respect to the front face of the crystal are shown in columns two and four. The translations of these depths with respect to the ring in which the collimators were located is shown in columns three and five. A constant factor of 2.3mm must be subtracted from each depth when considering the measurements performed with the S003

detector.

A total of twelve banks of BGO detectors (33 tubes) and three NaI(Tl)detectors were positioned around the collimators to maximise the solid angle coverage of the set up. These banks were split into two categories, depending on the detector type:

1. BGO banks (Silena channels one to twelve) - Detectors acquired from the, now decommissioned, EUROBALL BGO Inner Ball. These detector banks were mounted in a formation that allowed each collimation depth of each rig to be split into two separate regions. Thus allowing scatters from different regions of the AGATA detector to be isolated. The preamplifier output from each bank was the sum of the energies deposited in each tube of that bank.

2. NaI(Tl) banks (Silena channels thirteen to fifteen) - Single NaI(Tl) detectors, 51mm in diameter and 76mm in length, coupled to a PMT and preamplifier. No energy summation was performed at the preamplifier stage of these detectors.

A detailed description of the location of each of the banks of detectors is given in *Table 5.3*. The positioning of the detectors with respect to the collimator rings can be seen in *Figures 5.5* and *5.6*. *Figure 5.6a* shows the first two lead scatter collimators and the BGO detectors used to construct the first collimation depth of rig one. The five BGO detectors split the depth into two regions, banks one and two. *Figure 5.6b* shows both halves of the collimation setup. *Figure 5.6c* and *Figure 5.6d* show the final BGO and NaI(Tl) arrangements utilised in each rig. Once positioned, the detectors were powered up and gain matched. In order to perform the gain matching, ^{241}Am and ^{137}Cs sources were suspended at different locations around the scintillators and left to count until several thousand counts were present in each photo-peak. The 662keV peak was adjusted to be at half the range of the 8192 channel spectrum to compress the broad peaks. The centroids of the peaks for all the ADC inputs were then aligned by generating the appropriate coefficients in software. Although the scatter collimators and scatter detectors were only required for the coincidence measurements, they were left in position throughout the singles scan to ensure that the data were comparable with that collected in coincidence mode.

Silena Channel	Input	Rig	Depth [Bank]	No. of Detectors in Bank
1	BGO	1	1 [1]	2
2	BGO	1	1 [2]	3
3	BGO	2	1 [3]	2
4	BGO	1	2 [1]	2
5	BGO	1	2 [2]	3
6	BGO	2	1 [4]	3
7	BGO	1	3 [1]	3
8	BGO	1	3 [2]	3
9	BGO	1	4 & 5 [1]	3
10	BGO	1	4 & 5 [2]	3
11	BGO	1	6 [1]	3
12	BGO	1	6 [2]	3
13	NaI(Tl)	2	2, 3 & 4 [1]	1
14	NaI(Tl)	2	2, 3 & 4 [2]	1
15	NaI(Tl)	2	2, 3 & 4 [3]	1
16	AGATA Core	-	-	-
17	TAC	-	-	-

Table 5.3: A table showing the inputs to the Silena ADC. Channels one to fifteen recorded the CAEN sixteen channel amplifier outputs resulting from the scintillation detectors. Each bank of BGO detectors was read out as the sum energy of the constituent detector signals. The NaI(Tl) detector readouts were recorded individually, one detector per channel. Channel sixteen digitised the AGATA centre contact signal after shaping by an ORTEC 671 spectroscopy amplifier ($6\mu s$ shaping time). The TAC signal generated by coincidences between the core and any scintillation detector channel was digitised in channel seventeen.

Having finished the setup of all the auxiliary scatter detectors, the positioning of the AGATA detector was checked with spirit levels to ensure that it was not skewed in the z-plane. The spirit levels were placed at various x-y orientations on the back of the dewar. It was assumed that the back surface of the dewar was aligned parallel to the front face of the crystal inside the cryostat. The detector was then rotated so that the outer walls of the cryostat that bounded sectors A and B and D and E were parallel to the y-axis of the scanning table. The detector bias was then applied so a test scan could be performed. The

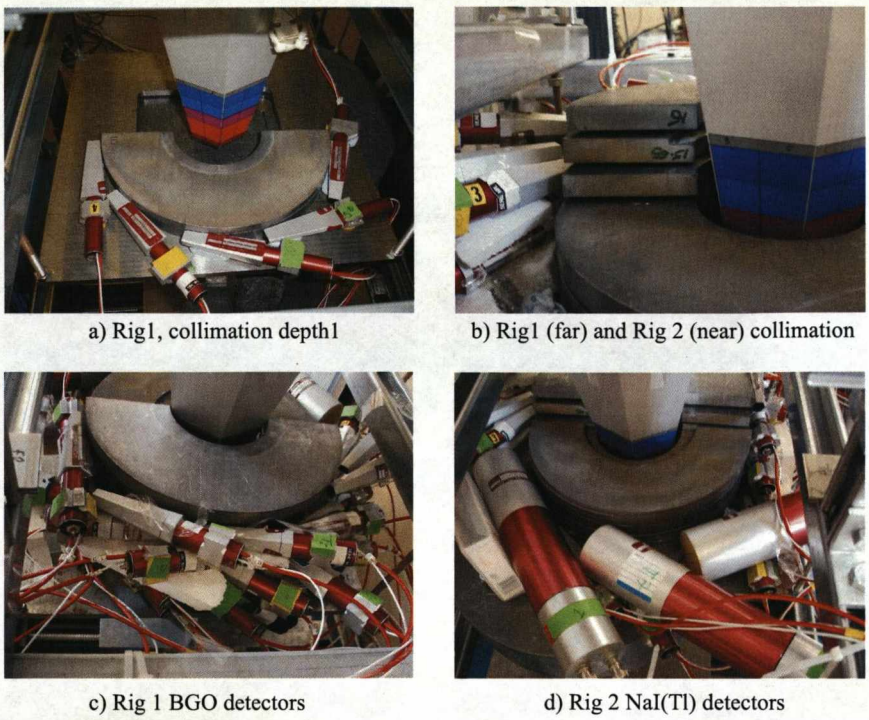

a) Rig1, collimation depth1

b) Rig1 (far) and Rig 2 (near) collimation

c) Rig 1 BGO detectors

d) Rig 2 NaI(Tl) detectors

Figure 5.6: Photographs showing the stages of construction of the scatter collimator rig. The rig was built in two halves. Rig one surrounded sectors A, F and E of the AGATA detector, while rig two surrounded sectors B, C and D. a) lead sheets and five BGO detectors (two banks) for collimation depth one of rig one. b) View showing the sheets of lead that form the six collimation depths of rig one and four collimation depths of rig two. c) Final BGO detector arrangement for rig one. d) Final BGO (depth one) and NaI(Tl) (depths two to four) detector arrangement for rig two.

test scan enabled the inspection of the orientation of the capsule relative to the cryostat to be validated. From this initial scan, it could be seen that the segmentation lines of the detector were offset from the scanning table by a rotation of $\sim 3^o$ in the x-y plane, implying that the capsule was rotated inside the cryostat. To compensate for this offset, the cryostat was rotated back and the test scans were repeated until the segmentation lines were parallel with the scanning table. Following the alignment, the detector remained static in its position for two months while the front face singles and coincidence scans were performed. After this period, the detector bias was powered down and the scatter collimation and support structure were removed. This ensured enough free space for the

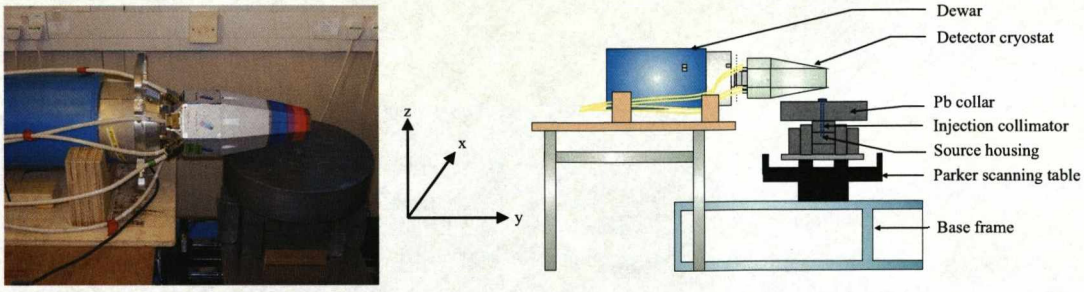

a) Photograph

b) Schematic representation

Figure 5.7: Schematic representation of the side scan configuration for the S002 AGATA symmetric prototype detector. a) Photograph of the AGATA detector mounted on its side over the Parker scanning table. b) Schematic representation of a). The side scan allowed the depth profile of each detector to be characterised.

AGATA cryostat to be mounted perpendicular to the z-axis of the scanning table in order that the response from scanning the side of the detector could be characterised, see *Figure 5.7*. The side-scan allowed the pulse shape response as a function of depth through the detector to be investigated. It also allowed the effective segmentation through the depth of the crystal to be localised. The side-scan was the final measurement performed with each detector.

5.4 Scanning Electronics

Figure 5.8 shows a schematic representation of the signal processing chain used for the characterisation measurements. The grey tracks highlight the extra modules incorporated in the coincidence measurement. A complex series of analogue and digital processing units were required to perform the scans. The architecture is summarised below. The reader should note that the S9418 Silena Analogue to Digital Converter (ADC), Silena ADC Controller (SAC) and GRT4 cards are VME modules. All other modules are standard NIM units. The trigger for each set up required the use of fast processing units. The combination of a Timing Filter Amplifier (TFA) and discriminator, either Constant Fraction (CFD) for germanium or Leading Edge (LED) for scintillators, were utilised.

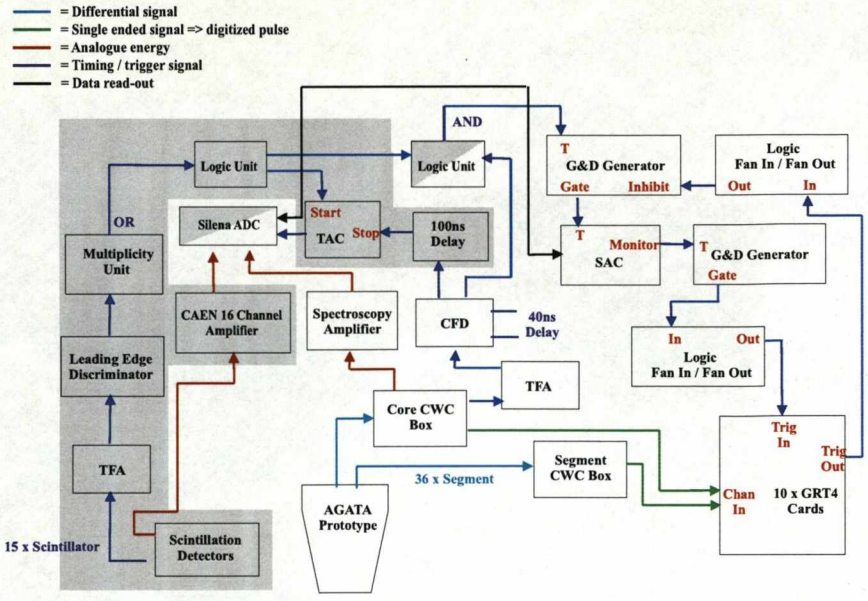

Figure 5.8: A schematic diagram of the electronics architecture for the singles and coincidence measurements. The grey tracks highlight the additional modules required for the coincidence scans. When running in singles mode, the GRT cards were triggered from the centre contact CFD. However, when the system was switched to coincidence mode, the cards were triggered on the *AND* of the AGATA core CFD with the *OR* of the 15 scintillator banks. The GRT cards, Silena ADC and Silena ADC controller (SAC) were VME modules. All other modules were operated from a standard NIM crate.

Each symmetric AGATA prototype detector was furnished with 37 differential preamplifiers with 100mV / MeV gain. The segment preamplifiers were mounted three to a board, thus there were two boards per sector of the detector. The centre contact preamplifier was mounted separately. All 37 preamplifier signals were extracted with seven Low Voltage Differential Signaling (LVDS) cables, one for each sector of segment preamplifiers plus one for the core. Each LVDS cable was connected to a separate converter box. Each box converted the differential preamplifier outputs into single-ended signals appropriate for digitisation in the GRT4 cards. The core converter box had three outputs that provided replicas of the signal. The segment converter boxes fanned out the LVDS signals into the six separate segment channels, but only provided one copy of each. The set up of the data acquisition system for running in both singles and coincidence modes required the AGATA detector

centre contact to provide three signal streams. One to generate time information as part of the trigger, one for analogue energy information for validation of the detectors operating performance, and one for digitisation.

The 36 single-ended segment outputs and one of the core outputs were fed into the inputs of ten, four channel, GRT4 VME cards [Laz03]. Each GRT4 card channel contains two 200k Xilinx Spartan Virtex II FPGAs. The first FPGA is responsible for the energy calculation, trigger control, and timestamp generation. The energy is derived from the Moving Window Deconvolution (MWD) algorithm [Geo93] programmed into the FPGA. The second FPGA is responsible for buffering and other processing controls. The input stage of each channel incorporated a Nyquist high-frequency filter and 14 bit, 80 MHz (12.5ns per sample) Flash ADC. The analogue signals were digitised over a range of $\pm$1V ($\pm$10MeV). Each pulse shape was sampled two hundred and fifty times, thus 3.1μs of trace per channel per event were read out. The GRT cards required an external trigger. This master trigger, from the core, was duplicated by a Lecroy 429A logic Fan-In / Fan-Out unit, enabling all ten of the GRT cards and the Silena ADC to be read out. Following a valid trigger, data were read out sequentially. The data collection was inhibited during the read out by utilising the *busy* signal from the GRT4 cards. The data were transmitted by the VME crate CPU through an ethernet connection to the acquisition PC.

5.4.1 Singles Trigger

For both the singles front-face and side scans, the acquisition system was triggered on the signal generated by the centre contact of the AGATA prototype detector. The Ortec 474 TFA was set to maximum differentiation and minimum integration. The Ortec 935 CFD threshold was set to ~420keV, see *Figure 5.9*, thus enabling the rejection of the majority of the Compton background. The maximum trigger rate on the core was 720Hz when the collimated source was positioned beneath the centre of the detector. A background rate of 40Hz was observed when the source was moved outside of the profile of the detector. Although up to 720 events per second were requested, the limited bandwidth of VME BUS allowed only approximately two hundred events per second to be transmitted. For every trigger event, the CFD signal was passed to the Philips Scientific 794 Gate & Delay

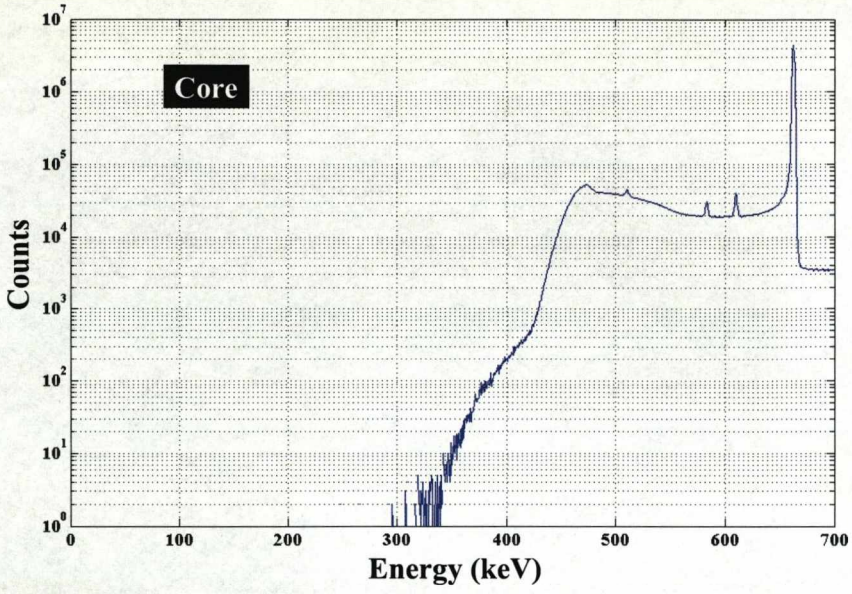

Figure 5.9: MWD energy spectrum for the centre contact from the ^{137}Cs (662keV) AGATA S002 front-face singles scan. The CFD threshold was set to ~420keV, ensuring that only events that deposit their full energy trigger the system.

Generator (G & D), forming the master trigger signal for the acquisition. For every master trigger, the analogue AGATA core energy was also recorded in channel sixteen of the Silena ADC. The CWC output was first shaped using an Ortec 671 Spectroscopy Amplifier (Spec-Amp) with a 6μs shaping time, prior to being measured by the ADC.

5.4.2 Coincidence Trigger

For the coincidence scans, the acquisition required a time correlated coincidence between the centre contact of the AGATA prototype detector and any of the fifteen banks of scintillation detectors, see *Table 5.3.* To achieve this, the signals from each of the fifteen preamplifier outputs were split in order to provide both time (trigger) and energy information. The time information for each channel was derived by shaping the preamplifier signal with a TFA. However, Lecroy 821 LEDs were used instead of CFDs as the fast pulse shape response from scintillation detectors was more uniform than that for the AGATA detector. The threshold of each LED was set to ~100keV, while the threshold of the core was set to 200keV. The

LED outputs were fed into a Lecroy multiplicity unit that took the logical OR of all fifteen channels. The resulting signal was split into two to provide one input to the trigger and one to the *start* of the Ortec 566 Time-to-Amplitude Converter (TAC). The master trigger was the logical AND of this trigger with the AGATA centre contact CFD signal, and was realised if both signals were generated within a 280ns time window. The AGATA centre contact CFD signal was also the *stop* for the TAC. The TAC measured the time difference between the *start* and *stop* signals. The output signal was proportional to this difference and was measured in channel seventeen of the Silena ADC. Off-line analysis of the TAC spectrum allowed the discrimination between true and random coincidences. The energy information from the scintillator preamplifier signals was obtained by shaping the pulses in a CAEN sixteen channel amplifier, set with 1μs shaping time. For every master trigger, the analogue energy information for all fifteen scintillation detector banks plus the AGATA core energy and TAC output were recorded by the Silena ADC.

5.5 Singles Front Face Scan

The singles front face scan was comprised of 6,972 x-y positions. The scanning table was held in each position for sixty seconds. Approximately 898GB of data, corresponding to over forty million events, were collected and written to SDLT tape in less than five days. For every trigger event, the 37 preamplifier outputs were digitised. On an event-by-event basis, each of the 37 waveforms were categorised as real charge, image charge or noise. A pulse shape was defined as a real charge pulse if its magnitude was $>3\sigma$ of the base-line noise, where σ was equal to 4.7keV. A pulse shape was defined as an image charge if its average absolute area was $>1.2\sigma$ of the base-line noise. The remaining pulses that did not pass these criteria were classed as noise. The number of segments in which a real charge pulse was measured per trigger is defined as the fold and the mean fold was calculated to be 1.82. The average number of measured image charges per trigger was 10.32. Thus a large number of measurable image charges can be extracted for successful Pulse Shape Analysis (PSA).

5.6 Singles Detector Response

The experimental pulse shapes were analysed in the MTsort environment which allowed the data to be processed (sorted) with different gating conditions. To minimise the sort time, the data was initially filtered (pre-sorted) utilising a geometrical suppression routine that invalidated all but the following pulses:

1. Interaction segment - real charge pulse.
2. Centre contact - real charge pulse.
3. Adjacent lateral segments - image charge pulses.
4. Next but adjacent lateral segments - image charge pulses.
5. Adjacent vertical segments - image charge pulses.

The term adjacent referred to those segments for which the long segment boundaries were shared. For example, for segment E4, the segments classed as adjacent were E3, E5, D4 and F4. For interactions that occurred in the front ring, the term adjacent also included the segment directly opposite the interaction segment. For segment E4, the term next-but-adjacent referred to segments E6, E2, C4 and A4. As well as this geometric channel suppression, an energy gate of 618keV to 668keV was applied to the data. This combination of event criteria reduced the data set to 180GB, twenty five million events, of useful pulse shapes.

When sorting the data, each event was defined in terms of its fold, energies, interaction positions, rise times and image charge asymmetry. In the following sections, the results from the pre-sorted data set are discussed.

5.6.1 Fold

By gating on the 662keV centre contact Full Energy Peak (FEP), the term fold now only accounts for the number of segments in which each Full Energy Event (FEE) interacted. The FEE fold distribution for the pre-sorted data set is presented in *Figure 5.10.* It can be seen that for 662keV photons, 34% interacted in a single segment, 42% interacted in

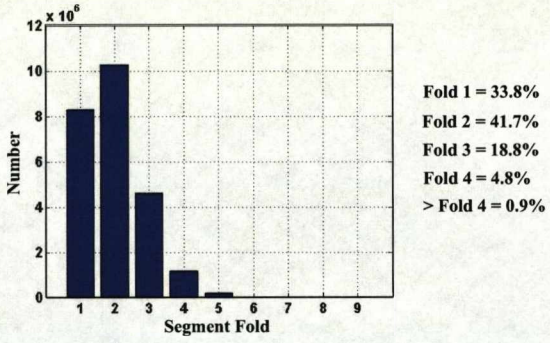

Figure 5.10: A plot showing the fold calculated for all Full Energy Events (FEE) in the ^{137}Cs front-face singles scan of the AGATA S002 prototype detector. It can be seen that 34% of the 662keV gamma rays interacted in a single segment, 42% interacted in two segments and <19% interacted in three segments

two segments and <19% interacted in three segments. The reader should note that in the following discussions, nearest neighbour refers to any electrode that shares any region of its segment boundary with any other. For interactions in the middle four rings, there are eight nearest neighbour electrodes. Of the fold two events, 83% of interactions occurred between nearest neighbour segments, 47% were confined to a sector and 28% were confined to a ring. Thus demonstrating the increased probability of forward focussed, small angle scattering, as predicted by the Klein Nishina distribution, *Equation 2.4*. For events that did scatter out of a single segment, the majority were fold two. This is the result of the large segment size in the AGATA prototype detectors, which favours low fold interactions at 662keV. To illustrate this point, *Figure 5.11* shows interaction segment versus interaction segment for all fold two events. The diagonal regions of maximum intensity show the favoured scatter combinations. It can be seen that scatters between nearest neighbour pairs were most probable.

For all event folds, the segment energies were added back to reconstruct the outer contact FEP, as shown in *Figure 5.12a*. The respective energies observed on the centre contact are displayed in *Figure 5.12b*. It can be seen that as the event fold increases, the outer contact FEP shifts down in energy and gets broader. The observed shift in energy is the result of proportional cross-talk, while the effect of the broadening is due to the increased terms in the

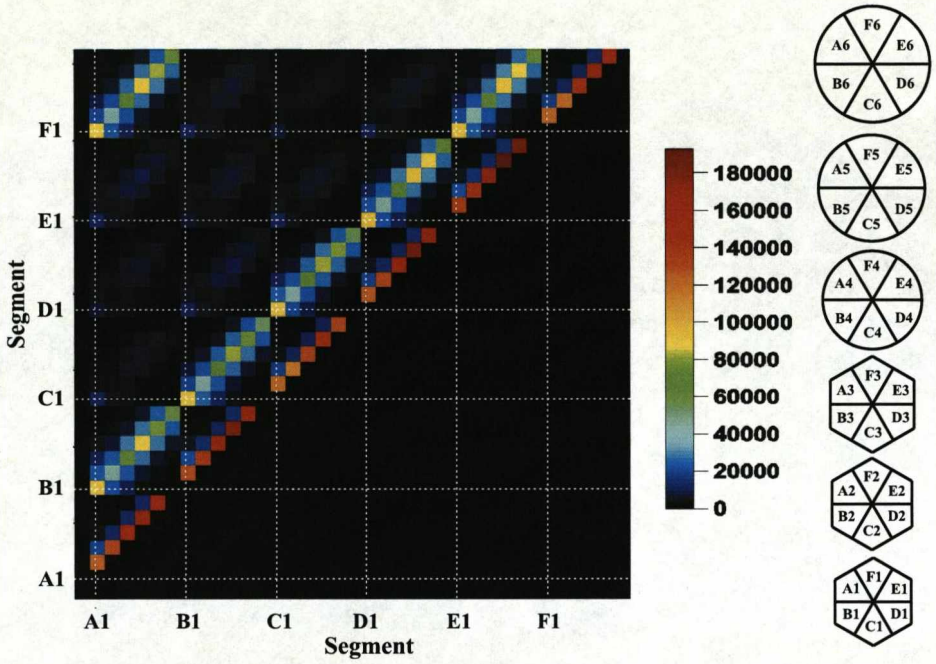

Figure 5.11: A plot showing segment versus segment for all fold two full energy events in the S002 front-face scan. The diagonal regions of maximum intensity show the favoured combinations. The lowest and most intense of the diagonal stripes shows that forward scatters within a sector of the detector dominated over perpendicular scatters confined to a ring, as shown by the other two stripes.

quadrature sum of the noise on each signal. Cross-talk in general refers to the phenomenon by which the detector responses on different electrodes can influence each other. Cross-talk has two components, proportional and derivative, both of which have been extensively investigated in large volume HPGe detectors by [Bru06b]. In this work, a theoretical model that describes the capacitive coupling between the channels of the segmented Miniball detectors enabled compensation for the cross-talk effects by parameterising the various contributions. Proportional cross-talk is due to the undesired coupling between electronics channels and results in the shift of the baseline of segments neighbouring the interaction segment. This effect can be minimised by improving the shielding of the components that convey the signal from the contacts to the preamplifier. The level of proportional cross-talk measured from the shift in peak energy presented in Figure 5.12a is $0.11 \pm 0.05\%$ at 662keV. The specifications for the AGATA capsules state that the level of segment to segment

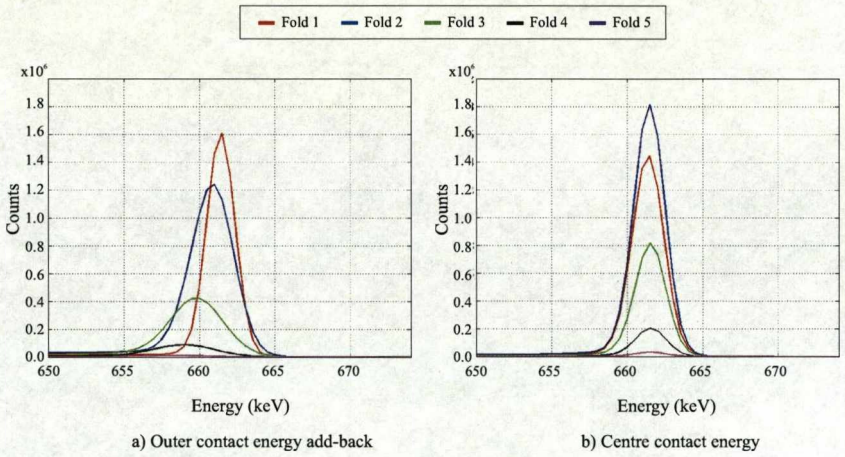

Figure 5.12: Addback spectra for fold one to fold five events in the S002 AGATA prototype detector. a) Outer contact addback spectra. The peaks shift down in energy due to proportional cross-talk resulting from the capacitive coupling between the channels. The peaks also appear broadened due to the increased terms in the quadrature sum of the noise on each signal. b) Centre contact spectra for the addback spectra presented in a).

proportional cross-talk should not exceed 0.1%. These figures are in agreement within the associated uncertainty. The effects of derivative cross-talk have been investigated in *Section 6.1.2.*

5.6.2 Energy

The energy information for all 37 channels was derived by the MWD algorithm in the GRT cards. This method of trapezoidal filtering corrects for the decay of the preamplifer. The resulting step like function with a flat top is then sampled at a given point. The difference between the baseline and this value yields the energy of the interaction. As the top of the trapezoid was flat, the variance in the calculated energy was small and therefore the FWHM of the FEP was also small. Performing MWD with the parameters specified in *Appendix B* was equivalent to using an analogue shaping time of 3μs. In order to validate the MWD algorithms performance the centre contact energy was also calculated using conventional analogue electronics. As a final check, the energy was calculated in software by taking a simple baseline difference, without correcting for the preamplifier decay. *Figure 5.13* shows

the energy resolution for the centre contact of the S002 AGATA prototype detector as a function of energy for all three of the techniques described above. It can be seen that the Silena ADC (blue) gave systematically better results than the MWD (red). This was due to the combination of the 6μs shaping time and the fact that the 100mv/MeV preamplifier signals were digitised over a $\pm$1V range in the GRT cards. As expected, the simple baseline difference calculation (green) was shown to give the poorest FWHMs. A detailed discussion of the energy measurement techniques and the resolutions achieved is presented in *Appendix B.*

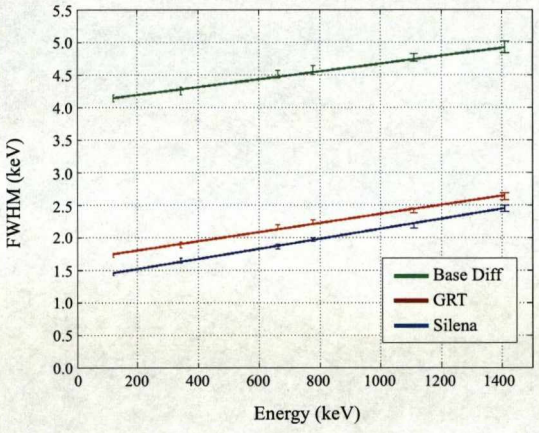

Figure 5.13: Plot showing fits to experimental data for three different energy calculations for the centre contact of the S002 AGATA prototype detector. The analogue Silena ADC measurement (blue), performed with 6μs shaping time, was shown to provide the best FWHM as a function of energy. The resolution calculated by the MWD algorithm was worse as a result of the smaller 3μs shaping time and limited range over which the signal was sampled. The simple baseline difference calculation (green) gave the worst results.

5.6.3 Interaction Position

Figure 5.14 shows the number of photo-peak events (656keV to 668keV) as a function of scanning table position, for the S002 front-face singles scan. The regions of low intensity, at large and small radii, are the result of reduced absorption of the 662keV gamma rays. This is due to the tapered shape of the front of the crystal and the centrally drilled hole respectively. By gating on fold one photo-peak events, and indexing by the ring of interaction, the effective segmentation is observed. *Figure 5.15a* and *Figure 5.15b* show the indexed distributions for rings one and three respectively. The photo-peak intensity is shown to vary strongly as a function of radius and depth. If the detector were cylindrical, these distributions would show the number of photo-peak events to be greatest in the centre of each segment. This is because in regions close to segment boundaries, the drilled hole and the detector edges, the probability of the gamma rays Compton scattering out of a single segment increases. These effects would decrease as a function of depth, as at 662keV, the gamma rays will be absorbed in the front of the detector. However, the tapered front of the AGATA crystals results in the collimated photon beam probing the back rings directly. Therefore, at large radii, fringes of high intensity are observed.

The absolute x-y interaction position was determined by the position of the scanning table relative to the centre of the detector. Thus the uncertainty on the x-y position was governed by:

1. The uncertainty on the scanning table position, $\pm 100\mu$m.

2. Beam divergence. The finite length of the collimator resulted in a spread in the diameter of the beam spot, s, as a function of distance from the collimator head. This relationship has been investigated by Monte Carlo simulation in [Gro05] and is given as,

$$s = A\left(1 + \frac{2D}{L}\right), \tag{5.1}$$

where A is the diameter of the inner hole of the collimator, L is the length of the collimator and D is the distance from the head of the collimator to the depth of interaction. *Equation 5.1* was extended to account for the variation in position uncertainty

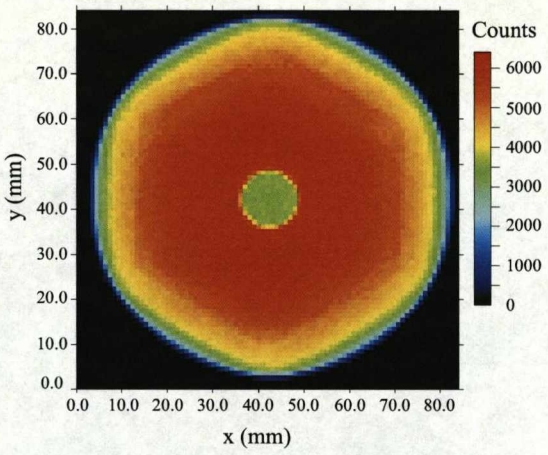

Figure 5.14: Intensity profile for the ^{137}Cs front-face singles scan of the S002 prototype detector. The distribution shows the number of photo-peak events as a function of scanning table position. The regions of low statistics at large and small radii are the result of reduced absorption of the 662keV gamma rays due to the tapered shape of the front of the crystal and the centrally drilled hole respectively.

resulting from Compton scattering and the change in absorption probability as a function of energy. Such an extension has not been investigated for the AGATA prototype detector geometry as the main focus of this work is the analysis of the coincidence data for which such an extension was not required.

The distance from the collimator head to the front face of the S002 and S003 detectors was ~23mm and ~20mm respectively. Calculated values for the diameter of the beam spot at the front and back faces of the S002 and S003 detectors were between ~1.3mm and ~3.0mm in each case. These measurements are summarised at the end of this section in *Table 5.4*.

3. Rotation of the symmetry axis of the detector with respect to the scanning table. Each of the crystals was rotated slightly from its central position inside its respective cryostat. As a result, the cryostat had to be twisted by the same amount when the detector was mounted on the scanning table. The accuracy with which such movements could be performed was limited, resulting in some finite degree of rotation relative to

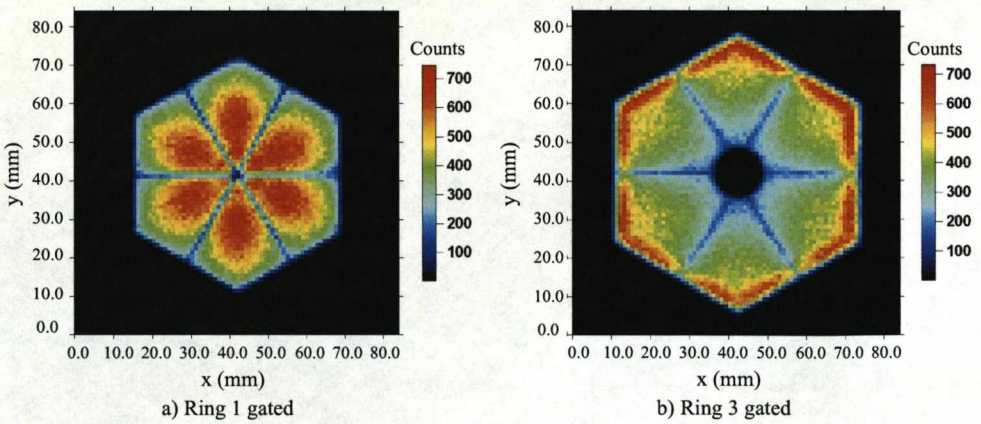

Figure 5.15: Intensity profiles for the ^{137}Cs front-face singles scan of the S002 prototype detector. Distributions a) and b) show the number of photo-peak events confined to a single segment at each scanning table position, in rings one and three respectively. The highest fraction of counts is observed in the centre of the segments in the front ring of the detector. The statistics are lowest at the segment boundaries and in proximity to the drilled hole, due to the increased probability of a gamma ray scattering out of a single segment. An example of the bright fringes observed at large radii in the back four rings is shown for ring three. At large radii, the tapered front portion of the crystal enables the beam to probe these regions directly.

the scanning table. The angle of rotation of the S002 detector was calculated from the gradient of the segment boundary from *Figure 5.15b*. A similar calculation was performed from the distribution for the S003 detector. The calculated angles of rotation were 0.9 ± 0.3^o and 1.2 ± 0.3^o for the respective detectors. These results are also summarised in *Table 5.4*.

4. The uncertainty on the location of the centre of the detector. The centre position of each detector was initially determined by superimposing a grid with 0.5mm spacing over *Figure 5.15a* and calculating the position at which the segment lines crossed. The values calculated from this analysis for the S002 and S003 detectors were $x = 42.0\pm0.5mm$, $y = 42.0\pm0.5mm$ and $x = 35.0\pm0.5mm$, $y = 39.25\pm0.5mm$ respectively. The coincidence scan positions for each detector were collected relative to these positions. However, following subsequent detailed analysis of the ring gated intensity distributions, it has shown that each detector was tilted off axis. *Figure 5.16* shows

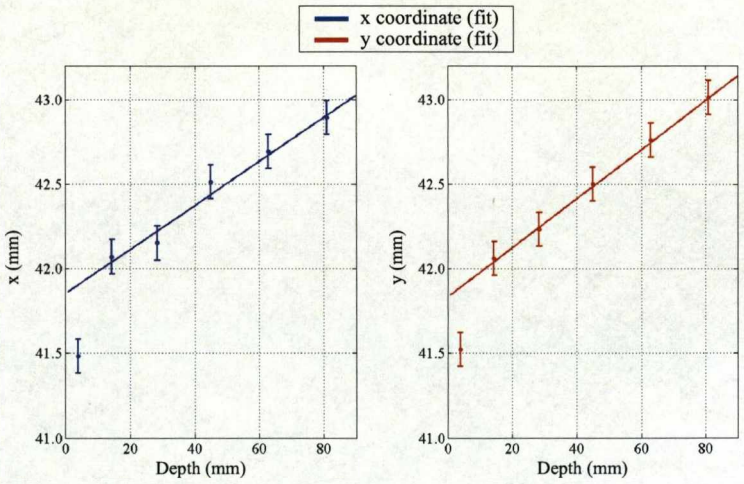

Figure 5.16: A plot showing the translation of the x and y coordinates of the centre of the S002 detector plotted as a function of half depth of the six rings. The values were determined using a routine that calculates the smallest radius circle that bounds a given distribution.

the change in position of the x and y coordinates of the centre of the S002 detector as a function of depth. For rings two to six, the values were determined using a routine that calculates the smallest radius circle [Cox67] that bounds the bore hole in each distribution. For ring one, the same routine was used however with respect to the position at which the segment boundaries cross. The tilt in both x and y shows a linear trend for rings two to six. However, the centre of ring one does not appear to lie on the corresponding line of best fit. Thus suggesting that the point at which the segment boundaries cross on the front face of the crystal is not aligned with the centre of the bore hole. The x-y interaction positions in the remainder of this work have been adjusted for the calculated offset shown in *Figure 5.16*. The tilt of each detector is presented in *Table 5.4*.

The following sections discuss the rise time and image charge asymmetry profiles through the detector volume. For each example, the distributions for rings one and three will be presented as representative of the general trends in the different zones of the crystal. The combination of these two slices show the effects of the complex planar electric field in the front region and the bulk electric field in the back four rings. The distributions for all six

	AGATA S002	AGATA S003
Step size (mm)	1.0±0.1	1.0±0.1
Detector centre [x,y], ring one (mm)	[42.0±0.5,42.0±0.5]	[35.0±0.5,39.3±0.5
Azimuthal rotation (θ) (^{o})	0.9±0.3	1.2±0.3
Tilt in depth (ϕ) (^{o})	1.1±0.2	0.8±0.2
Spot diameter FWHM - front face (mm)	1.5	1.3
Spot diameter FWHM - back face (mm)	3.0	2.8

Table 5.4: Summary of the scan precision for the S002 and S003 AGATA symmetric prototype detector measurements. The x-y interaction positions depend upon the uncertainty of the scanning table location (±100μm), the uncertainty on the centre of the detector and the divergence of the collimated beam [Gro05].

rings, as well as those for the intensity profile described above, are presented in *Appendix D.*

5.6.4 Rise time Parameterisation

Figure 5.17 and *Figure 5.18* shows the mean, fold one, centre and outer contact rise time distributions as a function of scanning table position, for rings one and three. The mean T30 and T90 values were calculated from individual pulse shapes. The crystallographic lattice orientation is mapped onto each distribution. The reader should note that in all cases, the x and y axes correspond to the scanning table coordinates. *Figure 5.19* shows slices through the T30 and T90 distributions, for all six rings along the x = 42mm direction. The error bars, of the order of ±6ns, have been omitted for clarity. By studying these rise time distributions, the response across the detector has been assessed.

- For each of the six rings, the core T30 is generally shown to increase as a function of radius from the centre as the distance to the anode increases. For rings two to six, interactions very close to the central anode appear to show longer T30s. This effect is a consequence of the parameterisation [Tur06]. The t10 lower threshold is not sensitive to the initial fast rise as the highest rate of change in the leading edge occurs before this point. In this instance, the use of a t5 threshold would be more suited, however, the effects of the baseline noise prevent this for an event by event

parameterisation. The fastest T30s of ~20ns occur directly under the central anode where the electric field is strongest and the distance between the outer and centre contacts is smallest. In contrast, the corners of the detector show very long T30s, of the order of 80ns, where the electric field is weakest.

- In all but the front ring, the core T90 distributions show long rise times of the order of 200 to 240ns at large and small radii, with minima at central radii. The values of these maxima and minima increase with ring number as the average radius of the detector increases. These effects can be seen more clearly in *Figure 5.19c*. The longest T90s occur for interactions very close to the central anode, as the rise of the pulse depends entirely on the slower drift of the *holes* to the cathode. The four fold symmetric region of fast rise times that appears in the centre of each of the ring gated distributions in *Figure 5.17* shows the effect of the anisotropic drift velocity in germanium. The faster rise times extend to larger radii along the fastest axes of the crystal. This effect is most clearly visible for the centre contact distributions as the central anode weighting potential has a uniform symmetric distribution in all directions. Thus allowing the decoupling of the weighting field and anisotropy contributions to the T30.

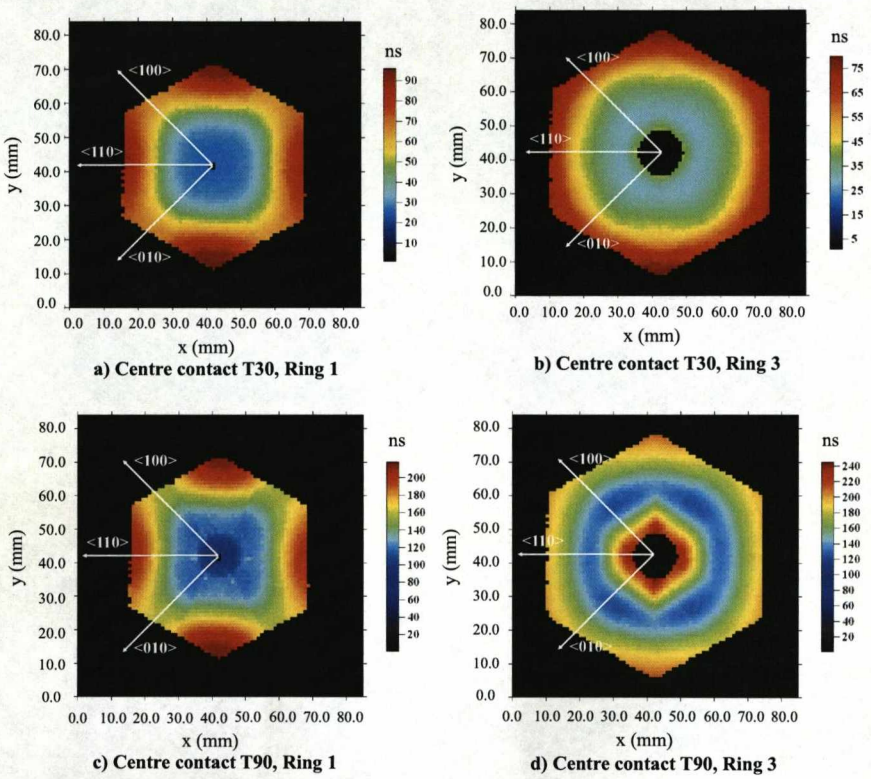

Figure 5.17: Centre contact T30 and T90 distributions for fold one events in rings one and three. The crystallographic directions are indicated with the white arrows. The core T30 is shown to increase as a function of radius from the core for the front and bulk regions. The effect of the anisotropic drift velocity is shown by the four fold symmetric regions of fast rise times. The T90 parameter is greatest at small and large radii. The longest rise times are close to the centre contact where the charge carrier drift is dominated by the transport of the *holes*.

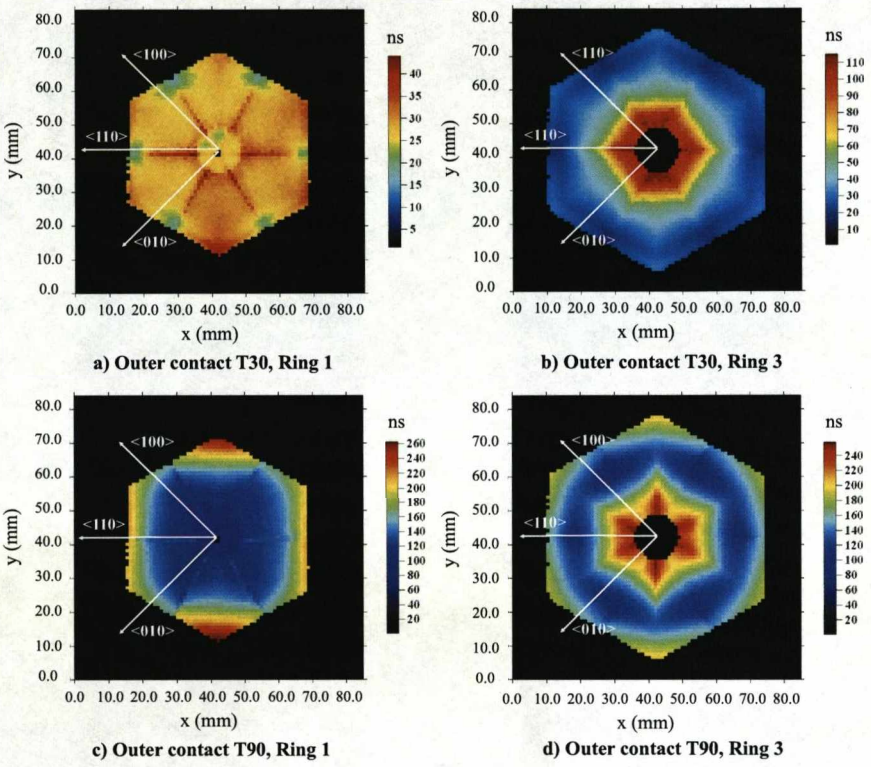

Figure 5.18: Outer contact T30 and T90 distributions for fold one events in rings one and three. The crystallographic directions are indicated with the white arrows. The segment T30 is shown to increase as a function of radius from the outer surface for the bulk regions. The effect of the anisotropic drift velocity and the complex weighting field distributions is shown by the six fold symmetric region of slow rise times. The T90 parameter is greatest at small and large radii. The longest rise times are close to the centre contact where the charge carrier drift is dominated by the transport of the *holes*. For ring one, T30 is shown to stay approximately constant as a function of x-y position. T90 is fastest close to the core where the drift distance is shortest.

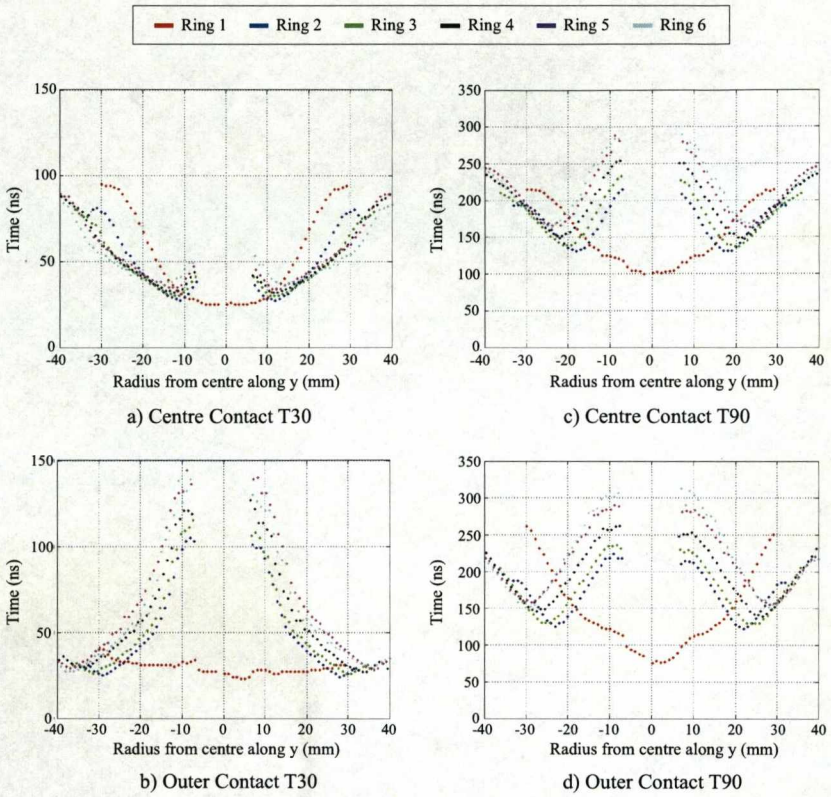

Figure 5.19: Rise time distributions calculated from slices through the x = 42.0mm plane for the ring gated centre and outer contact distributions. The error bars have been omitted for clarity. a) and b) show the centre and outer contact T30 distributions. For rings two to six, the rise times increase as a function of distance from each respective contact. c) and d) show the centre and outer contact T90 distributions. For rings two to six the shift in position of the V shaped distributions, resulting from the increase in crystal radius as a function of depth, can be seen. The ring one distributions are more complex due to the effects of the closed ended shape of the crystal. The symmetry of the distributions show good alignment of the crystal.

- For rings two to six, the outer contact T30 is shown to increase as a function of radius from the outer surface. The six fold symmetric region of long rise times that surrounds the central anode in each ring, shown in *Figure 5.18b*, is the result of the interplay between each cathode weighting potential and the anisotropic *hole* drift velocity. The shape of the hexagonal faces of these six fold distributions mirrors the bow of the iso-surfaces of the weighting potential demonstrated in *Section 4.4.7*. The shape of the iso-surfaces causes the projection of the weighting potential along the segment boundaries to fall away faster than that for the centre of a segment, thus giving rise to a slower T30. To ensure that the lower statistics at the segment boundaries did not affect these distributions, equivalent rise time matrices were produced for full energy events confined to each ring, as opposed to each segment. The resulting trends were identical to those shown in *Figure 5.18*. The T30 distribution for ring one shows little variation. This is because the distance between the interaction positions at shallow depths in ring one and the outer contact does not vary much as a function of x-y position. The effect on the detector response is demonstrated in *Figure 5.20*, which shows the average pulses for the outer and centre contacts for six radial interactions in ring one. The interaction positions are along the x = constant = 42.0mm projection at 2.0mm, 7.0mm, 12.0mm, 17.0mm, 22.0mm and 27.0mm radii. The pulses shown in blue are for interactions at small radii, while those shown in red are for positions at large radii. It can be seen that the initial rise of each of the outer contact pulses is similar, verifying the lack of sensitivity of the T30 parameter. However, the large variation in drift distance to the core, results in large variations in the final rise of the pulses.

- The outer contact T90 distributions for rings two to six show the characteristic long-short-long rise time configuration as a function of radius. For ring one, T90 is fastest for interactions close to the centre of the detector where the distance between the electrodes is shortest.

5.6.5 Image Charge Parameterisation

For the asymmetry calculations performed in this analysis, *Equation 4.5* was modified to enhance the difference in image charge area relative to the sum. A factor of 1024 was added

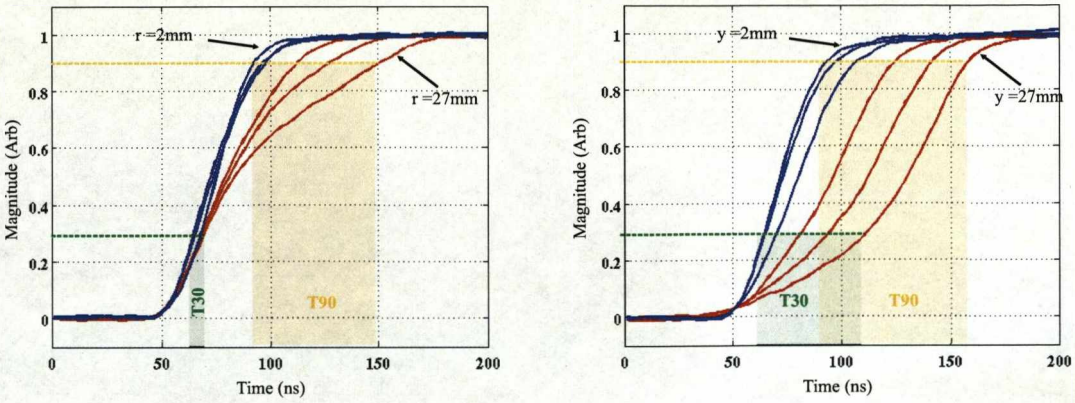

a) Outer contact pulse shapes

b) Centre contact pulse shapes

Figure 5.20: Outer and centre contact average pulse shapes for six interaction positions along the x = 42.0mm projection. The pulses shown in blue are for interactions at 2.0mm, 7.0mm and 12.0mm radii. While those shown in red are for the 17.0mm, 22.0mm and 27.0mm radii. It can be seen that there is little variation in the initial rise to T30 of the outer contact pulse shapes, thus the T30 parameter is not sensitive to the change in radius. The fastest pulses for both the outer and centre contact are those approaching the core, where the distance between the electrodes is smallest.

to make all values positive for the plotting routine. The resulting parameter was defined as,

$$ICA_{Area} = \left(\frac{(Area_m - Area_n) \cdot 1000}{Area_m + Area_n} \right) + 1024. \tag{5.2}$$

Figure 5.21a and *Figure 5.21b* show the ICA_{Area} for fold one events for the electrodes laterally adjacent to the interaction segment. The lateral asymmetry shows large variations as a function azimuthal angle. The largest difference in image charge magnitudes and hence the largest asymmetry is for interactions close to the anticlockwise segment boundary. This is intrinsic to the calculation as the difference is taken as the anticlockwise image charge minus the clockwise image charge. The distribution would simply be inverted if m and n were interchanged. The regions of low sensitivity in the centre of each segment are the result of the bipolar image charge shape. In these instances, the subtraction of the absolute area of one bipolar image charge from another cancels, reducing the magnitude of the asymmetry parameter.

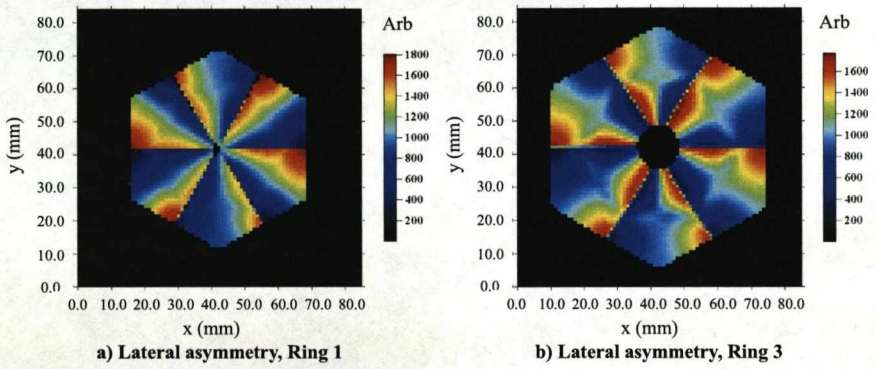

Figure 5.21: Ring gated lateral image charge asymmetry distributions for the AGATA S002 prototype detector. The asymmetry parameter is calculated as the difference in area of the image charge on the electrode clockwise of the interaction segment with respect to that on the anticlockwise electrode. The asymmetry is maximum for interactions close to the anticlockwise segment boundary and falls away as a function of azimuthal angle approaching the clockwise boundary.

5.7 Coincidence Front Face Scan

Coincidence data were collected for the same 230 x-y interaction positions in both the S002 and S003 detectors, within the uncertainties defined in *Table 5.4*. As each x-y location probed eight depths, a total of 1840 interaction sites were characterised. The depths were spaced throughout the 90mm long crystal at, 6.4mm, 17.9mm, 33.1mm, 33.4mm, 51.0mm, 51.8mm, 67.2mm and 85.9mm, from the front face. Important areas of focus for the scans were sensitive regions of the detector where the pulse shapes varied strongly as a function of position, and positions close to the centre and outer contacts where the geometry of the crystal effects the electric field lines. The data set for each detector was comprised of four azimuthal and eighteen radial scans. A summary of these scans is listed below. To aide the reader, schematic representations are also presented in *Figure 5.22a* and *Figure 5.22b* respectively.

1. Azimuth 1 - 0^o to 360^o azimuthal scan, 24mm radius, 4mm (9.6^o) steps
2. Azimuth 2 - 0^o to 180^o azimuthal scan, 27mm radius, 4mm (8.5^o) steps
3. Azimuth 3 - 0^o to 360^o azimuthal scan, 31mm radius, 5.2mm (9.6^o) steps
4. Azimuth 4 - 0^o to 360^o azimuthal scan, 7mm radius, 3.7mm (30^o) steps1
5. Line 1 - Line scan through centre of sectors F and C
6. Line 2 - Line scan 7.5^o clockwise from A/F segment boundary
7. Line 3 - Line scan along A/F segment boundary
8. Line 4 - Line scan 7.5^o anticlockwise from A/F segment boundary
9. Line 5 - Line scan 15^o from A/B segment boundary
10. Line 6 - Line scan 7.5^o anticlockwise from F/E segment boundary
11. Line 7 - Line scan 15^o clockwise from F/E segment boundary
12. Line 8 - Line scan 30^o clockwise from F/E segment boundary
13. Line 9 - Line scan 7.5^o anticlockwise from E/D segment boundary

14. Line 10- Line scan 7.5^o anticlockwise from C/B segment boundary
15. Line 11- Line scan along C/B segment boundary
16. Line 12 - Line scan 7.5^o clockwise from C/B segment boundary
17. Line 13 -Line scan 7.5^o anticlockwise from C/B segment boundary
18. Line 14 Line scan 7.5^o clockwise from C/D segment boundary
19. Line 15 - Line scan 15^o anticlockwise from C/D segment boundary
20. Line 16 - Line scan 30^o clockwise from E/D segment boundary
21. Line 17 - Line scan 7.5^o clockwise from E/D segment boundary
22. Line 18 - Line scan 10^o clockwise from F/E segment boundary (fast axis)

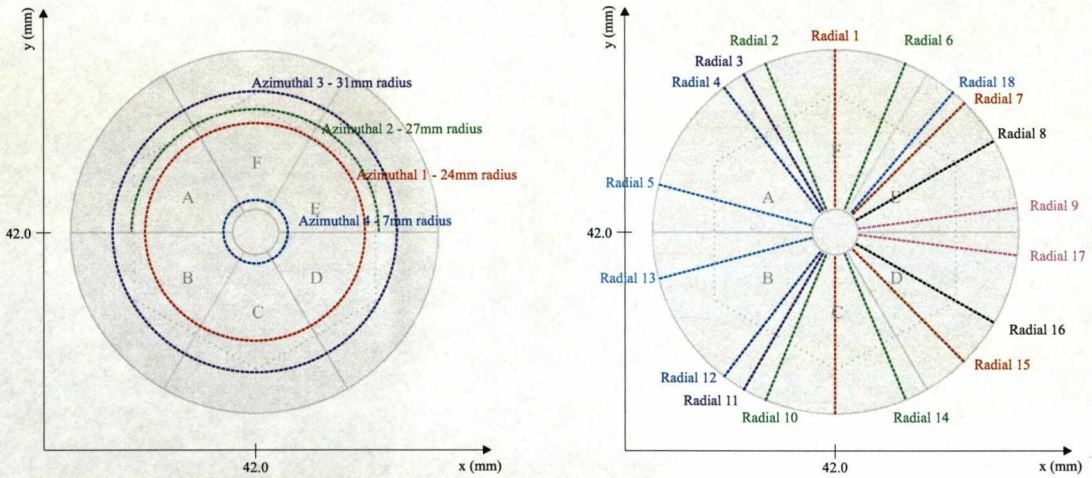

Figure 5.22: Schematic representation of the scanning table positions for the twenty two coincidence scans performed with each detector. The centre position of the S002 AGATA prototype detector is shown. The coordinates are defined with respect to the *home* position of the scanning table, 0.0mm,0.0mm. For the S003 detector, the scanning positions were simply translated with respect to its centre. a) Diagram showing the four azimuthal lines at 24.0mm, 27.0mm, 31.0mm and 7.0mm radii, with respect to the centre of each detector. b) Diagram showing the eighteen radial scan lines.

The aim of the analysis of this data was to generate a database of 37 average pulse shapes at every precisely determined 3D interaction position, for each detector. Thus allowing the comparison of experimentally measured pulses with those calculated by the MGS simulation. It was also important to compare the two experimental data sets in order that a cross-validation of the scanning procedure could be performed and that differences in the detector characteristics could be identified. The generation of a database of average pulse shapes reduced the contribution from random noise, allowing an accurate χ^2 comparison to be performed. The procedure used to generate the experimental database is documented in this section.

5.8 Coincidence Database Generation

In order to construct average pulse shapes, the number of events required at each scan position had to be determined. *Figure 5.23* shows how the standard deviation of the baseline noise varies as a function of the number of events in the average. The gradient of the distribution is steep for less than twenty events and begins to plateau at approximately one hundred events, decreasing slowly beyond this point. Ideally, many hundreds of pulse shapes would have be collected at each position, however the limited time constraints of the project required that the most efficient means of scanning each detector was utilised. Attenuation effects at 662keV, as described in *Figure 5.15*, meant that it would have been too time intensive to try and achieve good statistics in the back two rings of the detector. Thus, the decision was made to hold the scanning table at each position for a sufficient length of time, so as to collect one hundred good coincidence events for the collimation depths in ring four of the detector. A good coincidence was determined by a detailed analysis procedure that utilised a series of energy, fold and time gates.

The function used to describe the time required to collect one hundred good events as a function of radius and depth was calculated from a test scan through the centre of the detector. Fourteen x-y positions, where x = constant = 42.0mm, were interrogated with the collimator held in each location for two hours. The pulses from each x-y position were split according to a matrix of AGATA interaction segment versus scintillation bank. By gating on the required combinations, the events used to construct the average pulse shape

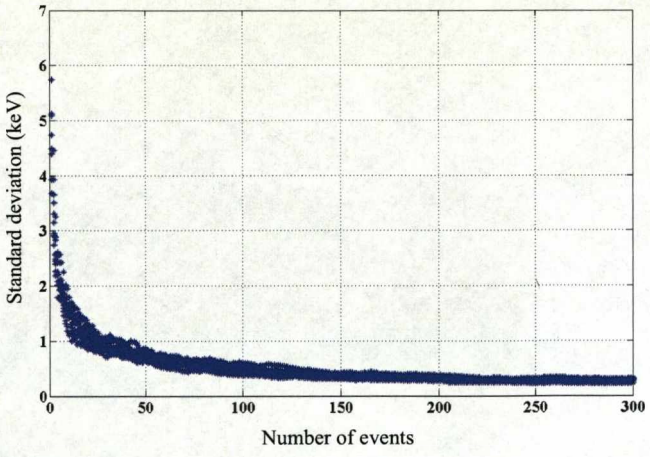

Figure 5.23: Standard deviation of the baseline noise as a function of the number of events used to construct an average pulse shape. The distributions for six randomly chosen channels of the detector are shown. The average standard deviation for a single event was 4.7keV. The distribution reaches a plateau at approximately one hundred events.

at each collimation depth for each x-y position were output into their respective arrays. *Figure 5.24* shows how this procedure was applied to the test scan for depths, z = 6.4mm, z = 51.8mm and z = 51.0mm.

For z = 6.4mm, ring one, the events at each x-y coordinate were selected according to those for which C1 or F1 had triggered in coincidence with Silena channels 1 and 2, and 3 and 6. In *Figure 5.24a* it can be seen that the variation in the number of coincidences achieved between a given segment and scintillation bank decreased as a function of distance from that bank. This was the result of the increased probability that the scattered gamma ray would be absorbed in the germanium before leaving the detector. It was for this reason that many hours of scanning were required to collect sufficient statistics to construct average pulse shapes for interaction sites close to the centre contact. A similar trend was observed in *Figure 5.24b.*

The energy gate used to determine *good* coincidence events was calculated from the Compton scatter formula, *Equation 5.3.* The kinematics of Compton scattering requires that for a 662keV gamma ray scattering once through 90^o, the scattered photon will carry

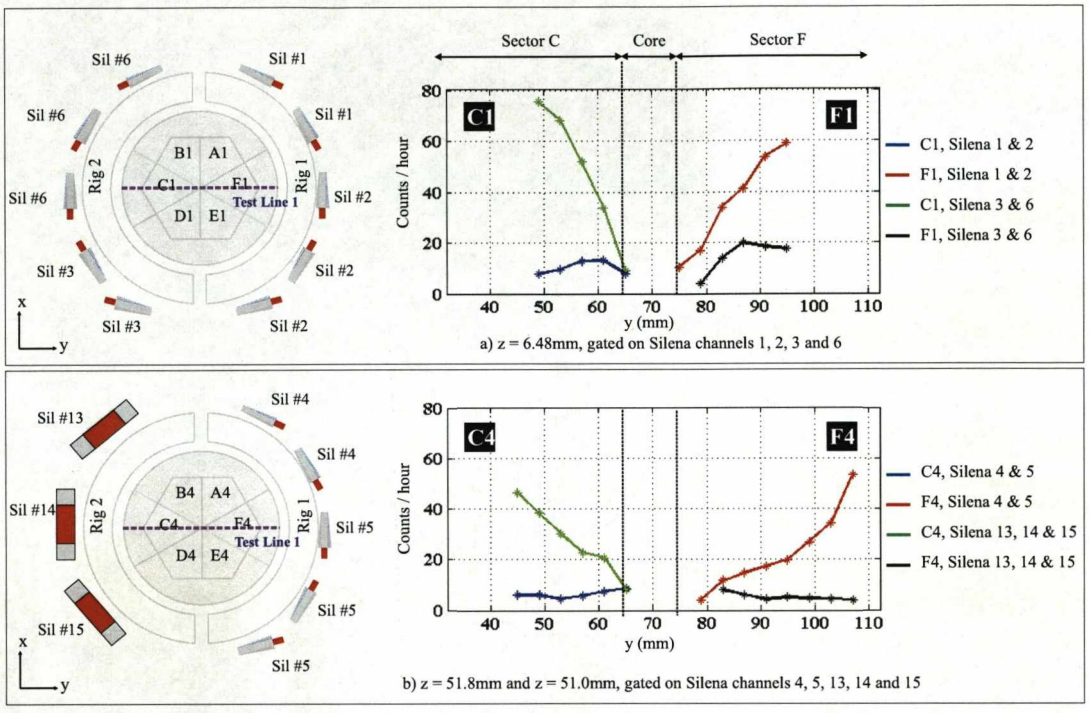

Figure 5.24: A plot showing the coincidence count rate as a function of radius through the detector, for test line one at collimation depths in rings one and four. a) The observed change in count rate at z = 6.4mm. The count rate decreases as the distance between the scintillation detectors and interaction position in the AGATA detector increases. b) The observed change in count rate at z = 51.8mm and z = 51.0mm. A similar trend to that observed in a) can be seen for the two different collimation depths in the ring four.

off an energy of 288keV. Thus the energy deposited in the scattering medium, the AGATA prototype detector, is 374keV. By definition, the 90^o scatter must occur at a single site, thus a fold one gate was applied with respect to the AGATA detector. To correlate the scattered gamma ray to the interaction segment, the photon also had to deposit its full 288keV in a scintillation detector. For a 288keV photon interacting in dense material such as BGO or NaI, the probability of it scattering between multiple detectors is low. As such, only events

in which a single scintillation detector channel triggered were considered.

$$E_{\gamma'} = \frac{E_\gamma}{1 + \frac{E_\gamma}{m_0 c^2}(1 - cos\theta)} = \frac{662}{1 + \frac{662}{511}(1 - 0)} = 288keV. \tag{5.3}$$

In order to select the *good* coincidence events, a matrix of the event-by-event AGATA centre contact energy versus that recorded in the scintillation detector bank for each coincidence trigger was constructed. A plot of the energy matrix, along with the centre contact energy spectrum for the AGATA S002 detector, is presented in *Figure 5.25.* The small circular shaped region of high intensity in the centre of the plot corresponds to the 90^o scatters. By gating on this region, the distribution could be sorted on an event-by-event basis in terms of the scintillation detector that triggered with respect to the AGATA segment in which 374keV had been deposited. As the trigger window was of finite size and the lead collimators did not provide perfect attenuation, random and off-angle coincidences also caused the data acquisition (DAQ) to collect data. A line at 662keV can be observed at all scintillation detector energies within the matrix. These random coincidences were the result of photons, emanating from the source, penetrating the lead shielding and interacting in the AGATA detector. The diagonal line that extends through either side of the 90^o scatter region of high intensity corresponds to scattering angles, other than 90^o, through which the gamma rays could pass between the collimation gaps.

The pre-sorting procedure was further refined as it was possible to reject the random coincidences by reference to the TAC timing signal, instrumented in channel seventeen of the ADC. This method of random event rejection required the reconstruction of the TAC spectrum for each scan line, allowing a gate to be set as the time window that corresponded to the true coincidences. *Figure 5.26a* shows total Time to Amplitude Converter (TAC) spectrum (black) for all events that interacted in segment C1 for line one of the coincidence scan. Also shown, are the components of this total spectrum corresponding to three of the twenty scan positions along the line, y = 53.0 (blue), y= 57.0mm (red) and y = 61.0mm (green). It can be seen that the TAC distribution shifted in time as a function of scan position. This was the result of the large deviation in the shape of the leading edge of the centre contact pulse shape as a function of interaction position. The discretisation of the continuous TAC distribution required the use of a large series of dynamic gates. However,

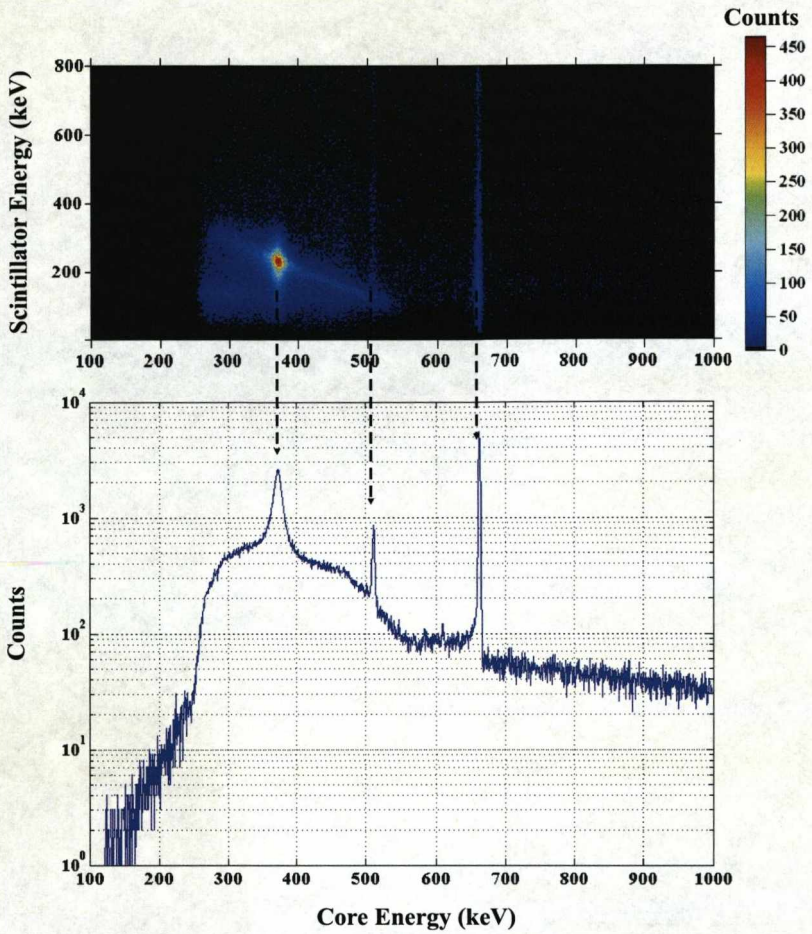

Figure 5.25: a) Matrix of the centre contact energy versus scintillation detector energy for all fold one events that triggered the acquisition. A fold one gate was also applied to the scintillation detector banks. The small circular shaped region of high intensity in the centre of the matrix corresponds to the 90^o scatters. The diagonal line that extends through either side of this region corresponds to other scattering angles through which the gamma rays could pass between the collimation gaps. The 662keV photo-peak was the result of random coincidences with photons, emanating from the source, penetrating the lead shielding and interacting in the AGATA detector.

it has been proven that the application of the energy and fold gates refined the data to such a degree that this technique was not necessary. This result is demonstrated in *Figure 5.26b*, which shows the TAC spectra for the same three interaction positions, following pre-selection of the data with respect to the energy and fold gates specified above. It can

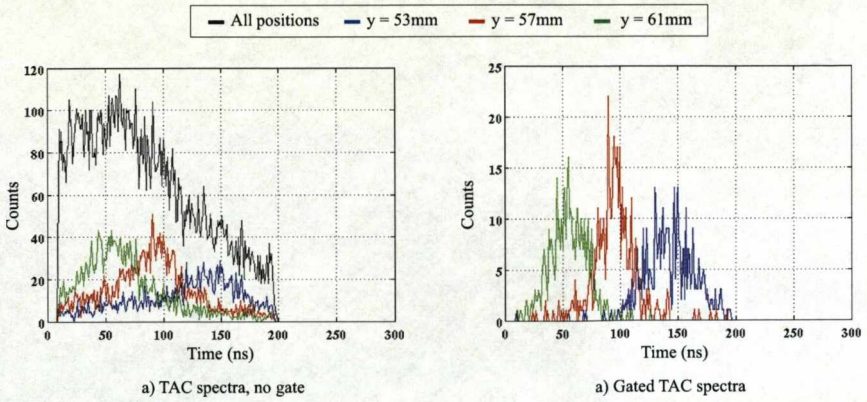

Figure 5.26: AGATA S002 TAC spectra for data collected at interaction positions along line one of the coincidence scan. a) The black distribution is the total TAC spectrum for interactions in segment C1. The components of this TAC spectrum resulting from x-y positions, (72.0,53.0), (72.0,57.0) and (72.0,61.0) are shown in blue, red and green respectively. The true coincidences are the events that occur in the peaks of these distributions. b) The same TAC spectra components as shown in a), following the application of fold one and energy gates. These distributions are well resolved peaks with little tailing, thus no advantage is gained in applying the extra constraint of a time window.

be seen that each of the spectra appears as a well resolved true coincidence peak, thus the application of the dynamic gates would not have improved the quality of the data. The poor time resolution, of the order of 60ns FWHM, resulted from the limited bandwidth of the preamplifier sum boxes that interfaced the BGO detectors. For a typical germanium - BGO coincidence configuration, a FWHM of the order of $\sim$ 10ns can be achieved [Coo07].

The arrays of pulse shapes were output in ASCII format for subsequent processing. Of the ten collimation depths described in *Figure 5.5*, the first two in each rig were identical, thus the contributions were summed, leaving eight different depths. Also, the effective segmentation in the front of the detector meant that for interactions at z = 17.9mm, the gamma ray could scatter from either the first or second ring, depending on the radius of the scanning table. This effect is demonstrated in *Figure 5.27* for two scanning table positions in the same sector of the AGATA prototype detector, x,y and x',y'. The interactions at z = 17.9mm were split according to the ring in which they occurred, thus a total of nine depth categories were considered. *Figure 5.28* shows the total number of events collected at each

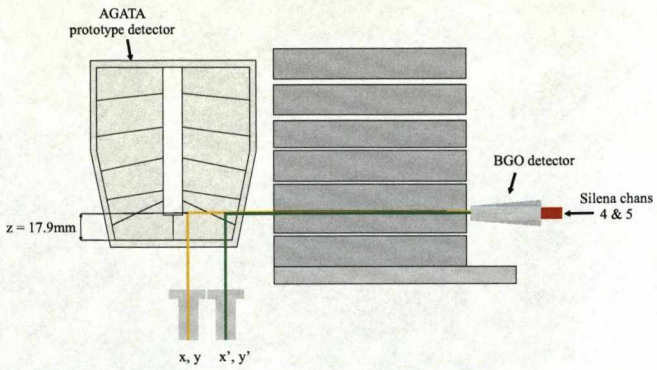

Figure 5.27: Schematic representation of the AGATA coincidence scan for two collimator positions, x,y and x',y'. It can be seen that both rings one and two are interrogated for the different radii at a constant depth of z = 17.9mm. This is the result of the complex electric field distribution caused by the hexaconical tapered geometry of the crystal and the positioning of the central anode.

x-y position of the full S002 coincidence scan, for each of the nine depths. The red markers signify those positions for which more than one hundred events were collected. It can be seen that for the front four rings of the AGATA prototype detector, the collective collimation depths yield statistics above the required one hundred count threshold. However, for rings five and six, the statistics are significantly less. The count times ranged from ninety minutes per position for large radii, to ten hours per position for radii close to the core.

The ascii file for each single site interaction position was read into an algorithm that processed the data and constructed the corresponding set of 37 average pulse shapes for that position. The algorithm utilised a series of functions, described in *Figure 5.29*, to determine the *best* set of pulses for each average. The functions are summarised below:

1. Gain Match - The 37 waveforms for each event in the array were scaled by their pre-calculated gain factors, derived from the ^{152}Eu baseline difference spectra.

2. Reset Baseline - The average baseline for each waveform was calculated and set to zero.

3. Interpolate - Each pulse was interpolated from 12.5ns per sample to 2.5ns per sample to ensure accurate time alignment. The function performed a five-point linear interpolation followed by a three-point moving average.

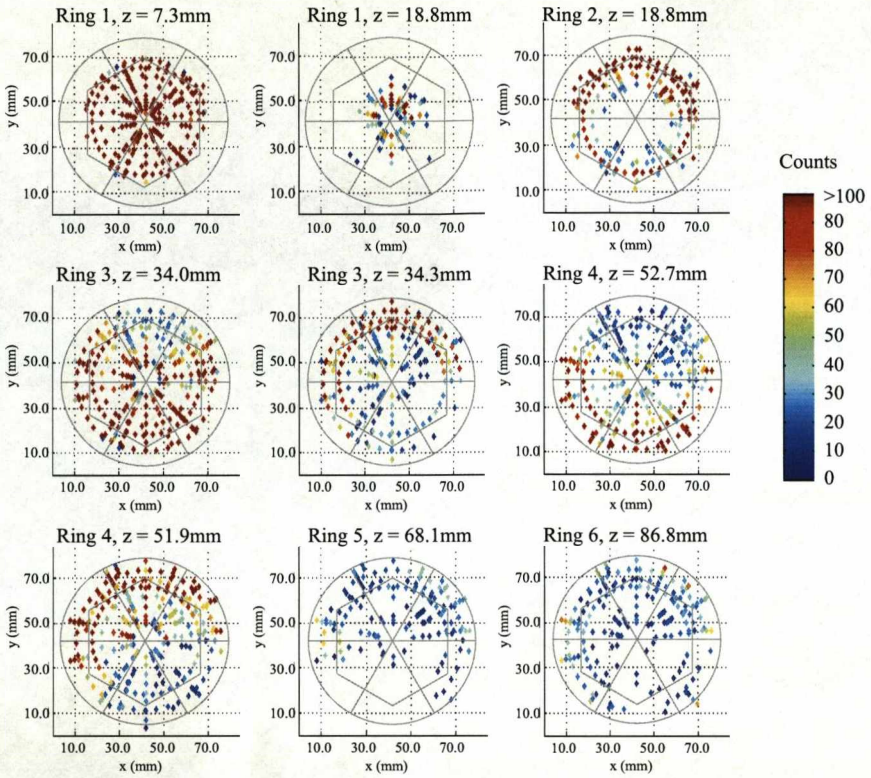

Figure 5.28: Intensity distribution showing the total number of good coincidence events, that passed the energy and fold gates, for each depth of the coincidence scan.

4. Decay Correct - All 37 pulses were multiplied by a sample-by-sample factor that accounted for the average decay time constant of the preamplifier. Thus the resulting compensated real charge pulses had a constant flat top from the point of maximum rise.

5. Normalise - The maximum amplitudes of the real charge outer and centre contact pulses were averaged and normalised to one. The remaining 35 pulses were scaled by the same factor.

6. Time Align - As the GRT cards do not have a global clock, the pulses had to be aligned independently on an event-by-event basis. The t10s of both the centre and outer contact real charge pulses were calculated per event. Each pulse was then

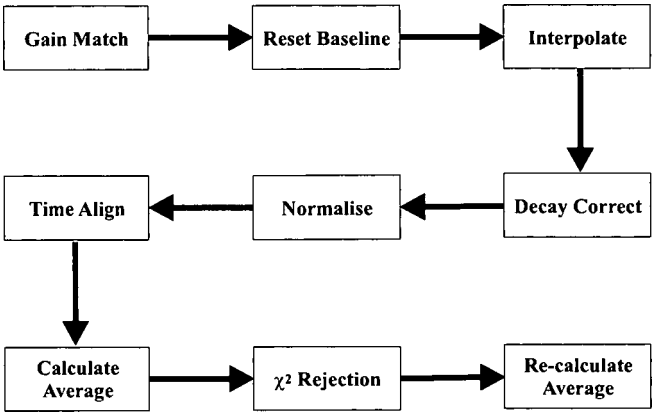

Figure 5.29: Flow diagram showing the analysis procedure for processing the array of pulse shapes at each precisely determined 3D interaction position.

shifted so that the t10 position was tracked to a pre-determined sample number. The remaining 35 pulses were shifted by the same coefficient as calculated for the core.

7. Calculate Average - The set of 37 average pulses was calculated by summing down the columns of the array of manipulated pulse shapes and dividing by the number of pulses in the sum.

8. χ^2 Rejection - The χ^2 distribution for each position was calculated by comparing the centre and outer contact real charge pulses, and nearest neighbour image charge pulses of the average distribution to the individual pulse shapes that constituted the average. Each χ^2 value was calculated using,

$$\chi^2 = \frac{1}{(i \cdot j) - j} \cdot \sum_{j=1}^{N_{IC}+2} \sum_{i=t0}^{t100} \left(\frac{x_i - \mu_i}{\sqrt{\sigma_x^2 + \sigma_\mu^2}} \right)^2, \tag{5.4}$$

where x_i is the sample of a single constituent pulse, μ_i is the sample of the average pulse, N_{IC} is the number of image charges in the sum, σ_x is the standard deviation of the baseline noise of pulse x and σ_μ is the standard deviation of the baseline noise of the average pulse. *Figure 5.30* shows the χ^2 distribution as a function of the pulse number in the sum, for a selection of positions at each of the nine depth categories. The vertical red lines indicate the maximum χ^2 values for which pulse

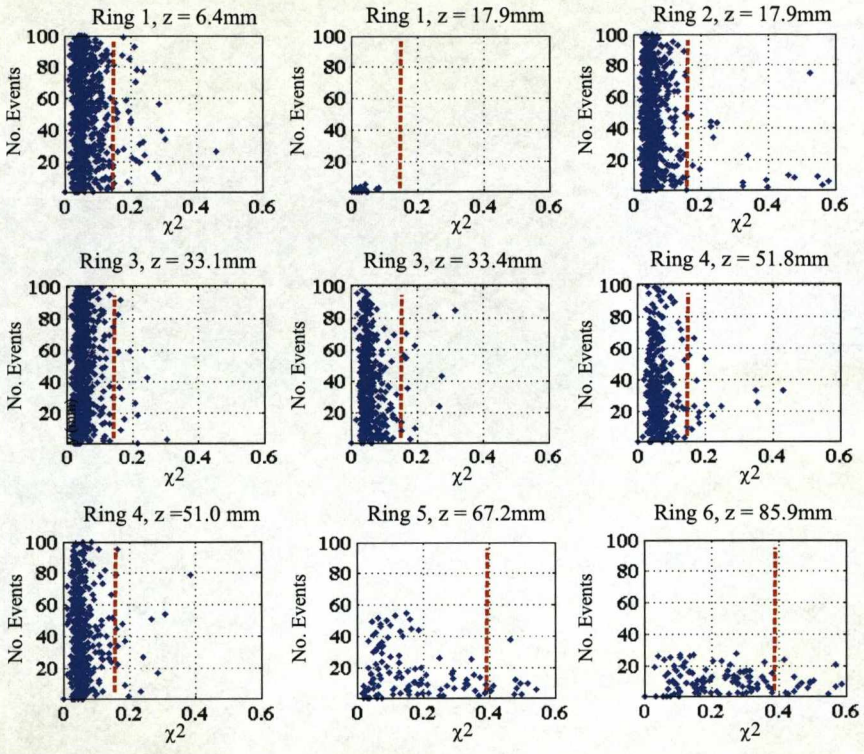

Figure 5.30: Plot showing the χ^2 calculations for the constituent pulse shapes used to construct average experimental pulses, with respect to the averages. The χ^2 distributions are shown for a selection of positions at each of the nine depth categories. The vertical red lines indicate the maximum χ^2 values for which pulse shapes were accepted. It can be seen that the shape of the distribution increases as a function of depth as the uncertainty in the interaction position also increases.

shapes were accepted. The quality of the data is represented by the consistency of the χ^2 as a function of event number in each average. It can be seen that the shape of the distribution changes as a function of increasing depth as the uncertainty in the interaction position also increases.

9. Re-calculate Average - The set of 37 average pulses was then recalculated, excluding those events for which the χ^2 was deemed too large. *Figure 5.31* shows the average (red) and constituent (blue) pulse shapes for an interaction at $x = 78.8mm$, $y = 49.0mm$, $z = 33.1mm$, following the χ^2 rejection. The effect of the cancellation of

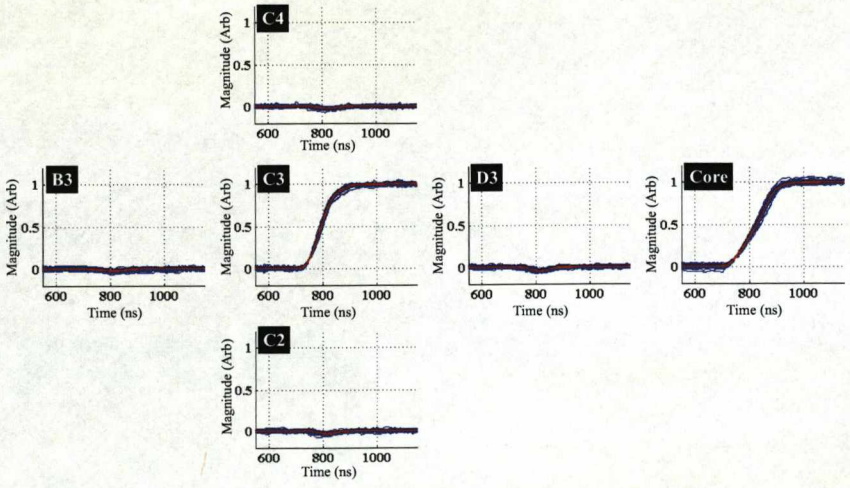

Figure 5.31: Average (red) and all constituent (blue) pulse shapes for an interaction at $x = 78.8mm$, $y = 49.0mm$, $z = 33.1mm$ in segment C3, following the χ^2 rejection.

the random noise across the pulses is clearly visible. The standard deviation of the baseline noise for the average pulses is 0.9keV, as opposed to 4.7keV. *Figure 5.32* shows the comparison of the pulse shapes from a single constituent event against the average pulse shapes. The average pulses are shown to be representative of the constituent pulses.

The average pulse shape databases for both the S002 and S003 detectors were stored for comparison to the pulses derived from the MGS software. A detailed analysis and discussion of these comparisons is presented in *Section 6.2.*

5.9 Singles Side-scan

The side-scan consisted of 3496 x-y scanning table positions. Due to time constraints, the collimated source was held at each position for ten seconds. The trigger architecture and thresholds were identical to those specified for the singles front-face scan. The positioning of the AGATA detector was such that the collimated beam entered the detector in a direction perpendicular to the front face of the detector. *Figure 5.33a* shows the intensity profile for

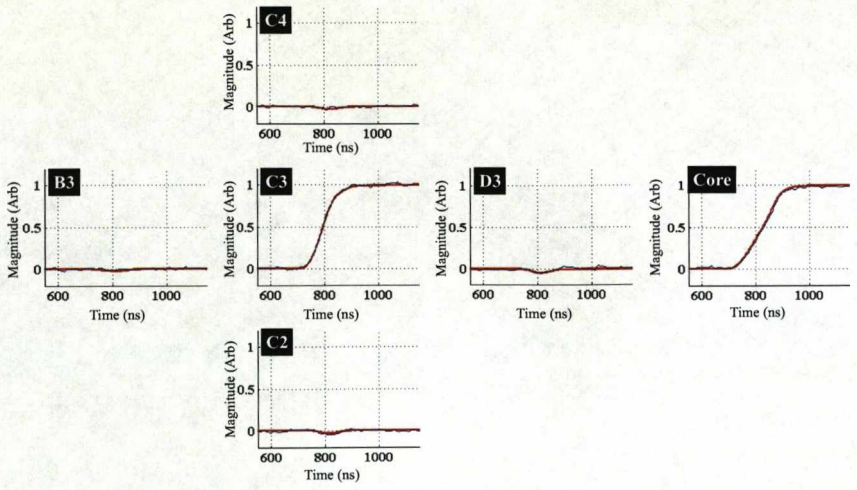

Figure 5.32: Average (red) and single constituent event (blue) pulse shapes for an interaction at x = *78.8mm*, y = *49.0mm*, z = *33.1mm*, following the χ^2 rejection. The average pulses are shown to be representative of the constituent pulses.

all events that triggered the acquisition system. The central bore hole is visible as a region of lower intensity as the reduced thickness of germanium results in an increased probability of 662keV gamma rays passing through this region without depositing the 500keV required to trigger the system. *Figure 5.33b* shows the intensity distribution for events that deposit 662keV in a single segment confined to sector D of the detector. The warped segment shapes in rings one and two are clearly visible. At radii close to the core, the boundary of segment D1 is shown to encroach into the volume that would be occupied by segment D2, if the detector were entirely coaxial.

Figure 5.34 presents the image charge asymmetry for vertically adjacent segments in sector D. The upper portion of the plot shows the asymmetry values for all x-y positions, while the lower portion shows a slice through this distribution at x = constant = 25.0mm. For the middle four rings, the vertical asymmetry was calculated as the subtraction of the area of the image charge on the electrode immediately below the interaction segment from that of the electrode immediately above using *Equation 5.2*. However, for interactions in

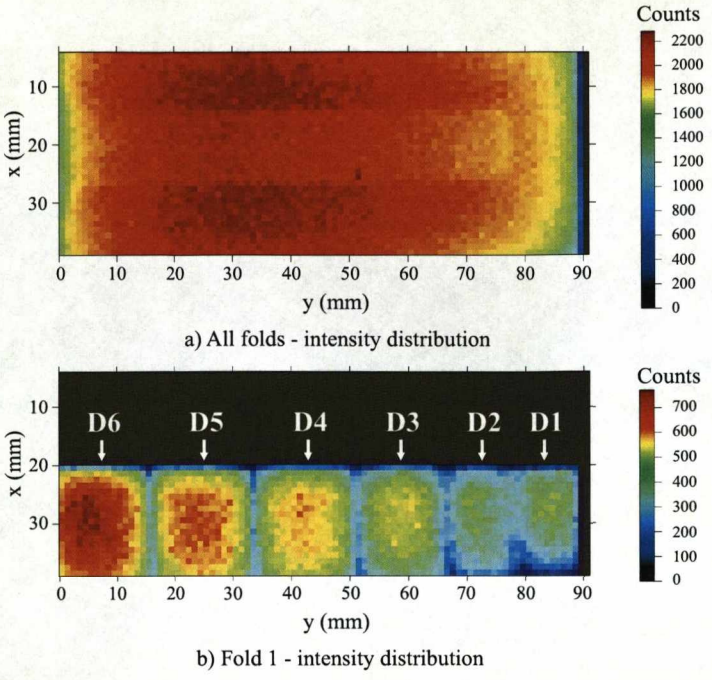

Figure 5.33: Side-scan intensity and image charge asymmetry profiles for the S002 AGATA prototype detector. a) Intensity profile for all events that triggered the acquisition. b) Intensity distribution for events that deposit 662keV in a single segment confined to sector D of the detector. The warped segment shapes in rings one and two are clearly visible.

rings one and six, where no lower or upper image charges were present respectively, the asymmetry calculation was modified to,

$$ICA_{Area} = \left(\frac{Area_m \cdot 100}{E_\gamma} \right) - c, \tag{5.5}$$

where E_γ was the gamma-ray energy in keV and c was a normalisation coefficient utilised for the plotting routine. The asymmetry distribution for segments D2 to D5 shows a reduction in asymmetry as a function of decreasing depth within each segment, as a result of the change in proximity of the interaction between the upper and lower segment boundaries. This distribution is shown to vary relatively uniformly as a function of radius. For rings one and six, the asymmetry is a direct measure of the change in image charge magnitude in rings two and five respectively. The warped field in both regions of the detector result in asymmetric distributions as a function of depth.

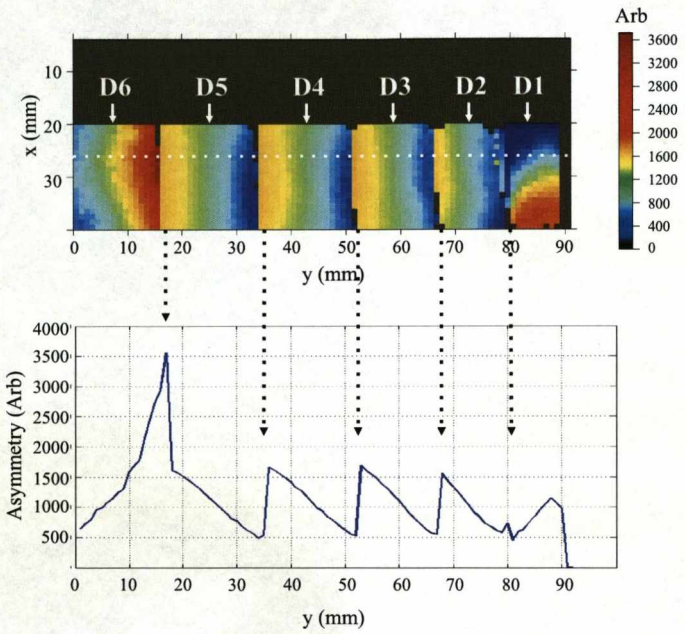

Figure 5.34: Side-scan image charge asymmetry profile for the S002 AGATA prototype detector. The upper portion of the plot shows the asymmetry for vertically adjacent segments in sector D, at all x-y positions. For rings one and six, the calculation only considers the upper or lower image charges respectively. The lower portion shows a slice through the distribution at x = constant = 25.0mm. For rings two to five, the asymmetry is shown to vary approximately linearly as a function of proximity to the upper and lower segment boundaries. For rings one and six, the warped electric field lines give rise to the more complex and less uniform distributions.

Chapter 6

Characterisation Results

Pulse shape databases have been generated from simulated and experimental data for the S002 and S003 AGATA symmetric prototype detector geometries. Each database contains sets of 37 pulses for each of the 2490 single site interaction positions described in *Section 5.7*. By performing a detailed comparison between the experimental and simulated data, it has been possible to quantify the agreement between the simulated and experimentally measured pulse shape response. The validity of the use of the MGS software to generate a basis for on-line Pulse Shape Analysis (PSA) has been assessed. The comparison of the equivalent experimental databases has also allowed the efficacy of the scanning procedure to generate reproducible data sets to be tested. In this chapter, the results of detailed pulse shape comparisons between the S002 experimental and theoretical data sets are presented and the detector sensitivity is quantified. A comparison between the S002 and S003 experimental data sets is also evaluated.

6.1 Database Manipulation

The experimental, MGS and official AGATA coordinate systems are all offset from one another by a series of rotational and translational transformations. *Figure 6.1* shows the three coordinate systems, the relative segment labelling conventions and the crystallographic planes. The experimental and MGS databases were generated independently before being merged and transformed into the official AGATA frame of reference. The anisotropy angle of -14.9^o was calculated by [Bru07] and this value was validated from the distributions

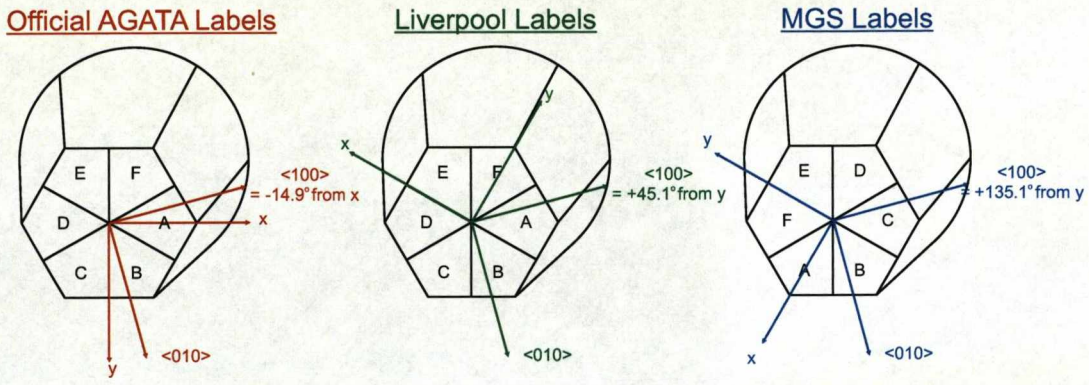

Figure 6.1: A schematic representation of a) the official, b) Liverpool and c) MGS coordinate systems. The labelling conventions and crystallographic planes are shown for each case. The anisotropy angle of -14.9^o was calculated by [Bru07] and validated from *Figure 5.15*.

shown in *Figure 5.15*. In the specifications agreed between the AGATA collaboration and Canberra, the fast axis is required to be parallel to the x axis with an uncertainty of $\pm 3^o$. The measured value is shown to be outside these error bars.

6.1.1 Scanning Table Correction

The x, y and z coordinates read into the MGS simulation were derived from the Liverpool scanning table positions. Before a transformation into the MGS frame of reference could be performed, the misalignment of the crystal relative to the scanning table had to be corrected. This misalignment was due to the symmetry axes of the encapsulated crystal being offset from those of the cryostat. Following the experimental optimisation of the alignment, as specified in *Section 5.6.3*, a finite offset in rotation between the crystal and the scanning table still remained. To account for this, a correction to the coordinate system that comprised of a tilt in the z plane and a rotation in the x-y plane was applied to both the S002 and S003 data sets. The corrections with respect to the S002 detector are shown schematically in *Figure 6.2a*. The rotation through θ was implemented utilising the transform matrix, R, where,

$$R = \begin{pmatrix} cos\,(\theta) & -sin\,(\theta) \\ sin\,(\theta) & cos\,(\theta) \end{pmatrix}.$$

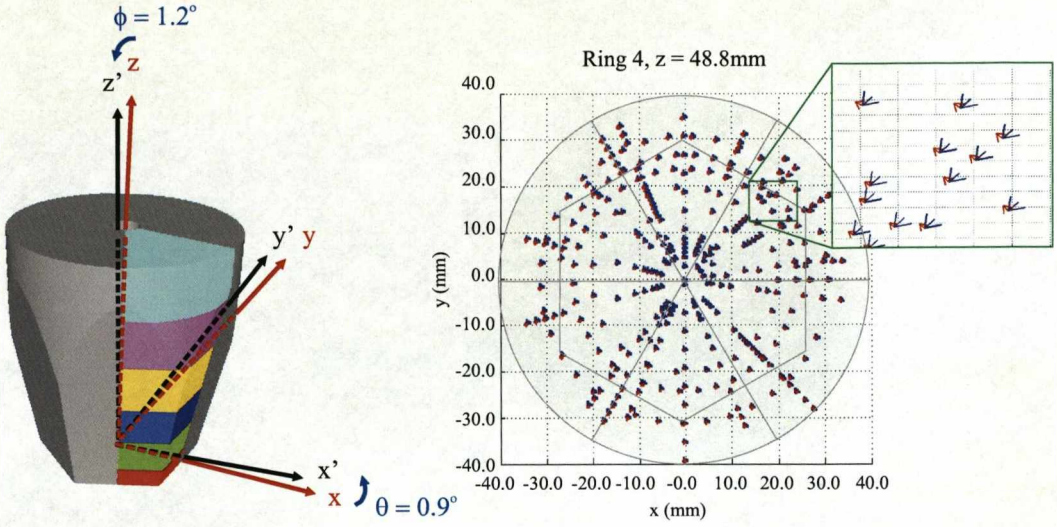

a) Schematic model of the S002 detector - scanning table offset

b) S002 correction vectors, z = 48.8mm

Figure 6.2: a) A schematic representation of the tilt (ϕ) and rotation (θ) of the S002 AGATA prototype detector relative to the axes of the scanning table. b) A vector plot showing the translation of the scanning table coordinates for interactions at $z = 48.8mm$ into absolute coordinates in the Liverpool frame of reference. The blue arrows correspond to the adjustment in ϕ, while the red arrows correspond to the adjustment in θ. These corrections were accounted for before transforming the coordinates into the MGS frame of reference in order to calculate the simulated pulse shape response at each experimental position.

The tilt in ϕ was implemented by offsetting the coordinates of the interaction positions at each depth by the angle calculated from *Figure 5.16*. *Figure 6.2b* shows an example of this two-step vector transform for the 48.8mm collimation depth. For each position, the blue arrow corresponds to the adjustment in ϕ, while the red arrows correspond to that in θ. The uncertainties resulting from the angular corrections for both the S002 and S003 detectors are presented in *Table 5.4*. The total uncertainty on each x-y interaction position, $\sigma(x,y)$, was calculated by deriving the FWHM of the beam divergence, relative to the tilt of the crystal, and dividing by 2.35. The total uncertainties for both the S002 and S003 detectors are summarised in *Table 6.1*.

	S002	S003
σ(x,y), z = 0.0mm	0.6mm	0.6mm
σ(x,y), z = 90.0mm	1.3mm	1.2mm

Table 6.1: A table showing the uncertainty in the measured x,y interaction position, $\sigma(x,y)$, as a function of depth for the S002 and S003 AGATA symmetric prototype detectors.

6.1.2 Cross-talk Correction

Cross-talk is the phenomenon by which the detector responses from different channels can influence each other and can be categorised as either proportional or derivative. The magnitude of proportional cross-talk depends on the interaction segment, however, is independent of the interaction position within that segment. This magnitude was measured for different channels, as described in *Section 5.6.1* and was found to remain relatively constant. The term channel refers to the response of any of the outer contact preamplifiers or the core preamplifier. The proportional cross-talk in the S002 prototype detector is 0.11±0.05% and was measured at 662keV. Derivative cross-talk results in the observation of a signal component that is proportional to the derivative of the induced signal in a neighbouring electrode. However, unlike proportional cross-talk, its origin is not well understood. In previous work with highly segmented HPGe detectors, two contrasting techniques have been utilised to quantify the level of derivative cross-talk observed. These are:

1. *Flood measurement method* [Rad08] - ^{60}Co flood data were collected for a sufficient length of time that interactions occurred at all positions inside a GRETINA detector. The time aligned event-by-event pulses were then summed on a segment-by-segment basis, with the assumption that any residual observed in the segments other than the interaction segment was the result of cross-talk.

2. *Subtraction method* [Bru06b] - ^{241}Am data were collected by placing a collimated source at each segment boundary on the outer surface of a MINIBALL detector. The responses from average pulse shapes for interactions in neighbouring segments were subtracted on a segment-by segment basis. Thus, as the interaction position in each of the neighbouring segments was essentially the same, any residual observed in the segments other than the neighbouring interaction segments was the result of cross-talk.

To investigate the magnitude of the derivative cross-talk in the AGATA S002 prototype detector, the technique described in [Bru06b] has been implemented. It allows the isolation of this residual from the observed pulse shapes by considering the response of two neighbouring segments to the same interaction position. *Figure 6.3* presents a schematic illustration of this technique. The green circle in *Figure 6.3a* represents the beam spot. The red and blue lines show the trajectories of the electrons and *holes* respectively. Interactions occurred in either of the two laterally adjacent segments due to the divergence of the collimated beam. The large radius of interaction minimised the effect of the outer geometry, due to the taper, on the pulse shape response. The channel-by-channel subtraction of the pulses from an interaction in segment A4, from those for an interaction in F4, should result in zero residual for all but channels A4 and F4. Any non-zero residual must be the result of noise, cross-talk effects and the uncertainty in interaction position. This argument is shown schematically in columns *b*, *c* and *d* of *Figure 6.3*. To minimise the effects due to random noise and the uncertainty on the interaction position, average pulses from coincidence data at the position $x = 30.7 \pm 0.9mm$, $y = -16.3 \pm 0.9mm$, $z = 48.8 \pm 0.3mm$ were used. The pulses were sorted by gating on the interaction segment and average pulse shapes were generated by the technique described in *Section 5.8*. The average pulse shapes for event categories one (red) and two (blue), for all 37 channels, are presented in *Figure 6.4*. Close-up views of the responses from nine of the channels are shown in the centre of the figure. The good agreement between the two centre contact signals implies that the uncertainty in the interaction position is small.

Figure 6.5 shows the residual calculated from the channel-by-channel subtraction of the average pulse shapes for event category two from those for event category one. The scale is truncated to enhance the effect. The channels in sector A are highlighted in red, as well as the lateral neighbour B4. Similarly, the channels in sector F are highlighted in blue, as well as the lateral neighbour E4. The residuals from all other channels are shown in black. The effect of derivative cross-talk from the interaction in segment A4 can be seen in all channels of sector A as the positive residuals that are proportional to the derivative of the response in A4. Similarly, the cross-talk effects from the interaction in segment F4 can be seen as the negative residuals that are proportional to the derivative of the response in F4. Residuals are also observed in the laterally adjacent channels B4 and E4. As for sectors A

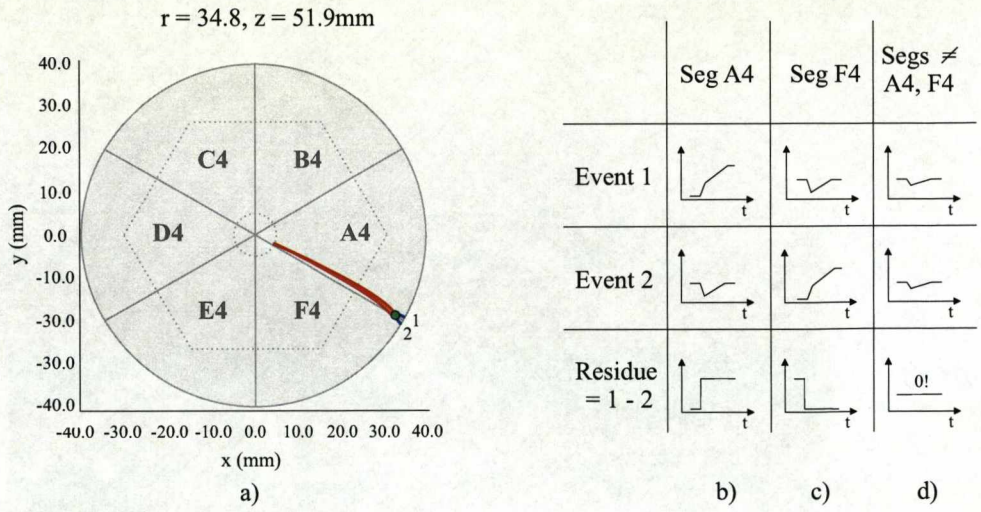

Figure 6.3: A schematic representation of the technique devised by [Bru06b] for observing the derivative cross-talk in highly segmented HPGe detectors. This technique has been adapted for the AGATA symmetric prototype detectors. The green circle represents the injection collimator position which has sufficient divergence to probe laterally adjacent segments. By subtracting the average pulse shape response for event one from those for event two, the pulse shape representations in row three of the matrix are expected. Any residual in segments other that A4 or F4 is the result of noise, cross-talk or the difference in interaction position. By using average coincidence pulses from the same scanning table position, the resulting residuals are predominantly due to cross-talk.

and F, the polarity of the residual gives information on the identification of the coupling channel. The absolute magnitude of the residuals is related to the magnitude of the coupling between the channels. This is observed to be maximal for the channels corresponding to the segments directly above the interaction segments. The observation of derivative cross-talk in all segments of the two sectors is the result of the FET mountings that confine the six FETs of each sector to a single board. The observation of cross-talk in B4 and E4 may be the result of the close proximity of the FET mother boards for the neighbouring sectors. No significant derivative cross-talk is seen in the signals in the remaining channels.

In order to quantify the magnitude of the cross-talk, the residual has been fitted with a function that accounts for both the integral, $m \cdot f_j(t)$, and derivative, $n \cdot \frac{d}{dt} f_j(t)$, cross-talk components. The function that describes the cross-talk between any two channels i and j

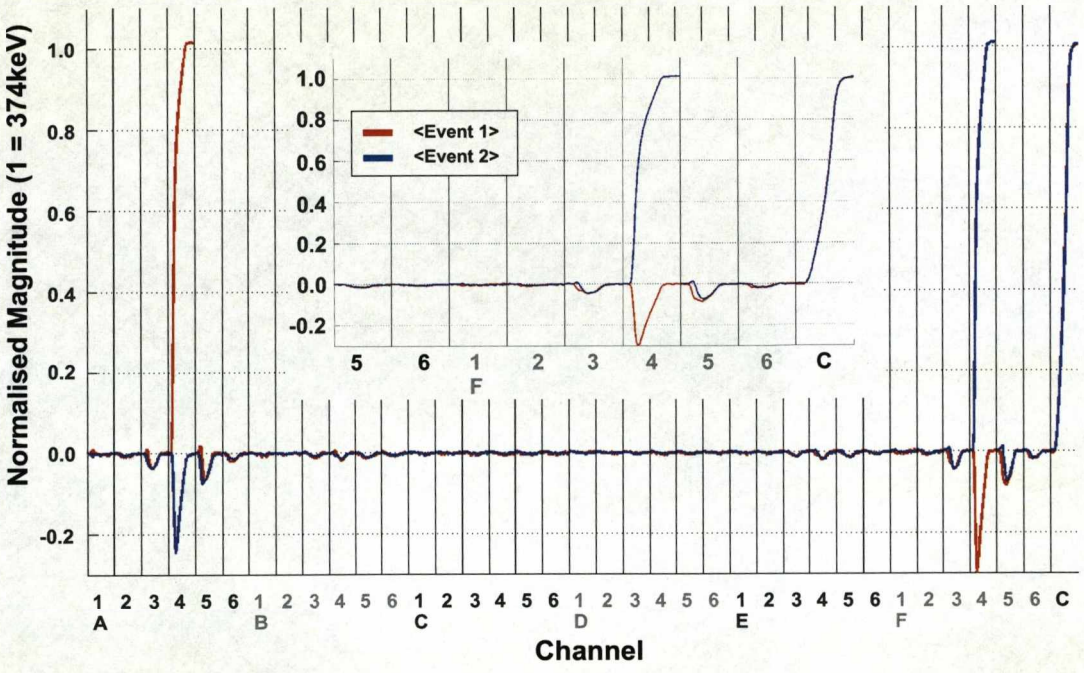

Figure 6.4: A figure showing the average pulse shapes for event categories one (red) and two (blue) at x = 30.7±0.9mm, y = -16.3±0.9mm, z = 48.8±0.3mm in the S002 prototype detector. The good agreement between the two centre contact signals implies that the uncertainty in the interaction position is small.

can be expressed as,

$$f_{ij}(t) = m \cdot f_j(t) + n \cdot \frac{d}{dt} f_j(t), \tag{6.1}$$

where m and n are percentages that account for the energy dependence of the signal magnitude. A value of $m = 0.11\%$ was used for all fits for the S002 prototype detector. An example of the fit used to determine the level of derivative cross-talk between channels A4 and A5 is presented in *Figure 6.6.*

The residual observed in A4, from the subtraction of the pulses from event categories one and two, is shown in red. The corresponding residual from segment A5 is shown in blue. Finally, the fit to the residual from A5, from the derivative of the residual in A4, is plotted in green. A positive shift of five interpolated samples, equivalent to one 12.5ns (80MHz)

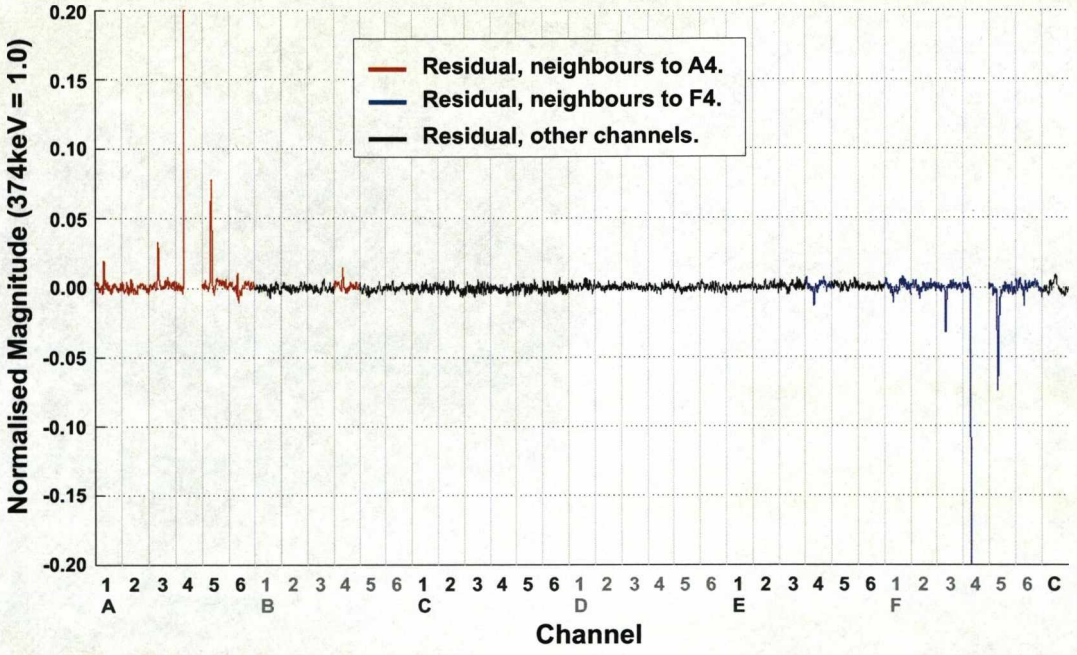

Figure 6.5: The residual from the channel-by-channel subtraction of the 37 average pulse shapes for event category two from event category one. The channels in sector A are highlighted in red, while those in sector F are highlighted in blue. Channels B4 and E4 are also highlighted with reference to their nearest neighbour. The residuals from all other channels are shown in black. The effect of derivative cross-talk in all channels of sectors A and F, as well as in channels B4 and E4 can be seen.

sample, was also required to obtain this fit. This shift accounted for the offset in the clock synchronisation between the digitiser channels for A4 and A5, which were in different GRT cards. A scaling factor equal to 534% of the magnitude of the residual A4 was folded into the calculation to achieve the best fit to the residual A5. Derivative cross-talk correction factors can be calculated for all combinations of channels in each detector however they cannot be applied to this data as the GRT cards do not have a global clock to maintain relative alignment of the channels. Each GRT card has a 40MHz time-stamp clock that runs independently but should maintain the same constant phase difference relative to the core. However, it was found that the phase drifted from card to card. If the effect of derivative cross-talk could be accurately corrected for, the level of cross-talk between the core and the segments could then be evaluated by comparing the sum of the segment pulses to the centre

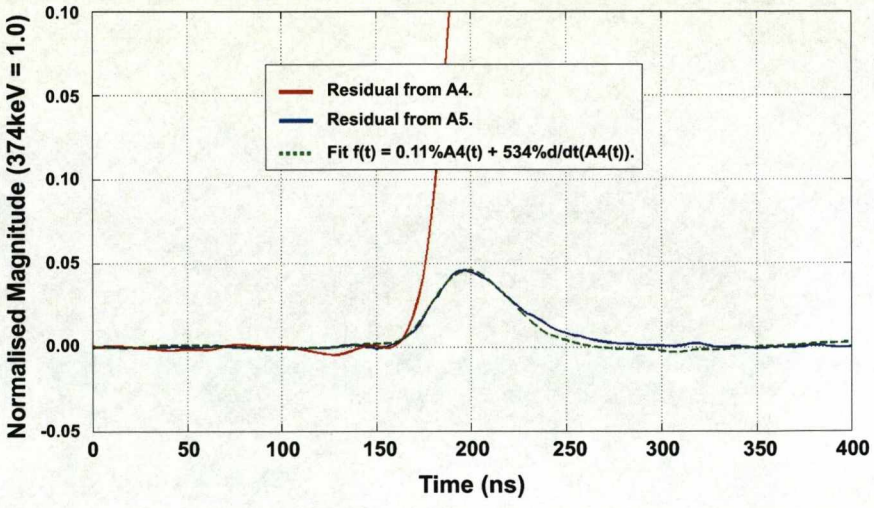

Figure 6.6: A figure showing the fit to obtain the derivative cross-talk components, assuming proportional cross-talk of 0.11% between all pairs of channels. The residual observed in channel A4, for the subtraction of average pulses from events one and two, is shown in red. The residual observed in channel A5 is plotted in blue and the fit to the derivative is plotted in green. A positive shift of five samples (2.5ns / sample) was also required to obtain an accurate fit.

contact pulse, as these should be equal. This comparison does however also rely on good time alignment.

6.1.3 Depth Offset Correction

The final correction applied to the data accounted for the uncertainty in the absolute depth of each interaction in the crystal. The relative depth of the centre of each collimator gap was determined with an uncertainty of $\pm$0.2mm, however the absolute depths were only known with >1.0mm uncertainty. This was the result of uncertainties in the positioning of the crystal relative to the cryostat, as well those from the measurement of the distance from the Tungsten collimator head to the front face of the cryostat, due to the positioning of the lead colimators. In order to test the depth correlation between the measured and simulated S002 data sets, a similarity minimisation was performed. The experimental pulse shapes at all nine depths for five different x-y interaction positions, $x^{z,k}_{offset}$, were compared to those calculated by MGS, $\mu^{z,k}_{offset}$. The calculation of the similarity parameter was iterated by

shifting all nine depths at each of the five positions by 0.1mm increments in depth. The similarity is expressed as,

$$\Delta s_{offset} = \frac{1}{t_{tot}} \sum_{z=1}^{9} \sum_{k=1}^{6} \sum_{t=t5}^{t90} \left[\frac{x_{offset}^{z,k}(t) - \mu_{offset}^{z,k}(t)}{\sigma_{offset}^{z,k}} \right]^2, \tag{6.2}$$

where z is the depth number, k is the channel number, t is the sample number and σ is the standard deviation of the baseline noise. The six channels included in the sum were the interaction segment, the core, and the clockwise, anticlockwise, upper and lower nearest neighbours. *Figure 6.7a* shows how the similarity varies as a function of offset in z. The calculated Δs_{offset} values are shown by the blue dots and the fourth order polynomial fit to the distribution is shown by the red solid line. The distribution is an asymmetric parabola with a minimum at an offset of -3.1mm. The asymmetry probably results from the derivative cross-talk that is not accounted for in the simulated basis. The minimum implies that there is a systematic offset of 3.1mm between the true and measured interaction depths in the crystal. The uncertainty associated with this fit was taken to be plus or minus two data points which equated to ±0.2mm. By combining this in quadrature with the ±0.2mm uncertainty from the relative collimator positioning, a total uncertainty in the central position of each collimator gap of ±0.3mm was obtained.

In order to validate the shift in depth, the positions for which the MGS and experimental interaction segment identities agreed for the second collimation depth were also investigated. *Figures 6.7b* and *6.7c* show these respective positions for ring one (blue) and ring two (red), at the measured depth of 18.8±0.3mm and the optimised depth of 15.7±0.3mm. The 18.8mm distribution shows discrete regions where no data points are present at radii between 7mm<r<12mm. This effect is due to the gradient of the field lines between rings one and two, that split the radial positions into the inner and outer configurations. If the depth of interaction entered into the simulation is too large, the interaction segment will correspond to ring two, rather than ring one as is observed experimentally. The increase in statistics observed in *Figure 6.7c* verifies that the optimised shift in depth was valid. The experimentally measured and optimised depths are displayed in *Table 6.2.*

The effect of the -3.1mm displacement of the MGS database on the pulse shape response is demonstrated in *Figure 6.8*, for the interaction position at x = *1.5±0.6mm*, y = *-2.9±0.6mm*, z = *4.2±0.3mm*. The 37 experimental average pulses for this zone one interaction (see *Figure 4.6 for a schematic representation of the zone classification*) beneath the central anode, are shown in red. The MGS calculated responses for z = *7.3mm* and z = *4.2mm* are overlaid on the same axes and shown in blue and green respectively. The figure shows that at a depth of 7.3mm, the image charges in the neighbouring segments in ring one are positive polarity, when experimentally they are observed to be negative. The agreement between the z = *4.2mm* data set and experiment is qualitatively good. The greatest discrepancy is for the image charge pulse observed in the segment vertically adjacent to F1, F2. Deviations can also be observed between the experimental and simulated centre and outer contact real charge pulses for the final rise of the pulse, for samples $>$*T90*. These deviations would be less if an appropriate derivative cross-talk correction could have been applied to the pulse shapes.

Depth No.	Measured Depth (mm)	Optimised Depth (mm)	Ring No.
1	7.3±0.3	4.2±0.3	1
2	18.8±0.3	15.7±0.3	1
3	18.8±0.3	15.7±0.3	2
4	34.0±0.3	30.9±0.3	3
5	34.3±0.3	31.2±0.3	3
6	52.7±0.3	49.6±0.3	4
7	51.9±0.3	48.8±0.3	4
8	68.1±0.3	65.0±0.3	5
9	86.8±0.3	83.7±0.3	6

Table 6.2: A table showing the measured and optimised depths for the single site interactions from the AGATA S002 AGATA symmetric prototype detector coincidence scan.

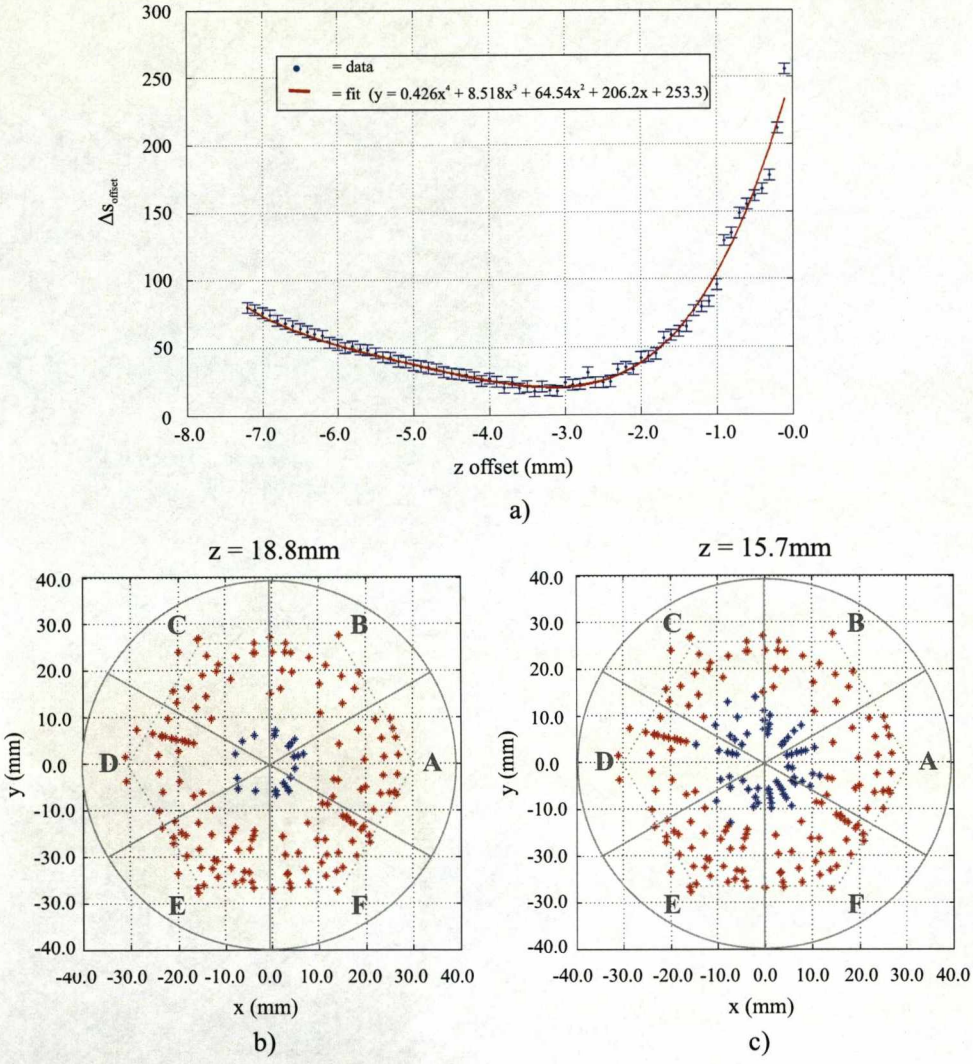

Figure 6.7: a) A figure showing the similarity minimisation of the interaction depths in the S002 symmetric detector. The experimental pulses from all nine depths for five interaction positions were compared to those calculated by MGS. The MGS data set was regenerated for 0.1mm steps in z and the calculation iterated. The distribution was fitted with a fourth order polynomial and an optimised offset in z of -3.1mm was determined. b) and c) show plots of all interaction positions at the experimentally measured and optimised second collimation depths respectively, for which the interaction segment agrees. The interactions in ring one are shown in blue and those in ring two are shown in red. The missing data points at intermediate radii in b) were the result of the interaction position occurring in the incorrect ring.

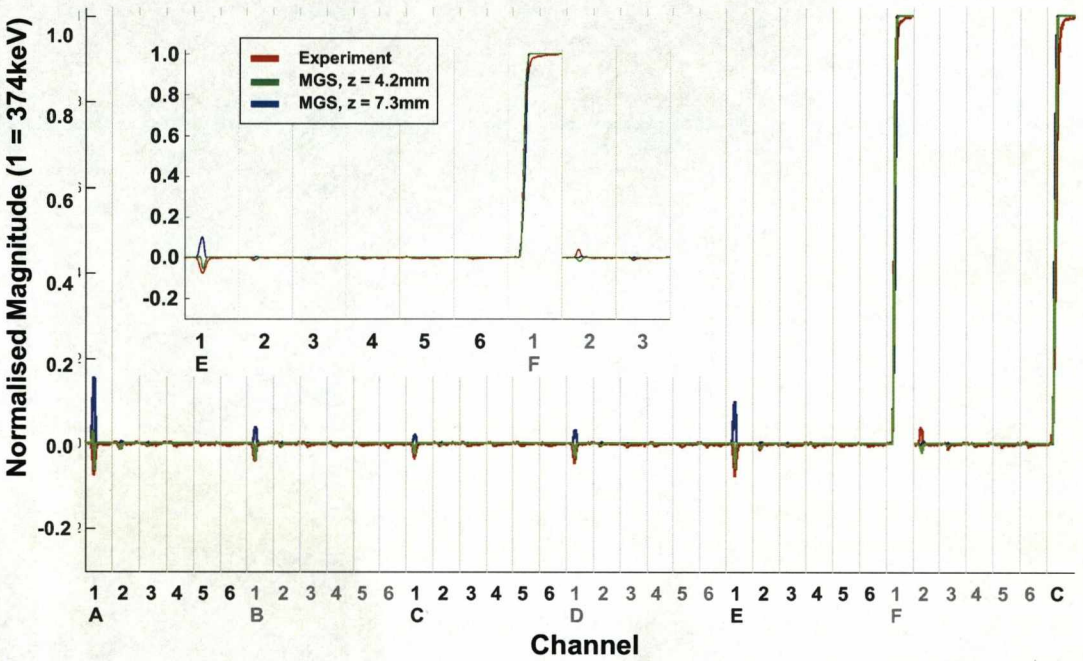

Ring one depth comparison, x = 1.5±0.6mm, y = -2.9±0.6mm.

Figure 6.8: A figure showing the 37 charge pulses from the S002 prototype detector for an interaction at the first collimation depth with coordinates $x = 1.5 \pm 0.7mm$, $y = -2.9 \pm 0.7mm$. The average experimental pulses are shown in red. The MGS calculated responses for $z = 7.3mm$ and $z = 4.2mm$ are overlaid on the same axes and shown in blue and green respectively. The observed negative polarity of the image charges is shown to be reproduced by MGS for an interaction depth of 4.2mm. The inset section of the figure shows the expanded region between pulse shapes E1 and F3.

6.1.4 Comparison of the Data

Each detector database consists of $N \times 37$ arrays of size $T \times 2$ elements, where N is the number of scan positions for which a set of average pulse shapes could be generated (a minimum of ten events were required) and $T(= 700)$ is the number of data samples in 2.5ns intervals. The t5 of each experimental and simulated real charge pulse was aligned to sample 200, where t5 corresponds to the sample at which the pulse reaches 5% of its maximum amplitude. The t30 of each image charge pulse was also aligned to sample 200, where t30 corresponds to the sample at which the image charge pulse reaches 30% of its maximum amplitude. The alignment samples would ideally have been t0 in both instances, however the level of baseline noise would not allow this. The iterative alignment of the pulses was required due to the non-time-aligned nature of the GRT4 data acquisition.

Rise time plots were generated to evaluate the symmetry of the distributions in the S002 detector as an initial validation of the geometrical corrections applied to the data. *Figures 6.9a* and *6.9b* show the experimental and simulated ring one outer contact T90s as a function of x-y position. The experimental T90 plot was generated from the average rise time value at each scanning table position for 662keV fold one events. These average values included events that interacted at any depth in ring one and also events where the gamma ray Compton scattered but was confined to a single segment. The simulated T90 plot was generated from the pulse shapes for single site interactions at a depth of 4.2mm inside the crystal. Both distributions show good qualitative agreement and are symmetric through the A / B sector boundary and also along the line that runs through the centre of sectors C and F. As expected, the experimental T90 values are on average slower than those from the simulation. This is due to the relatively shallow depth of the front ring, of between 8mm and 13mm. This shallow depth constrains the scattering angle, for events that Compton scatter in the segment, resulting in the generation of multiple charge clouds at sites with a greater average radius than for a single site interaction. The drift of these charge clouds will therefore contribute to longer average rise times.

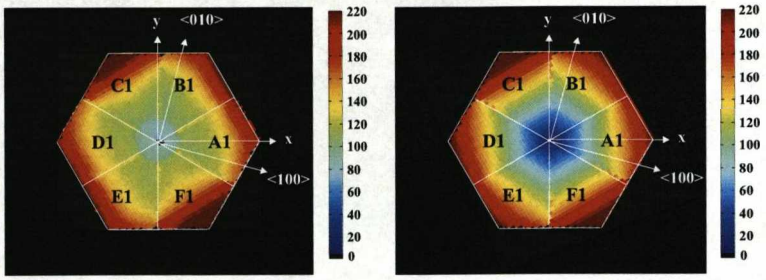

Figure 6.9: A figure showing the outer contact T90 rise time distributions for interactions in ring one of the S002 prototype detector. a) Average experimental T90 distribution for 662keV fold one events, as a function of scanning table position. The average values included events that interacted at any depth in ring one and also events where the gamma ray Compton scattered but was confined to a single segment. b) Simulated T90 distribution for single site events that interacted at a depth of 4.2mm inside the crystal. The experimental T90 values are on average longer than those from single site interactions.

6.2 S002 Experimental and Theoretical Pulse Shape Comparison

This section of the work describes detailed comparisons between the S002 experimental and simulated databases, with the offset of -3.1mm folded in to the MGS coordinate system. As demonstrated in *Figure 6.8*, a reasonable agreement is observed in zone one, directly beneath the central anode. To demonstrate the level of agreement in zones two and three, the pulse shape response at positions $x = 5.7 \pm 0.7mm$, $y = -9.4 \pm 0.7mm$ $z = 15.7 \pm 0.3mm$ and $x = 18.1 \pm 1.0mm$, $y = -29.4 \pm 1.0mm$ $z = 48.8 \pm 0.3mm$ are presented in *Figures 6.10* and *6.11* respectively. The average experimental pulses are shown in red, while those from MGS are overlaid on the same axes and shown in blue. In each case, the residual, calculated as the sample-by-sample subtraction of the MGS magnitude from the experimental magnitude, is plotted in black. Zone two of the detector encompasses the regions where the electric field distribution is semi-planar and where the *hole* trajectories may terminate on the front sur-

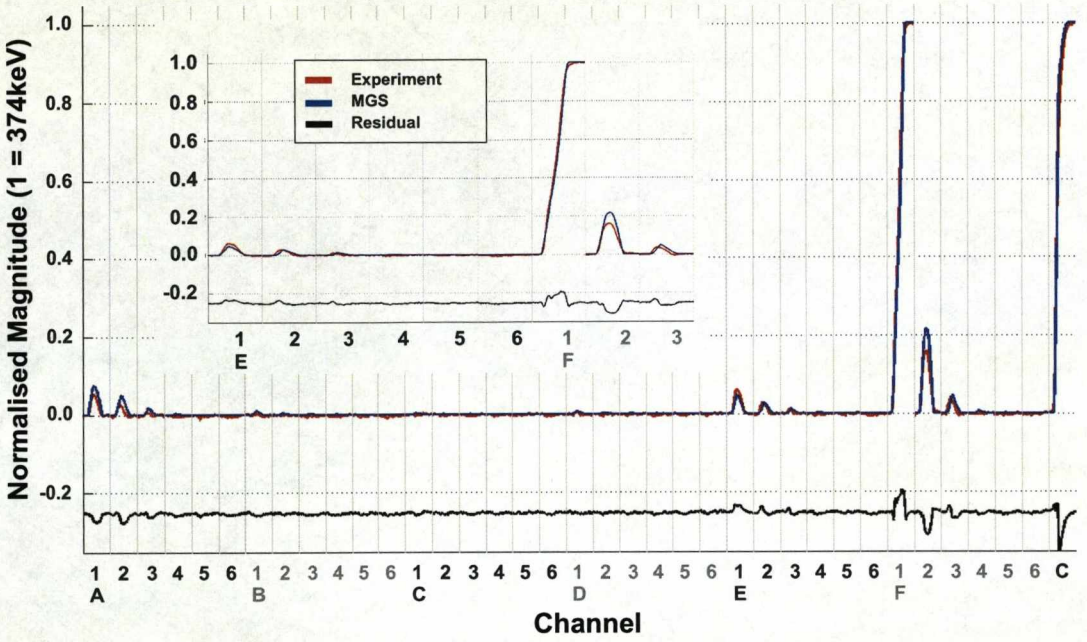

Zone 2, x = 5.7±0.7mm, y = -9.4±0.7mm, z = 15.7±0.3mm.

Figure 6.10: A figure showing the 37 charge pulses from the S002 prototype detector for an interaction in zone two at $x = 5.7 \pm 0.7mm$, $y = -9.4 \pm 0.7mm$, $z = 15.7 \pm 0.3mm$. The average experimental pulses are shown in red, the MGS calculated responses are shown in blue and the difference in magnitude between the two pulse shape data sets is shown in black. The inset section of the figure shows the expanded region between pulse shapes E1 and F3.

face or tapered sides of the crystal. For zone three, the electric field lines are approximately parallel to the front face of the crystal and the geometry is coaxial. The residual in *Figures 6.10* and *6.11* show the agreement is worst for the image charges in segments vertically adjacent to the interaction segment, F2 and F5 respectively. The deviation between the experimental and simulated centre and outer contact real charge pulses is greatest at the final rise of the pulse for samples $> T90$. These effects are the combined result of capacitive coupling between the channels (derivative cross-talk) together with the fact that the derivative cross-talk correction was not performed before the depth minimisation.

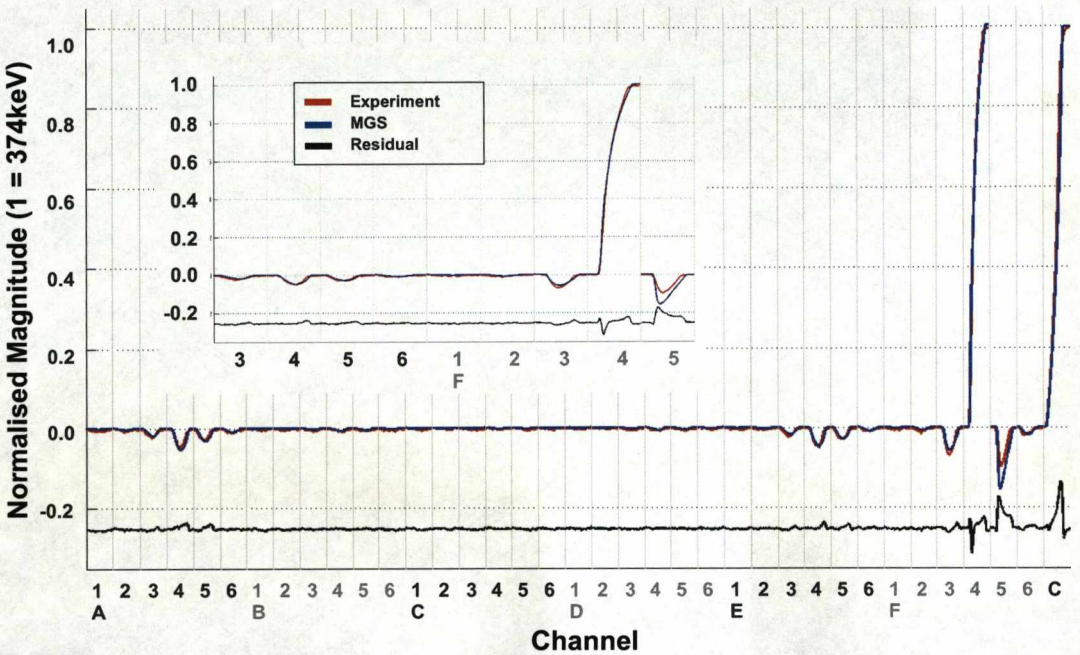

Zone 3, x = 18.1±0.9mm, y = -29.4±0.9mm, z = 48.8±0.3mm.

Figure 6.11: A figure showing the 37 charge pulses from the S002 prototype detector for an interaction in zone three at $x = 18.1 \pm 0.9mm$, $y = -29.4 \pm 0.9mm$, $z = 48.8 \pm 0.3mm$. The average experimental pulses are shown in red, the MGS calculated responses are shown in blue and the difference in magnitude between the two pulse shape data sets is shown in black. The inset section of the figure shows the expanded region between pulse shapes E3 and F5.

6.2.1 Similarity Parameterisation

In order to quantify the agreement between the experimental and simulated pulse shape data sets, an adapted form of the similarity parameter, Δs, has been calculated for each channel, at each interaction position. It accounts for the change in rise time and image charge magnitude as a function of position by normalising with respect to the absolute area of each pulse. The similarity parameter, Δs, is expressed as,

$$\Delta s = \frac{1}{Area} \sum_{t=t0}^{t90} \left[\frac{x_i(t) - \mu_i(t)}{\sigma_i} \right]^2, \tag{6.3}$$

where $t0 = constant$ is an arbitrary sample number that precedes the initial rise of any pulse shape, x_i and μ_i are the magnitudes of the experimental and simulated super-pulses (average pulse trains) at position i and σ_i is the standard deviation of the baseline noise, typically 1.0keV. *Table 6.3* summarises the variation in $log_{10}\Delta s$ for the examples presented in *Figures 6.8*, *6.10* and *6.11*.

The parameter is plotted as $log_{10}\Delta s$ to encompass the wide variation in Δs, of between 100 and 10,000, resulting from the small magnitude of the baseline noise incorporated as the denominator in *Equation 6.5*. From observation, a small value of $log_{10}\Delta s$, typically between

Channel	$\log_{10}\Delta$s, zone 1	$\log_{10}\Delta$s, zone 2	$\log_{10}\Delta$s, zone 3
Interaction segment	2.70±0.03 (F1)	2.13±0.03 (F1)	2.19 (F4)±0.03
Centre contact	3.74±0.03 (C)	3.06±0.03 (C)	2.87 (C)±0.03
Clockwise image charge	3.50±0.03 (E1)	1.64±0.03 (E1)	1.66 (E4)±0.03
Anticlockwise image charge	3.10±0.03 (A1)	2.16±0.03 (A1)	2.42 (A4)±0.03
Upper image charge	3.94±0.03 (F2)	2.65±0.03 (F2)	3.50 (F5)±0.03
Lower image charge	-	-	2.25 (F3)±0.03
Arbitrary	2.81±0.03 (C3)	2.86±0.03 (C3)	2.70 (C3)±0.03
<Total>	3.47±0.03	2.67±0.03	2.83±0.03

Table 6.3: A table showing the variation in the logarithm of the similarity parameter, for the example interactions presented in *Figures 6.8*, *6.10* and *6.11*. The parameter that quantifies the average total agreement between the experimental and MGS pulse shapes is shown to be worst (greatest) beneath the central anode.

two and three represents a good match. *Table 6.3* shows that $log_{10}\Delta s$ for the centre contact (core) pulse shape comparison decreases as a function of increasing interaction depth. Thus implying that the agreement between the experiment and simulation is best in the coaxial regions of the detector (zone three). The outer contact segment-by-segment agreement is more complex than for the core. The similarity parameter is shown to decrease and then plateau for both the interaction segment and clockwise image charge. The variation in similarity for the anticlockwise and upper image charges is more varied and no real conclusions can be drawn. For segments non-adjacent to the interaction segment, termed arbitrary due to the small signal size, the agreement remains relatively constant. The mean total agreement, <total>, has also been calculated and is presented in *Table 6.3*. This parameter only considers the contributions from the interaction segment, centre contact and clockwise, anticlockwise, upper and lower image charges. The magnitude of <total> is shown to be greatest for the zone one interaction beneath the central anode. This poor agreement is likely to be due to the uncertainty in the interaction depth which will have the greatest effect on the pulse shape response in this region due to the planar electric field distribution.

In order to gain a greater understanding of the differences between the experimental and simulated data sets, the similarity parameter, $log_{10}\Delta s$, has been calculated for all 2490 interaction positions in the S002 detector. The values for the interaction segment, centre contact and clockwise, anticlockwise, upper and lower image charges at each position are plotted as a series of 2D surface maps. Each of these figures, presented in *Appendix E*, shows the variation in $log_{10}\Delta s$ for all x-y interaction positions at each of the nine depths (see *Table 6.2* for a summary of the interaction depths). A sub-set of these distributions is presented in *Figure 6.12* and the observed trends are discussed in this section.

Figures 6.12a, *6.12b* and *6.12c* show the variation in $log_{10}\Delta s$ for the interaction segment, clockwise image charge and upper image charge respectively. In each figure, the distributions are shown for the 4.2±0.3mm (zone one) and 48.8±0.3mm (zone three) interaction depths. To aid the discussion several sets of pulse shapes, refered to in the text below, are also presented in *Figures 6.14*, *6.15* and *6.16*. These pulse shapes from interaction positions along coincidence line scan one, shown schematically in *Figure 6.13*, lie on the symmetry

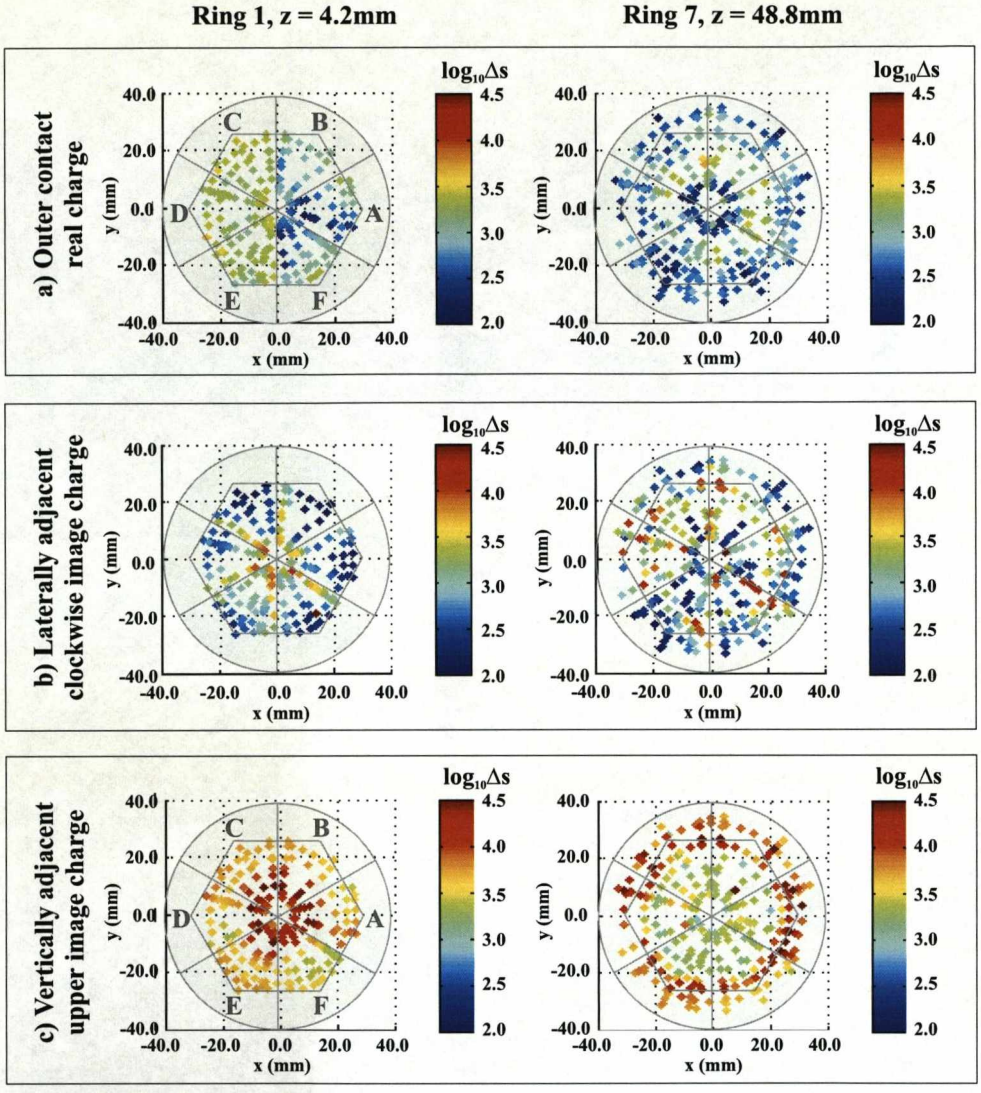

Figure 6.12: A figure showing the similarity parameter $log_{10}\Delta s$ as a function of interaction position. a) to c) show the distributions for the interaction segment, clockwise image charge and upper image charge respectively. In each case the plots for both the 4.2±0.3mm (zone one) and 48.8±0.3mm (zone three) collimation depths are presented. The similarity parameter quantifies the difference between the experimental and simulated pulses as a fraction of their area and is shown to vary considerably across the detector.

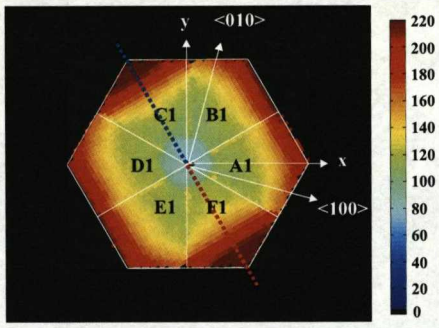

Figure 6.13: A schematic representation of the interaction positions from coincidence line scan one, overlaid on the singles fine-scan T90 distribution for ring one. This scan line is shown to run along the symmetry axis through the centre of sectors C and F. Thus the pulse shapes generated at equal radii from the centre of the detector should be similar.

axis through the centre of sectors C (blue dashed line) and F (red dashed line). In each figure the pulses from three interaction radii, small medium and large, for the 4.2 and 48.8 interaction depths are shown. For each radius the pulses from both sectors C and F are shown in blue and red respectively. The experimental pulses are displayed as solid lines and the MGS pulses as broken lines. The calculated $log_{10}\Delta s$ values are also shown in their respective colours.

Figure 6.12a shows that at a depth of 4.2mm the outer contact real charge pulse distribution is asymmetric (with the best agreement in sectors *A B* and *F*). The parameter $log_{10}\Delta s$ is shown to vary between 2.0 and 3.5. This asymmetry can be understood from the analysis of the pulse shapes shown in *Figures 6.14a* to *6.14d*. For the 4.2mm interaction depth, the constituent pulses of each pair at each of the three radii are shown to differ. However, each pair of MGS pulses lie on top of each other. Thus, the asymmetry is the result of the fact that the geometric corrections applied for the tilt and rotation of the detector have not changed the interaction position in MGS to a sufficient degree as to account for the deviations in the experimental data. From the analysis of these pulse shapes it can also be seen that although the initial rise of both the experimental and MGS pulses is similar, the experimental pulses start to slow between t30 and t90, with the final 5% of the pulse rising slower still. The slow rise between t30 and t90 may be the result of regions of unsaturated

charge carrier drift velocity, not calculated by the simulation. A fraction of this deviation will also be attributed to derivative cross-talk effects.

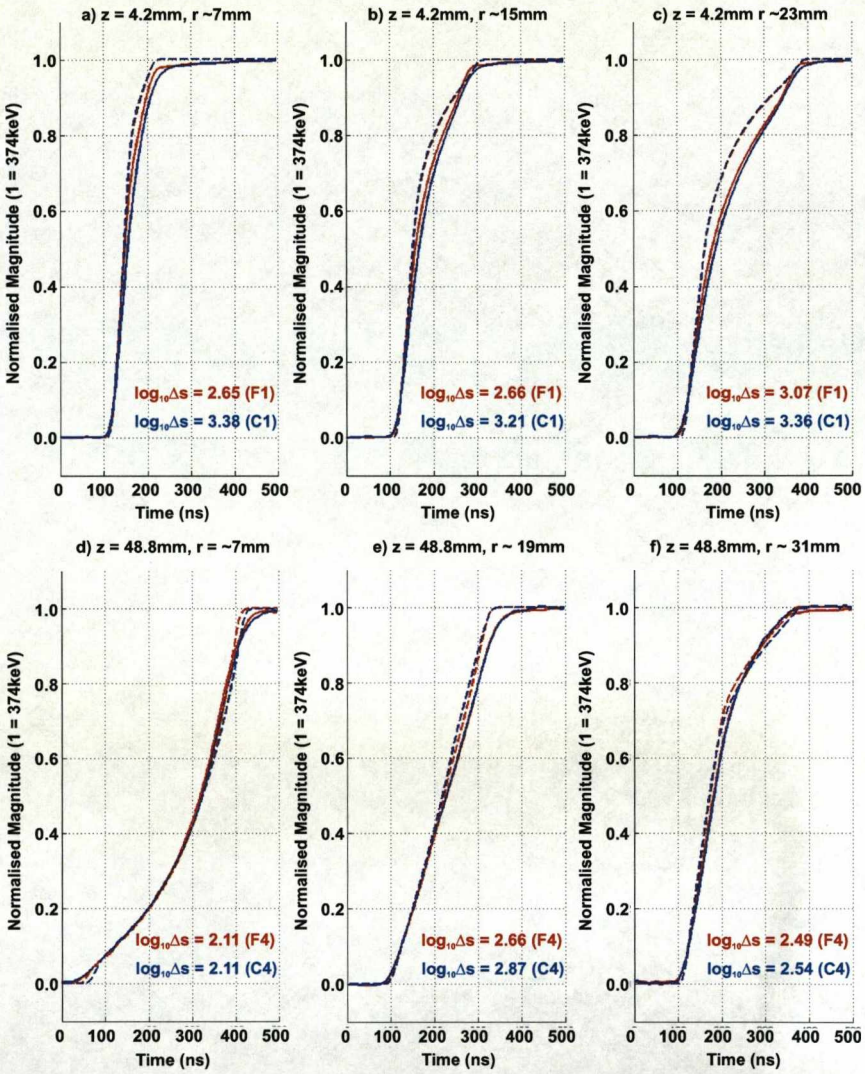

Figure 6.14: A figure showing the outer contact real charge pulse shapes from coincidence line scan one. a) to c) and d) to f) show the responses for small medium and large interaction radii at depths of 4.2±0.3mm and 48.8±0.3mm respectively. In each case, the experimental pulses are displayed as solid lines and the MGS pulses as broken lines. Also, the interactions in sector C are coloured blue, while those in sector F are coloured red. The calculated $log_{10}\Delta s$ values are also shown. The agreement between experiment and simulation is shown to be systematically worse for the 4.2±0.3mm collimation depth.

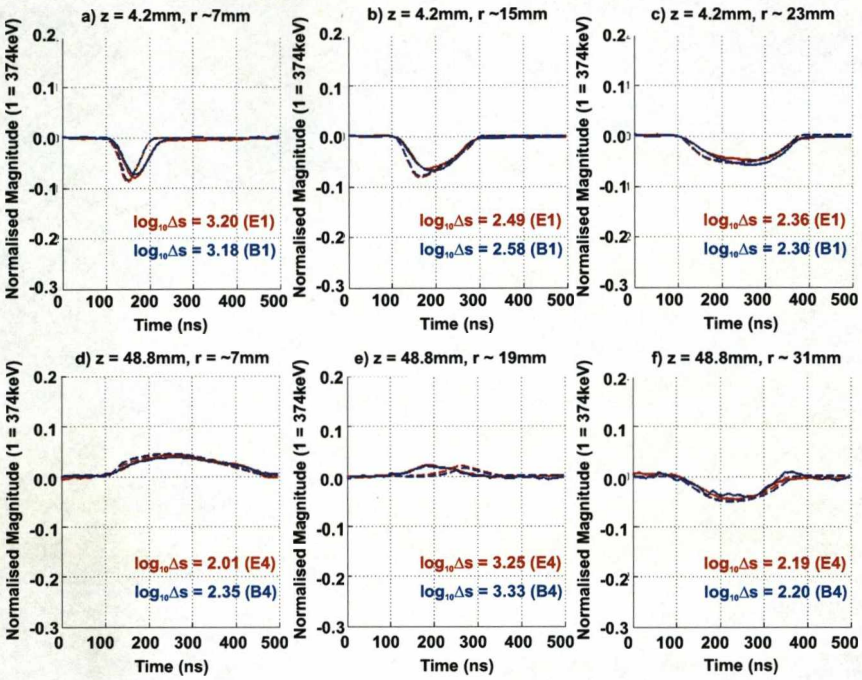

Figure 6.15: A figure showing the image charge pulses in the channels laterally adjacent, in the clockwise direction, to the interaction segments defined in *Figure 6.14*. a) to c) and d) to f) show the responses at depths of 4.2±0.3mm and 48.8±0.3mm respectively. In each case, the experimental pulses are displayed as solid lines and the MGS pulses as broken lines. Also, the interactions in sector C are coloured blue, while those in sector F are coloured red. The calculated $log_{10}\Delta s$ values are also shown. The agreement is shown to be good for all but the 19mm radius in ring four, where the pulse shapes match well but the automated alignment routine has misidentified the alignment sample.

The corresponding $log_{10}\Delta s$ distribution in *Figure 6.12b* for the 48.8mm depth shows a symmetric trend with discrete regions of good and poor agreement. The experimental and simulated pulses are shown to match best for interactions at small and large radii. This trend can be observed from the pulse shapes in *Figures 6.14d* to *6.14f*. At the 7mm and 31mm radii, both sets of pulses match well until T90. The symmetry observed for the 48.8mm depth may also be consistent with a discrepency in the correction of the tilt of the detector, since at 48.8mm a fractional gradient in depth of interaction across the diameter of the crystal will not manifest itself in a significant change in the pulse shape response. In general, the agreement at a depth of 48.8mm is shown to be superior to that at a depth of 4.2mm. For the interaction at a radius of ~19mm the agreement is good for the initial fast rise of the pulse, but deviates after 40% of the maximum rise as the experimental pulses begin to slow.

Figure 6.12b shows how $log_{10}\Delta s$, for the channels laterally adjacent in the clockwise direction to the interaction segment, varies across the detector. At a depth of 4.2mm the match is shown to be best for interaction positions at angles close to the clockwise segment boundary, where the image charge magnitude is greatest. However, at 48.8mm the agreement in clockwise image charge is more varied and follows no clear trend. *Figures 6.15a* to *6.15c* and *6.15d* to *6.15f* show the image charge pulses observed in the channels laterally adjacent, in the clockwise direction, to the interaction segments defined in *Figure 6.14*. Line one intersects the middle of the each sector, therefore the variation in magnitude of the image charges is relatively small. The agreement in pulse shape response is shown to be very good at both depths. However, for small image charges such as these, the greatest discrepency is due to misalignment of the leading edges of the pulses. As such, the patterns observed in *Figure 6.12b* will depend almost entirely on the alignment of the pulses, rather than the ability of MGS to reproduce the experimentally observed image charge response. These discrepencies highlight the need for a global clock in the acquisition system.

Figure 6.12c shows the agreement between the experimental and simulated pulses in the channels vertically adjacent, in the upward direction, to the interaction segment. The match at both depths is shown to be systematically worse than for the the laterally adjacent image charges. This is thought to be due to the effects of derivative cross-talk that have been shown

to have a significant effect on the pulse shapes observed in the channels vertically adjacent to the interaction segment. At a depth of 4.2mm, the agreement is worst for small radii. Conversely, at a depth of 48.8mm, the agreement is worst at medium to large radii. In each case, these interaction positions are consistent with the regions of the detector where the outer contact pulse shapes are fastest. Thus the effects of derivative cross-talk are enhanced. *Figures 6.16a* to *6.16c* and *6.16d* to *6.16f* show the image charge pulses observed in the channels vertically adjacent, in the upward direction, to the interaction segments defined in *Figure 6.14*. In all cases the agreement is shown to be poor. The similarity parameter is greatest for the ~7mm radius at a depth of 4.2±0.3mm. The image charges at this radius are shown to be of the opposite polarity to those observed experimentally. This discrepency is likely to be due to the uncertainty in the depth of the interaction, as well as derivative cross-talk effects.

From the analysis of all the distributions presented in *Appendix E* several conclusions can be drawn:

1. *Centre contact real charge response* - The agreement is best for interactions at intermediate radii in zones two and three, where $log_{10}\Delta s$ is <2.5. For these interaction positions the experimental rise times are fastest (see *Section 5.6.4*) and follow the fast rise times observed in the simulation. For the front ring the agreement is more complex and varied as the surface on which the *hole* trajectories terminate changes.

2. *Outer contact real charge response* - The agreement is generally good and is best in zones two and three for interactions at large radii, where the outer contact pulse shape has a fast T30 (see *Section 5.6.4*). For these interaction positions $log_{10}\Delta s$ ~2.5. As for the core, the pulse shapes follow the fast rise times observed in MGS. However, there is also good agreement at small radii, close to the core, where the drift is entirely dominated by the *hole* transport. In the front ring the distribution is varied and no clear conclusions can be drawn. For both the centre and outer contact real charge pulses, the greatest contribution to the similarity parameter is from the samples >T90.

3. *Outer contact lateral image charge response* - The agreement between the experimental and simulated image charge response for the segments laterally adjacent to the

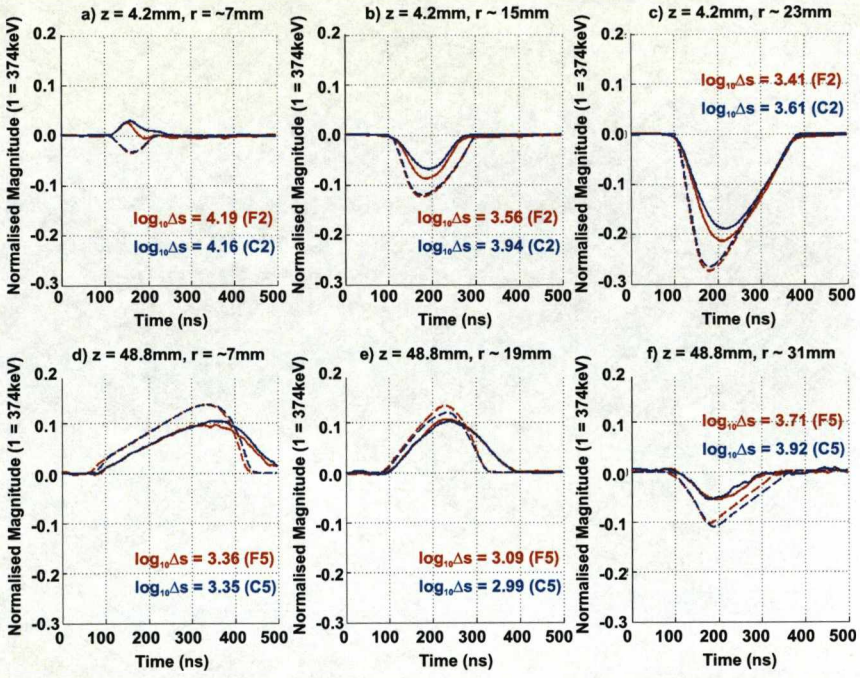

Figure 6.16: A figure showing the image charge pulses in the channels vertically adjacent, in the upwards direction, to the interaction segments defined in *Figure 6.14*. a) to c) and d) to f) show the responses at depths of 4.2±0.3mm and 48.8±0.3mm respectively. In each case, the experimental pulses are displayed as solid lines and the MGS pulses as broken lines. Also, the interactions in sector C are coloured blue, while those in sector F are coloured red. The agreement between experiment and simulation is shown to be systematically worse than for the lateral image charges. This discrepency is also likely to be due to cross-talk.

interaction segment is very good and improves as a function of increasing magnitude. This is due to the more precise time alignment for the signals with a larger signal to noise ratio, when the pulse shape database was generated in software.

4. *Outer contact vertical image charge response* - The agreement between the experimental and simulated image charge response for the segments vertically adjacent to the interaction segment is reasonable. However, the general trend is worse than for the laterally adjacent image charges. This is primarily due to the levels of cross-talk that were not accounted for in the database and that also affected the precision of the depth minimisation.

Following the analysis of each individual distribution the total mean similarity, $log_{10}<\Delta>$, was calculated at each interaction position. This figure of merit quantifies the total difference between the experimental and simulated pulses when considering the responses from the interaction segment, core, and clockwise, anticlockwise upper and lower image charges. *Figure 6.17* shows these distributions for each of the nine collimation depths. The distributions are all azimuthally symmetric but vary as a function of radius. At a depth of 4.2mm the agreement is shown to be poorest for radii <10mm. The magnitude of $log_{10}<\Delta s>$ varies between 3.0 and 4.5. For the coaxial regions of the detector (depths 30.9mm to 83.7mm) the distributions are shown to be relatively uniform with values of $log_{10}<\Delta s>$ ~3.0, with rings of interaction positions that show poor agreement at increasing radii as a function of depth, ranging from ~18mm to ~25mm. The figures appear to show some average trend that shares the attributes of those for the upper and lower image charge responses, as presented in *Figures E.5* and *E.6*. This pattern may also be the result of discrepencies in the charge carrier mobilities. Further investigation with time aligned data is required in order to deconvolve these effects.

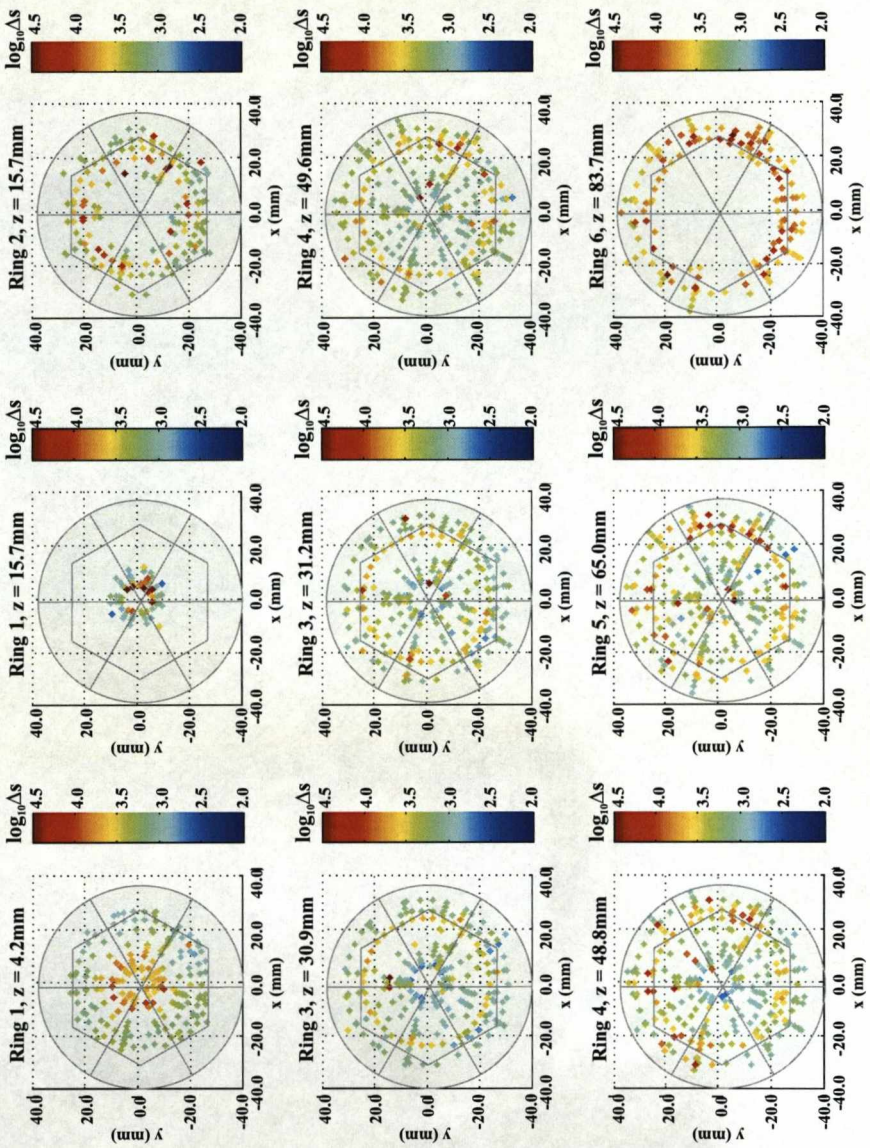

Figure 6.17: A figure showing the variation in the average total similarity parameter, $log_{10}<\Delta s>$, as a function of interaction position for each of the nine collimation depths. These distributions quantify the total difference between the experimental and simulated pulses, when considering the responses from the interaction segment, core, and clockwise, anticlockwise upper and lower image charges. The distributions are shown to be azimuthally symmetric but vary as a function of radius.

6.3 S002 Iterative Basis Matching

In the previous sections of this work, the pulse shape comparisons have been performed with an MGS basis generated from the precise interaction positions determined from the experimental scan. In order to investigate the geometric corrections applied to the data and also the calibration in absolute position localisation with respect to a basis data set, each experimental interaction position has been compared to a new MGS basis generated on a 1.0mm $\times$ 1.0mm grid at each optimised collimation depth in the S002 detector geometry. A set of 37 pulses was stored at every 1.0mm grid point in x and y. The pulse shapes from the centre contact, interaction segment and clockwise, anticlockwise, upper and lower image charge neighbours for each experimenatl position were compared to those at every MGS basis site. The interaction site that gave the lowest mean similarity, $<log_{10}\Delta s>$, for the six pulse shape comparisons, was stored. *Figures 6.18* to *6.20* show the displacement from the measured interaction position to the position deemed the *best* match in the MGS basis for three different depths. Each figure shows the vectorial displacement and vectorial magnitude maps, side by side. For the former, the start of each arrow is the measured position and the head of the arrow is the best match. For the latter, the colour at each position represents the absolute length of the displacement between the two positions. *Figure 6.18a* shows that at a depth of 4.2mm, the arrows on the vector map are focussed towards the centre of the detector in a symmetric distribution around the core. The magnitudes of the displacements are shown to be relatively consistent with typical values of between 1.5mm and 3.0mm. The largest displacements occur in the corners of the detector where the rise times are very slow, of the order of 260ns in the front ring.

Figure 6.19a shows the displacement vectors for the 15.7mm interaction depth. The blue arrows represent the interactions in ring one, while the red arrows represent those in ring two. As for *Figure 6.18a*, the vectors are focussed towards the centre of the detector, however, they are also directed towards the centre of the segments. The displacement magnitudes, shown in *Figure 6.19b*, show an average displacement of $\sim$1.0mm in the centre for ring one, with an average displacement of $\sim$2.5mm at large radii for the interactions in ring two. *Figure 6.20a* shows the displacement vectors for the 48.8mm interaction depth. As for the 15.7mm distribution, the arrows are focussed towards the centre of the segments

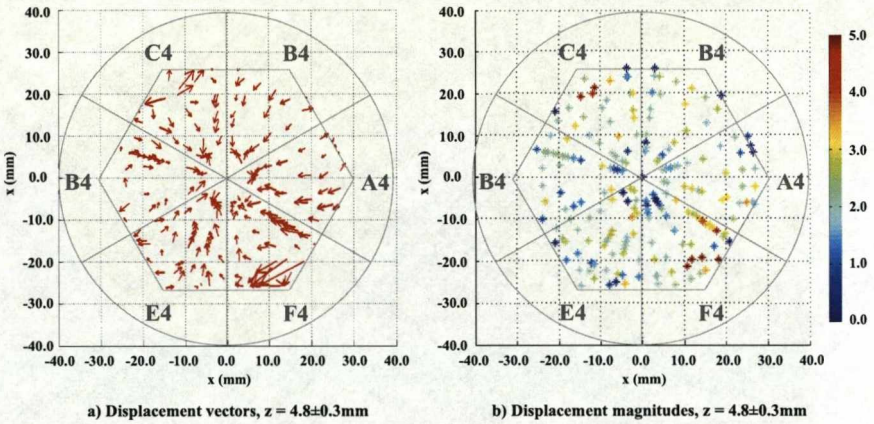

Figure 6.18: A figure showing the difference between the experimentally measured interaction positions and the site in the MGS basis that gives the best $<log_{10}\Delta s_{Tot}>$ match, for all interactions at a depth of 4.2±0.3 in the S002 crystal. a) The vectorial displacement map, where the start of the arrow is the measured position and the head of the arrow is the best match. The arrows are focussed towards the centre of the detector. b) The vectorial magnitude map, where the colour at each position represents the absolute length of the displacement between the two positions. The magnitudes are relatively similar and the mean displacement is 2.2mm.

and also the centre of the detector.

The symmetry of the distributions for each segment independently showing a preferential displacement towards the centre of the detector infers that the rotational corrections applied to the data are correct. Fundamentally, the reason for these displacements is believed to be due to derivative cross-talk which results in longer average rise times. As the similarity comparison is calculated from five outer contact pulse shapes (the interaction segment plus the four image charges), the minimisation against all possible interaction positions tends towards a general convergence biased towards the centre of the detector. As for the discrepencies observed in *Figure 6.17*, these observations may also be caused by incorrect charge carrier mobilities calculated in the simulation.

Table 6.4 shows a summary of the variation in displacement for *Figures 6.18* to *6.20*. The displacements are shown to range from 0.1mm to 17.3mm. The uncertainties are given as the standard deviations of the distributions. The mean values are between ~2mm and ~3mm

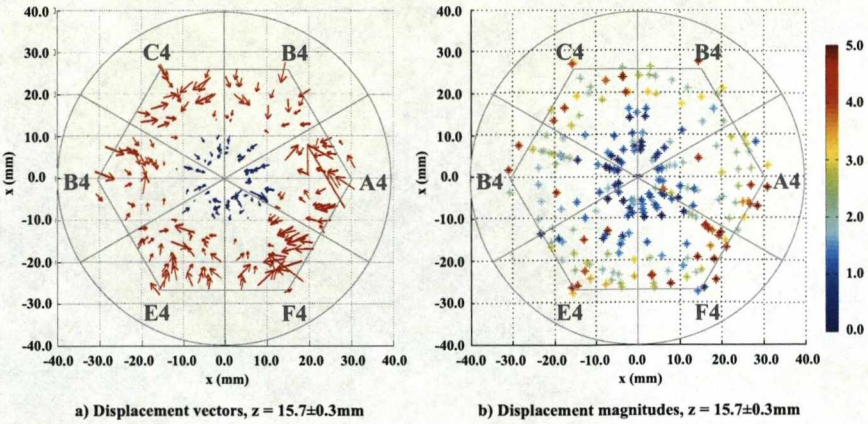

Figure 6.19: A figure showing the difference between the experimentally measured interaction positions and the site in the MGS basis that gives the best $<log_{10}\Delta s_{Tot}>$ match, for all interactions at a depth of 15.7±0.3 in the S002 crystal. a) The vectorial displacement map, where the start of the arrow is the measured position and the head of the arrow is the best match. The arrows are focussed into the centre of the segments and into the centre of the detector. The blue arrows represent the interactions in ring one, while the red arrows represent those in ring two. b) The vectorial magnitude map, where the colour at each position represents the absolute length of the displacement between the two positions. The magnitudes are relatively similar and the mean displacement is 2.7mm.

and show that the maximum displacements are spurious points in the data. The minimum average displacement of 2.2mm occurs for interaction at a depth of 4.2mm. This may be the result of the increased sensitivity in the front ring due to the strongly varying electric field, which gives rise to large fluctuations in pulse shape for small changes in interaction position. In order to test the tilt of the detector a similar point-by-point comparison in depth is also required. However, the time scale required to run this simulation was beyond the scope of this work.

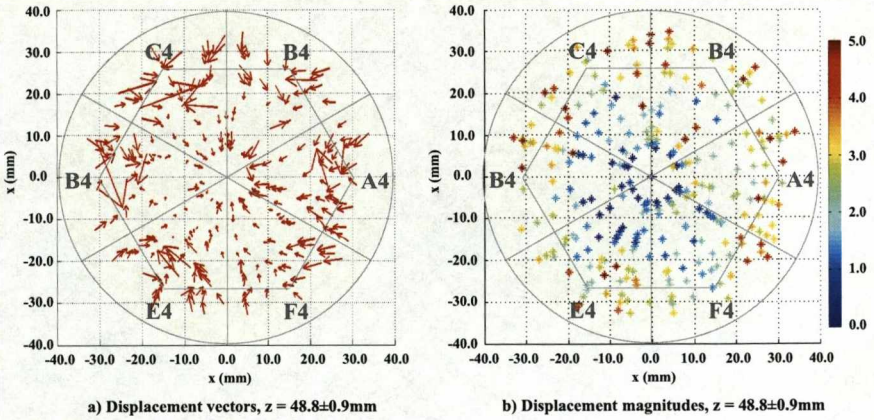

Figure 6.20: A figure showing the difference between the experimentally measured interaction positions and the site in the MGS basis that gives the best $<log_{10}\Delta s_{Tot}>$ match, for all interactions at a depth of 48.8±0.3 in the S002 crystal. a) The vectorial displacement map, where the start of the arrow is the measured position and the head of the arrow is the best match. The arrows are focussed into the centre of the segments and into the centre of the detector. b) The vectorial magnitude map, where the colour at each position represents the absolute length of the displacement between the two positions. The magnitudes are relatively similar and the mean displacement is 2.6mm.

Depth (mm)	Ring	Min Displacement (mm)	Max Displacement (mm)	<Displacement (mm)>
4.2±0.3	1	0.1±0.4	11.9±0.4	2.2±0.4
15.7±0.3	1	0.2±0.6	17.3±0.6	2.7±0.6
48.8±0.3	4	0.1±0.7	17.0±0.7	2.6±0.7

Table 6.4: A table showing the variation in the magnitude of the displacement vectors for the 4.2mm, 15.7mm and 48.8mm comparisons between the experimental pulses and the 1.0mm MGS basis.

6.4 S002 and S003 Experimental Pulse Shape Comparison

The AGATA array will be constructed from triple cluster cryostats containing three different shaped asymmetric hexaconical crystals. It is expected that three of each geometry, in single cryostats, will be scanned to test that their responses are consistent. To ensure that the data sets are comparable from detector to detector, it is important that the reproducibility of the scanning procedure is validated for the symmetric geometries, as symmetry arguments can be utilised to test the data. In this section, experimental pulse shapes from equivalent interaction positions in the S002 and S003 coincidence databases are compared. Two representative positions from the centre of a segment in ring three have been compared. *Figure 6.21* shows the pulse shape comparisons for the interaction segment, core and clockwise, anticlockwise, upper and lower image charges. For each plot, the S002 pulses are shown as solid lines and the S003 pulses as broken lines. The pulses for the interaction at *Position 1*, a 7mm radius, are coloured red. Whilst those for the interaction at *Position 2*, a 27mm radius, are coloured blue. The coordinates for the two interaction positions are x = *3.7±0.8*, y = *-5.7±0.8*, z = *31.2±0.3* and x = *13.9±0.8*, y = *-22.8±0.8*, z = *31.2±0.3* respectively. The similarity parameters calculated for this experimental pulse shape comparison, as defined in *Section 6.2.1*, are presented in *Table 6.5*. The S002 and S003 pulse shape responses are shown to agree well for all but the vertically adjacent image charges and the centre contact for the 27mm radius. The differences in vertically adjacent image charges may be the result of different levels of cross-talk in each detector. There is no clear explanation for the large discrepancy between the centre contact responses. The good agreement between the two data sets implies that the detectors respond in a similar manner and that the consecutive scans have been performed to a high precision.

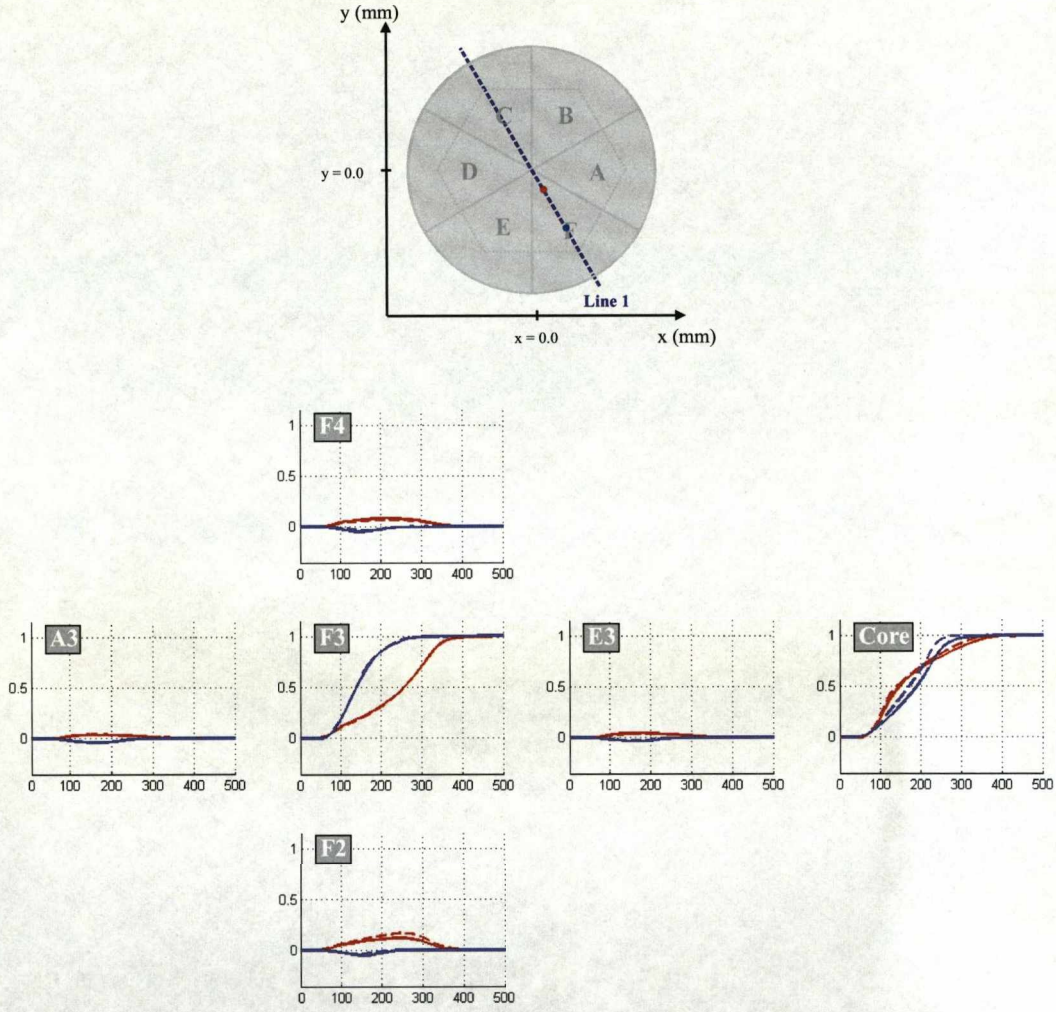

Figure 6.21: A figure showing the pulse shape comparison for two equivalent interaction positions in the S002 (shown with the solid lines) and S003 (shown with the broken lines) experimental coincidence data sets. The two interactions positions are at coordinates x = *3.7±0.8*, y = *-5.7±0.8*, z = *31.2±0.3* (Position 1 = red) and x = *13.9±0.8*, y = *-22.8±0.8*, z = *31.2±0.3* (Position 2 = blue). The data from the S002 detector is shown to be in good agreement with that from the S003 detector.

Channel	$\log_{10}\Delta s$, Position 1 (red)	$\log_{10}\Delta s$, Position 2 (blue)
Interaction segment	1.58±0.03 (F3)	1.07±0.03 (F3)
Centre contact	2.04±0.03 (C)	3.08±0.03 (C)
Clockwise image charge	1.82±0.03 (E3)	2.03±0.03 (E3)
Anticlockwise image charge	1.94±0.03 (A3)	2.20±0.03 (A3)
Upper image charge	2.46±0.03 (F4)	2.47±0.03 (F4)
Lower image charge	3.18±0.03 (F2)	2.89±0.03 (F2)
Arbitrary	2.13±0.03 (C3)	2.19±0.03 (C3)
<Total>	2.62±0.03	2.65±0.03

Table 6.5: A table showing the variation in the logarithm of the similarity parameter, for the example interactions presented in *Figure 6.21*. The agreement between the S002 and S003 data sets is best for the interaction segment and the laterally adjacent image charges.

6.5 S002 Detector Sensitivity

In this work the S002 prototype detector pulse shape response has been compared against a basis derived from MGS and a selection of interaction positions from the S003 experimental basis. However, a measure of the sensitivity of the detector has not yet been quantified. The sensitivity of the detector is determined by the ability to measure a difference in response for two closely spaced interaction positions. The standard metric for performing the sensitivity, S_{ij}^2, was presented in *Section 4.3.9* and is expressed as,

$$S_{ij}^2 = \frac{\Delta r_{ij}^2}{\Delta s_{ij}^2}, \tag{6.4}$$

where Δr_{ij}^2 is the distance between two interaction positions i and j, and Δs_{ij}^2 quantifies the difference of the signals, defined as,

$$\Delta s_{ij}^2 = \sum_{k=1}^{37} \sum_{t=t10}^{t90} \left[\frac{q_i^k(t) - q_j^k(t)}{\sqrt{2}\sigma^k} \right]^2, \tag{6.5}$$

where k is the channel number, and σ is a measure of the signal noise. A value of σ = 1keV was used for these comparisons as the average experimental pulses at each interaction position were summed from 100 events. Therefore a high sensitivity refers to a small value of S_{ij}^2. *Figures 6.22* and *Figures 6.23* show the calculated values of S_{ij}^2 for consecutive positions within sector F of the detector for coincidence line scan one and the 24mm azimuthal scan. Coincidence data were only collected for a relatively asymmetric and sparse number of interaction positions through out the S002 detector. Thus, the magnitude of the value of S_{ij}^2 calculated from each consecutive pair of positions is plotted at the radius or angle of the first position for each comparison. This method for plotting the data enables the relative separation of each pair of positions to be observed. In each figure, S_{ij}^2 has been calculated from the experimental (red asterisks) and MGS (blue asterisks) pulses for interactions at depths of 4.2±0.3mm and 48.8±03mm. Trend lines have been fitted to the experimental data to enable the reader to follow the distributions, shown as red solid lines. From *Figure 6.22* it can be seen that at both depths, the distributions calculated from the experimental and simulated data are in qualitative agreement and show minima of ~0.03mm at radii between 10mm and 12mm. Experimentally a separation of this order of magnitude is not

achievable on an event-by-event basis, however, this metric gives a consistent number with which to compare the pulse shape variation in different regions of the same detector and also in other detectors. For the 4.2mm interaction depth, the magnitude of the experimental sensitivity, relative to that from simulation, is generally larger (worse) at small radii but better at large radii. Thus implying there is a greater difference between the simulated pulse shapes at small radii, relative to those from experiment. For the 48.8mm depth, this difference at small radii can also be observed, however, both data sets are generally more consistent. The change in pulse shape response as a function of radial interaction position has the greatest effect on the shape of the centre and outer contact real charge pulses. The small magnitude of S_{ij}^2 of <0.45mm, shows how relatively small changes in the real charge pulse response can give rise to regions of high sensitivity (a small value of S_{ij}^2).

Figure 6.23 shows how S_{ij}^2 varies as a function of azimuthal angle for interactions at depths of 4.2±0.3mm, a), and 48.8±03mm, b). Data points are shown for a small section of the data that crosses sector F. At 4.8mm, the value of S_{ij}^2 is smallest at the segment boundaries due to the increased size of the image charges in the laterally adjacent segments. The fluctuation in sensitivity is large, as expected for the strongly varying electric field. At 48.8mm, the variation in S_{ij}^2 is relatively constant. At both depths the experimental and simulated data sets agree qualitatively, however, they are also offset from each other in terms of magnitude.

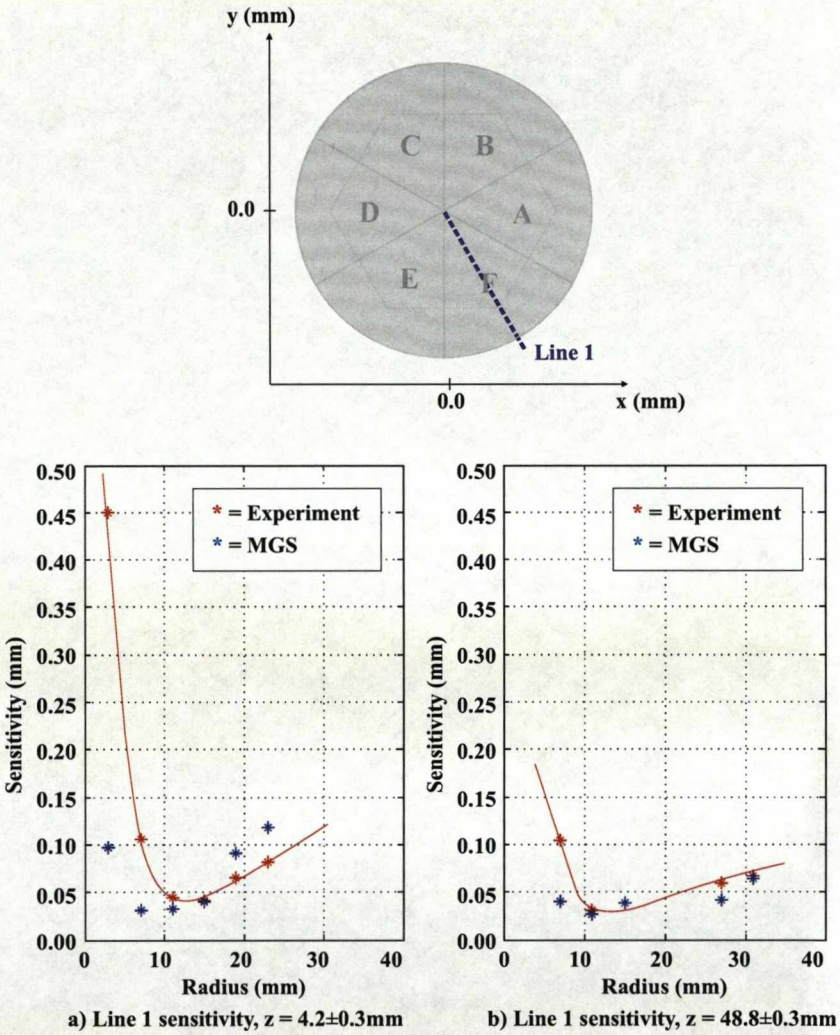

Figure 6.22: A figure showing the detector sensitivity, S_{ij}^2, for line scan one in the S002 detector. The sensitivity has been calculated from the experimental (red asterisks) and MGS (blue asterisks) pulses for interactions at depths of 4.2±0.3mm, a), and 48.8±03mm, b). The variation between experiment and simulation is shown to be qualitatively similar however the magnitudes are offset. S_{ij}^2 has a minimum of ~0.03mm at radii between 10mm and 12mm.

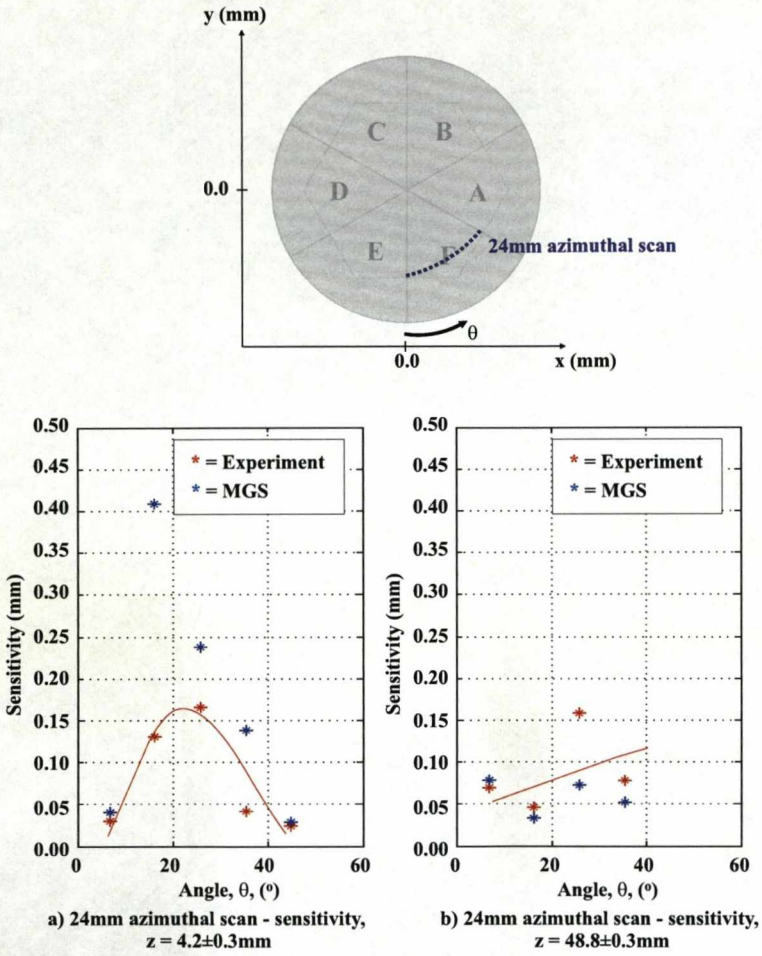

Figure 6.23: A figure showing the detector sensitivity, S^2_{ij}, for a section of the 24mm azimuthal scan in the S002 detector. The sensitivity has been calculated from the experimental (red asterisks) and MGS (blue asterisks) pulses for interactions at depths of 4.2±0.3mm, a), and 48.8±03mm, b). The variation between experiment and simulation is shown to be qualitatively similar however the magnitudes are offset. S^2_{ij} has a minimum of ~0.03mm at angles close to the segment boundaries in ring one.

Chapter 7

Conclusions and Discussion

The experimental and simulated results presented in this work have shown the methodology utilised to characterise AGATA symmetric prototype detectors. This characterisation has included initial testing of each detector, detailed scans with well defined spatial localisation of the gamma-ray interaction positions, full electric field simulations to enhance the understanding of the position dependent response, validation of this simulation with experimental data, a comparison of the experimental data sets collected with the S002 and S003 AGATA symmetric prototype detectors and quantification of how the position sensitivity varies in different regions of the symmetric prototype detector geometry.

7.1 Initial performance

Both the S002 and S003 detectors showed good energy resolution performance at both low and high energy. The mean FWHMs of the photo-peaks from both ^{241}Am (60keV) and ^{60}Co (1.3MeV) for each detector are displayed in *Table 7.1*. The S002 detector was shown to have superior high energy performance, but worse low energy performance than the S003 prototype detector. This was probably due to the different segment preamplifiers on each detector, GANIL for S002 and Milan for S003. The centre contact energy resolutions were systematically poorer than for the segments, however, this was due pile-up resulting from the much higher count rates on the core.

The main focus of this work was the analysis of data from the S002 detector. As such, the remaining sections of this conclusions and discussion chapter will refer mostly to this detector. The average RMS noise was measured to be 0.99mV and the average standard deviation of the baseline noise was ~4.7keV. The relative efficiency of the S002 detector was measured to be 73.5±2.5% at 1.3MeV, compared to 71.3% as specified by the manufacturer, Canberra Eurisys. The level of proportional cross-talk, determined from adding-back the energies of events that Compton scattered between segments, was calculated to be 0.11±0.05%. This is within the specifications supplied by Canberra (<0.1%). The angle of anisotropy, defined as the angle of the <100> fast axis relative to the x axis was validated as -14.9^o (previously measured by [Bru07]). In the specifications agreed between the AGATA collaboration and Canberra, the fast axis was required to be parallel to the x axis with an uncertainty of ±3^o. The measured value has been shown to be outside these error bars.

7.2 Validation of MGS

Experimental coincidence (single site interaction) data were collected for the S002 detector over an eight week period. Sets of average pulse shapes were generated for the 37 channels of the detector at each of 2490 well-defined interaction positions. The levels of derivative cross-talk were measured but could not be accounted for due to the lack of a global clock in the digital acquisition cards (GRT4 cards). The tilt and rotation of the crystal relative to the scanning table were measured and corrected. A depth minimisation was performed to correct for the systematic offset of the measured collimator positions relative to the true positions. However, this correction was impeded by not accounting for the derivative

Measurement	S002	S003
<FWHM$_{Seg}$ at 60keV >	1.10	1.00
<FWHM$_{Seg}$ at 1.3MeV>	1.96	2.02
FWHM$_{Core}$ at 60keV	1.24	1.51
FWHM$_{Core}$ at 1.3MeV	2.31	2.48

Table 7.1: A table summarising the S002 and S003 AGATA prototype detector analogue energy resolutions measured with ^{241}Am (60keV) and ^{60}Co (1.3MeV) sources.

cross-talk that distorts the pulse shapes. The uncertainties on the x and y interaction positions were calculated to be between $\pm$0.6mm and $\pm$1.2mm, depending on the depth of the interaction. The majority of this uncertainty arose due to the divergence of the gamma-ray beam resulting from the finite length of the collimator (120mm). The uncertainty in the depth of interaction was measured to be $\pm$0.3mm. The absolute experimental coordinates for each interaction position were then transformed into the MGS electric field simulation frame of reference and a corresponding set of calculated pulse shapes were generated. The simulated pulses were corrected for experimental factors including the preamplifier response function and the limited sampling and resolution of the 14-bit, 80MHz FADCs.

Following the generation of these databases, detailed pulse shape comparisons were performed throughout the detector. A similarity parameter, $log_{10}\Delta s$, was calculated at each position and plotted as a series of 2D surface maps to extract any trends observed in the data. A small magnitude of $log_{10}\Delta s$ of between two and three was deemed to show a good quantitative match between the experimental and simulated pulses. Several conclusions can be drawn from this analysis:

- *Centre contact real charge response* - The agreement was best for interactions at intermediate radii in the coaxial regions of the detector, where $log_{10}\Delta s$ was $<$2.5. For these interaction positions the experimental rise times are fastest and follow the fast rise times observed in the simulation. For the front ring the agreement was more complex and varied due to the complex electric field in the tapered hexagonal geometry.

- *Outer contact real charge response* - The agreement was generally good and also matched best in the coaxial regions of the detector at large radii where the outer contact pulse shape has a fast rise to 30% of its maximum amplitude. For these interaction positions the magnitude of the similarity parameter, $log_{10}\Delta s$, was $\sim$2.5. As for the core, the pulse shapes followed the fast rise times observed in MGS. However, there was also good agreement at small radii, close to the core, where the drift is entirely dominated by the *hole* transport. In the front ring the distribution was varied and no clear conclusions could be drawn. For both the centre and outer contact real charge pulses, the greatest contribution to the similarity parameter was from the

samples for the final 10% of the rise of the pulse.

- *Outer contact lateral image charge response* - The agreement between the experimental and simulated image charge response for the segments laterally adjacent to the interaction segment was very good and improved as a function of increasing signal magnitude. This was due to the more precise time alignment for the signals with a larger signal to noise ratio, when the pulse shape database was generated in software. Manual time alignment was required due to the lack of a global clock in the acquisition cards.

- *Outer contact vertical image charge response* - The agreement between the experimental and simulated image charge response for the segments vertically adjacent to the interaction segment was reasonable. However, the general trend was worse than for the laterally adjacent image charges. This was primarily due to the levels of cross-talk that were not accounted for in the database and that also affected the precision of the depth minimisation.

- The total mean similarity, $<\Delta s>$, was calculated at each interaction position. This figure of merit quantified the total difference between the experimental and simulated pulses when considering the responses from the interaction segment, core, and clockwise, anticlockwise upper and lower image charges. The distributions for each of the nine collimation depths were shown to be azimuthally symmetric but vary as a function of radius. At a depth of 4.2mm the agreement was shown to be poorest for radii <10mm. The magnitude of $log_{10}\Delta s$ varied between 3.0 and 4.5. In the coaxial regions of the detector the distributions were shown to be relatively uniform with values of $log_{10}\Delta s$ of $\sim$3.0 and a ring of interaction positions that showed poorer agreement at between $\sim$18mm and $\sim$25mm, dependent on the depth of interaction. The figures appeared to show some average trend that shared the attributes of those for the upper and lower image charge responses. This pattern may also be the result of discrepancies in the charge carrier mobilities. Further investigation with time aligned data is required in order to deconvolve these effects.

In general the agreement between MGS and the experimental data was very good. However, several key points must be raised.

- For future accurate validation of the simulated data it is imperative that the acquisition system has a high frequency global clock to ensure accurate time alignment of the data.
- The effects of derivative cross-talk cannot be underestimated and must be corrected for to a high degree of precision to truly extract the deviations between the simulated and experimental data sets.
- The simulation must incorporate the inter-segment gaps in order that the magnitudes of the weighting fields be correctly calculated. The absence of these gaps in the MGS simulation may have lead to an overestimate of the magnitude of the weighting field that extends into the neighbouring segments. This would result in image charges with a larger than observed magnitude.

7.3 S002 Iterative Basis Matching

In the previous sections of this work, the pulse shape comparisons were performed with an MGS basis generated from the precise interaction positions determined from the experimental scan. In order to investigate the geometric corrections applied to the data and also the calibration in absolute position localisation with respect to a basis data set, each experimental interaction position has been compared to a new MGS basis generated on a 1.0mm $\times$ 1.0mm grid at each optimised collimation depth in the S002 detector geometry. A set of 37 pulses was stored at every 1.0mm grid point in x and y. The pulse shapes from the centre contact, interaction segment and clockwise, anticlockwise, upper and lower image charge neighbours for each experimental position were compared to those at every MGS basis site. The interaction site that gave the lowest mean similarity, $<log_{10}\Delta s>$, for the six pulse shape comparisons, was stored.

For each of the three depths presented, a systematic trend of a displacement towards the centre of the segment and also the centre of the detector was observed. Each of the distributions were symmetric, thus validating the 0.9^o rotation applied to account for the

offset relative to the scanning table. The magnitudes of the displacements were shown to be relatively consistent with mean values of ~2.5mm. These displacements are small in magnitude and show that the MGS database has been calibrated to within a small uncertainty at each interaction position. The shift towards the centre of the detector is believed to be an effect of derivative cross-talk which makes the rise time of the pulses longer. As the similarity comparison was calculated from five outer contact pulse shapes (the interaction segment plus the four image charges), the minimisation against all possible interaction positions tended towards a general convergence biased to the centre of the detector. It is also possible that these observations could be explained if the charge carrier mobilities calculated in the simulation were incorrect.

7.4 S002 and S003 scan comparison

The AGATA array will be constructed from triple cluster cryostats cotaining three different shaped asymmetric hexaconical crystals. It is expected that three of each geometry, in single cryostats, will be scanned to test that their responses are consistent. To ensure that the data sets are comparable from detector to detector, it was important that the reproducibility of the scanning procedure was validated for the symmetric geometries, as symmetry arguments could be utilised to test the data. Two representative positions from the centre of a segment in ring three have been compared. The S002 and S003 pulse shape responses have been shown to agree well for all but the vertically adjacent image charges and the centre contact for the interaction at a large radius. The differences in vertically adjacent image charges may be the result of different levels of cross-talk in each detector. There is no clear explaination for the large discrepency between the centre contact responses. The good agreement between the two data sets implies that the detectors respond in a similar manner and that the consecutive scans have been performed to a high precision.

7.5 S002 Detector Sensitivity

The sensitivity of the detector, the ability to measure a difference in response for two closely spaced interaction positions, has been measured for the S002 detector. Values of the sensitivity, S^2_{ij}, were calculated for consecutive positions within sector F of the detector for

coincidence line scan one and the 24mm azimuthal scan respectivley. For each scan, S_{ij}^2 was calculated for the experimental and MGS pulses for interactions at depths of 4.2±0.3mm and 48.8±03mm. It has been observed that for the scan line through the middle of sector F of the detector, at constant angle and depth, the distributions calculated from the experimental and simulated data are in qualitative agreement and show minima of ~0.03mm at radii between 10mm and 12mm. Although this magnitude of separation is not achievable on an event-by-event basis, it gave a consistent number with which to compare the pulse shape variation in different regions of the same detector. For the azimuthal scan line S_{ij}^2 was shown to be smallest at the segment boundaries, with a magnitude of ~0.03mm, due to the increased size of the image charges in the laterally adjacent segments. The fluctuation in sensitivity was greatest in the front ring, due to the strongly varying electric field distribution. The experimental and simulated data sets were shown to agree qualitatively.

7.6 Future developments

The first asymmetric prototype detector (C001) arrived in Liverpool at the end of February 2008. The scanning procedure outlined in this doccument will be followed in order to validate the detectors performance relative to the symmetric prototype detectors. To improve the quality of the scanning procedure, collimated ^{241}Am data will be collected for 1mm steps across the entire outer surface of the detector. This will allow detailed cross-talk analysis as well as an investigation into the transport properties of the asymmetric crystal. To ensure accurate time alignment of the data, a clock pulse will be fed into one channel of each of the GRT cards. Thus, a full cross-talk correction will be performed. MGS has been shown to reproduce well the experimentally observed pulse shape response. Future measurements will ensure its continued development so that the software becomes viable for producing a full basis of simulated pulse shapes for on-line pulse shape analysis.

Appendix A

Detector Data Sheets

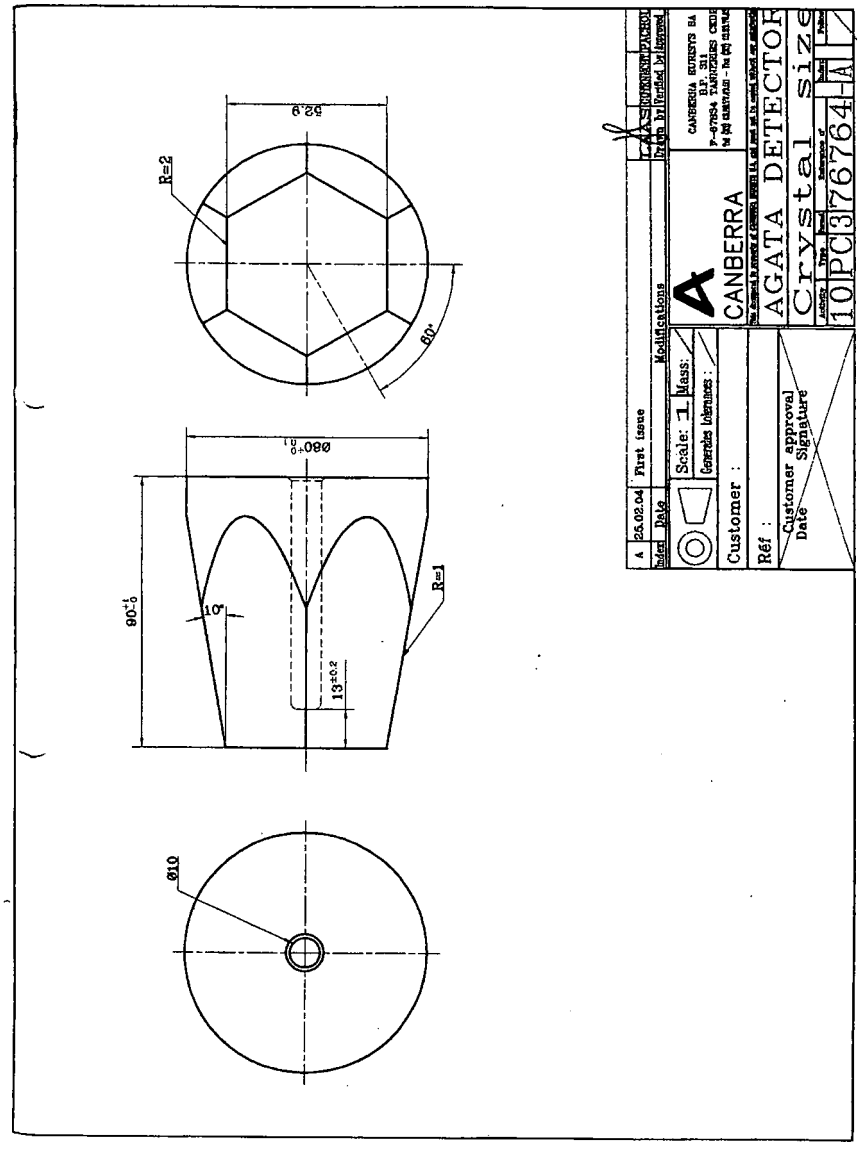

Figure A.1: Canberra Eurisys technical drawing of the S002 AGATA prototype crystal with tolerances.

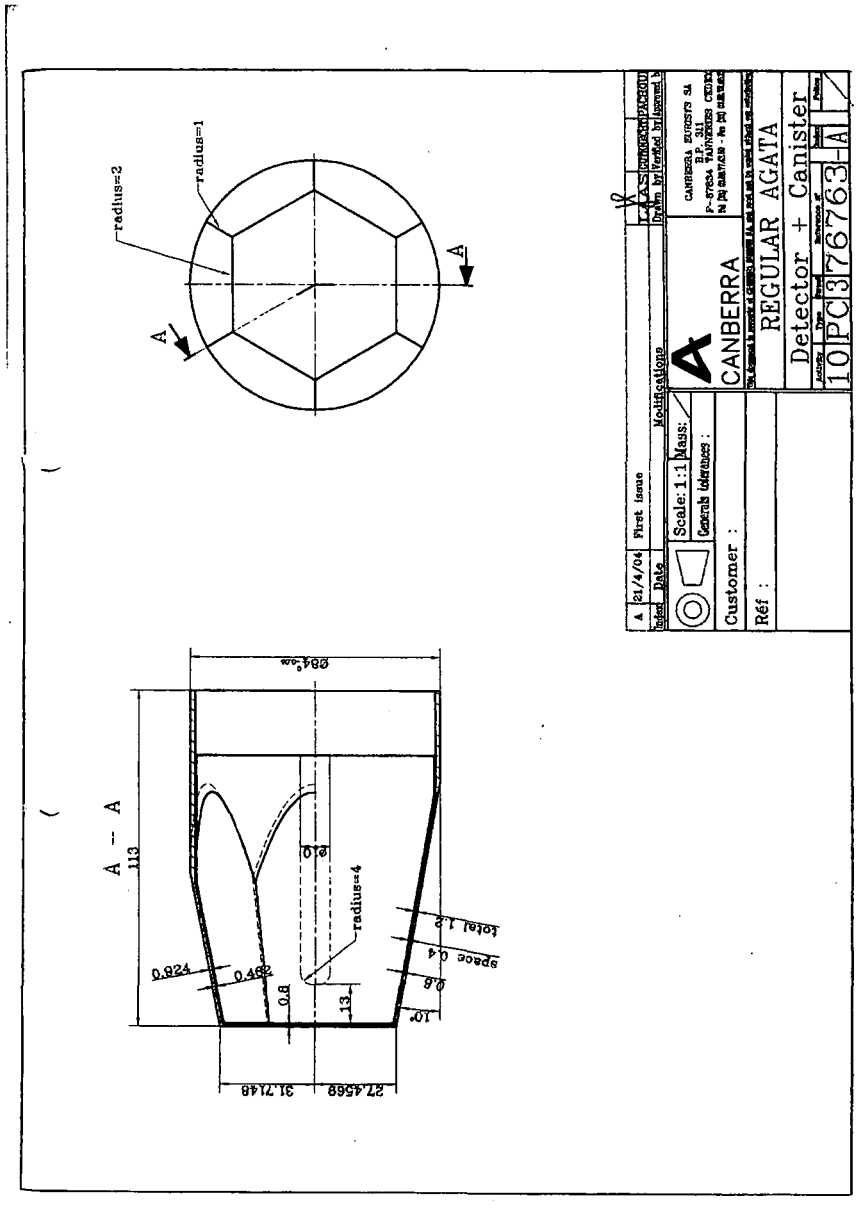

Figure A.2: Canberra Eurisys technical drawing of the S002 AGATA prototype encapsulated crystal with tolerances.

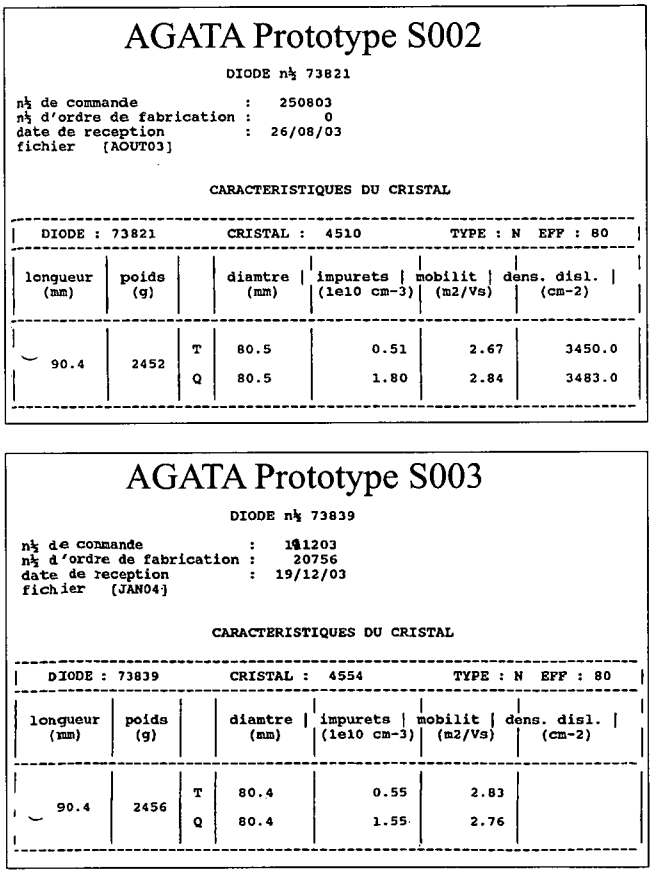

AGATA Prototype S002

DIODE n½ 73821

n½ de commande : 250803
n½ d'ordre de fabrication : 0
date de reception : 26/08/03
fichier [AOUT03]

CARACTERISTIQUES DU CRISTAL

DIODE : 73821 CRISTAL : 4510 TYPE : N EFF : 80

longueur (mm)	poids (g)		diamtre (mm)	impurets (1e10 cm-3)	mobilit (m2/Vs)	dens. disl. (cm-2)
90.4	2452	T	80.5	0.51	2.67	3450.0
		Q	80.5	1.80	2.84	3483.0

AGATA Prototype S003

DIODE n½ 73839

n½ de commande : 1[illegible]1203
n½ d'ordre de fabrication : 20756
date de reception : 19/12/03
fichier [JAN04]

CARACTERISTIQUES DU CRISTAL

DIODE : 73839 CRISTAL : 4554 TYPE : N EFF : 80

longueur (mm)	poids (g)		diamtre (mm)	impurets (1e10 cm-3)	mobilit (m2/Vs)	dens. disl. (cm-2)
90.4	2456	T	80.4	0.55	2.83	
		Q	80.4	1.55	2.76	

Figure A.3: Table showing Canberra Eurisys impurity concentration measurements for the S002 and S003 symmetric AGATA prototype detectors.

AGATA Prototype S002

SPECIFICATIONS SHEET OF REGULAR AGATA DETECTOR			
CANISTER N° 002		CRISTAL N° 73821	
FULL VOLUME PERFORMANCES			GARANTEED SPECIFICATIONS
OPERATING HIGH VOLTAGE (POSITIVE)	+5000 V / 4µs		
Fwhm at 1.33 meV (^{60}Co)	2.07		< 2.35 keV
Efficiency	71.3%		
Fwtm/Fwhm at ^{60}Co	1.82		< 2
Peak / Compton	72		
Fwhm at 60 keV (^{241}Am)	1.18		< 1.35
OUTER CONTACTS PERFORMANCES			< 1.2 keV at ^{241}Am < 2.1 keV at ^{60}Co

		1	2	3	4	5	6
α	60 keV	0.92	0.92	0.99	1.02	0.96	0.90
	1.33 MeV	2.10	2.05	2.12	1.99		
β	60 keV	1.08	1.20	0.92	0.84	0.94	1.02
	1.33 MeV	2.00	2.07	1.88	1.84	2.15	
γ	60 keV	0.87	0.87	0.84	0.87	1.02	0.99
	1.33 MeV				1.89	1.96	
δ	60 keV	0.97	0.93	0.97	0.94	0.98	0.91
	1.33 MeV						
ε	60 keV	0.91	0.95	0.91	1.02	0.99	0.89
	1.33 MeV						
φ	60 keV	0.90	0.94	0.98	0.96	1.06	0.93
	1.33 MeV						

AGATA Prototype S003

SPECIFICATIONS SHEET OF REGULAR AGATA DETECTOR			
CANISTER N° A 003		CRISTAL N° : 73839	
FULL VOLUME PERFORMANCES			GARANTEED SPECIFICATIONS
OPERATING HIGH VOLTAGE (POSITIVE)	+4000 V / 6µs		
Fwhm at 1.33 MeV (^{60}Co)	2.13		< 2.35 keV
Efficiency	70 %		
Fwtm/Fwhm at ^{60}Co	1.90		< 2
Peak / Compton	71		
Fwhm at 122 keV (^{57}Co)	1.10		< 1.35
OUTER CONTACTS PERFORMANCES	*At ^{241}Am* *Max value < 1.40 keV* *Mean value < 1.20*		*At ^{60}Co* *Max value : < 2.30 keV* *Mean value < 2.10 keV*

		1	2	3	4	5	6
α	60 keV	0.91	0.86	0.88	0.79	0.86	0.82
	1.33 MeV			2.05			
β	60 keV	0.85	0.93	0.90	0.83	0.85	0.91
	1.33 MeV			1.88	1.87		
γ	60 keV	0.90	0.83	0.91	0.83	0.84	0.86
	1.33 MeV	1.95					
δ	60 keV	0.90	0.91	0.93	0.91	0.88	0.81
	1.33 MeV			2.10			
ε	60 keV	0.92	0.92	0.99	0.85	1.05	0.89
	1.33 MeV		2.05				
φ	60 keV	0.98	0.86	0.94	0.85	0.94	0.93
	1.33 MeV					2.12	1.91

Figure A.4: Table showing Canberra Eurisys energy resolution measurements for the S002 and S003 symmetric AGATA prototype detectors.

Appendix B

Energy Measurements

Three techniques have been used to record the event-by-event energy deposited in the S002 and S003 AGATA symmetric prototype detectors, analogue sampling, Moving Window Deconvolution (MWD) and baseline difference. Each of these techniques is discussed in this section.

B.1 Analogue Energy Extraction

Initial testing of each AGATA symmetric prototype detector was performed with analogue electronics to verify the manufacturers resolution specifications. This involved connecting each channel (one at a time) to a spectroscopy amplifier, measuring the pulse height with an 8092 channel (8k) ADC and recording the resulting spectra with Multi-Channel Analyser (MCA) software. The steps for recording the analogue energy spectra are described below. Special care was taken when setting up the system, so as to ensure that HV supply would not shut down.

1. Test that the NIM crate supplies +/- 6V, +/-12V and +/-24V to all rails with an appropriate multimeter.

2. Check that the Ortec 659 High Voltage (HV) supply gives a positive polarity output. The shutdown jumper was set to *bypass* and the supply was switched off and set at zero volts before being inserted into the NIM crate.

3. Insert the Low Voltage (LV) distribution box into the NIM crate. The voltage on each

pin was then tested with an appropriate multimeter and resistor. The nine-pin cable supplied +/- 6V for the back end of the pre-amps and +/-12V for the front-end.

4. Insert the the centre contact CWC converter box, one segment CWC converter box and an Ortec 671 spectroscopy amplifier into the NIM crate.
5. Connect LDVS cables between the detector and corresponding CWC boxs.
6. Connect the HV and LV cables between the detector and corresponding modules.
7. Connect the CWC outputs for the centre contact and a single segment to an oscilloscope.
8. Place a source under the detector.
9. Switch the NIM crate power supply on.
10. Check that the correct pre-amplifier signals can be seen on both channels of the oscilloscope.
11. Switch the HV unit on but leave the voltage at zero. Press, hold and release the reset button.
12. Increase the high voltage to ~50V. The HV was then increased in 50V increments until a bias of ~2000V was reached. At which point the detector was left for ~10 minutes to stabilise. The HV was then increased in 50V increments until the recommended bias was applied.
13. Leave the detector for ~1 hour to stabilise.
14. Connect the centre contact CWC output to the Ortec 671 spectroscopy amplifier. A shaping time of 6μs and an appropriate gain were set.
15. Perform pole-zero correction.
16. Connect the amplifier output to 8k ADC.
17. Record spectrum with Ortec Maestro MCA software.
18. Repeat steps 14 to 16, one channel at a time for each of the 36 segments.

The analogue energy resolution results at 1.3Mev and 60keV for the S002 and S003 detectors are presented in *Tables B.1* and *B.2* and *Tables B.3* and *B.4* respectively. Resolutions measured at 1.3MeV with the S002 detector were systematically better than those measured with the S003 detector. The opposite is true for the resolutions measured at 60keV The S002 and S003 detectors had different segment preamplifiers and these results demonstrate the difference in their performance.

Chan No.	Chan Label	S002 FWHM (keV)	S003 FWHM (keV)
1	A1	1.91 (0.19)	2.00 (0.05)
2	A2	1.95 (0.02)	2.05 (0.03)
3	A3	1.88 (0.05)	1.94 (0.08)
4	A4	1.97 (0.04)	1.99 (0.09)
5	A5	1.97 (0.04)	2.01 (0.06)
6	A6	2.04 (0.05)	1.81 (0.11)
7	B1	2.00 (0.03)	1.95 (0.04)
8	B2	1.89 (0.02)	2.02 (0.04)
9	B3	1.91 (0.07)	1.97 (0.04)
10	B4	1.92 (0.03)	2.09 (0.06)
11	B5	1.89 (0.05)	1.95 (0.12)
12	B6	1.94 (0.04)	2.08 (0.04)
13	C1	2.00 (0.16)	2.08 (0.13)
14	C2	1.97 (0.03)	2.01 (0.04)
15	C3	2.13 (0.03)	1.99 (0.06)
16	C4	1.85 (0.05)	2.13 (0.05)
17	C5	2.03 (0.07)	2.03 (0.05)
18	C6	2.07 (0.04)	2.07 (0.05)
19	D1	1.89 (0.07)	2.03 (0.06)
20	D2	1.94 (0.03)	1.85 (0.10)

Table B.1: Table to show the analogue energy resolution measurements recorded with ^{6}0Co for the S002 and S003 AGATA symmetric prototype detectors. The S002 detector performance was best, with systematically smaller FWHMs than the S003 detector.

Chan No.	Chan Label	S002 FWHM (keV)	S003 FWHM (keV)
21	D3	1.97 (0.03)	1.85 (0.07)
22	D4	1.78 (0.05)	2.06 (0.06)
23	D5	2.07 (0.03)	1.98 (0.08)
24	D6	1.89 (0.05)	2.08 (0.04)
25	E1	1.88 (0.04)	2.11 (0.07)
26	E2	1.84 (0.03)	2.05 (0.03)
27	E3	1.83 (0.03)	1.97 (0.06)
28	E4	1.97 (0.03)	1.98 (0.07)
29	E5	2.03 (0.03)	2.01 (0.04)
30	E6	1.97 (0.04)	2.02 (0.06)
31	F1	2.05 (0.04)	2.09 (0.08)
32	F2	1.88 (0.04)	1.91 (0.20)
33	F3	1.95 (0.04)	2.22 (0.03)
34	F4	2.03 (0.03)	2.33 (0.05)
35	F5	2.13 (0.02)	2.05 (0.13)
36	F6	1.99 (0.05)	2.01 (0.08)
37	Core	2.31 (0.04)	2.48 (0.05)

Table B.2: Table to show the analogue energy resolution measurements recorded with $^{6}0$Co for the S002 and S003 AGATA symmetric prototype detectors. The S002 detector performance was best, with systematically smaller FWHMs than the S003 detector.

B.2 Moving Window Deconvolution

The preamplifier output is described by a convolution between the charge distribution function and the preamplifier impulse response. The Moving Window Deconvolution (MWD) algorithm [Geo93], implemented in the FPGAs of the GRT cards [Laz03], deconvolves these distributions allowing a true measurement of the total charge. The algorithm effectively performs the moving average of a differential deconvolution, the steps of which are shown schematically in *Figures B.1a* and *B.1b*. The height of the resulting trapezoid is proportional to the magnitude of the charge pulse. Thus, by sampling the flat top of the trapezoid, the energy of the interaction can be determned. It should be noted that accuracy of the measurement depends on the gradient of the flat top, which is in turn determined by

Chan No.	Chan Label	S002 FWHM (keV)	S003 FWHM (keV)
1	A1	1.18 (0.01)	1.09 (0.01)
2	A2	0.99 (0.03)	1.01 (0.01)
3	A3	1.08 (0.07)	1.05 (0.01)
4	A4	1.16 (0.02)	1.06 (0.01)
5	A5	1.17 (0.01)	1.06 (0.01)
6	A6	1.06 (0.02)	0.96 (0.01)
7	B1	1.11 (0.01)	0.99 (0.01)
8	B2	1.06 (0.02)	0.94 (0.02)
9	B3	1.10 (0.01)	0.94 (0.01)
10	B4	1.13 (0.02)	1.00 (0.01)
11	B5	1.14 (0.02)	0.95 (0.01)
12	B6	1.07 (0.03)	0.92 (0.02)
13	C1	1.11 (0.02)	1.08 (0.01)
14	C2	1.07 (0.02)	0.98 (0.01)
15	C3	1.10 (0.01)	1.04 (0.01)
16	C4	1.17 (0.02)	1.05 (0.01)
17	C5	1.22 (0.02)	1.08 (0.02)
18	C6	1.18 (0.02)	0.96 (0.01)
19	D1	1.14 (0.07)	1.00 (0.01)
20	D2	1.06 (0.03)	0.96 (0.01)

Table B.3: Table to show the analogue energy resolution measurements recorded with $^{2}41$Am for the S002 and S003 AGATA symmetric prototype detectors. The S003 detector performance was best, with systematically smaller FWHMs than the S002 detector.

the correction for the preamplifier decay constant.

The implementation of this algorithm in the GRT cards is controlled by ten user specified parameters. The optimum values for these parameters were deduced from a series of systematic measurements. Initial analysis of the data gave rise to unexpected vales, however it was later established that there were several bugs in the implementation of the VHDL code. In order to compensate for this, the values that yielded the best results were utilised. The ten parameters, along with their optimum values are presented in *Table B.5*. A fully functioning version of the MWD algorithm would have provided results comparable to those

Chan No.	Chan Label	S002 FWHM (keV)	S003 FWHM (keV)
21	D3	1.07 (0.02)	1.01 (0.01)
22	D4	1.08 (0.03)	1.00 (0.01)
23	D5	1.13 (0.03)	1.03 (0.01)
24	D6	1.09 (0.01)	0.97 (0.01)
25	E1	1.11 (0.02)	1.03 (0.01)
26	E2	1.02 (0.02)	0.96 (0.01)
27	E3	1.06 (0.02)	0.99 (0.01)
28	E4	1.10 (0.01)	0.97 (0.01)
29	E5	1.10 (0.03)	1.01 (0.01)
30	E6	1.12 (0.03)	0.91 (0.01)
31	F1	1.18 (0.04)	1.08 (0.01)
32	F2	1.03 (0.02)	0.99 (0.01)
33	F3	1.07 (0.05)	1.06 (0.01)
34	F4	1.08 (0.02)	1.11 (0.01)
35	F5	1.13 (0.02)	1.05 (0.01)
36	F6	1.06 (0.02)	0.89 (0.01)
37	Core	1.24 (0.02)	1.51 (0.01)

Table B.4: Table to show the analogue energy resolution measurements recorded with $^{2}41$Am for the S002 and S003 AGATA symmetric prototype detectors. The S003 detector performance was best, with systematically smaller FWHMs than the S002 detector.

presented in *Tables B.1* and *B.2*. However due to the faulty algorithm, the digitally acquired energy resolution results were ~0.3keV worse than the analogue variants. For completeness, front-face singles scan energy spectra from the 36 segments of the S002 prototype detector are presented in *Figure B.2*.

B.3 Baseline Difference

The principle of the baseline difference calulation is similar to, however more crude than, MWD. It is effectively the subtraction of the baseline before the leading edge, from the average decay value soon after the maximum pulse height is reached. This calculation takes no account of the time constant of the decay and as such, the variance of the difference is

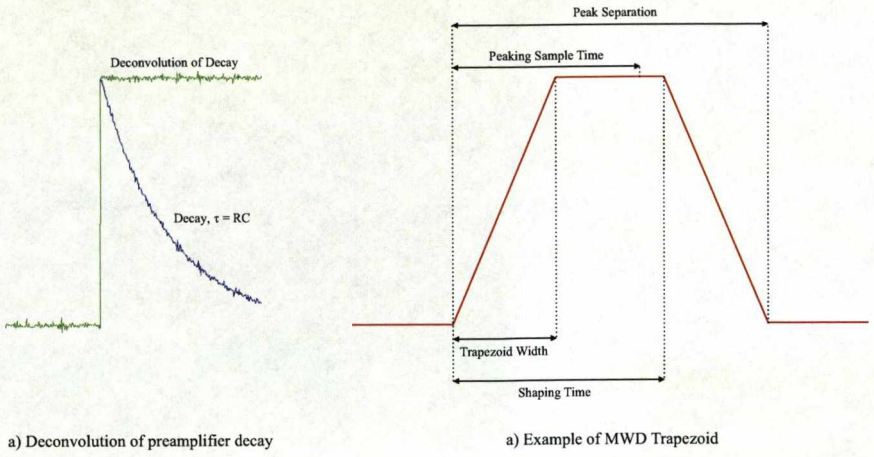

Figure B.1: A schematic representation of the two stages of the Moving Window Deconvolution (MWD) calculation. a) An example of the differential deconvolution of the charge distribution function from the preamplifier impulse response. b) An example of the trapezoidal function that results from performing a moving average of a).

Parameter	Value
Clock frequency	80.0MHz
Decimation factor	4.0
Shaping time	8.0μs
Trapezoid width	5.5μs
Peak separation	12.0μs
Decay time constant	50.0μs
Peak sample time	7.8μs
Baseline update time	2.0μs
Baseline average	4.0μs

Table B.5: Moving Window Deconvolution (MWD) parameters. The values for the parameters were determined from a series of experimental measurements.

greater than that of the MWD calculation. Thus resulting in a poorer energy resolution.

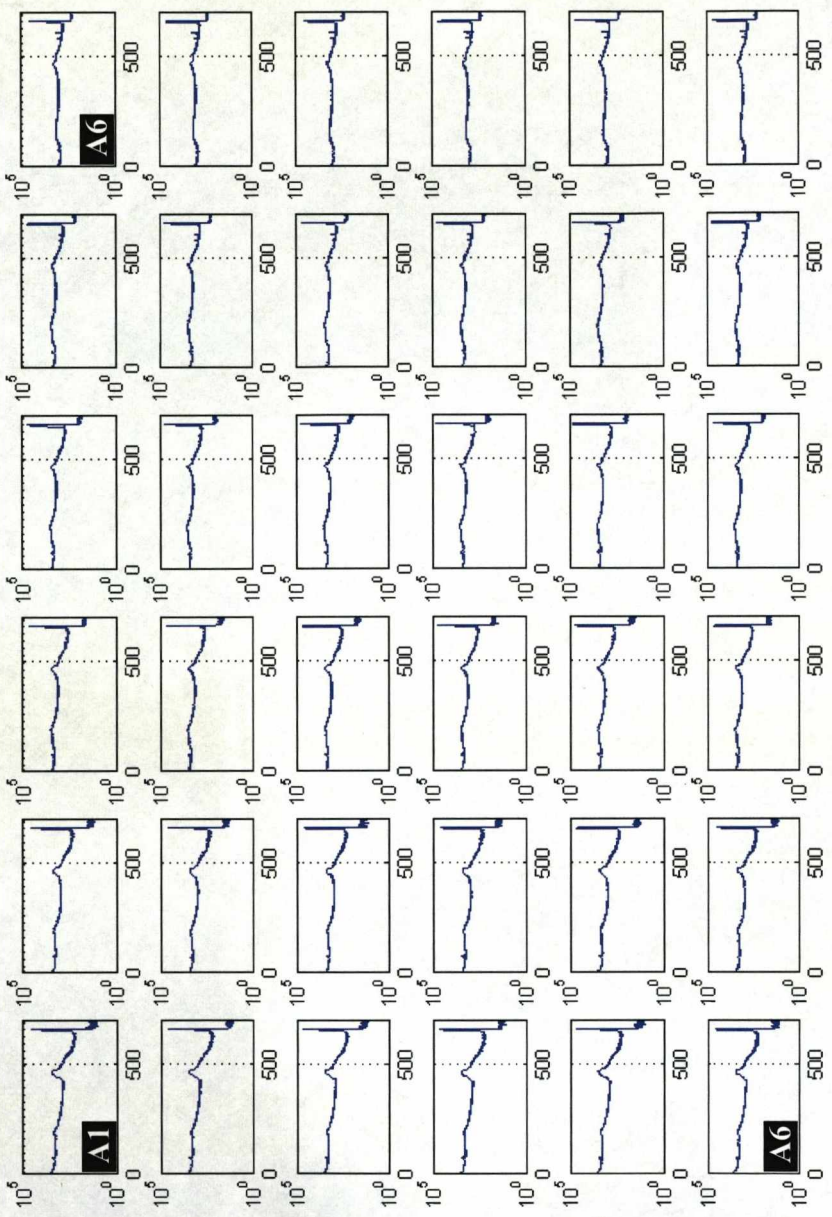

Figure B.2: Energy spectra for the 36 outer contacts from the ^{137}Cs (662keV) AGATA S002 singles scan.

Appendix C

Evolution of the MGS AGATA Detector Simulation

The pulse shape response calculated by the electric field simulation code MGS was investigated for sample positions in the S002 AGATA prototype detector geometry. This initial investigation was carried out in order to debug the software before a full validation against experimental data could be undertaken. The problems encountered and the solutions rendered are discussed in this appendix.

C.1 Simulation of the AGATA Geometry

The user specified input parameters entered for the initial simulation are presented in *Table C.1.* The values specified are shown schematically in *Figure C.1.* The isolant refers to the passivation layer at the back of the crystal. Passivation of the back surface of the crystal limits the surface leakage currents resulting in lower detector noise and improved energy resolution [Ryb01]. However the passivated surface can also distort the internal electric field lines [Hul95], thus the passivation should be included in the simulation in order to reproduce the experimentally observed pulse shape response.

Figure C.2 shows the electric potential surface map calculated for the parameters specified in *Table C.1.* The electric field vectors $\vec{E}$ are perpendicular to the electric potential surfaces as,

Parameter	S002 Value
Grid size	1mm
Inner contact voltage	5000V
Outer contact voltage	0V
Impurity concentration (front)	$1.8\text{x}10^{10}\text{cm}^{-3}$
Impurity concentration (back)	$5.1\text{x}10^{9}\text{cm}^{-3}$
Temperature	88K
Forward spacing	1mm
Back spacing	10mm
Lateral spacing	1mm
Distance to cathode	13mm
Anode radius	5mm
Length of layers	8:13:15:18:18:18
Consider isolant	yes
Isolant thickness	1mm
Isolant impurity concentration	$5.1\text{x}10^{9}\text{cm}^{-3}$

Table C.1: MGS input parameters for simulation of the S002 AGATA prototype detector.

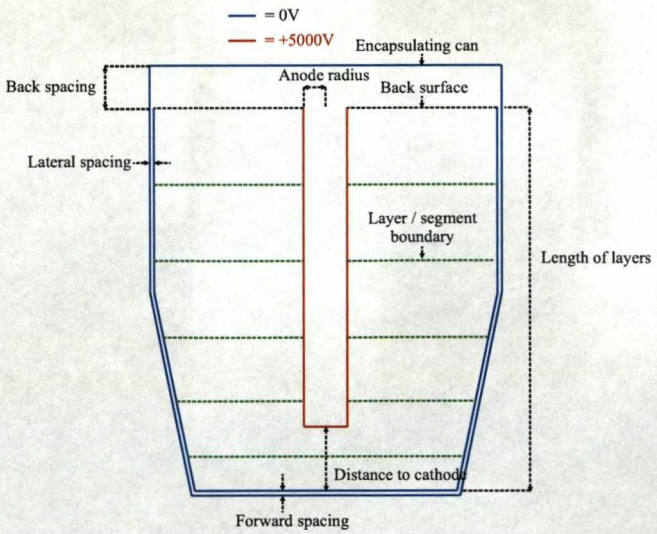

Figure C.1: A schematic representation of the MGS geometry specifications described in *Table C.1.* The surfaces coloured red are held at +5000V, where as those coloured blue are held at ground.

$$dV = -\vec{E} \cdot \vec{dl} = 0, \tag{C.1}$$

where dV is the change in potential along a line $\vec{dl}$. The potnetial surfaces for the bulk region should lie approximately parallel to the bore hole. Therefore, the electric field vectors and hence the charge carrier drift velocity vectors enable the electron and *hole* to drift linearly to the contacts. The distorted potential presented shows a large warped region surrounding the anode at depths between 55mm and 85mm. This region occurs due to the narrow 10mm spacing between the back of the crystal and the back of the aluminium encapsulation maintained at 0V. The charge carrier drift velocities observed in this region are of the order of $<2\text{x}10^6\text{cms}^{-1}$, as opposed to $1\text{x}10^6\text{cms}^{-1}$ in the surrounding volume. In order to demonstrate the effects this region has on the drift path of the charge carriers, the trajectories from four depths in the detector are displayed. At a depth of 55.0mm, *Figure C.2b*, the potential is only slightly distorted and the electron (red) and *hole* (blue) drift paths are as expected in the bulk region. However at depths of 65.0mm, 67.0mm and 85.0mm, the electron drift paths are shown to deviate wildly from that in *Figure C.2b*. For the interaction at 85.0mm, a further effect of the termination of the *hole* trajectory on the back surface of the detector is also demonstrated. Although this further effect is expected in the back region, due to the termination of the potential surfaces, the potential is far more distorted than would typically be oberved.

Figures C.3a to *C.3d* show the MGS calculated centre (red) and outer (blue) contact responses for the interactions described above. The pulses terminate following complete charge collection and the pulse heights at this point should reach unity. The deviations in electron trajectories for the interactions at depths of 65.0mm, 67.0mm and 85.0mm are shown to result in unphysical charge collection times of >800ns and the core pulse heights not reaching their maxima. The termination of the *hole* trjectory on the passivated back surface, for the interaction at 85.0mm, also results in the outer contact charge pulse reaching only 20% of its maximum amplitude. In order to check the effect of the isolant on the electric potential, the simulation was re-run without any passivation. It was found that the the lack of the presence of passivation alleviated the compression of the potential surfaces resulting in less deviation of the electron trajectories as they approached the central anode.

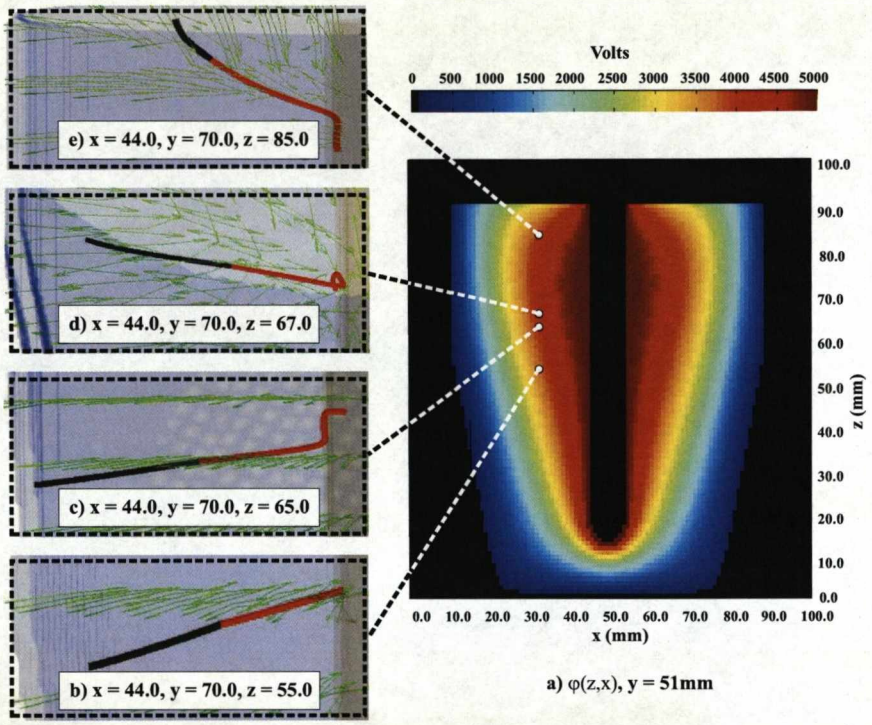

Figure C.2: a) A plot showing the MGS calculated potential surface map for the S002 AGATA symmetric prototype detector. The user supplied input parameters are displayed in *Table C.1.* The distorted potential presented shows a large warped region surrounding the anode at depths between 55mm and 85mm. b) to d) show the electron (red) and *hole* (blue) trjectories for sample interaction positions at depths of 55.0mm 65.0mm, 67.0mm and 85.0mm respectively. The influence of this warped potential on the electron trajectories, for the 65.0mm, 67.0mm and 85.0mm interactions, is shown by the deviations from their intended paths.

The complex geometry and high fold segmentation of the AGATA prototype detector also results in charge carrier trajectory complications at the segment boundaries. The definition of a tapered hexaconical crystal with azimuthal sementation on a cubic grid, results in segmentaion lines that intersect neighbouring grid points. Thus segment boundaries have an associated uncertainty and a complex series of interpolation steps is required to determine the shapes of the pulses on the outer contact electrodes as the charges migrate through the crystal. These effects are shown in *Figure C.4* for interactions at 331.0^o, 331.5^o, 332.0^o and 332.5^o, where the depth and radius of interaction were kept constant. The core pulses

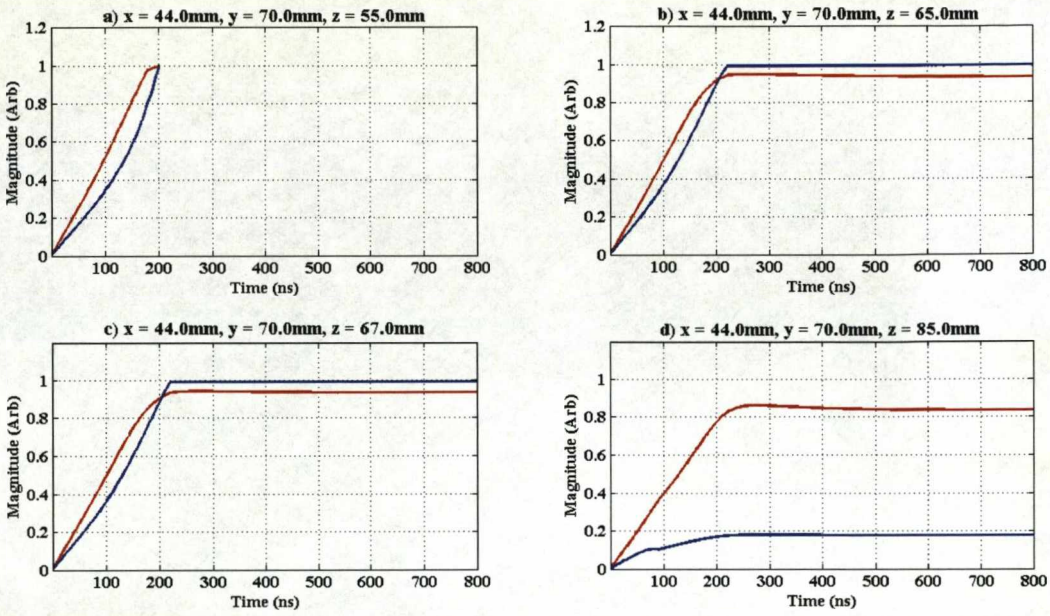

Figure C.3: A plot showing the MGS calculated centre (red) and outer (blue) contact pulse shapes for the 55.0mm 65.0mm, 67.0mm and 85.0mm depth interactions described in *Figure C.2.* The core pulses for the 65.0mm, 67.0mm and 85.0mm interaction show unphysical charge collection times and do not reach their maximum amplitudes. For the 85.0mm interaction, the termination of the *hole* trajectory on the passivated back plane also results a reduced outer contact pulse height.

are shown in red, the interaction segment pulses in blue and the other outer contact pulse shapes in green. The segment boundary between sectors B and A should occur at 330.0^o, however the transition is shown to occur at some angle between 331.0^o and 332.5^o. Also, for interactions that occur at angles of up to $\pm 2^o$ from the segment boundaries, the interpolation steps show quasi charge pulses induced on neighbouring segments. This result is unphysical and the distorted pulses cannot be utilised for validation purposes. Charge sharing can occur experimentally [Coo07], however it would require the simulation to model and track the diffusion of electron and *hole* charge clouds. The interpolation problems described above also extend to interactions that occur <2mm from any surface of the crystal. Thus there are significant portions of the geometry that cannot be included in the validation.

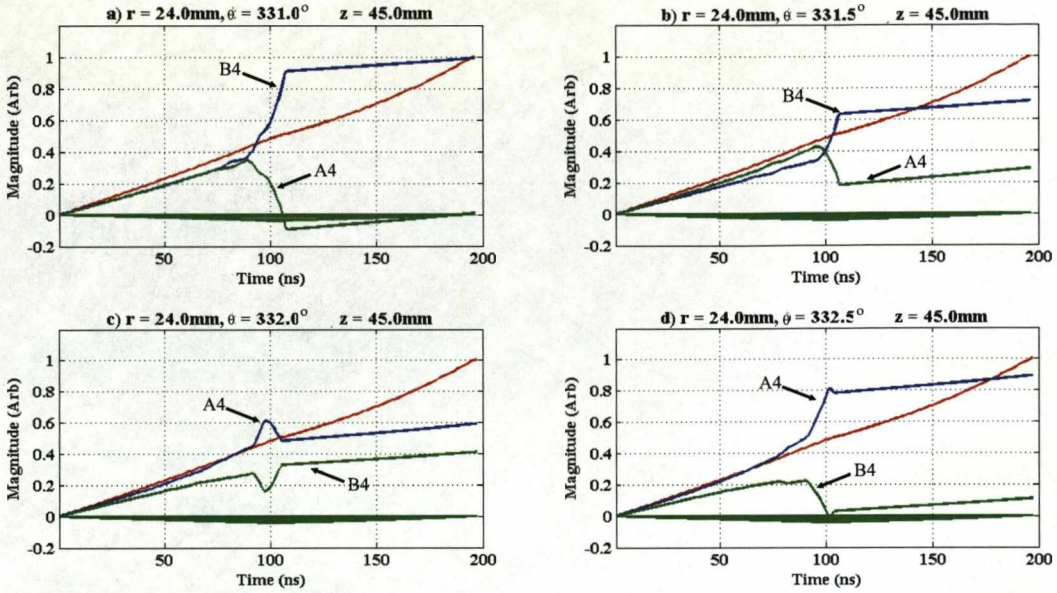

Figure C.4: A plot showing the MGS calculated pulse shapes for a range of azimuthal interaction angles that cross the boundary between sectors B and A. a) to d) show the response for interactions at angles of 331.0°, 331.5°, 332.0° and 332.5° respectively. The depth and radius of interaction were kept constant. The sector boundary should occur at 330.0°, but is shown to be at $sim331.5°$. Also, the pulses calculated for the neighbouring outer contact segments are shown to be unphysical and distorted. These results are a direct consequence of the definition of the hexaconical geometry on a cubic grid and the interpolation steps required to track the charges as they migrate through the crystal.

The details of the final set of MGS input parameters used in the validation against experimental data are described in *Section 4.4*. To overcome the limitations of the electric potential calculation, the back spacing was adjusted to 50mm in order to mirror the length of the prototype detector. This adjustment maintains the linearity of the potential surfaces resulting in a greater fraction of simulated pulses that can be validated against the experimental data. The passivation was also neglected as its presence compounded the effects on the electric potential in a way that is not fully understood.

Appendix D

Singles Front-Face Scan Results

Intensity, rise time and image charge asymmetry distributions have been derivedfrom the ^{137}Cs front-face singles scan of the S002 AGATA symmetric prototype detector. A detailed discussion of the trends observed can be found in *Section 5.5.* A brief description of the distributions for each of the six rings of the detector is presented below.

D.1 Intensity Profile

Figure D.1a to *Figure D.1f* show the fold one, photo-peak, ring gated response as a function of x-y position. The number of counts is highest in the centre of each segment in ring one. This is due to the high probability of absorption of the 662keV gamma-rays in the front region of the crysatal. At the edges of the segments, the number of counts is significantly lower due to the increased probability of the photons scattering out of the segment. If the detector were cylindrical, the distributions for rings two to six would be qualitatively similar, but with ever decreasing statistics as a function of depth. However the tapered edges of the crystal allow gamma-rays to probe the outer radii of the segments directly, giving rise to the bright fringes of intensity observed in *Figures D.1b to D.1f.* Also, the introduction of the bore hole in rings two to six reduces the probability of each photon remaining confined to a single segment, resulting in a reduction of counts at radii between 5mm and 15mm. This is also the reason as to why the segment boundaries are visible as lines of minimum intensity.

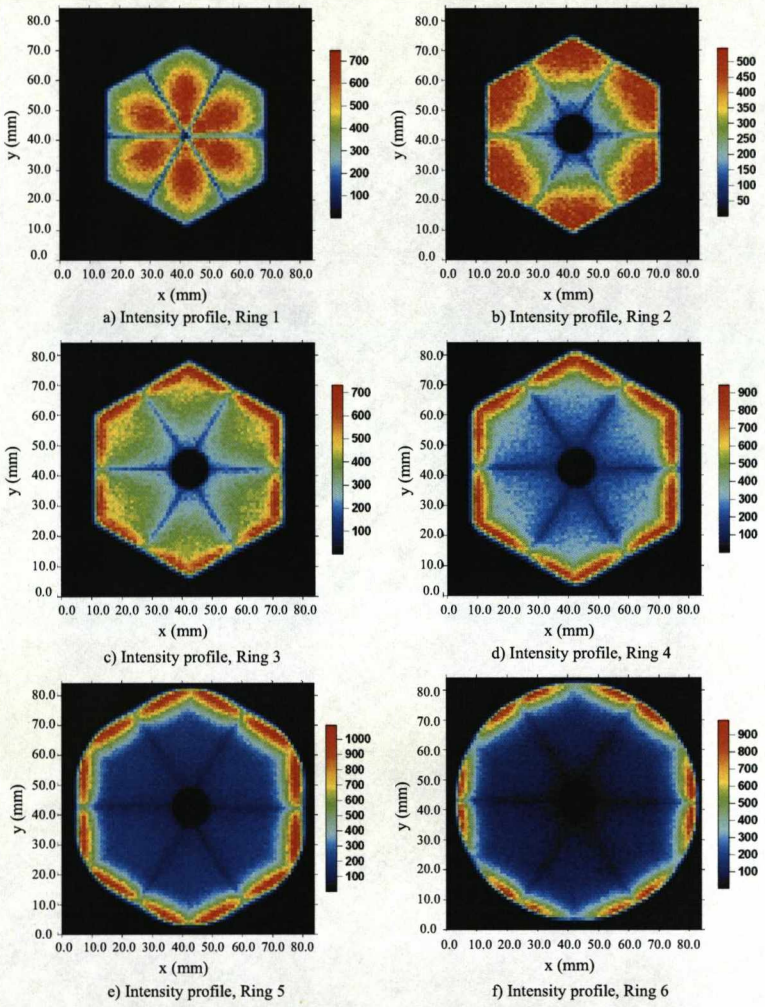

Figure D.1: Intensity profile showing the number of fold one photo-peak events as a function of scanning table position, for the six rings of the AGATA S002 prototype detector. The highest fraction of counts is observed in the front rings of the detector. The bright fringes in rings three to six are a result of the geometry of the crystal. At large radii, the tapered front portion of the crystal allows the beam to probe these rings directly. The segment boundaries are clearly visible as the projections require the event to be confined to a single segment and the there is an increased probability of inter-segment scattering as the boundary is approached.

Rise time Parameterisation

Figure D.2a to *Figure D.2f* and *Figure D.3a* to *Figure D.3f* show the mean centre contact T30 and T90 distributions as a function of scanning table position for each of the six rings

of the AGATA S002 prototype detector. *Figure D.4a* to *Figure D.4f* and *Figure D.5a* to *Figure D.5f* show equivalent outer contact distributions. The values were calculated from fold one photo-peak events. The crystallographic lattice orientation is mapped onto each distribution. The reader should note that in all cases, the x and y axes correspond to the scanning table coordinates.

- For each of the six rings, the core T30 is generally shown to increase as a function of radius from the centre, as the distance to the anode increases. Contrastingly, for rings two to five, the outer contact T30 increases as a function of radius due to the increased distance to the cathode. The outer contact T30 for ring one shows a relatively uniform distribution as the average interaction distance from the front face of the crystal stays relatively constant as a function of radius. It is the combination of the electrostatic coupling with the varying electric field strength and anisotropic charge carrier drift velocities that gives rise to the wide variation in rise time as a function of position in the majority of the crystal.

- For rings two to five, the centre and outer contact T90 distributions show the characteristic long-short-long variation as a function of radius. The shortest rise times occur at central radii where the charge carriers have equal drift times. The ring one gated distributions show the shortest rise times under the central anode where the distance between the electrodes is small.

Image Charge Parameterisation

Figure D.6 shows the image charge asymmetry, as a function of position, for the segments laterally adjacent to the interaction segment. For the calculation, the difference was derived as the area of the image charge in the anticlockwise segment minus that of the image charge in the clockwise segment. As such, the asymmetry parameter is maximum close to the anticlockwise segment. The regions of low sensitivity in the centre of each segment are the result of the bipolar image charge shape.

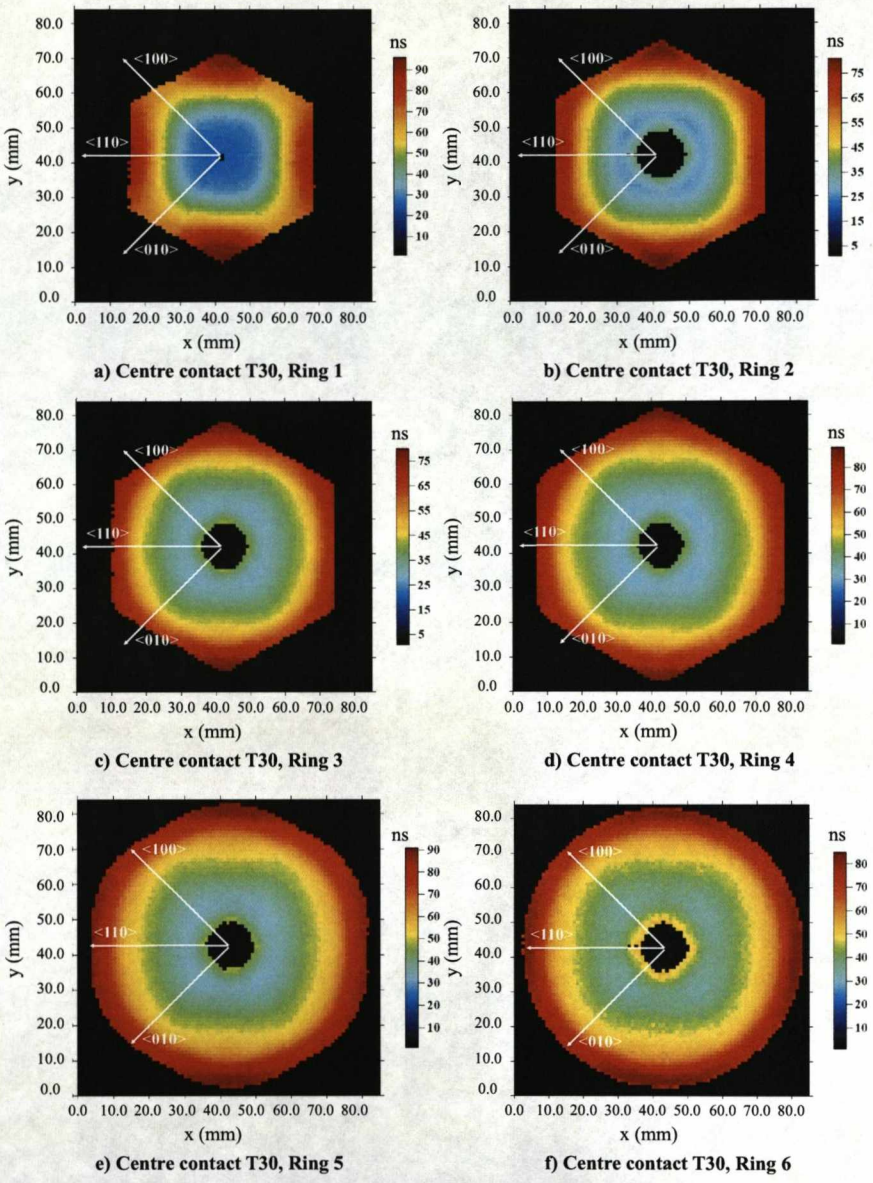

Figure D.2: Mean centre contact T30 distribution for fold one photo-peak events, gated on the ring in which the interaction occurred. The crystallographic planes are indicated with the white arrows. T30 is shown to increase as a function of radius from the core, for all six rings. The effect of the anisotropic mobility due to the angle between the electric field vector and lattice orientation is shown by the square region of fast rise times. The fastest T30 values are shown to correlate with the alignment of the electric field to the <110 > direction.

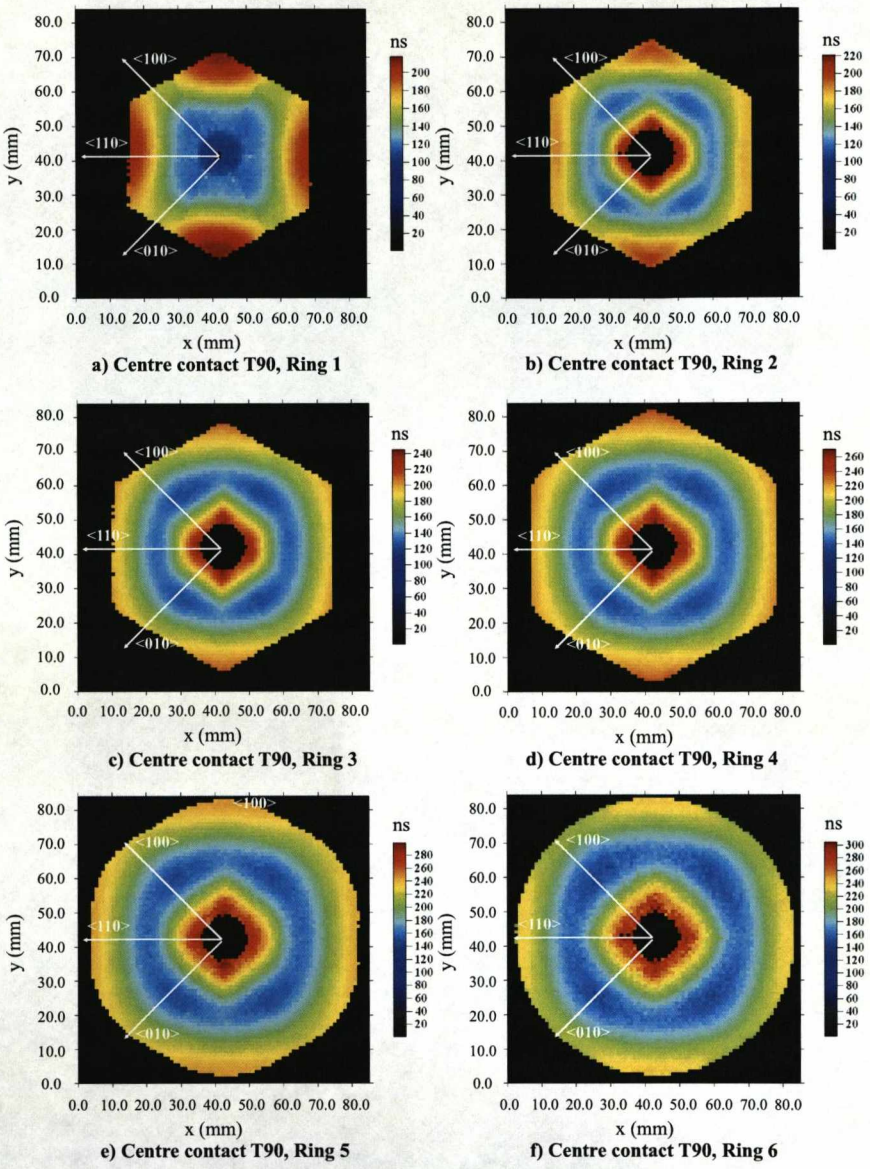

Figure D.3: Mean centre contact T90 distribution for fold one photo-peak events, gated on the ring in which the interaction occurred. The crystallographic planes are indicated with the white arrows. The slowest T90 values are at small and large radii, with the minima at mid-radii. The longest rise times are close to the centre contact where the charge carrier drift is dominated by the transport of the *holes*.

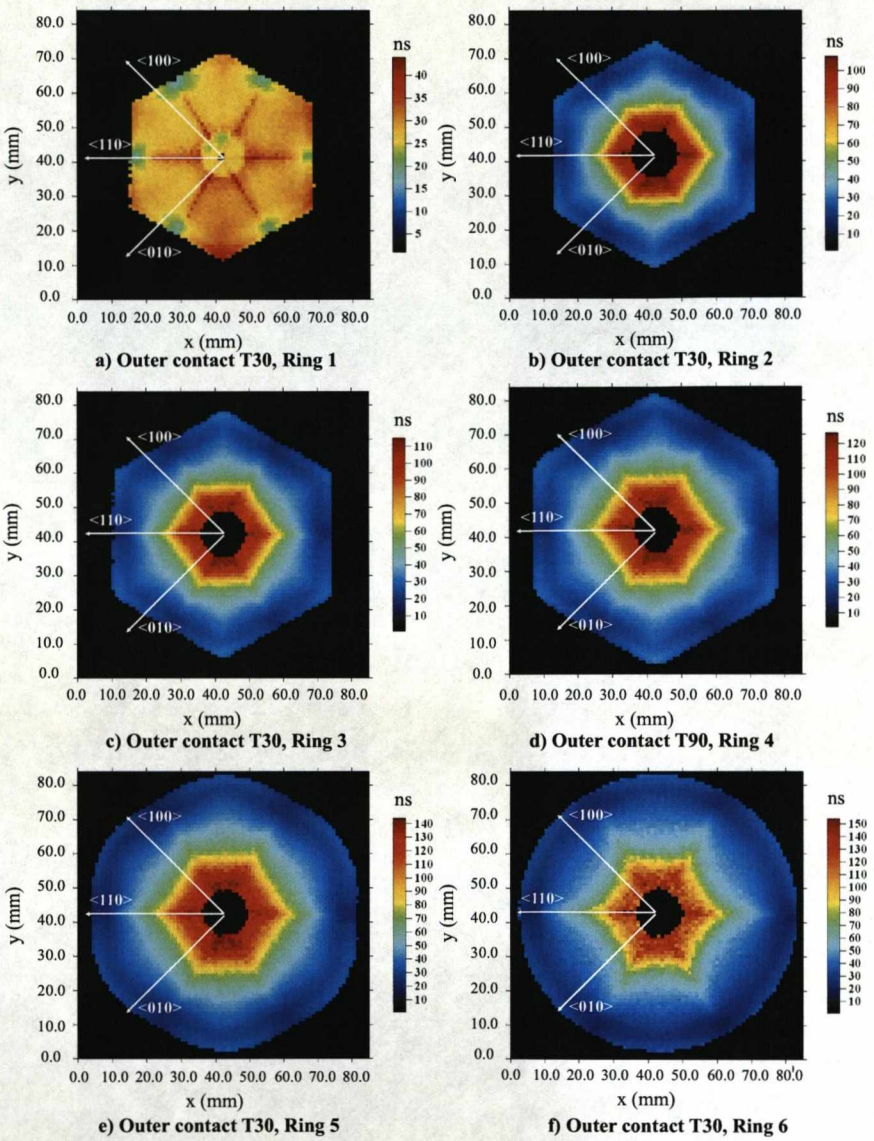

Figure D.4: Mean outer contact T30 distribution for fold one photo-peak events, gated on the ring in which the interaction occurred. The crystallographic planes are indicated with the white arrows. For rings two to six, T30 is shown to decrease as a function of radius from the core. The effect of the rate of change of weighting potential as a function of azimuthal angle gives rise to the hexagonal region of slow rise times that surrounds the central anode. For ring one, the steep gradient of each cathode weighting potential that extends from the front face and sides of the crystal causes a similar fast initial rise to the pulse shape at all interaction positions.

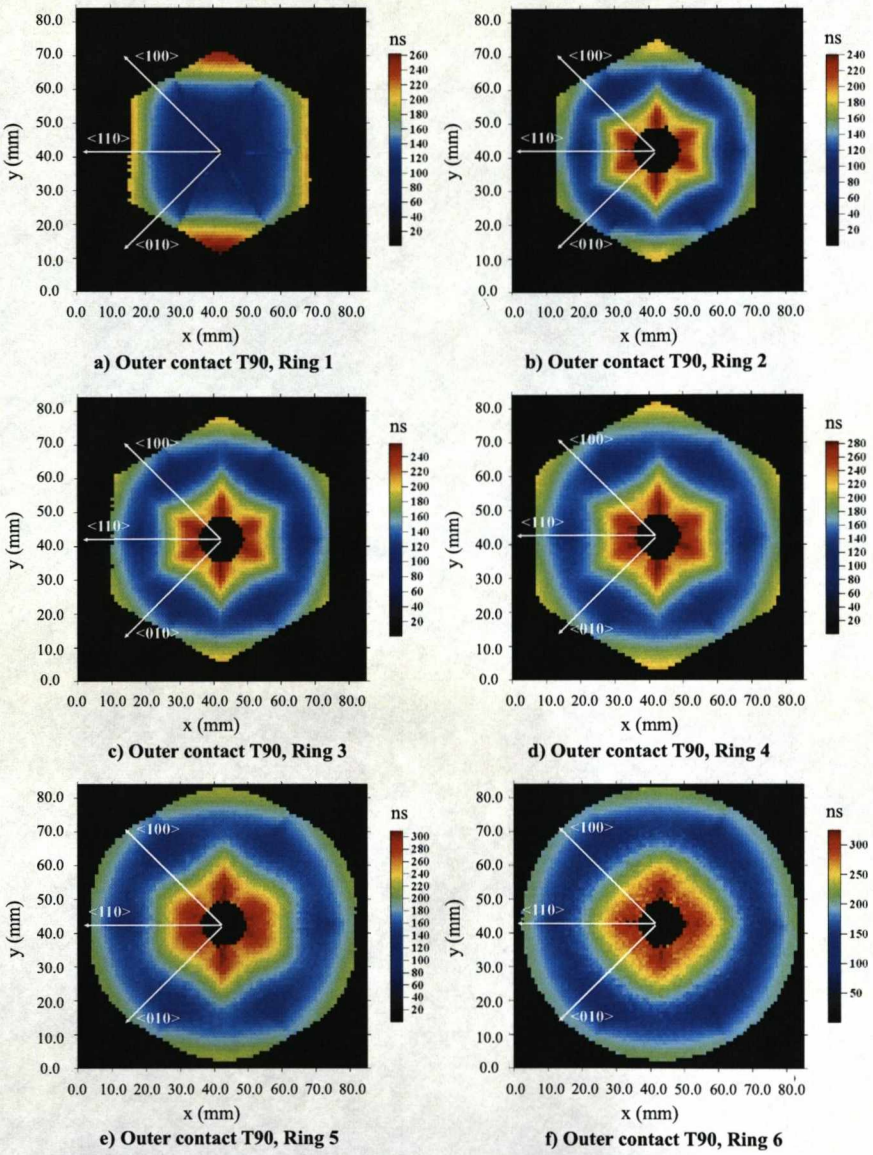

Figure D.5: Mean outer contact T90 distribution for fold one photo-peak events, gated on the ring in which the interaction occurred. The crystallographic planes are indicated with the white arrows. The slowest T90 values are at small and large radii, with the minima at mid-radii. The longest rise times are close to the centre contact where the charge carrier drift is dominated by the transport of the *holes*.

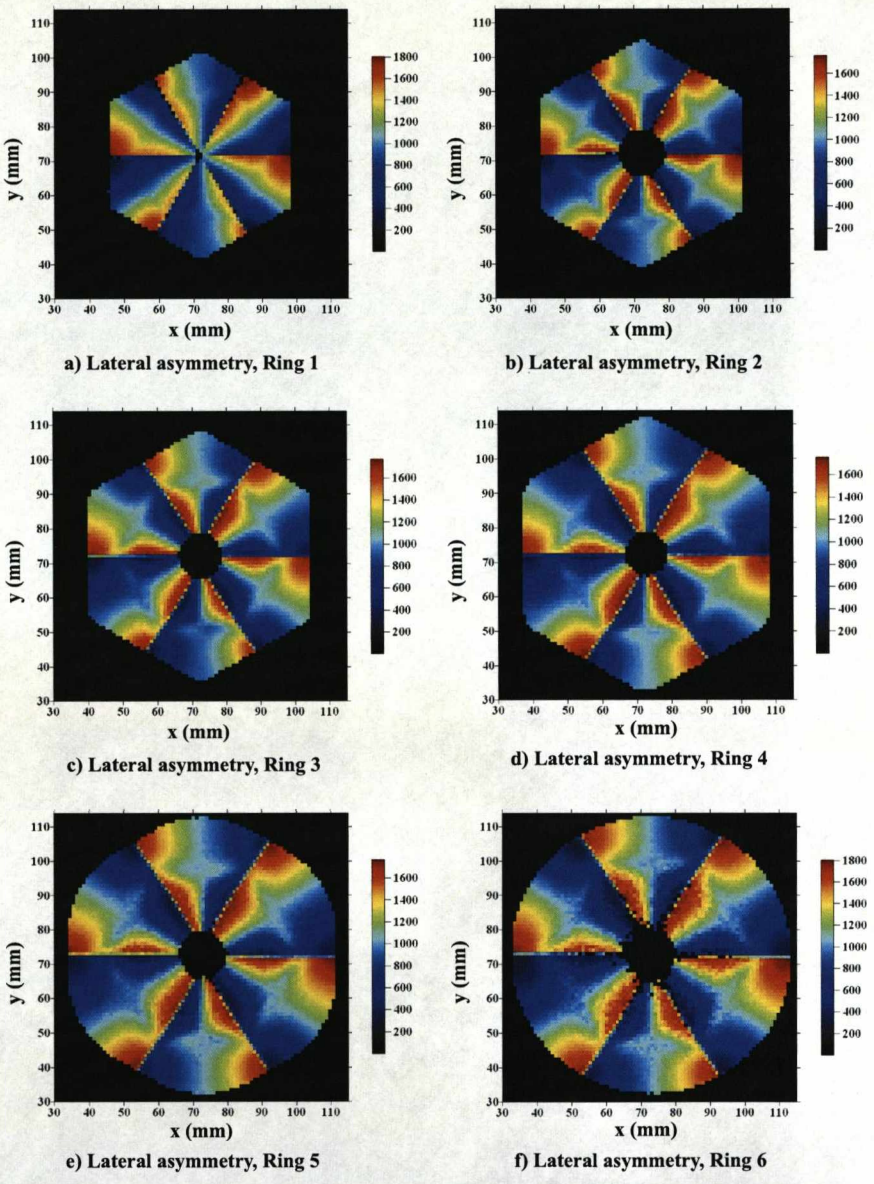

Figure D.6: Ring gated lateral image charge asymmetry distributions for the AGATA S002 prototype detector. The asymmetry parameter is calculated as the difference in area of the image charge on the electrode clockwise of the interaction segment with respect to that on the anticlockwise electrode. The asymmetry is maximum for interactions close to the anticlockwise segment boundary and falls away as a function of azimuthal angle approaching the clockwise boundary.

Appendix E

S002 Similarity Parameterisation

Detailed comparisons of the experimental and simulated S002 pulse shape databases have been performed in order to validate the performance of MGS. This appendix contains the graphical representations of these comparisons, referred to in the main text. The 2D surface plots showing the variation in the similarity parameter, $log_{10}\Delta s$, at all x-y positions for the interaction segment, centre contact, and clockwise, anticlockwise, upper and lower image charges are presented below. The overall distributions show several systematic trends:

1. *Centre contact real charge response* - The agreement is best for interactions at intermediate radii in zones two and three For these positions the experimental rise times are fastest and follow the fast rise times observed in the simulation. For the front ring the agreement is more complex and varied.

2. *Outer contact real charge response* - The agreement is generally good and is best in zones two and three for interactions at large radii. As for the core, the pulse shapes follow the fast rise times observed in MGS. However, there is also good agreement at small radii, close to the core, where the drift is entirely dominated by the *hole* transport. In the front ring the distribution is varied.

3. *Outer contact lateral image charge response* - The agreement between the experimental and simulated image charge response, for the segments laterally adjacent to the interaction segment, is very good and improves as a function of increasing magnitude. This is due to the improved time alignment.

4. *Outer contact vertical image charge response* - The agreement between the experimental and simulated image charge response, for the segments vertically adjacent to the interaction segment, is reasonable and also improves as a function of increased magnitude. Again this is due to the increased precision with which the pulses were time aligned. The agreement is however worse than for the laterally adjacent image charges. This is primarily due to the levels of cross-talk that were not accounted for in the database.

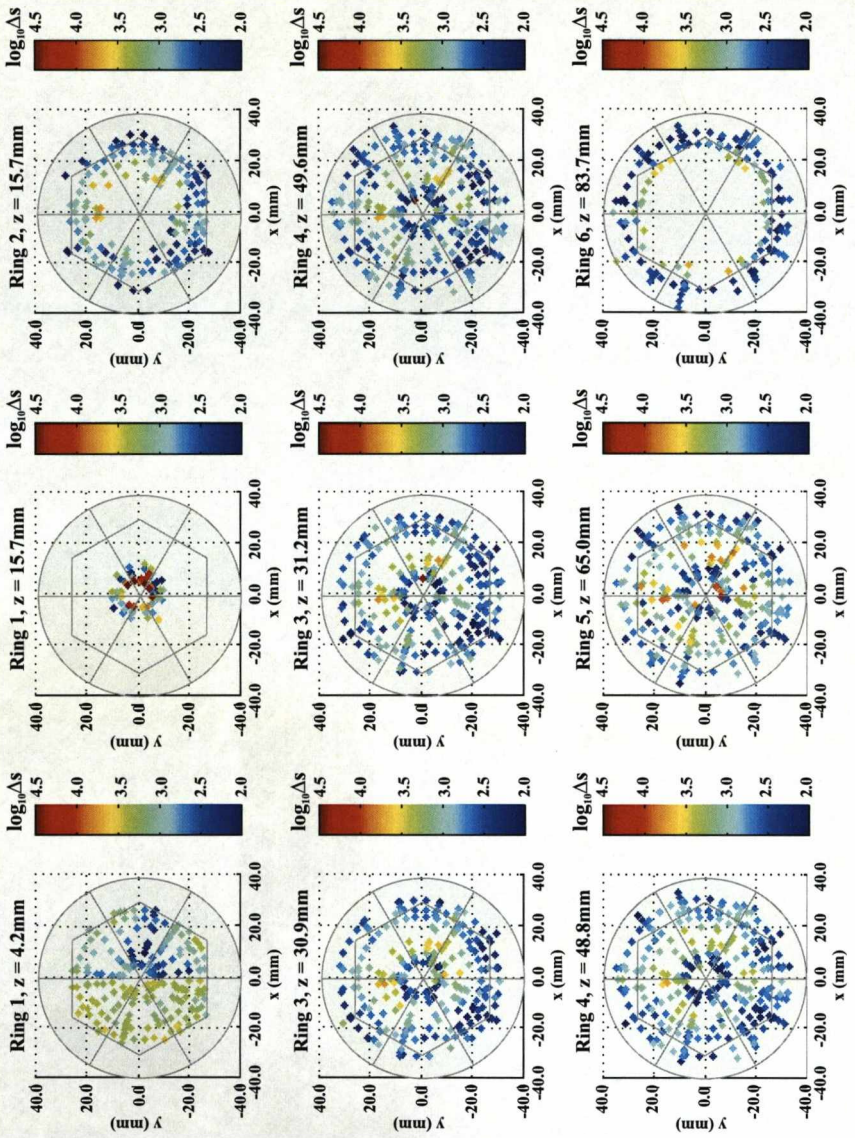

Figure E.1: A figure showing the similarity parameter for the outer contact real charge pulses, as a function of x-y position in each of the nine depth categories. The distributions show a measure of the difference between the experimental and simulated S002 pulse shapes throughout the detector volume.

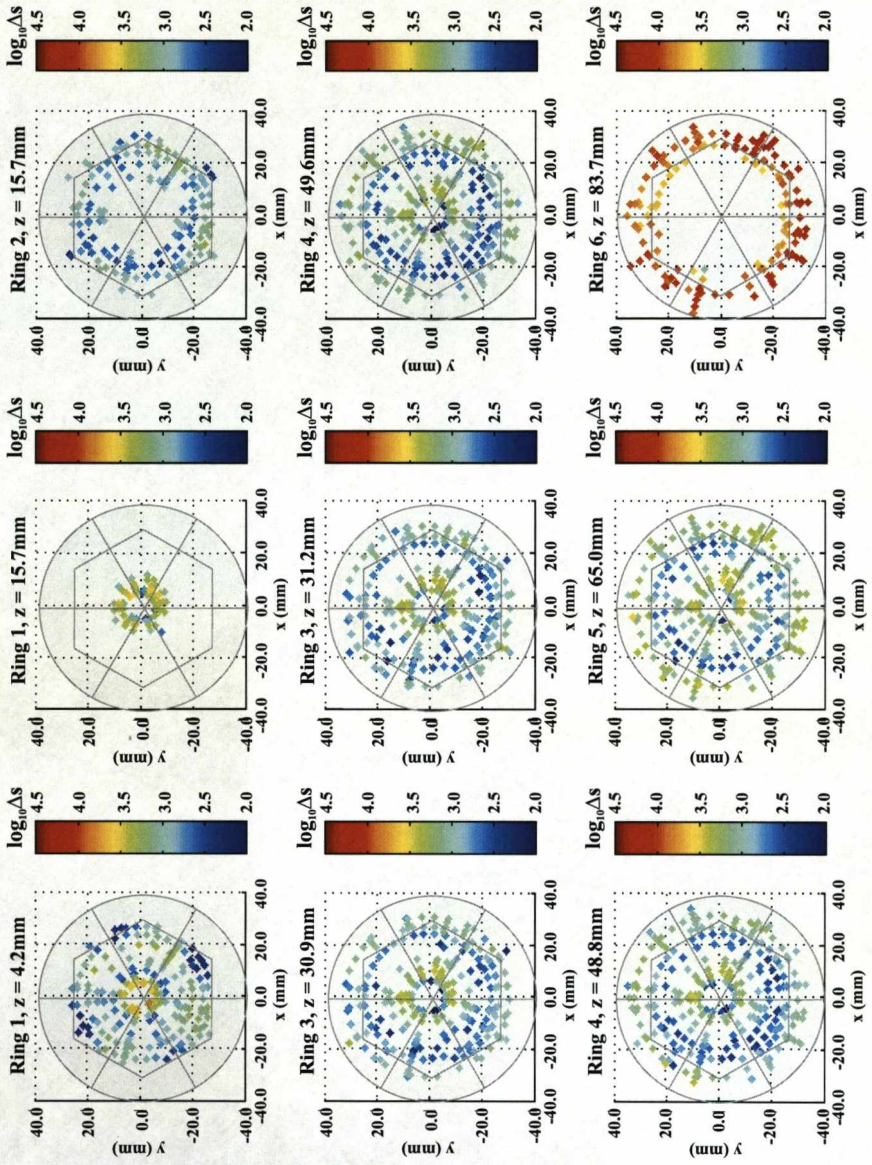

Figure E.2: A figure showing the similarity parameter for the centre contact real charge pulses, as a function of x-y position in each of the nine depth categories. The distributions show a measure of the difference between the experimental and simulated S002 pulse shapes throughout the detector volume.

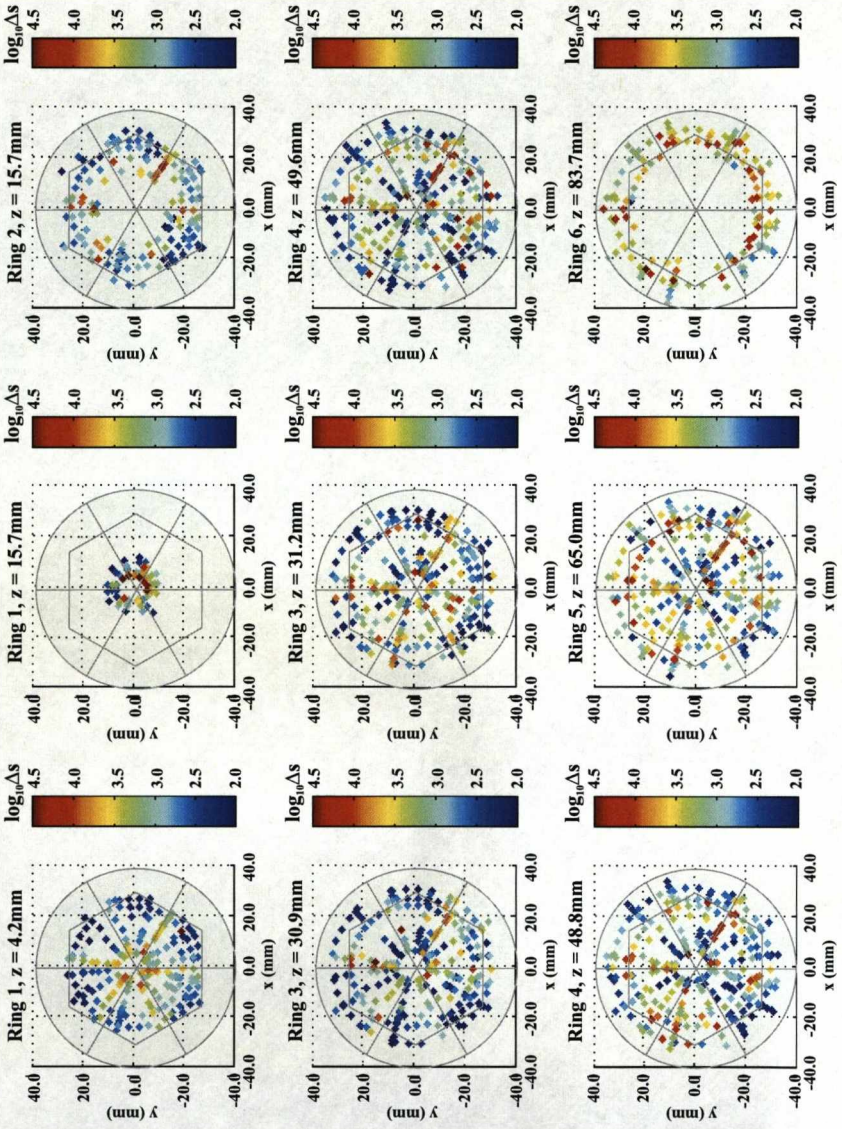

Figure E.3: A figure showing the similarity parameter for the clockwise horizontally adjacent image charge pulses, as a function of x-y position in each of the nine depth categories. The distributions show a measure of the difference between the experimental and simulated S002 pulse shapes throughout the detector volume.

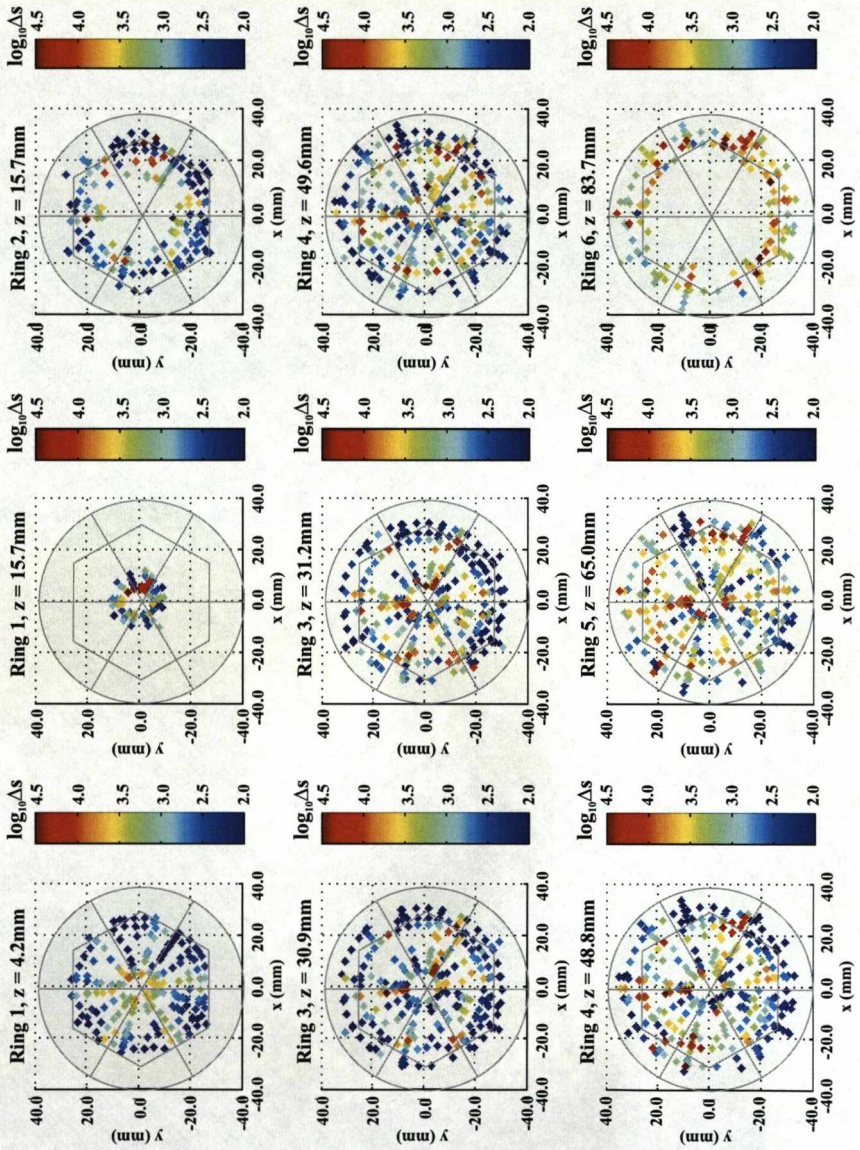

Figure E.4: A figure showing the similarity parameter for the anticlockwise horizontally adjacent image charge pulses, as a function of x-y position in each of the nine depth categories. The distributions show a measure of the difference between the experimental and simulated S002 pulse shapes throughout the detector volume.

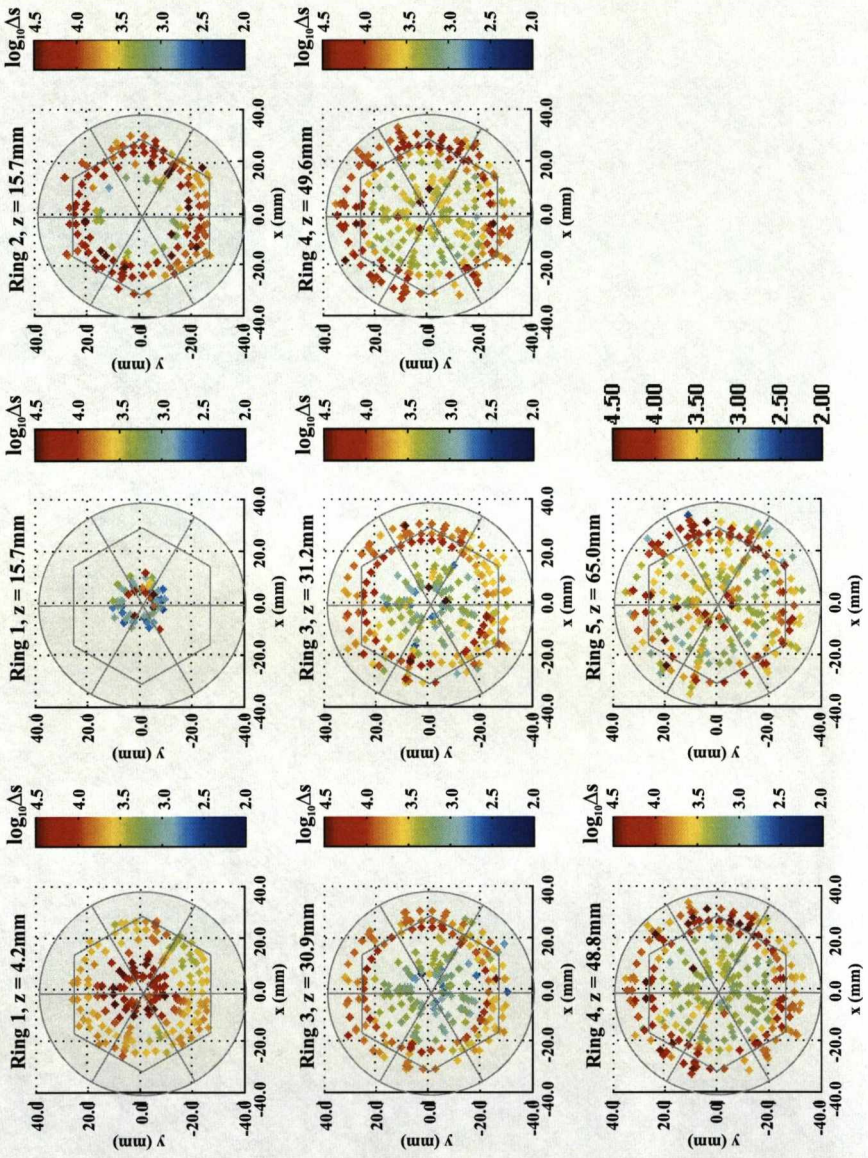

Figure E.5: A figure showing the similarity parameter for the upper vertically adjacent image charge pulses, as a function of x-y position in each of the nine depth categories. The distributions show a measure of the difference between the experimental and simulated S002 pulse shapes throughout the detector volume.

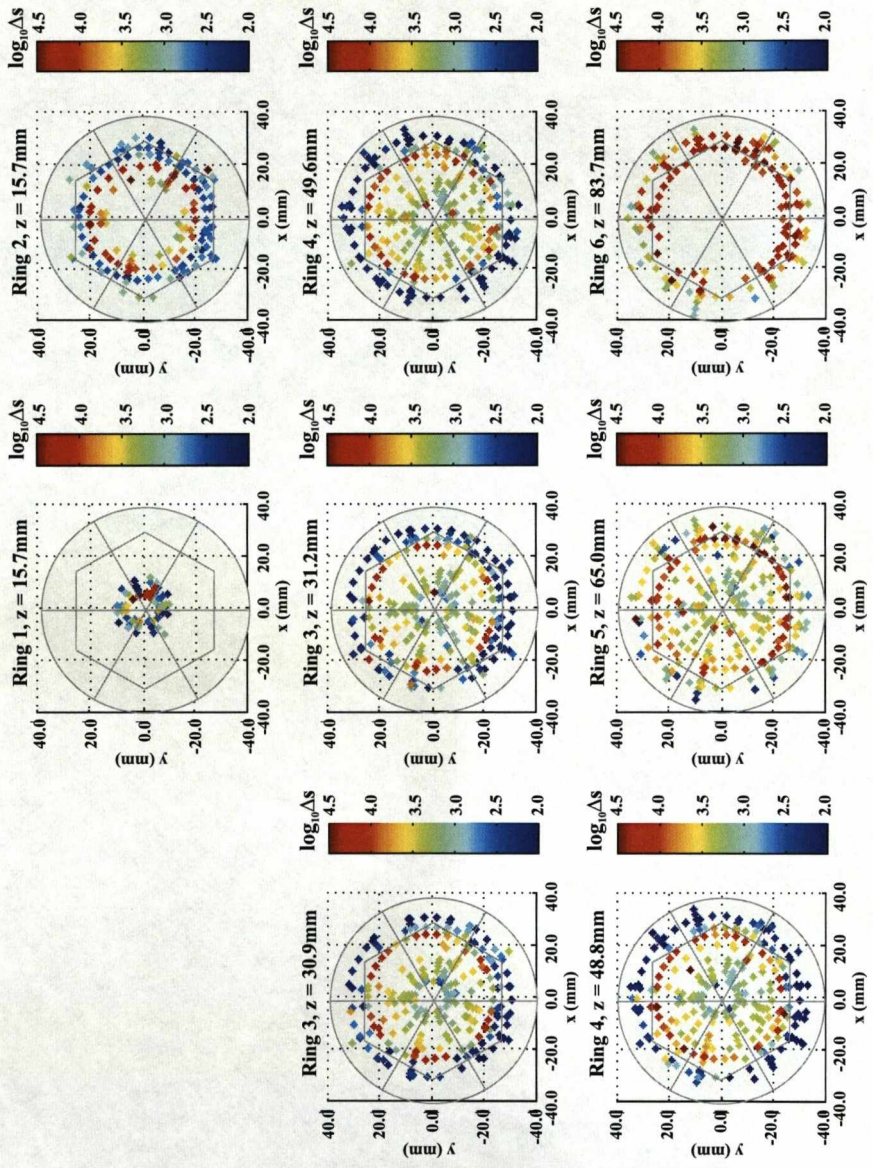

Figure E.6: A figure showing the similarity parameter for the lower vertically adjacent image charge pulses, as a function of x-y position in each of the nine depth categories. The distributions show a measure of the difference between the experimental and simulated S002 pulse shapes throughout the detector volume.

Bibliography

[Alv03] Gamma-ray Tracking, C. Rossi Alvarez, AGATA GLP Meeting, Legnaro, (2003).

[Alv04] The Advance Gamma Tracking Array (AGATA), C. Rossi Alvarez, Braz. Jour. Phys, Vol.34, p995 (2004).

[Asa97] A five-HPGe detector system for γ-γ angular correlation measurements for mass-separated short-lived nuclei, M. Asai, K. Kawade, H. Yamamoto et al, Nucl. Instr. Meths. Phys. Res. A, Vol.398, p265 (1997).

[Bau07] AGATA LLP Digitiser specifications draft 4.1, R. Baumann, P.J. Coleman-Smith, I.H. Lazarus, P. Medina, C. Santos, J. Thornill, D. Wells, Private communication - University of Liverpool (2006).

[Bea95] Large arrays of escape suppressed spectrometers for nuclear structure experiments, C.W. Beausang and J. Simpson, J. Phys. G. Nucl. Part. Phys, Vol.22, p527 (1996).

[Bea03] GRETA: The Gamma-Ray Energy Tracking Array. Status of the development and physics opportunities, C.W. Beausang, Nucl. Instr. Meths. Phys. Res. B, Vol.204, p666 (2003).

[Bla05] Spectroscopy with radioactive ion beams at the HRIBF for nuclear astrophysics, J.C. Blackmon et al, J. Phys. G: Nucl. Part. Phys, Vol.31, p1405 (2005).

[Bru06a] Characterization of large volume HPGe detectors Part I: Electron and hole mobility parameterization, B. Bruyneel, Nucl. Instr. Meths Phys. Res. A, Vol.569 p764 (2006).

[Bru06b] Characterization of large volume HPGe detectors Part II: Experimental results, B. Bruyneel, Nucl. Instr. Meths Phys. Res. A, Vol.569, p774 (2006).

[Bru07] AGATA Characterisation, B. Buryneel, AGATA Week Presentation (2007).

[Cav71] Extension of Ramo's theorem as applied to induced charge in semiconductor detectors, G. Cavalleri et al, Nucl. Instr. Meths. Phys. Res. Vol.92, p137 (1971).

[Che07] Web page: http://www.chemicalelements.com, last accessed 28/04/08.

[Coo07] Performancs of the SmartPET positron emission tomography system for small animal imaging, R. Cooper, PhD Thesis, University of Liverpool (2007).

[Cox67] Geometry Revisited, The mathematical association of America, H. Coxeter (1967).

[Cre07] A pulse shape analysis algorithm for segmented HPGe detectors, F. Crespi et al, Acta. Phys. Pol. B, Vol.38 p4 (2007).

[Dav52] Gamma-Ray absorption coefficients, C.M. Davisson, R.D. Evans, Rev. Mod. Phys, Vol.24 p79 (1952).

[Del99] GRETA: Utilizing new concepts in gamma-ray detection, M.A. Deleplanque, I.Y. Lee, K. Vetter, G.J. Schmid, F.S. Stephens, R.M. Clark, R.M. Diamond, P. Fallon, and A. O. Macchiavelli, Nucl. Instrum. Meths. Phys. Res. A, Vol.430, p292 (1999).

[Des05a] In-beam measurement of the position resolution of a highly segmented coaxial germanium detector, M. Descovich, I.Y. Lee, P. Fallon, M. Cromaz, A.O. Macchiavellia D.C. Radford, K. Vetter, R.M. Clark, M.A. Deleplanque, F.S. Stephens, D. Ward, Nucl. Instr. Meths. Phys. Res A. Vol.553, p535 (2005).

[Des05b] Effects of neutron damage on the performance of large volume segmented germanium detectors, M. Descovich, I.Y. Lee, P.N. Luke et al, Nucl. Instr. Meths. Phys. Res A. Vol.545, p199 (2005).

[Dif07] Web page: http://www.diffpack.com, last accessed 28/04/08.

[Fan47] Ionization yield of radiations. II. the fluctuations of the number of ions, U. Fano, Phys Rev, Vol.72, p26 (1947).

[Fem07] Web Page: http://www.femlab.com, last accessed 28/04/08.

[Geo93] Digital pulse processing in high resolution, high throughput, gamma-ray spectroscopy, U. Georgiev and W. Gast, IEEE Trans Nucl. Sci. Vol.40, p770 (1992).

[Gil95] Practical gamma-ray spectrometry, Jonh Wiley and Sons, G. Gilmore and J. Hemingway (1995).

[Gor01] Magnetic rotation in ^{197}Pb and ^{198}Pb, A. Gorgen et al, Nucl. Phys. A, Vol.683, p109 (2001).

[Gor03] Position sensitivity of the AGATA prototype crystal analysed using a database of calculated pulseshapes, A. Gorgen, CEA Saclay communication, (2003).

[Gro05] Characterisation of an EXOGAM clover germanium detector, S. Gross, PhD Thesis, University of Liverpool (2005).

[Ham04] Ambiguity in gamma-ray tracking of two-interaction events, N.J. Hammond, T. Duguet, C.J. Lister, Nucl. Instr. Meths. Phys. Res. A, Vol.547, p535 (2005).

[He00] Review of the Shockley Ramo theorem and its application in semiconductor gamma-ray detectors, Z. He, Nucl. Instr. Meths. Phys. Res. A, Vol.463 (2001).

[Hul95] Temperature sensitivity of surface channel effects on high-purity germanium detectors, E. Hill, Nucl. Instr. Meths. Phys. Res. A, Vol.364, p488 (1995).

[Iba95] Solid State Physics, Second Edition, Springer, H. Ibach, p349 (1995).

[Jer77] The Shannon sampling theorem. Its various extensions and applications: A tutorial review, A.J. Jerri, Proceedings of the IEEE, Vol.65, p1565 (1977).

[Jon02] Calibration of Compton polarimeters, G.D. Jones, Nucl. Instr. Meths. Phys. Res. A, Vol.491, p452 (2002).

[Kno00] Radiation Detection and Measurement, Third Edition, John Wiley and Sons Inc, G.F. Knoll, (2000).

[Knp65] Interaction of electrons, North Holland, G. Knop, W. Paul (1965).

[Kro01] Simulation and analysis of pulse shapes from highly segmented HPGe detectors for the gamma-ray tracking array MARS, T. Kroll and D. Bazzacco, Nucl. Instr. Meths. Phys. Res. A, Vol.463, p227 (2001).

[Kro06] A genetic algorithm for the decomposition of multiple hit events in the γ-ray tracking detector MARS, T. Kroll, D. Bazzacco, Nucl. Instr. Meths. Phys. Res. A, Vol.565, p691 (2006).

[Laz03] The GRT4 VME pulse processing card for segmented Germanium detectors, I.H. Lazarus et al, IEEE Trans. Nucl. Sci, Vol.51, p1165 (2004).

[Laz05] AGATA Preprocessing Document, I. Lazarus, Private communication (2005).

[Lee90] The GAMMASPHERE, I.Y. Lee, Nucl. Phys. A, Vol.520, p641 (1990).

[Lee06] The future of gamma-ray spectroscopy: GRETA, The Gamma-Ray Energy Tracking Array - Contribution to the NSAC long-range plan, I.Y. LEE, (2006).

[Leo94] Techniques for nuclear and particle physics experiments, Second Edition, Springer Verlag, R. Leo (1994).

[Lis00] How far from stability can we go using Gammasphere and the FMA? C.J. Lister et al, J. Res. Natl. Inst. Stand. Technol, Vol.105, p137 (2000).

[Lop04] Gamma-ray tracking algorithms: A comparison, A. Lopez-Martens, K. Hauschild, A. Korichi, J. Roccaz, J-P. Thibaud, Nucl. Instr. Meths. Phys. Res. A, Vol.533, p454 (2004).

[Mar04] AGATA DAQ and global level processing, Private communication, G.Maron (2004).

[Mat07] Web page: http://www.mathworks.com, last accessed 28/04/08.

[Med04] A simple method for the characterisation of HPGe detectors, P. Medina, C. Santos, Di Villaume, Istr. Meas. Tech. Conf (2004).

[Mil03] Improvements in γ-ray reconstruction with positive sensitive Ge detectors using the backtracking method, L. Milechina, B. Cederwall, Nucl. Instr. Meths. Phys. Res. A, Vol.508, p394 (2003).

[Mil04] Performance considerations for γ-ray tracking detectors, L. Milechina, B. Cederwall, Nucl. Instr. Meths. Phys. Res. A, p525 (2004).

[Mih00] The influence of anisotropic electron drift velocity on the signal shapes of closed-end HPGe detectors, L. Mihailescu, W. Gast, R.M. Lieder, H. Brands, Nucl. Instr. Meths. Phys. Res. A, Vol.447, p350 (2000).

[Muk76] Range of electrons and positrons, T. Mukoyama, Nucl. Instr. Meths. Phys. Res, Vol.34 p125 (1976).

[Nat63] Anisotropy of the conductivity of n-type germanium at high electric fields, M.I. Nathan, Phys Rev, Vol.130, p2202 (1963).

[Nel08] A method to evaluate the efficacy of a γ-ray tracking array, L. Nelson, PhD Thesis, University of Liverpool (2008).

[Nil95] Shapes and shells in nuclear structure, S. Nilsson and I. Ragnarsson, Cambridge University Press (1995).

[Nol90] EUROGAM - A high efficiency escape supressed spectrometry array, P.J. Nolan, Nucl. Phys. A, Vol.520, p657 (1990).

[Nol94] Large Arrays of escape supressed gamma-ray detectors, P.J. Nolan, F.A. Beck, D.B. Fossan, Annu. Rev. Nucl. Part. Sci, Vol.45 p561 (1994).

[Ola06] Pulse Shape Analysis for the location of the interactions in AGATA, A. Olariu, P. Desesquelles, C. Diarra, P. Medina, C. Parisel, and C. Santos, IEEE Trans. Nucl. Sci, Vol.53, p1028 (2006).

[Oma87] Drift velocity and diffusivity of hot carriers in germanium: Model calculations, M. Omar and L. Reggiani, Solid State Electronics, Vol.30, p1351 (1987).

[Pal96] A new method for the determination of the entry position of gamma-rays in high purity germanium detectors by current pulse analysis, L. Palafox Gamir, PhD Thesis, Cranfield University (1996).

[Pig01] The experiments on EUROBALL: Status and perspectives, M. Pignanelli, Czech. Jour. Phys, Vol.51, p41 (2001).

[Pre99] Numerical Recipes in C, Cambridge University Press, W.H. Press, (1990).

[Pul05] AGATA hybrid preamplifiers with pulser V2.1, A. Pullia and G. Pascovici, Private communication (2005).

[Rad95] ESCL8R and LEVITSR: Software for interactive graphical analysis of HPGe coincidence data sets, D.C. Radford, Nucl. Instr. Meths. Phys. Res. A, Vol.361, p297 (1995).

[Rad00] Web page: http://radware.phy.ornl.gov/gf3/gf3.html, last accessed, 28/04/08.

[Rad08] Status of GRETINA signal decomposition, D. Radford, Presentation at GRETINA meeting (2008).

[Rak88] Low-noise techniques in detectors, V. Radeka, Ann, Rev. Nucl. Part. Sci, Vol.38, p224 (1988).

[Ram39] Currents induced by electron motion, S. Ramo, Proc. Inst. Radio. Eng, Vol.27, p584 (1939).

[Rec07] In-beam test of the AGATA prototype tripple cluster, F. Recchia, Act. Phys. Pol B, Vol.38, p1297 (2007).

[Reg77] Hole drift velocity in germanium, L. Reggiani, Phys. Rev. B, Vol.16, p2781 (1977).

[Rei62] Drift velocity and anisotropy of hot electrons in n germanium, H.G. Reik and H. Risken, Phys. Rev, Vol.126, p1737 (1962).

[Rip06] Segmented quasi-coaxial HP-Ge detectors optimized for spatial localization of the events, G. Ripamonti, P. Pulici, R. Abbiati, Nucl. Instr. Meths. Phys. Res. A, Vol.568, p440 (2006).

[Ryb01] Influence of detector surface processing on detector performance, A.V. Rybka et al, Nucl. Instr. Meths. Phys. Res. A, Vol.458, p248 (2001).

[SB00] Solid State Elecrtonic Devices, Fifth Edition, B.G. Streetman and S. Banerjee, Prentice Hall (2000).

[Scb05] AGATA preamplifier response simulation manual, M. Schlarb, Private communication (2005).

[Sch99] A gamma-ray tracking algorithm for the GRETA spectrometer, G.J. Schmid, et al., Nucl. Instr. Meths. Phys. Res. A, Vol.430, p69 (1999).

[Sct94] A cryogenically cooled single-crystal BGO anti-Compton spectrometer, P. Schotanus et al, IEEE Trans. Nucl. Sci. Vol.41, p730 (1994).

[Sim97] The Euroball Spectrometer, J. Simpson, Z. Phys. A, Vol.358, p139 (1997).

[Sim05] The AGATA project, J. Simpson, J. Phys. G, Vol.31, p72 (2005).

[Sta03] Background subtraction for Doppler-shift attenuation and angular correlation measurements with multi-detector Ge arrays, K. Starosta et al, Nucl. Instr. Meths. Phys. Res. A, Vol.515, p771 (2003).

[Suf92] Silicon photodiode readout of scintillators and associated electronics, M. Suffert, Nucl. Instr. Meths. Phys. Res. A, Vol.322, p523 (1992).

[Sze01] Semiconductor devices physics and technology, Second Edition, Argosy Publishing, S.M. Sze (2001).

[Tur06] Characterisation of a planar HPGe detector, G. Turk, PhD Thesis, University of Liverpool (1997)

[Vet00] Three-dimensional position sensitivity in two-dimensionally segmented HPGe detectors, K. Vetter et al, Nucl. Instr. Meths. Phys, Res. A, Vol.452, p223 (2000).

[Val03] Performance of a 6 X 6 segmented germanium detector for gamma-ray tracking, J.J. Valiente-Dobion, C.J. Pearson, P.H. Regan, P.J. Sellin, Nucl. Instr. Meths. Phys. Res. A, Vol.505, p174 (2003).

[Ven07] Grid Search - A possible PSA algorithm for the AGATA demonstrator, R. Venturelli, Presentation, AGATA Week (2007).

[Wie02] Gamma-ray tracking with segmented HPGe detectors, O. Wieland, Braz. Jour. Phys, Vol.33, p206 (2003).

[Wys86] Doppler Effects in high spin spectroscopy, R. Wyss, Nucl. Instr. Meths. Phys. Res. A, Vol.256, p499(1987).